8-2016

Modeling transport phenomena and uncertainty quantification in solidification processes

Kyle S. Fezi
Purdue University

Graduate School Form
30 Updated 12/26/2015

PURDUE UNIVERSITY
GRADUATE SCHOOL
Thesis/Dissertation Acceptance

This is to certify that the thesis/dissertation prepared

By Kyle S. Fezi

Entitled

MODELING TRANSPORT PHENOMENA AND UNCERTAINTY QUANTIFICATION IN SOLIDIFICATION MODELING

For the degree of Doctor of Philosophy

Is approved by the final examining committee:

Matthew J.M. Krane
Chair

David Johnson

Kevin Trumble

Timothy Fisher

To the best of my knowledge and as understood by the student in the Thesis/Dissertation Agreement, Publication Delay, and Certification Disclaimer (Graduate School Form 32), this thesis/dissertation adheres to the provisions of Purdue University's "Policy of Integrity in Research" and the use of copyright material.

Approved by Major Professor(s): Matthew J.M. Krane

Approved by: David Bahr 5/12/2016

Head of the Departmental Graduate Program Date

MODELING TRANSPORT PHENOMENA AND UNCERTAINTY QUANTIFICATION IN SOLIDIFICATION PROCESSES

A Dissertation

Submitted to the Faculty

of

Purdue University

by

Kyle S. Fezi

In Partial Fulfillment of the

Requirements for the Degree

of

Doctor of Philosophy

August 2016

Purdue University

West Lafayette, Indiana

For my wife and family

ACKNOWLEDGEMENTS

First I would like to thank my wife, Courteney, whose patience, understanding, and support made this endeavor possible. I am, and will be, forever grateful for having her in my life and I am excited to see where our future takes us. I would also like to thank my advisor Matthew J.M. Krane, who was always available with help and guidance. He had confidence in me when I did not, and his nomination for the Bilsland Fellowship, that I later received, gave me the freedom to pursue this work. I must also thank Alex Plotkowski, who was always available (and willing) to talk science and became a close friend.

Financial support for this work was from Shandong Nanshan Aluminum Co., Beijing Nanshan Institute of Aeronautical Materials and the Purdue University Bilsland Dissertation Fellowship.

Technical support was given by Martin Hunt and Professor Alejandro Strachan, who developed the PRISM Uncertainty Quantification tool. Special thanks to Martin, who took time to teach me how to use the software and develop a tool on nanohub.org.

TABLE OF CONTENTS

Page

Page

Page

LIST OF TABLES

Table Page

Table Page

Table Page

LIST OF FIGURES

Figure Page

Figure Page

Figure Page

Figure Page

Figure Page

Figure Page

Figure Page

Figure Page

Appendix Figure Page

Appendix Figure Page

NOMENCLATURE

Latin Symbols

A_{in}	Inlet area
B	Buoyancy force
C	Composition
c	Specific heat
D	Mass diffusion coefficient
d_{diam}	Free-floating particle size
EE	Elementary effects
F	Fluid volume fraction
f	Phase mass fraction
g	Phase volume fraction
$\vec{g}$	Gravity
H	Enthalpy
h	Heat transfer coefficient
K	Permeability
k	Thermal conductivity
k_p	Partition coefficient
L_f	Latent heat

Latin Symbols

L_h	Vertical thickness of rigid mushy zone
M	Macrosegregation number
m_l	Slope of liquidus
m_s	Slope of solidus
P	Pressure
Q	Volumetric water flow rate
q”	Heat flux
SD	Sump depth
T	Temperature
ΔT_m	Freezing range
t	Time
t_s	Solidification time
u	Axial velocity component for DC casting; horizontal velocity component for static casting
V_{in}	Inlet velocity
$\forall$	Volume
$\Delta\forall_{shrink}$	Change in volume due to shrinkage
V_{spec}	Ingot volume fraction outside compositional specification
$\vec{V}$	Velocity vector
V_c	Casting speed
v	Radial velocity component for DC casting; vertical velocity component for static casting

Latin Symbols

W^i	Normalized Weibull deviation
X	Generic model input parameter
Δx	Control volume width
Y	Generic model output parameter
Δy	Control volume height
Z	Ingot axial height

Greek Symbols

α	Weibull shape parameter
β_S	Solutal expansion
β_T	Temperature expansion
Γ	Gamma function
ε	Function relating temperature to liquid fraction
η	Viscosity
λ_2	Secondary dendrite arm spacing
μ	Mean/Average
ρ	Density
$\Delta\rho$	Solid-liquid density difference
σ	Standard deviation
ϕ	Ingot diameter
ψ	Stream function

Greek Symbols

ω	Weibull scale parameter

Subscripts

∞	Ambient temperature
boil	Boiling water temperature
H_20	Cooling water temperature
IB	Incipient boiling criteria
j	Array position
l	Liquid phase
Liq	Liquidus
o	Initial/Nominal
s	Solid phase
s,crit	Critical solid fraction
ss	Steady state
Sol	Solidus
wall	Wall temperature

Superscripts

*	Relating to sensitivity
i	Parameter of interest
n	Iteration level
o	Previous time step

ABSTRACT

Fezi, Kyle S. Ph.D., Purdue University, August 2016. Modeling Transport Phenomena and Uncertainty Quantification in Solidification Processes. Major Professor: Matthew J.M. Krane.

Direct chill (DC) casting is the primary processing route for wrought aluminum alloys. This semicontinuous process consists of primary cooling as the metal is pulled through a water cooled mold followed by secondary cooling with a water jet spray and free falling water. To gain insight into this complex solidification process, a fully transient model of DC casting was developed to predict the transport phenomena of aluminum alloys for various conditions. This model is capable of solving mixture mass, momentum, energy, and species conservation equations during multicomponent solidification. Various DC casting process parameters were examined for their effect on transport phenomena predictions in an alloy of commercial interest (aluminum alloy 7050). The practice of placing a wiper to divert cooling water from the ingot surface was studied and the results showed that placement closer to the mold causes remelting at the surface and increases susceptibility to bleed outs.

Numerical models of metal alloy solidification, like the one previously mentioned, are used to gain insight into physical phenomena that cannot be observed experimentally. However, uncertainty in model inputs cause uncertainty in results and those insights. The

analysis of model assumptions and probable input variability on the level of uncertainty in model predictions has not been calculated in solidification modeling as yet.

As a step towards understanding the effect of uncertain inputs on solidification modeling, uncertainty quantification (UQ) and sensitivity analysis were first performed on a transient solidification model of a simple binary alloy (Al-4.5wt.%Cu) in a rectangular cavity with both columnar and equiaxed solid growth models. This analysis was followed by quantifying the uncertainty in predictions from the recently developed transient DC casting model. The PRISM Uncertainty Quantification (PUQ) framework quantified the uncertainty and sensitivity in macrosegregation, solidification time, and sump profile predictions. Uncertain model inputs of interest included the secondary dendrite arm spacing, equiaxed particle size, equiaxed packing fraction, heat transfer coefficient, and material properties. The most influential input parameters for predicting the macrosegregation level were the dendrite arm spacing, which also strongly depended on the choice of mushy zone permeability model, and the equiaxed packing fraction. Additionally, the degree of uncertainty required to produce accurate predictions depended on the output of interest from the model.

CHAPTER 1. INTRODUCTION

This work focuses on numerical modeling solidification processes with an emphasis on the direct chill casting process. To better understand this process and modeling solidification, uncertainty quantification analysis is performed. This is initially done on simple models of solidification, increasing in complexity, before being applied to a newly developed model for DC casting. Therefore, the physical DC casting process is first introduced, followed by previous modeling efforts. Methods for uncertainty quantification are also explored, and the specific objectives of this work are presented.

1.1 Direct Chill Casting

Direct-chill (DC) casting is widely used to produce ingots of wrought aluminum, copper, zinc, and magnesium alloys. Ingot quality is of great importance to the properties of the final products which are used in various applications [1]. One measure of product quality, and focus of this study, is ingot scale chemical inhomogeneity. This type of casting defect is commonly called macrosegregation, which is problematic because it complicates subsequent heat treatment and deformation processing through nonuniform microstructure and mechanical properties in the final product [2]. Another concern is the internal stress state of the ingot, which has the potential to form cracks if the conditions

are extreme enough. The following description of the DC casting process is focused on these casting problems and modeling efforts aimed at understanding them.

1.1.1 Process Description

The schematic in Figure 1.1 shows the nature of the process, where liquid metal enters a static mold with a removable bottom block, on which it begins to freeze (primary cooling). This block is moved down and the solidifying metal is withdrawn out of the mold. Below the mold exit, the solid ingot surface is subjected to water sprays which provide the cooling needed to complete the liquid to solid phase change (secondary cooling). The commonly observed steady state radial segregation pattern for DC cast, grain-refined ingots consists of a solute enriched surface, depleted subsurface, slightly enriched mid-radius, and strongly depleted centerline [3]. This composition inhomogeneity leads to spatial variations in mechanical properties which remains in the final product [2]. The wrought alloys mechanical properties are dependent on the location, size, shape, and nature of precipitates that form during solidification and subsequent heat treatments and uniform distribution in the ingot is the ideal [2].

As the metal solidifies in a severely nonuniform temperature field, thermally induced strains develop in the ingot that may cause stresses large enough to permanently deform or crack the ingot either before or after complete solidification [1]. Cracked ingots must be discarded and severe distortions make downstream processing difficult and may also lead to ingot rejection. To reduce the heat extraction rate, and therefore the thermal strain, during the DC casting process, it is desirable to reduce the severity of the quench during secondary cooling. To this end, wipers are often placed below the mold to

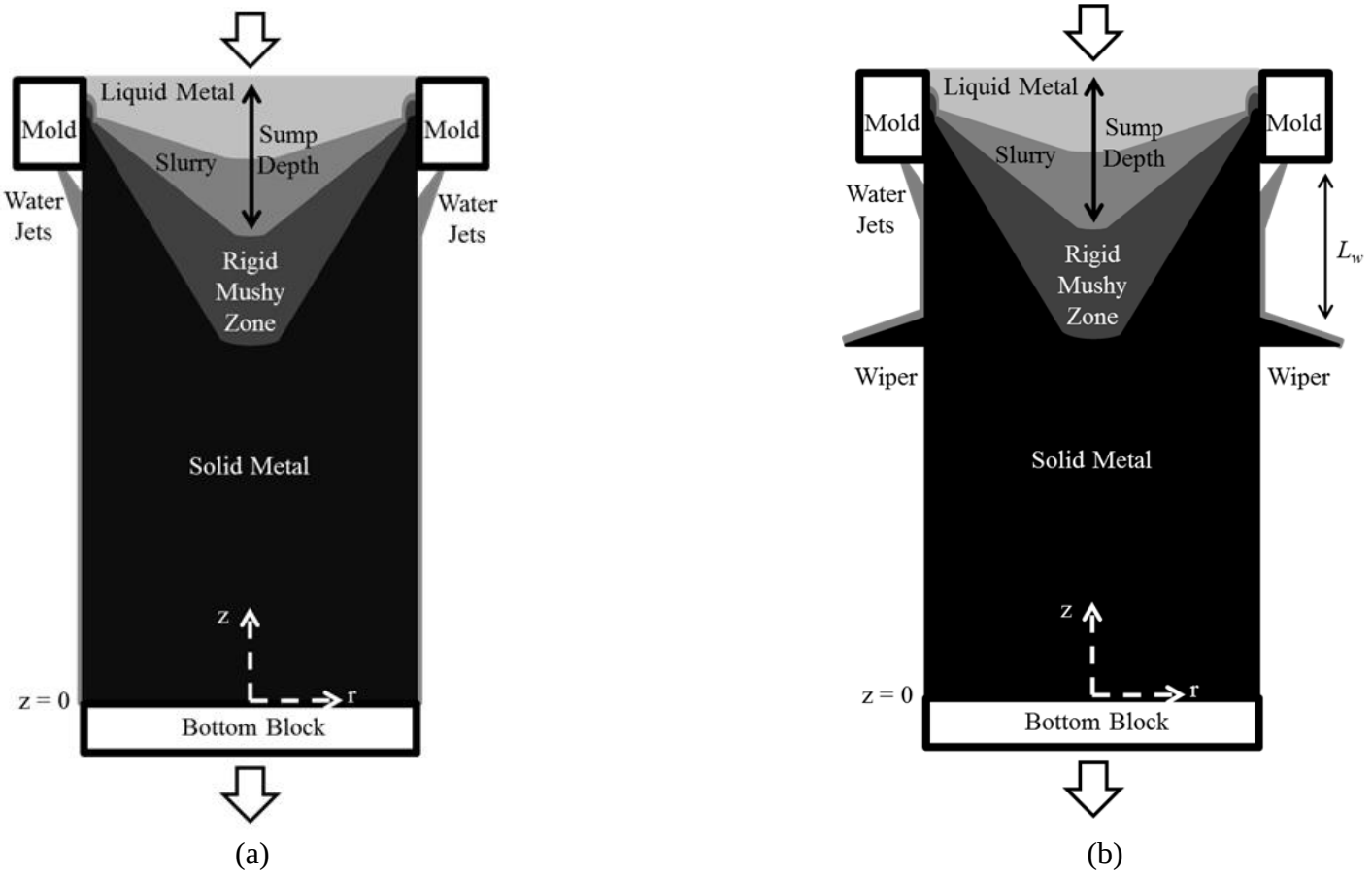

Figure 1.1: Schematic of direct chill casting process for round ingots (a) without a wiper and (b) with a wiper.

divert the free falling water away from the ingot surface, drastically reducing the heat extraction rate. (This device is shown in Figure 1.1(b).)

1.1.2 Direct Chill Casting Modeling Efforts

Numerical process modeling has been a very useful tool to gain insight into the fundamental transport phenomena that cause this radial segregation pattern in steady state DC casting. Reddy and Beckermann compared the steady state radial composition distribution in a fully columnar DC cast ingot and showed that shrinkage driven flows transport enriched liquid perpendicular to the solidification front, which motion includes a component away from the centerline, while buoyancy induced flows move enriched liquid towards the centerline [4]. Shrinkage driven flows were identified as the cause of solute enrichment on the outer surface. The predicted sump in this model consisted only of a rigid mushy zone, which is not typical of grain-refined alloys that also consist of a slurry region of free-floating solid [5]. Vreeman et al. have also observed these sometimes competing phenomenon governing macrosegregation in grain-refined DC casting alloys leading to this radial composition pattern [5,6]. Their flow fields were broken down into four distinct zones: the bulk liquid zone, slurry region (mixture of liquid and solid particles), mushy zone, and solid zone. In the solid zone, the ingot moves homogeneously at the casting speed. In the mushy zone, the flow feeds thermal contraction due to solidification shrinkage and acts perpendicular to the solidification front. The horizontal component of this flow transports solute towards the ingot surface. The flow in the slurry region consists of a recirculating cell that is driven by buoyancy

forces, and transports solid particles. The flow in the liquid region is also driven by buoyancy forces and this flow penetrates into the slurry and mushy zone regions.

A steady state mixture model of DC casting was developed by Vreeman et al. to gain insight into the radial composition profile that develops during the process [5]. This model accounted for heat and fluid flow, transport of solute and free-floating dendrites, and shrinkage driven flow for binary alloys, and was used to examine the effects of free-floating solid on the macrosegregation for 40 cm diameter Al-4.5 wt.% Cu and Al-6.0 wt.% Mg billets [6]. Their parametric study of the packing fraction (the volume fraction of solid at which the moving slurry becomes a rigid mushy zone) and the average free-floating particle diameter revealed the negative segregation at the centerline increased with values of both parameters. Increasing the particle diameter increased the rate at which solute-depleted particles accumulated at the centerline due to their increased tendency to settle. Higher packing fraction cases had lower temperatures and stronger buoyancy induced flow in the slurry region and so a larger volume of copper-depleted solid was swept towards the centerline. Results from this model were also compared to industrial scale experiments of 45 cm diameter billets of Al-6.0 wt. % Cu [7]. Good agreement was found between the measured and predicted temperature histories and sump profiles, but the predicted radial segregation profile was less negative at the centerline. The packing fraction was estimated to be less than 30 % solid, although they noted it should vary with position in the sump and with changes in the casting parameters. The simulations did compare well with industrial scale experiments in the steady state regime, but lacked the history of the entire transient process.

The vertical thickness of the rigid mushy zone, L_h, was shown by Eskin to be linked to the amount of solute transported by shrinkage-driven flow [8]. Additionally, the transport of free-floating equiaxed grains seeded by grain refiner was found to contribute to negative centerline segregation [6,7,9–13]. Eskin et al. has also examined the effect of ramping the casting speed, varying the superheat, and cooling water flow rate on the solidification structure and macrosegregation in 20 cm diameter Al-Cu ingots [3,14–16]. The casting speed had the largest effect on the sump depth and macrosegregation level, with lower casting rates leading to a shallower sump and therefore less segregation [3]. The water flow rates were varied from 0.0025 m^3/s to 0.0042 m^3/s for casting speeds of 120 and 180 mm/min. The water flow rate had a small effect on the centerline and mid-radius segregation, while the surface and subsurface were more affected. The effect of the water flow rate was exacerbated for the higher casting speed [3]. Changing the superheat had a small effect on the centerline segregation and sump depth. However, the segregation for the subsurface region was larger for the low superheat conditions because of a wider slurry and mushy zone regions with stronger flows transporting solute to the surface [14,15].

Flood and Davidson modeled the flow in DC casting to analyze the effect of the ingot size and casting speed on the centerline segregation seen in experimental trials [17]. An increase in ingot thickness from 40 to 60 cm at the same casting speed more than doubled the sump depth and an increase in the levels of negative centerline and positive surface segregation. Increasing the casting speed from 45 mm/min to 60 mm/min produced the same effect on the sump and macrosegregation level as the change in ingot size, but to a lesser degree.

The modeling efforts previously mentioned were focused on examining the steady state region of the process and ignored any transient effects, with the exception of Eskin et al. [3]. However, the model used by Eskin to examine the effects of ramping the casting speed had a uniform domain size with an inlet and outlet [3]. It did not treat the start up regime but simulated the change from one steady state condition to another. This modeling study focused only on transient behavior of the sump depth. One of the first fully transient models for DC casting was developed by Williams et al. and examined the initial process start up [18]. Initially, the mesh was condensed in the casting direction and the location of the top of the domain was fixed. The control volumes expanded downwards at the casting rate and the width of each control volume was constant throughout the process. The momentum, energy, and mechanical stress were calculated using this model for the start up phase of the process. This method of expanding the size of the domain does allow the momentum field to be calculated without any pulses to the pressure field; however this method does require numerous spatial interpolations to be made, as a consequence of the moving mesh, which would cause the composition field (if it were calculated) to becomed smeared [19].

Several other transient DC casting modeling efforts grow the domain by successively activating entire rows of control volumes at a rate corresponding to the casting speed [20–23]. These models are typically used to predict the temperature and stress field of the process, for which this method has proven satisfactory. The problem with this approach is when the flow field is considered. Adding entire control volumes during a single time step strongly influences the pressure field to which the momentum

equations respond. This process causes the pressure field to pulsate, as entire control volume additions are a shock to the system.

As previously mentioned, numerical models of DC casting have also been used to gain insight into the stress state and ingot distortions during the DC casting process in which the temperature, stress, and strain fields were examined [20,23–25]. Sengupta et al. [20] developed a 3D model to analyze the stress state of the start-up phase for rolling slab ingots. They showed how the ingot base deforms upward away from the bottom block, termed butt curl, due to the extreme heat extraction rates. Suyinto et al. performed laboratory experiments for 0.2 m ingot rounds of various Al-Cu alloys, examining the effect of casting velocity on hot tears [24]. Hot tears were shown to occur in the ingot center and were worsened at high casting rates. Numerical simulations of aluminum alloy 7050 performed by Lalpoor et al. showed similar results [23,25]. Along with the ingot center, Lalpoor et al. also showed the water impingement zone is susceptible to hot tearing [23,25]. Measurements and numerical calculations of wiper effects on the internal stress state and temperature field in rolling slab ingots were analyzed by Drezet and Pirling [26]. Their findings showed that their wiper implemention reduced the internal stress state by an average of 33%. This stress reduction was for a wiper placed at the position of the liquidus temperature at the center of the casting. However, these studies have not examined the effect of the wiper location on the development of the composition field, flow field, or sump shape.

1.2 Uncertainty Quantification in Numerical Modeling

Insight into solidification processes can be gained through use of these previously mentioned models that would be not be possible through laboratory experiments. However, the predictions made by these models are typically reported with arbitrary precision without regard for the uncertainty inherent in the numerical methods, the choice of model, or the values for properties or boundary conditions. This lack of knowledge of uncertainty propagation in solidification simulations can pose difficulties in using these models for process design. Understanding the effect of uncertain input parameters and quantifying their effect on the prediction uncertainty allows better calculations of margins of safety and improved estimates of reliability of the process. Also, when there is an apparent mismatch between experimental data (ideally with quantified probable variation) and predictions (which appear to have none), there is often an impulse to seek better agreement by improving existing or incorporating new physics in solidification models, without considering the kind of uncertainty that exists in a given numerical model. This approach ignores the actual uncertainty in the numerical results, which are required to find the probability that there is agreement with experiments. Model assumptions and probable input variability create a level of uncertainty in model predictions that has not been calculated in solidification modeling as yet.

The focus in this work is on two kinds of model uncertainty, neither associated with the numerical method, termed epistemic and aleatoric [27,28]. Epistemic uncertainty is the lack of knowledge about the system being simulated and can be manifested in uncertainty in the choice of models or the inclusion of particular physical phenomena. This type of uncertainty is typically resolved by improving models through

appropriate experimental measurements. Aleatoric uncertainty is the natural variability in measurements and random sampling of data and cannot be reduced without improved data collection methods.

One way to address aleatoric uncertainty is to perform a sensitivity study by varying select input parameters one at a time over a range and analyze how the numerical predictions respond [4,6,29,30]. This method is useful to gain an understanding of how various input parameters affect numerical predictions and their relative importance, but does not include the interactions of inputs or the probability distributions of either the inputs or the outputs. The most direct approach to quantify the aleatoric model uncertainty is through Monte Carlo methods [31]. This process generates probability density functions (PDFs) for output quantities by evaluating the numerical model for the entire input uncertainty range. Although Monte Carlo sampling methods are very effective, they are also computationally intensive, as they may require many thousands to millions of evaluations of the numerical model. Even for simple, quickly solved models, this number can be daunting; with the more sophisticated numerical models (e.g., models referenced above or those in this work) the computational expense is prohibitive. One way to reduce this cost is to construct a polynomial function that replaces the complicated numerical model and acts a surrogate, based on a limited number of numerical simulations. This surrogate is more computationally efficient than the numerical model and can substitute for it in the Monte Carlo evaluations. Researchers in related fields using similar numerical methods (e.g., heat transfer) have used such methods to construct response surfaces and to produce PDFs for their model outputs without making modifications or additions to the governing equations or model solver [32–35]. In this

work, thermophysical property data and boundary conditions are treated as having aleatoric uncertainty.

Another use of this type of analysis is the evaluation of the choice of model for a particular physical phenomenon. Solidification models such as in this study include a permeability model that represents resistance to flow through the solid-liquid mushy zone [36–42]. These models can be dependent and on the relative flow direction, morphology, arrangement and spacing of primary arms, and/or fraction solid. They require information about the microstructure obtained through experimental measurements that contain inherit uncertainty, either directly or through calculations that use experimentally measured alloy material properties and predicted temperature fields. These models also have a relationship between the permeability and the fraction solid, the accuracy of which is not well known through the entirety of the mushy zone, especially at low fraction solids. The aleatoric uncertainties in the outputs using different permeability models is characterized and compared to begin to shed some light on the epistemic uncertainty in the choice of model.

1.3 Research Objectives

This work uses a baseline solidification process model to study transport phenomena leading to macrosegregation. Primarily the focus is on understanding the fully transient DC casting process. However, the effect of uncertain inputs on solidification model predictions was explored for a more simplistic process before extending the analysis to a transient DC casting model. The objective of this pioneering work of quantifying uncertainty in solidification process models was not to develop a

new uncertainty quantification method, but apply non-intrusive techniques to existing solidification models.

1.3.1 Direct Chill Casting Objectives

The present study uses a fully transient DC casting model to analyze the effect of process parameters and ingot diameter on achieving process steady state and ingot macrosegregation for 70 cm and 50 cm diameter direct chill cast ingots of aluminum alloy 7050, with comparisons to segregation levels in previous studies. The process parameters examined are the ingot diameter, casting velocity, water flow rate from the cooling jets, casting superheat, and wiper placement. Additionally, a layer of pure liquid Al at startup is analyzed for its effect on macrosegregation and sump formation. The ingot macrosegregation was characterized in two ways, by fitting compositional data to a Weibull distribution and normalizing the deviation of the distribution (W^i) by the nominal composition. The macrosegregation level was also determined by comparing steady state radial composition distributions. The DC casting model is capable of predicting thermal, species, and flow fields for the transient process. The effect of local grid refinement will also be studied for its effect on the compositional field.

1.3.2 Uncertainty Quantification Objectives

As the first step towards understanding the effects of uncertain inputs on modeling solidification processes, uncertainty quantification and sensitivity analysis are performed on a transient model of Al-4.5 wt.% Cu in a rectangular cavity with both columnar and equiaxed solid growth models. The uncertain input parameters include the

choice of permeability model, microstructural model parameters, heat transfer coefficient, and material properties. The uncertainty in the predicted macrosegregation levels and solidification time were examined along with quantifying which input parameters had the largest effect on the outputs. Uncertainty quantification was also performed on the more industrial relevant DC casting model. The outputs of interest from the DC casting model were the macrosegregation level and steady state sump depth. This analysis will help determine the maximum uncertainty tolerated in model input parameters to obtain a minimum confidence in predicted output. The intent is to use the presented results to help make decisions during model development as to the proper way to distribute time and resources, not only in acquiring model inputs but determine areas of solidification modeling that needs further research investment. This work also shows an approach to the problem of quantifying uncertainty as it propagates through a model using a common approach to simulating solidification processing.

CHAPTER 2. NUMERICAL MODEL DESCRIPTION

In this chapter the numerical methods and equations solved in the general solidification model will be presented and additional considerations for modeling the DC casting process are discussed. The general solidification model is discretized using the implicit finite volume method with upwind differencing according to Patankar [43] and considers either fully equiaxed (grain refined) or columnar solidification morphologies. The equations for fluid flow are solved with the SIMPLER algorithm on an axisymmetric, staggered grid. The momentum, energy, and species equations are in the form of mixture quantities, as described by Bennon et al. [44]. Contributions from free-floating equiaxed particles are considered according to Vreeman et al. [5]. When considering equiaxed solidification, the discretization of the species equations was taken from Vreeman and Incropera [13]. The procedure for quantifying the model uncertainty is also presented, in which the existing Prism Uncertainty Quantification (PUQ) framework is used [28]. The uncertainty quantification procedure is performed on each solidification model presented in this work.

2.1 Mixture Conservation Equations

The advection-diffusion equations for mass, momentum, energy, and species are in the form established by Bennon and Incropera [44] for a mixture transport quantity θ:

$$\frac{\partial}{\partial t}(\rho\theta)+\nabla\bullet\left(\rho\bar{\boldsymbol{V}}\theta\right)=\nabla\bullet(\Gamma\nabla\theta)-\nabla\bullet\left(\rho\bar{\boldsymbol{V}}(\theta_s-\theta)\right)+S_\theta\,, \tag{2.1}$$

where ρ is the mixture density, Γ the diffusion coefficient, V the velocity field, and S_θ the source term for the mixture transport quantity. The mixture conservation equations are discretized into an algebraic form that connects transport quantities for a group of grid points in the solution domain using the finite volume method, as discussed by Pantankar [43]. The discretized advection-diffusion equations are solved using line-by-line TDMA with under relaxation. Iterations were performed until the difference between successive iterations dropped below the critical value chosen for each equation.

2.1.1 Mass and Momentum Conservation

The equations for the mixture velocities are a weighted average of the solid and liquid velocities ($\vec{\boldsymbol{V}}=\vec{\boldsymbol{V}}_{\boldsymbol{l}}(1-f_s)+\vec{\boldsymbol{V}}_{\boldsymbol{s}}f_s$). The mixture conservation equations for mass and momentum, including the effect of free-floating solid in axisymmetric coordinates, are given in Equations (2.2)-(2.4) [5].

$$\frac{\partial}{\partial t}(\rho)+\nabla\bullet\left(\rho\vec{\boldsymbol{V}}\right)=0 \tag{2.2}$$

$$\frac{\partial}{\partial t}(\rho u)+\nabla\bullet\left(\rho\vec{\mathrm{V}}u\right)=\nabla\bullet\left(\eta_l\frac{\rho}{\rho_l}\nabla u\right)+\nabla\bullet\left(\eta_l u\nabla\left(\frac{\rho}{\rho_l}\right)\right)$$
$$-\nabla\bullet\left(\eta_l\frac{\rho f_s}{\rho_l}\nabla u_s\right)-\nabla\bullet\left(\eta_l u_s\nabla\left(\frac{\rho f_s}{\rho_l}\right)\right)+\nabla\bullet\left(\eta_l u_s\nabla g_s\right) \qquad (2.3)$$
$$+\nabla\bullet\left(\overline{\eta}_s g_s\nabla u_s\right)-\nabla\bullet\left[\left(\frac{\rho f_s}{f_l}\right)\left(\vec{\mathrm{V}}-\vec{\mathrm{V}}_s\right)\left(u-u_s\right)\right]+\rho\mathrm{B}_z-\frac{\partial P}{\partial z}$$

$$\frac{\partial}{\partial t}(\rho v)+\nabla\bullet\left(\rho\vec{\mathrm{V}}v\right)=\nabla\bullet\left(\eta_l\frac{\rho}{\rho_l}\nabla v\right)-\eta_l\frac{\rho}{\rho_l}\frac{v}{r^2}$$
$$+\nabla\bullet\left(\eta_l v\nabla\left(\frac{\rho}{\rho_l}\right)\right)-\nabla\bullet\left(\eta_l\frac{\rho f_s}{\rho_l}\nabla v\right)+\eta_l\frac{\rho f_s}{\rho_l}\frac{v}{r^2} \qquad (2.4)$$
$$-\nabla\bullet\left(\eta_l v\nabla\left(\frac{\rho f_s}{\rho_l}\right)\right)+\nabla\bullet\left(\eta_l v\nabla g_s\right)+\nabla\bullet\left(\overline{\eta}_s g_s\nabla v\right)-\overline{\eta}_s g_s\frac{v}{r^2}-\frac{\partial P}{\partial r}$$

For equiaxed solidification morphology, solid is assumed to form initially as equiaxed particles that are free-floating until a critical solid volume fraction, $g_{s,crit}$, is reached, at which point the free-floating particles coalesce to form a rigid, permeable, solid structure with no motion relative to the ingot (u_s=v_s=0). The critical volume fraction solid, often termed the packing fraction, is generally a quantity of uncertain value related to the size and morphology of the equiaxed dendrites and the direction and magnitude of the liquid and solid motion relative to the rigid solid [45]. The packing fraction has been estimated to be below 30% [5,7] and for the subsequent studies, values in this range are used.

The flow is driven by thermal and solutal buoyancy forces, represented by the ρB_z term in the axial momentum equation (2.3):

$$\rho \mathrm{B}_z = g_s(\rho_s - \rho_l)g - g_s\rho_s\vec{g}\left[\beta_{T,s}(T - T_0) + \beta_{S,s}\left(C_s^i - C_0^i\right)\right] - g_l\rho_l\vec{g}\left[\beta_{T,l}(T - T_0) + \beta_{S,l}\left(C_l^i - C_0^i\right)\right] \quad (2.5)$$

The difference in solid and liquid densities contributes to momentum in the first term of equation (2.5) and also helps drive the flow through continuity, equation (2.2). The relative velocity of the solid and liquid is modeled with Stokes law,

$$\vec{\mathrm{V}}_\mathrm{s} - \vec{\mathrm{V}}_\mathrm{l} = \frac{(1 - g_s)}{18\eta_m}(\rho_s - \rho_l)d^2\vec{g}\,, \quad (2.6)$$

in which η_m is the mixture viscosity. This equation treats the equiaxed dendrites as uniform spheres of a specified diameter (d). The particle size chosen for this study is large enough to cause some settling, and small enough that the flow affects, but does not completely determine, the trajectory of the solid. The size of the free-floating particles is chosen to be constant and uniform, although it is likely an evolving distribution during solidification.

While the free-floating solid does not impede the fluid motion, the packed array of solid dendrites slows the flow in the rigid mushy zone. When the mushy zone is rigid ($g_s > g_{s,crit}$), the terms $\frac{\mu\rho}{K\rho_l}u$ and $\frac{\mu\rho}{K\rho_l}v$ are added to equations (2.3) and (2.4), respectively, to represent this drag, and terms accounting for solid motion are removed. The momentum equations (2.3) and (2.4) are rewritten in the rigid mushy zone as

$$\frac{\partial}{\partial t}(\rho u) + \nabla \bullet \left(\rho\vec{\mathrm{V}}u\right) = \nabla \bullet \left(\eta_l \frac{\rho}{\rho_l}\nabla u\right) - \frac{\eta_l\rho}{K\rho_l}u + \rho B_z - \frac{\partial P}{\partial z} \quad (2.7)$$

and

$$\frac{\partial}{\partial t}(\rho v)+\nabla\bullet\left(\rho\vec{\nabla}v\right)=\nabla\bullet\left(\eta_l\frac{\rho}{\rho_l}\nabla v\right)-\frac{\eta_l\rho}{K\rho_l}v-\eta_l\frac{\rho v}{\rho_l r^2}-\frac{\partial P}{\partial r}. \tag{2.8}$$

For columnar solidification morphology, equations (2.7) and (2.8) are used to predict the flow field, in which the last two terms in equation (2.5) are the only buoyancy terms driving the flow.

Unless otherwise stated, the Blake-Kozeny function is used for both solidification morphologies to model drag on the mushy zone flow due to the dendrite arms, where the isotropic permeability (K) is a function of the secondary arm spacing (λ_2) and the volume fraction solid (g_s):

$$K=\frac{\lambda_2^2}{180}\frac{(1-g_s)^3}{g_s^2}. \tag{2.9}$$

Equations (2.7) and (2.8) are also used in the fully solid region for both morphologies, where the permeability is low enough to cause $\vec{\boldsymbol{V}}=0$. In select cases, two additional permeability models that are also functions of λ_2 and g_s are analyzed for their effect on macrosegregation. All three models are shown in Figure 2.1. The permeability directly influences the magnitude of the liquid flow in the mushy zone and so the amount of solute transported on the macroscale and the overall level of ingot macrosegregation. The most commonly used permeability model is the Blake-Kozeny function [46], KI in Figure 2.1, developed for arrays of spheres or cylinders and commonly extended to dendritic structures. The other two permeability models are taken from a study by Kumar et al. [37] , and are examined along with the Blake-Kozeny model for their effect on the macrosegregation predictions. These three models all have the same relationship with the secondary dendrite arm spacing, ($K\sim\lambda_2$) but each have different relationships with

fraction solid (Figure 2.1). The second permeability model, KII, was developed by Kumar et al. [37] in which the authors artificially changed the exponent of the denominator in the KI model. The third permeability model, KIII, was originally developed by Thevik and Mo [47] for cylindrical secondary dendrite arms of uniform diameter surrounded by liquid. The Blake-Kozeny model is most permeable at low fraction solid and least permeable at high fraction solids. The KIII model has the lowest permeability across the majority of the mushy zone. Although the KII model was developed without a direct physical basis, it follows closely to the KIII model at low fraction solid and the KI model at high fraction solid.

KI: $K = \frac{\lambda_2^2 g_l^3}{180 g_s^2}$

KII: $K = \frac{\lambda_2^2 g_l^3}{180 g_s^{4/3}}$

KIII: $K = \frac{\lambda_2^2 g_l^3}{80 g_s}$

(a)

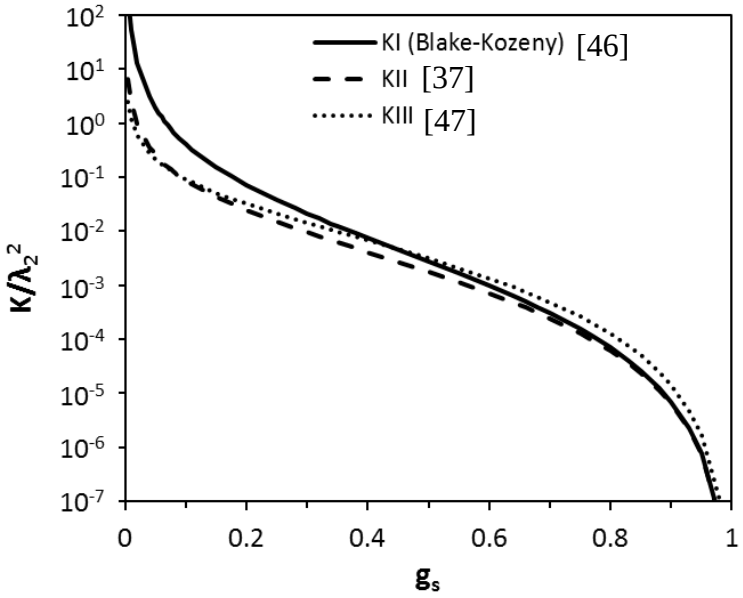

(b)

Figure 2.1: Mushy zone permeability as a function of secondary dendrite arm spacing and fraction solid showing (a) three different permeability functions and (b) normalized permeability as a function of solid fraction [37].

2.1.2 Temperature Conservation

The model uses a temperature formulation for energy conservation assuming constant and uniform specific heat [48],

$$\frac{\partial}{\partial t}(\rho cT)+\nabla\bullet\left(\rho cT\vec{\boldsymbol{V}}\right)=\nabla\bullet(k\nabla T)-\frac{\partial}{\partial t}\left(\rho f_l L_f\right)-\nabla\bullet\left(\rho f_l L_f\vec{\boldsymbol{V}}\right)$$
$$-\nabla\bullet\left\{\rho f_s L_f\quad\left(\vec{\boldsymbol{V}}-\vec{\boldsymbol{V}}_{\boldsymbol{s}}\right)\right\}, \tag{2.10}$$

the first three terms of which represent sensible energy storage, advection, and diffusion. The fourth term is the latent heat release rate during solidification, and the final two terms correspond to the advection of energy associated with the latent heat in the liquid. Equation (2.10) includes motion of free-floating equiaxed particles and is also used for columnar solidification, in which the solid velocity in the last term is zero and equation (2.10) becomes

$$\frac{\partial}{\partial t}(\rho cT)+\nabla\bullet\left(\rho cT\vec{\boldsymbol{V}}\right)=\nabla\bullet(k\nabla T)-\frac{\partial}{\partial t}\left(\rho f_l L_f\right)-\nabla\bullet\left(\rho L_f\vec{\boldsymbol{V}}\right). \tag{2.11}$$

The final three terms in (2.10) and final two terms in (2.11) are treated as source terms in a standard advection-diffusion equation for temperature. The transient latent heat term, $\frac{\partial\left(\rho f_l L_f\right)}{\partial t}$, is linearized using the method proposed by Voller and Swaminathan [49] for stability.

2.1.3 Species Conservation

The mixture species conservation equations, including the motion of solid equiaxed particles and assuming a constant and uniform diffusion coefficient, is given by:

$$\frac{\partial}{\partial t}\left(\rho C^i\right)+\nabla\bullet\left(\rho\vec{V}C^i\right)=\nabla\bullet\left(\rho f_l D\nabla C^i\right)+\nabla\bullet\left(\rho f_l D\nabla\left(C_l^i-C^i\right)\right)$$
$$-\nabla\bullet\left(\rho\left(\vec{V}-\vec{V}_s\right)\left(C_l^i-C^i\right)\right), \tag{2.12}$$

where i represents the species of interest. The first three terms in equation (2.12) represent species storage, advection, and diffusion. The last two terms represent the diffusion-like and advection-like source terms that arise due to treating species as a mixture quantity. The discretization of the species equations follows that of Vreeman et al. [13], in which special care was taken for the advection of solid mass fraction. When considering columnar solidification, the solid velocity in the last term in equation (2.12) is equal to zero.

2.2 Alloy Solidification Model

The solidification model uses phase diagram information of the alloy in question to relate the calculated temperature and mixture composition to the appropriate solid and liquid compositions and fraction solid. The alloy microsegregation model assumes complete mixing in the solid and liquid phases according to the equilibrium level rule, and assumes linear liquidus and solidus lines. This model is capable of handling binary and multicomponent alloy solidification. The required parameters for the case of binary alloy solidification, such as liquidus slope and partition coefficient, can be acquired by consulting the proper phase diagram. For the case of multicomponent alloy solidification, the liquidus temperature function is in terms of the melting temperature of the pure primary composition element and the liquidus composition of the alloying elements

$$T_{LIQ} = T_m + \sum_i^n \frac{\partial T_{LIQ}}{\partial C_l^i} C_l^i \,. \tag{2.13}$$

The slope of the liquidus temperature in terms of each alloying element, in equation (2.13) and the partition coefficients, which are assumed to be constant, are determined through use of a thermodynamic database program. For simplicity, equilibrium solid state is a single phase for multicomponent alloy solidification. Therefore, all freezing occurs during primary solidification.

2.3 Alloy Properties

In this work a binary and multicomponent Al alloy system are examined. The binary alloy system is Al-0.045 wt. fr. Cu, which is a simple binary eutectic on the aluminum rich side of the phase diagram. The partition coefficient for this binary alloy is $k_p = C_s/C_l = 0.17$, and the equations for the liquidus and solidus temperatures are shown in equations (2.14) and (2.15). Primary solidification is assumed to occur until either the solidus temperature or the eutectic temperature (821.2 K) is reached. Other thermophysical properties are given in Table 2.1.

$$T_{LIQ}(K) = 933.15 - 340.3 C_l^{Cu} \tag{2.14}$$

$$T_{SOL}(K) = 933.15 - 1987.6 C_s^{Cu} \tag{2.15}$$

Table 2.1:Thermophysical properties of Al-0.045 wt. fr. Cu.

Liquid Density (kg/m^3) [6]	2460	Liquid Thermal Expansion (1/K) [6]	$1.17x10^{-4}$
Solid Density (kg/m^3) [6]	2750	Liquid Solutal Expansion [6]	-0.73
Specific Heat (J/kg K) [6]	1006	Solid Thermal Expansion (1/K) [6]	$2.25x10^{-5}$
Latent Heat (J/kg) [6]	$3.9x10^5$	Solid Solutal Expansion [6]	-0.87
Thermal Conductivity (W/m K) [6]	137.5	Partition Coefficient	0.17
Liquid Viscosity (kg/m s) [6]	0.0023	Dendrite Arm Spacing (μm) [50]	91
Eutectic Temperature (K) [6]	821	Critical Packing Fraction	0.15

The multicomponent alloy analyzed in this work is aluminum alloy 7050 with a nominal composition (in wt. fr.) of Al – 0.062Zn – 0.023Cu – 0.0225Mg – 0.0012Zr – 0.00075Fe – 0.0006Si – 0.0003Ti – 0.0002Cr – 0.0005Mn, which are the midpoints of the allowable ranges given in Table 2.2 of ASTM B247 [51] or half the maximum allowable compositions.

Table 2.2: Chemical specification of aluminum alloy 7050 from ASTM B247 [51]. The elements tracked in the simulations are indicated with an asterisk.

Alloying Element	**Specification Range (weight fraction)**
Zn*	0.057-0.067
Cu*	0.02-0.026
Mg*	0.019-0.026
Zr	0.0008-0.0015
Fe	0.0015 max
Si	0.0012 max
Ti	0.0006 max
Cr	0.0004 max
Mn	0.001 max
Other	0.0005 max

Only three of these elements are tracked directly using equation (2.12) and included in the buoyancy term, equation (2.5). Zn, Cu, and Mg were chosen because their contributions to control solutal buoyancy and they segregate enough to alter T_{LIQ}. The function for the liquidus temperature (T_{LIQ}) used in the thermodynamic model is

$$T_{LIQ} = 933.15 + 0.63 - 174.16C_l^{Zn} - 271.55C_l^{Cu} - 494.68C_l^{Mg}. \quad (2.16)$$

where the temperature is in Kelvin and the compositions in weight fraction. The first two terms are the melting temperature of pure Al and an adjustment to it due to the trace elements not tracked in the model (Zr, Fe, Si, Ti, Cr, and Mn). The necessary partition coefficients ($k_p = C_s/C_l$) were found to be

$$k_p^{Zn} = 0.39,\ k_p^{Cu} = 0.09, \text{ and } k_p^{Mg} = 0.29. \quad (2.17)$$

The liquidus temperature function (2.16) and the partition coefficients (2.17) were determined through use of the thermodynamic database program Thermocalc^{TM} using the TCAL1 database. Relevant thermophysical property values for this alloy system are found in Table 2.3.

Table 2.3: Thermophysical properties of aluminum alloy 7050.

Property	**Reference**	**Value**
Liquid Density [kg/m^3]	[25]	2515.0
Solid Density [kg/m^3]	[25]	2744.1
Specific Heat [J/kg K]	[25]	1141.0
Latent Heat [J/kg]	[25]	3.76x10^5
Liquid Thermal Conductivity [W/m K]	[25]	83.2
Solid Thermal Conductivity [W/m K]	[25]	149.4
Liquid Viscosity [kg/m s]	[52]	0.0013
Average Solid Viscosity [kg/m s]	[53]	4.53μ_l for g_{scrit}=0.15 4.96 μ_l for g_{scrit}=0.3
Liquid Thermal Expansion [1/K]	[54]	1.5x10^{-4}
Solid Thermal Expansion [1/K]	[25]	2.29x10^{-5}
Liquid Solutal Expansion [1/K]	[54]	Zn: -0.65 Cu: -0.75 Mg: 0.53
Solid Solutal Expansion [1/K]	[52]	Zn: -1.43 Cu: -2.01 Mg: 0.31

2.4 Direct Chill Casting Model Considerations

The current model is a fully transient treatment of the entire ingot; therefore, the application to DC casting requires a method to grow the metal ingot as the process progresses and the application of realistic boundary conditions. The simulation domain consists only of the liquid and solid aluminum alloy, extending from the bottom block (just outside the domain) to the top of the mold (Figure 2.2). The axisymmetric coordinate system is fixed to the bottom of the ingot, and so the frame of reference moves at the casting speed (V_c) and all the velocities predicted in this model are relative to the ingot. The ingot frame of reference has no rigid fixed solid moving across control volume boundaries; use of this reference frame prevents smearing of the compositional field that can occur during the successive interpolations of a moving grid. At each time step, molten metal is added uniformly to the top of the domain so that the top of the liquid pool (aligned with the top of the mold) moves upward in the grid at V_c. Enough metal is added in each step to lengthen the ingot by $V_c \Delta t$ and to feed solidification shrinkage. Changes in local composition will affect the size of the freezing range and therefore influence the amount of shrinkage predicted by the model. The axial grid spacing is $\Delta z = 1$ cm, and radial is $\Delta r = 0.757$ cm (except as noted in subsequent chapters).

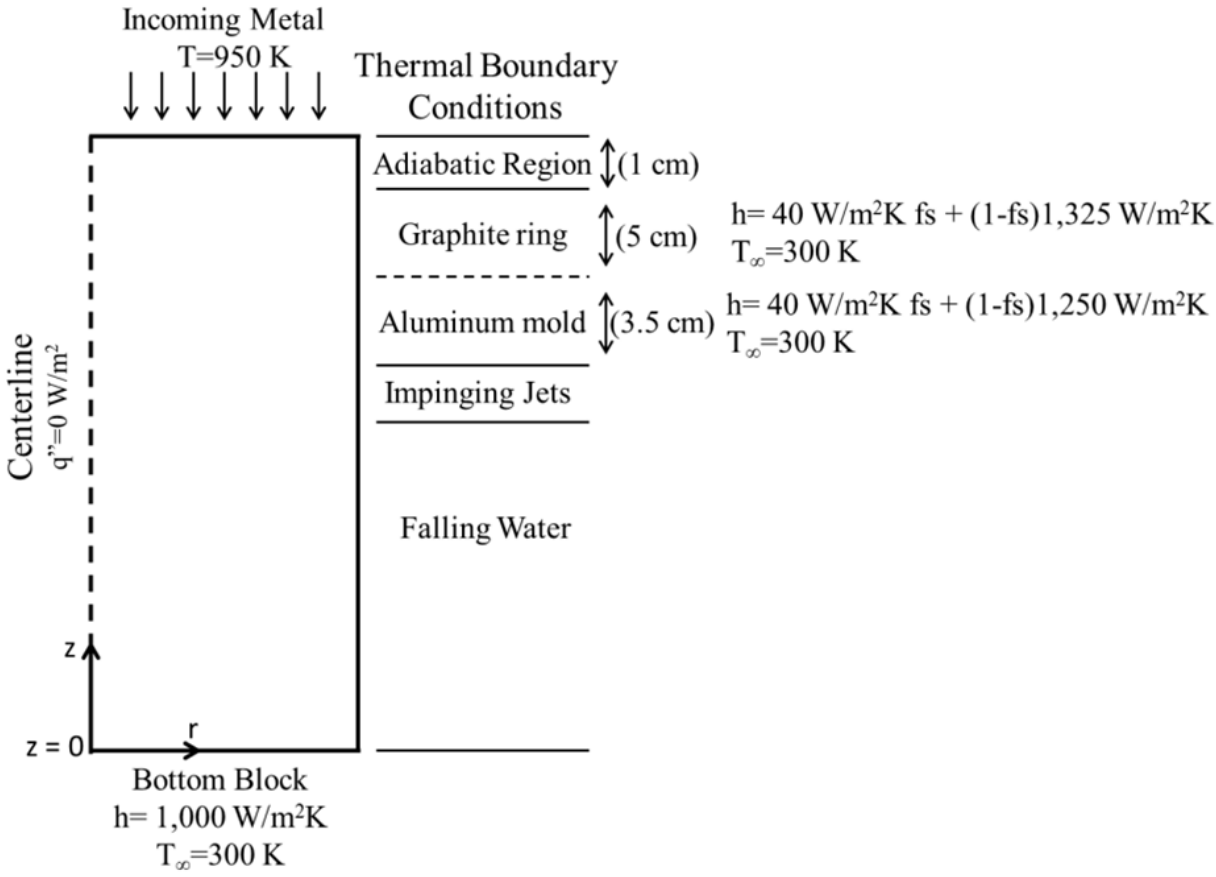

Figure 2.2: Schematic depiction of the simulation domain showing the thermal boundary conditions.

In order to accommodate the treatment of the top of the lengthening ingot, a volume of fluid (VOF) method is used to enable a smooth transition of the boundary conditions from one control volume to another and additions of control volumes to the top of the domain. The VOF method provides a convenient manner to smoothly move the boundary conditions and add additional control volumes to the domain without disrupting the velocity and composition fields. This VOF method tracks an interface between two fluids (liquid metal and air) at the top of the domain and the details are found in Yanke et al. [55]. The VOF method tracks the interface between the two very different fluids by calculating the fraction of each control volume occupied by liquid aluminum alloy [55–60], defined as:

$$F = \frac{\forall_{Al}}{\forall_{cv}}. \tag{2.18}$$

If $F = 1$, the control volume consists entirely of aluminum; if $F = 0$, the control volume consists entirely of air. The interface between the two fluids is defined by the control volumes with $0 < F < 1$. VOF methods typically consist of a scheme for the advection of F between control volumes and an interface reconstruction on a subgrid level [55–61]. The two fluids react to the solution of the flow field by maintaining volume conservation of the VOF variable as it is transported by advection,

$$\frac{\partial F}{\partial t} + \nabla \cdot \left(\vec{V} F\right) = S. \tag{2.19}$$

The source term, S, represents the addition of the liquid metal at the liquid-air interface as it moves upwards through the grid. This fluid interface acts as a metal inlet, and the top of the domain is an outlet for air to exit the domain as it is pushed out by the metal addition. When the metal-air interface crosses a row of control volume boundaries, a new

row of control volumes is activated at the top of the air. In this manner, the domain lengthens in discrete steps (Figure 2.3). When the VOF crosses a control volume boundary there is a brief disruption in the pressure field in the solid metal near the surface of the ingot. However, the flow in the liquid, slurry, and rigid mushy zone are unaffected. This method of expanding the domain is simpler than having an inlet at the top of the domain, because it allows for constant control volume sizes and adding more control volumes to the solution domain does not affect the flow field. Except for extreme cases of narrow nozzle geometry, the flow field and sump depth predictions are not significantly effected by the inclusion of a submerged nozzle [62].

The addition of metal at the top of the ingot is accounted for in the composition (2.12) and energy (2.10) equations by adjusting the converged solution at the previous time step due to the metal addition at the superheated temperature and nominal composition. This adjustment is made at the beginning of each new time step by

$$\bar{\gamma}(1-F) = \bar{\gamma}^{o}(1-F) + \left(F^{o} - F\right)\gamma_{in} + \Delta\forall_{shrink}(\gamma_{in} - \bar{\gamma}), \tag{2.20}$$

in which $\bar{\gamma}$ is the mixture metal enthalpy or composition and $\Delta\forall_{shrink}$ is the volume deficit due to solidification shrinkage in the entire domain. The first term on the right hand side of equation (2.20) is the mixture metal quantity from the previous converged solution. The second and third terms account for enthalpy and composition of the metal added to account for the casting velocity and to feed solidification shrinkage, respectively. The temperature at the interface is found by first accounting for the change in enthalpy due to the addition of metal with equation (2.20), and then updating the temperature by the definition of mixture enthalpy for two fluids indicated by superscripts:

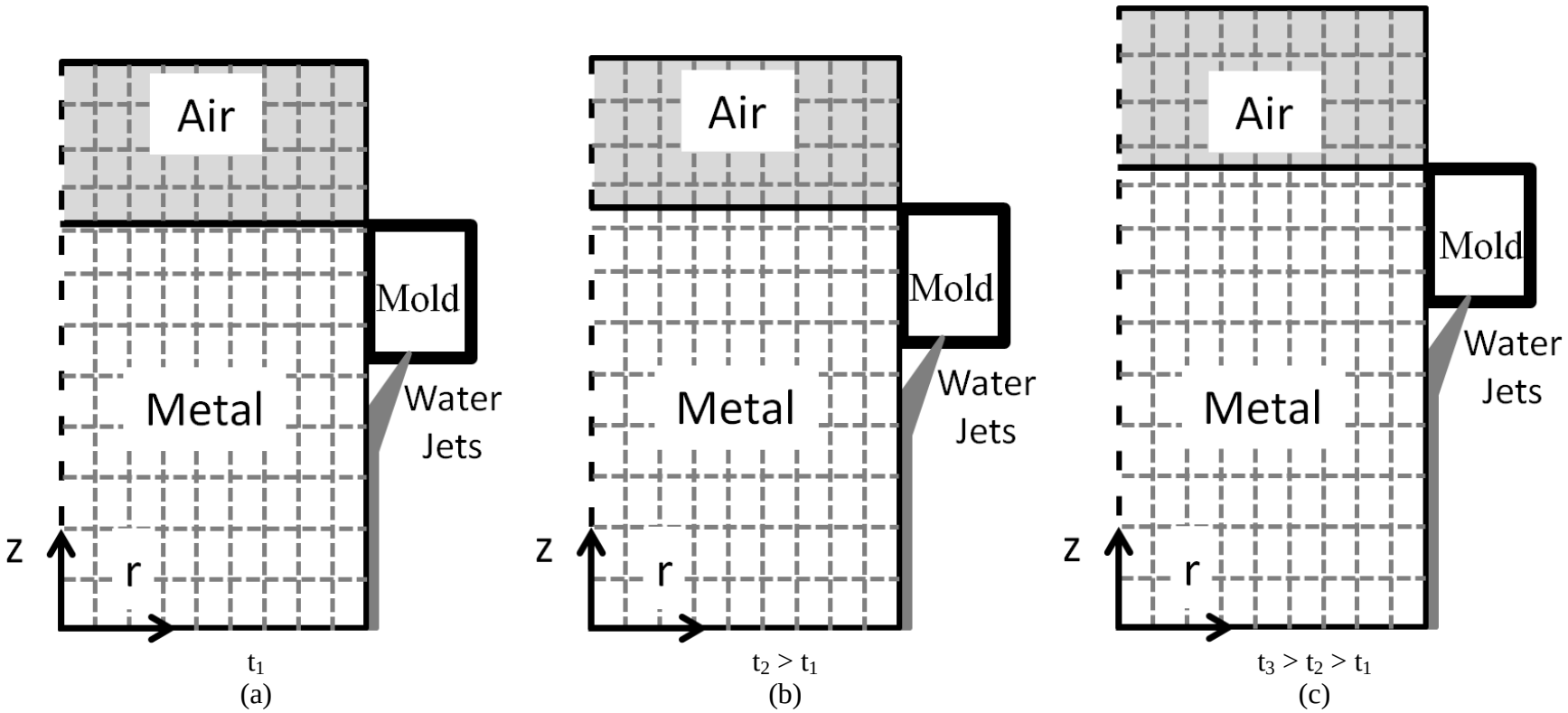

Figure 2.3: Schematic showing the progression through time of the liquid-air interface, thermal boundary conditions, and addition of a new row of control volumes containing air. (a) $t = t_1$ when the interface first enters a new row of control volumes, (b) $t = t_2$ when the interface is half way through the control volume row, and (c) $t = t_3$ after a new row of control volumes were added to the top of the domain.

$$\overline{H} = \left[f_s^1 c_s^1 T + \left(1 - f_s^1\right) \left(c_l^1 T + L_f^1\right)\right] F + \left[f_s^2 c_s^2 T + \left(1 - f_s^2\right) \left(c_l^2 T + L_f^2\right)\right] (1 - F), \tag{2.21}$$

which, solved for temperature, becomes:

$$T = \frac{\overline{H} - F f_l^1 L_f^1 + (F-1) f_l^2 L_f^2}{F f_s^1 c_s^1 + F f_l^1 c_l^1 + (1-F) f_s^2 c_s^2 + (1-F) f_l^2 c_l^2}. \tag{2.22}$$

2.4.1 Initial and Boundary Conditions

Initially the active domain height is 12 cm, of which the metal occupies the bottom 9 cm, the rest filled with air. This metal level occupies a mold which consists of a hot top, a graphite ring, and an aluminum mold, the dimensions and various thermal boundary conditions are shown in Figure 2.2. A constant heat transfer coefficient of 1000 W/m^{2}K was used for the bottom boundary, which assumes conduction through perfect contact between the metal and the bottom block throughout the casting process. This assumption is not perfect, because the bottom of the ingot is known to curl away from the bottom block [20]. However, the free-falling water does pool in the space between the bottom block and curled ingot bottom, which boils and enhances the heat transfer [20]. A heat transfer coefficient of 1000 W/m^{2}K is an estimate with high uncertainty and will influence the start up part of the process but, as the solidification front moves further away from the bottom block, the influence of that selected condition will lessen. The value picked does produce a transient temperature field for a length of roughly one diameter, which is typical for this process [63].

The heat transfer coefficients along the mold wall are functions of fraction solid. This adjustment allows for the effect of solidification shrinkage, which causes an air gap

to form between the metal and the mold. The heat transfer coefficients for the graphite ring and aluminum mold sections, which make up the primary mold chill, were found by using a thermal resistant network for each section independently (Figure 2.4). To initially determine the heat transfer coefficient, before shrinkage has an effect, perfect contact was assumed between the liquid and the mold surfaces. For the graphite ring, the heat is assumed to flow in series from the metal through a 4.5 mm thick, porous graphite ring filled with oil and a 6 mm thick aluminum block, before reaching the room temperature water cooling the mold. In the 4.5 mm thick graphite layer, three heat flow paths were considered to be operating in parallel; graphite layers aligned parallel to each other, layers aligned perpendicular, and a path containing only oil. For the aluminum mold portion, the heat flow path consisted of a 10.5 mm thick aluminum block separating the ingot from the water chill operating in series. To calculate the heat transfer coefficient which accounts for shrinkage, two parallel resistances (for radiation and convection across the gap) were added between the ingot and mold sections. These values of overall effective heat transfer coefficient for each mold section obtained from these networks were nearly identical (41.6 and 41.7 W/m^2K), so the same value was chosen for both. Property values for the resistances in the thermal network were taken from Incropera et al. [64].

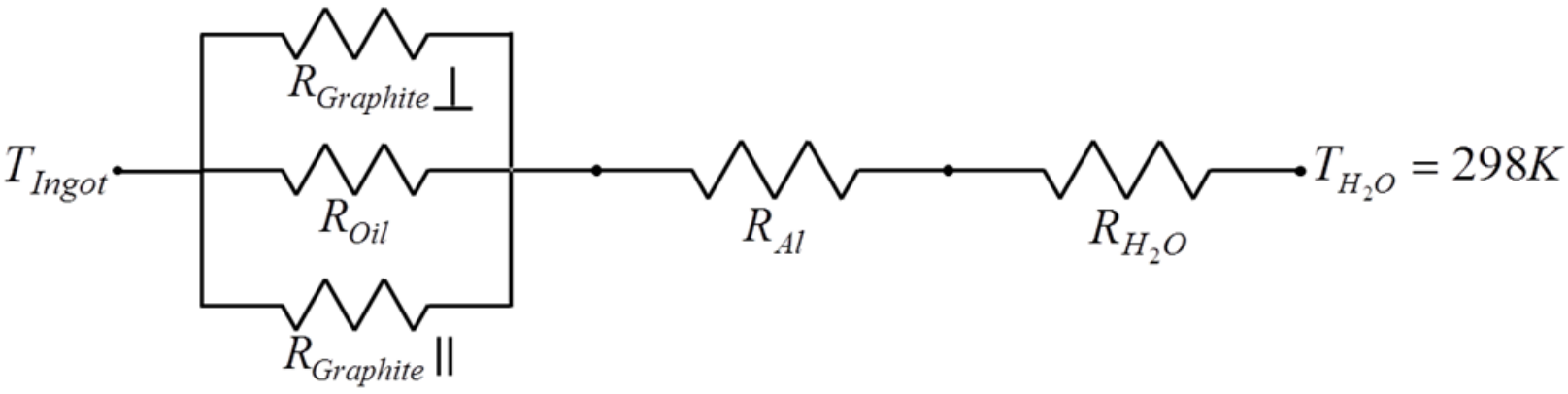

(a)

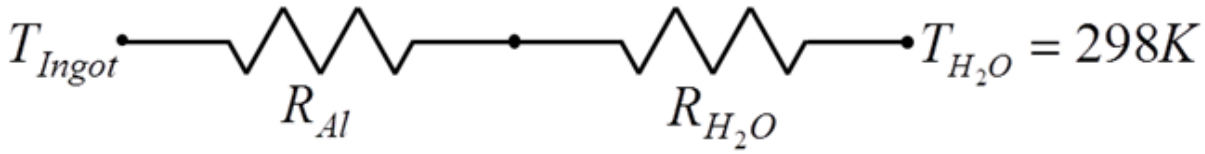

(b)

Figure 2.4: Schematic of the thermal resistance network for the (a) graphite ring and (b) aluminium block regions of the mold used to calculate the effective heat transfer coefficient.

For both alloys examined using this process model in this work, the entire domain is set initially to the pouring temperature of 950 K (677 ^{o}C) (superheat = 44.4 K), and the starting mixture composition. To simulate starting with different thicknesses of molten pure Al on the bottom block (so-called dilute start), the initial mixture composition was diluted accordingly, assuming the two fluids are well mixed during filling. The liquid is initially held in the mold without any addition of metal, in order to develop a solid shell near the mold wall. At 60 s, the casting speed (simulated by metal addition) is stepped to 50% of the steady state value, and linearly increased from there to the steady state value, which is reached when the ingot length is 0.35 m. This initial ingot acceleration depends on the steady V_c, and is 0.49 mm/min^2, 2.00 mm/min^2, and 4.55 mm/min^2 for casting velocities of 30, 60, and 90 mm/min, respectively.

The velocity boundary conditions are symmetry at the centerline and a free surface at the outer radius, and no slip at the bottom. An outflow condition at the top allows air to leave the domain as it is pushed out by the addition of metal at the VOF interface. The addition of molten metal at the VOF interface is treated as a volume source in the pressure and pressure correction equations of the SIMPLER algorithm, as shown in [55].

Below the mold, the ingot is directly cooled by impinging water jets and free falling water. The boundary conditions for this region are from Weckman and Niessan, who developed empirical correlations for the heat transfer coefficient for a free-falling turbulent film of water as a function of water temperature (T_{H_2O}), wall temperature (T_{wall}), ingot diameter (D), and volumetric water flow rate (Q) [65]. Two different correlations are used, the choice of which depends on whether or not the water on the

metal surface is boiling. To determine which coefficient to use, the heat flux for incipient boiling is found first:

$$q''_{IB} = 39100\left[\frac{W}{m^2 K^{2.16}}\right]\left(T_{wall} - T_{boil}\right)^{2.16}. \tag{2.23}$$

If the incipient heat flux, equation (2.23), is greater than the flux predicted using the heat transfer coefficient for a no-boiling condition,

$$h = \left[704\left[\frac{Ws^{1/3}}{K^2 m^{8/3}}\right]T_{wall} - 3.782x10^5\left[\frac{Ws^{1/3}}{Km^{8/3}}\right]\right]\left(\frac{Q}{\pi D}\right)^{1/3}, \tag{2.24}$$

and

$$q'' = h\left(T_{wall} - T_{H_2 0}\right), \tag{2.25}$$

then the coefficient in equation (2.24) is used. If the heat flux in equation (2.23) is less than the flux from equations (2.24) and (2.25), then the coefficient for boiling heat transfer,

$$h_b = \left[704\left[\frac{Ws^{1/3}}{K^2 m^{8/3}}\right]T_{wall} - 3.782x10^5\left[\frac{Ws^{1/3}}{Km^{8/3}}\right]\right]\left(\frac{Q}{\pi D}\right)^{1/3} + \frac{20.8\left[\frac{W}{m^2 K^4}\right]\left(T_{wall} - T_{boil}\right)^3}{\left(T_{wall} - T_{H_2 O}\right)}, \tag{2.26}$$

is used for the outer radius boundary condition.

In cases where there is a wiper present, a constant heat transfer coefficient of 5 W/m^{2}K is used below the wiper to model natural convection in air, and heat transfer through the wiper is ignored. The heat transfer coefficient below the wiper was

determined based on calculations for natural convection on a vertical flat plate. Naturally the heat extraction rate will decrease further from the wiper as the surface temperature decreases. The details of this effect were ignored in the current model because the heat transfer rate from the ingot radial surface is orders of magnitude less than through the bottom of the domain, even close to the wiper. Therefore, doubling or halving the coefficient will not significantly alter the temperature gradients of the ingot below the wiper.

2.5 Static Casting Model Considerations

A two dimensional, Cartesian, rectangular static casting is the other process of interest in this work (Figure 2.5). The domain is cooled from the left wall with a constant and uniform heat transfer coefficient and the other walls are adiabatic. Solidification shrinkage is considered in this model, so an inlet is placed at the top of the domain to allow incoming metal to feed the volume loss. The simulations begin with quiescent liquid with a superheat of 21.8 K (T_o = 940 K). The thermal boundary conditions are shown in Figure 2.5, in which the chill is applied as a constant and uniform heat transfer coefficient of h = 1,500 W/m^{2}K. All domain walls have a no-slip velocity boundary condition and are impermeable to species. The metal entering the domain through the inlet is at the superheated temperature and nominal composition. The instantaneous velocity of the incoming metal is set based on the volume that was lost due to shrinkage in a given time step. This velocity is found from

$$V_{in} = \frac{\Delta \forall_{shrink}}{\Delta t A_{in}} \tag{2.27}$$

at each iteration and is applied uniformly as $v = -V_{in}$ over the inlet. The shrinkage volume deficit is [66]

$$\Delta \forall_{shrink} = \sum_{i=1}^{n} \left(\frac{\rho_s - \rho_l}{\rho_l} \right) \Delta g_s^i \Delta x^i \Delta y^i \tag{2.28}$$

Due to the incoming metal having a superheated temperature, the simulation ends when 95% of the control volumes are fully solid.

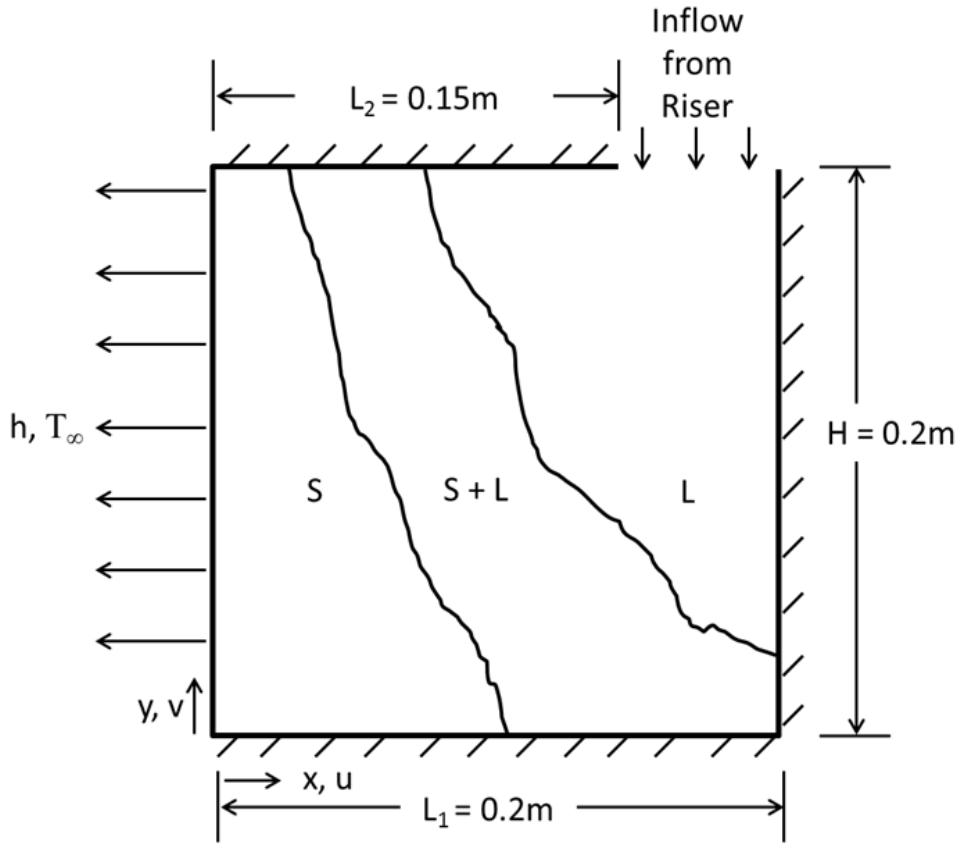

Figure 2.5: Schematic of the numerical domain showing the dimensions and thermal boundary conditions.

2.6 Macrosegregation Level Assessment

The commonly used macrosegregation number, $M^i = \left[\frac{1}{V_{ss}} \iiint_{Volume} \left(\frac{C^i}{C_o^i} - 1 \right)^2 dV \right]^{\frac{1}{2}}$, which is a normalized standard deviation of the predicted composition distribution over the ingot volume, has been used to quantify the overall level of segregation for castings, if the data are fit to a Gaussian distribution (see [67,68] for the earliest examples). However, it has been shown recently that the volume-based distribution of composition in most castings is not Gaussian and that the use of M^i can over-predict the segregation level [30,69]. Recently, there have been efforts to better quantify the macrosegregation level in ingot castings by using a cumulative distribution function to describe the composition field [69,70]. To more accurately characterize the macrosegregation level, another metric introduced in [69], and discussed in detail in Appendix A, will be used here.

The new metric uses Weibull and a cumulative volume function, which can be interpreted as a CDF. This function quantifies the ingot volume fraction that has a composition less than or equal to that unique value. A three parameter Weibull distribution is fit to the data set, and its normalized deviation, W^i, is used to represent the overall macrosegregation level:

$$W^i = \frac{\sqrt{{\omega^i}^2 \Gamma\left(1 + 2/\alpha^i\right) - {\omega^i}^2 \left[\Gamma\left(1 + 1/\alpha^i\right)\right]^2}}{C_o^i}. \tag{2.29}$$

2.7 Uncertainty Quantification Procedure

This study uses the publicly available PRISM Uncertainty Quantification (PUQ) framework to perform the uncertainty quantification. Details of this software can be found elsewhere [28], so only a brief description will be provided here. A simple example of how this framework can be used is given in Appendix B, and is also available through the nanohub.org [71]. PUQ calculates a PDF for each output quantity of interest, given the known uncertainty of select inputs. The outputs of interest are sampled from the full numerical model to generate a polynomial response surface, which acts as a surrogate to running the full process model. In PUQ, the computationally efficient Smolyak sparse grid algorithm [72–75] is used to determine simulation conditions of the runs required of the numerical model to generate an adequate surrogate model. A level 1 Smolyak grid varies each uncertain input independently and requires the least number of cases from the full process model. Polynomial chaos expansion (PCE) or global polynomial chaos (gPC) methods are used to generate functions fitted to those sparse model predictions [74]. Level 2 and 3 Smolyak calculations consider the effect of varying multiple inputs at a time and produce surrogate models that are polynomials of second and third order, respectively. The number of predictions with input interactions increases with the order of the polynomial function. Even higher Smolyak levels are possible, but require progressively more full process model cases to be run, raising the computational cost. For example, a level 1 Smolyak produces a first order polynomial and requires 1+2n model evaluations where n is the number of uncertain inputs. A level 2 Smolyak produces a second order polynomial and requires 1+4n+(4n(n-1))/2 model evaluations.

The fit of the polynomial response surface to the sampled process model outputs is quantified by using the root mean square error (RMSE). The surrogate model polynomials used during this study can be found in Appendix C. The output PDFs are calculated by using Latin Hypercube sampling to evaluate the surrogate model over the input uncertainty range. These output PDFs are characterized by their normal standard deviation and give the probability that the output has any value in its range.

The relative sensitivities of the outputs to changes in the input parameters are calculated using the Elementary Effects Method (EEM) [76,77]. The EEM uses the model predictions to calculate two sensitivity measures that determine whether the inputs have negligible, linear, or nonlinear effects on the outputs. A distribution of elementary effects is calculated for each input parameter by varying them independently with a constant step change across all levels of the other parameters. The definition of an elementary effect is shown in equation (2.30), in which $(X_{max} - Y_{min})$ is $6.15\sigma_X$, the standard deviation of input X. The elementary effect measures the change in the output over some fraction of the input uncertainty range.

$$d\left(X_j\right) = EE_j = \frac{\Delta Y_j}{\frac{\Delta X_j}{\left(X_{\max} - X_{\min}\right)}} \tag{2.30}$$

The mean sensitivity, μ^*, is the estimate of the mean of the distribution of the absolute value of the elementary effects: $\mu^* = \frac{1}{r}\sum_{j=1}^{r}\left|d\left(X_j\right)\right|$. For μ^* values near zero, the input has a small or negligible effect on the output; values much greater indicate the input plays a significant role in determining the output. This procedure is shown in Figure 2.6 for a

data set, where the mean input is 1,500 and standard deviation is 225, as an example of elementary effects calculations.

The second parameter, σ^*, is a measure of the standard deviation of the elementary effects. High values of σ^* (a wide distribution) indicate sensitivities are strongly influenced by other inputs. Low values of σ^* indicate linear dependence of the output on each input and little interdependence with other parameters. A study with a level 1 surrogate model can be used to make a crude assessment of which uncertain inputs have the most impact on the outputs of interest.

Input	Output
807	2295
1500	1406
2193	1102

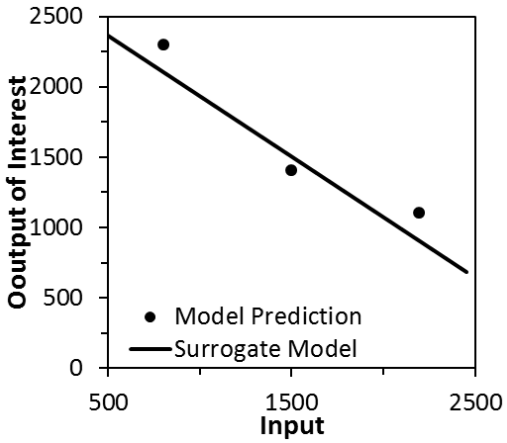

$$EE_1 = \frac{(2295-1406)}{\left(\frac{(1500-807)}{(2193-807)}\right)} = 1778 \qquad EE_2 = \frac{(1406-1102)}{\left(\frac{(2193-1500)}{(2193-807)}\right)} = 608$$

$$\mu^* = \frac{1}{2}(|1778| + |608|) = 1193$$

Figure 2.6: Plot of an example surrogate model fit to model predictions for a level 1 Smolyak run with the corresponding model results and elementary effects calculations.

CHAPTER 3. DIRECT CHILL CASTING OF ALUMINUM ALLOY 7050

The DC casting model has been used to study the solidification behavior and segregation characteristics of aluminum alloy 7050 ingots under a variety of process conditions similar to those found in practice. The results presented here give insight into the effect of jet water flow rate, casting speed, ingot diameter, and superheat on the macrosegregation and thermal behavior of the developing solid ingot. The standard operating conditions for this study are shown in Table 3.1. The effect of local grid refinement is also discussed, as it affects the packing model and results in axial streaks in the compositional field.

Table 3.1: Standard operating parameters for DC casting simulations.

Parameter		**Value**
Casting Speed	V_c	60 mm/min
Ingot Diameter	D	0.5 m
Particle Diameter	d	30 μm
Cooling Water Flow Rate	Q	0.002 m^3/s
Packing Fraction	$g_{s,crit}$	0.15
Superheat	ΔT_{super}	44.4 K

3.1 Standard Case

The temperature, flow, and compositional fields, and the sump shape for standard operating conditions during start-up and steady state are shown in Figure 3.1. Early in the process, Figure 3.1(a), the rigid mushy zone is relatively horizontal. At this point in the,

process, heat is extracted through the ingot surface and bottom block. At this time, solid has formed across the bottom of the ingot and, because the flow in the slurry is very weak the solid can settle and pack more uniformly. Because most of the sump profile is horizontal, shrinkage acts vertically and transports solute uniformly to the bottom of the domain, and does not contribute to radial macrosegregation. As the DC casting process progresses, Figure 3.1(b-c), and the solidification front moves farther away from the bottom block, the boundary of the rigid mushy zone develops a vertical component and forms a “V” shaped sump. Similarly, the flow field in the slurry region of the ingot also develops a vertical component, becomes stronger, and keeps the bulk composition in the slurry well mixed. At this point, most heat is removed radially and the solid forms inward from the outer radius and, before it packs, is transported towards the center by the flow field. The composition in the rigid mushy zone also becomes more segregated as the process approaches steady state. The flow in the rigid mushy zone now has a horizontal component and transports solute towards the ingot surface. This radial transport contributes to the ingot macrosegregation level, which increases as the process approaches steady state. Therefore, the composition field cannot reach a steady level until after the steady state sump shape and depth is established.

The flow field can be thought of in two ways, the flow relative to the ingot (Figure 3.1(d)), or flow relative to the mold in the laboratory frame (Figure 3.1(e)). In both reference frames, the liquid metal enters the top of the domain and immediately moves towards the mold wall due to the shrinkage that occurs as the solid shell forms. The liquid metal then flows down the solidification front, along the slurry-rigid mushy zone interface, before becoming entrained in the rigid mushy zone. In the rigid mushy

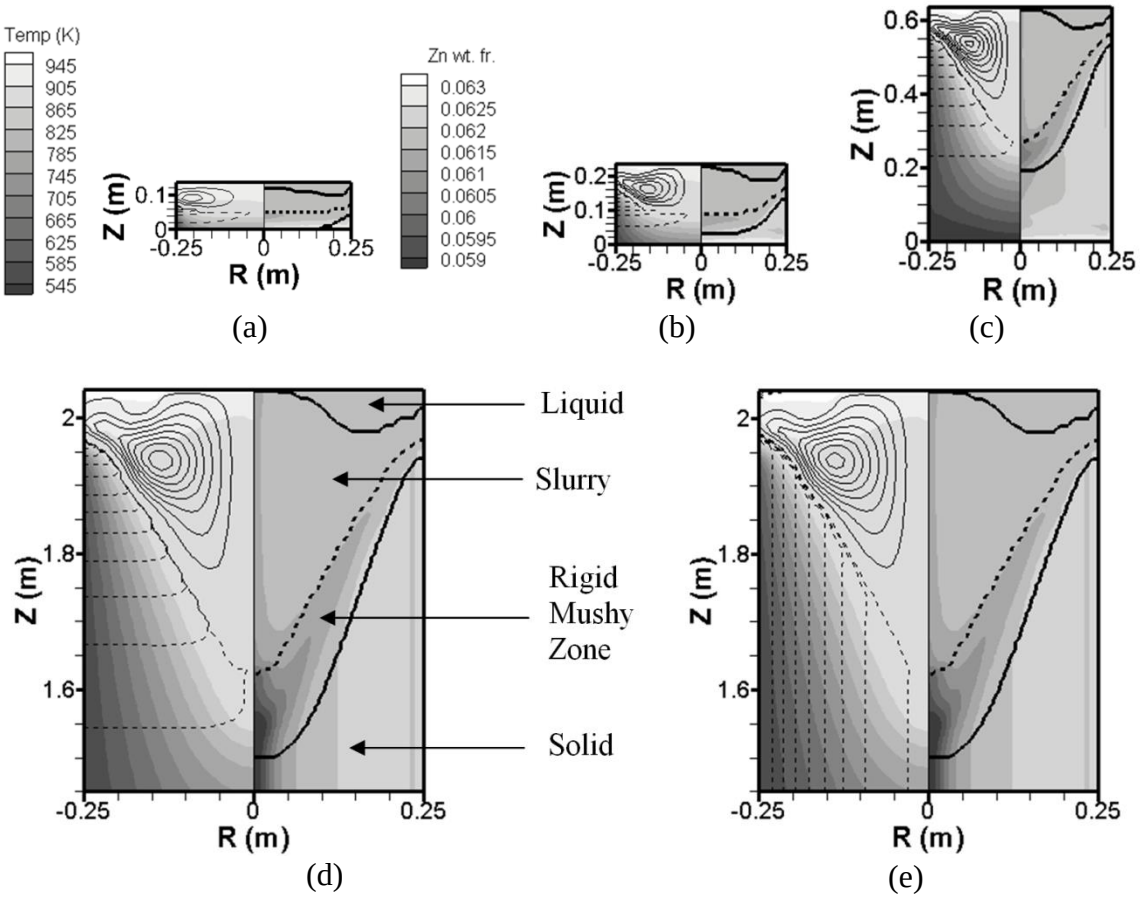

Figure 3.1: Contour plots of the temperature and Zn fields for the standard case during (a-c) start-up and (d-e) steady state process. In each, the Zn composition and sump profiles are on the right, with solid lines representing the liquidus and solidus and the dotted line indicating the packing location of the free-floating solid. On the left are liquid flow streamlines and the temperature field. The solid streamlines show the counter clockwise flow with $0.1< \rho\Psi < 1$ and $\Delta\rho\Psi=0.1$ kg/s and dotted streamline show the clockwise shrinkage driven flow with $-0.005< \rho\Psi < -0.000025$ and $\Delta\rho\Psi=0.0004975$ kg/s for (a) 103 s, (b) 198 s, and (c) 598 s. For the steady state process in (d) and (e) the dotted stream lines rotating clockwise are (d) $-0.000025< \rho\Psi <-0.005$ and $\Delta\rho\Psi=0.0004975$ kg/s, in the ingot frame of reference and (e) $-0.1< \rho\Psi < -0.001$ and $\Delta\rho\Psi=0.0099$ kg/s, in the laboratory frame of reference.

zone, the shrinkage driven flow is shown directly by the dotted streamlines in Figure 3.1(d) acting perpendicular to the solidification front. For streamlines shown in the mold frame of reference, Figure 3.1(e), the radial component of shrinkage driven flow is not as apparent. However, since the model in this study uses the VOF interface as the metal inlet, in which metal is added with no initial velocity, the radial location of the metal inflow is not part of the flow cell. In both reference frames the shrinkage driven flow transports the enriched interdendritic liquid deep into the mushy zone, from the center of the ingot towards the surface due to the "V" shaped steady state sump profile. This basic flow and segregation patterns are similar to those seen in previous work, e.g. [7,12].

The axial location at which the process was deemed to be at steady state was where the radial macrosegregation level, Figure 3.2(a), fluctuations are less than $1x10^{-4}$ wt. fr. The volume of the ingot occupied at the surface of the ingot in Figure 3.2(a) is larger than the volume at the center of the ingot. Therefore, the are under the curve in the positively segregated regions is not the same as the area above the curve in the negatively segregated regions in Figure 3.2(a). The radial macrosegregation level was calculated at each axial position using the normalized Weibull deviation, W^i, which weights each composition in the distribution by the volume of the cell in which it is predicted. The results from the standard case are shown in Figure 3.2(b). Generally, the radial macrosegregation level increases with the axial position and eventually approaches a steady state value. The initial sharp increase in macrosegregation level near the bottom of the ingot occurs during the one minute hold time before metal is added to the domain. For the standard case, the process achieves steady state at 57.5 cm, which is slightly more

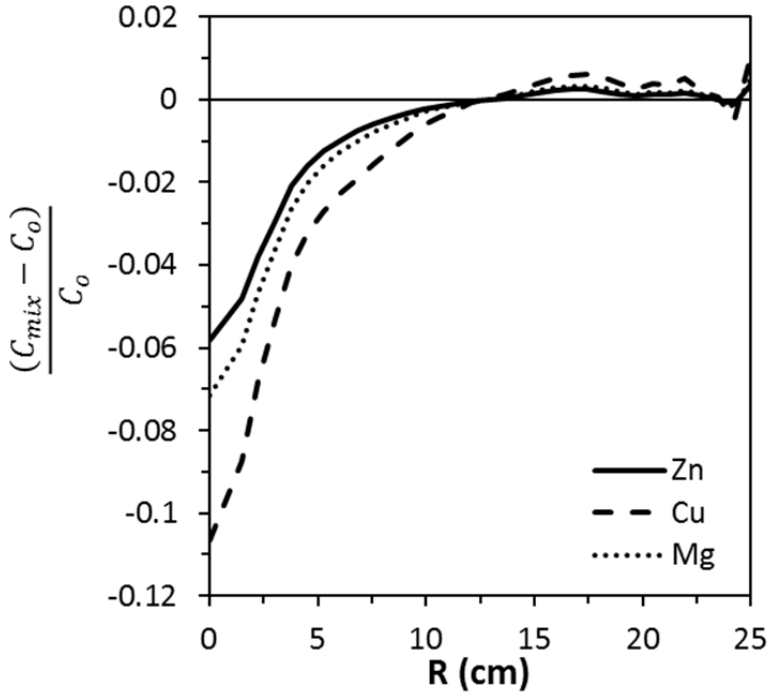

(a)

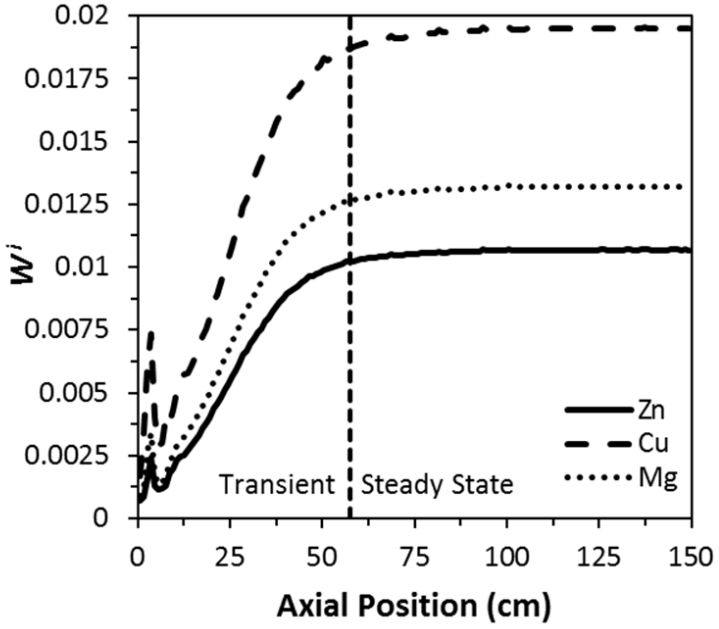

(b)

Figure 3.2: Level of macrosegregation for each alloying element showing (a) the deviation from the nominal composition as a function of radial position and (b) W^i as a function of the axial position showing the macrosegregation level reaching a steady state value.

than the diameter of the ingot. The steady state values for W^{Zn}, W^{Cu}, and W^{Mg} are 0.0106, 0.0194, and 0.0131, respectively.

3.2 Effect of Local Grid Refinement

The resolution of the surface enrichment of the ingot, radial temperature gradient, and flow field can be improved while limiting the computational expense of having a uniformly fine grid by locally refining the near-surface control volumes. Two examples of this kind of refinement can be seen in Figure 3.3(b) and (d), in which the first 16 and 32 control volumes are 0.5 cm and the remaining control volumes are 1 cm in the radial direction. However when this refinement is used, the abrupt change in grid spacing causes a region depleted in solute to form along the interface between the two grid sizes (Figure 3.3(a) and (c)), because it directly affects how the control volumes pack when forming the rigid mushy zone. Figure 3.4 illustrates this point by examining how the grid size can change the pattern of packing even with the same distribution of solid. In this figure, a schematic of individual solid grains (not simulated here) are overlaid by the two numerical grids, in which the shaded areas are considered packed. When a smaller control volume reaches the packing fraction, a larger control volume, having the same amount of solid, has a solid volume fraction smaller than gs,crit. This difference is shown in the lower right corner of the domain at time 1 in Figure 3.4. Therefore, the smaller control volumes can better resolve the packed interface of the mushy zone than the larger control volumes.

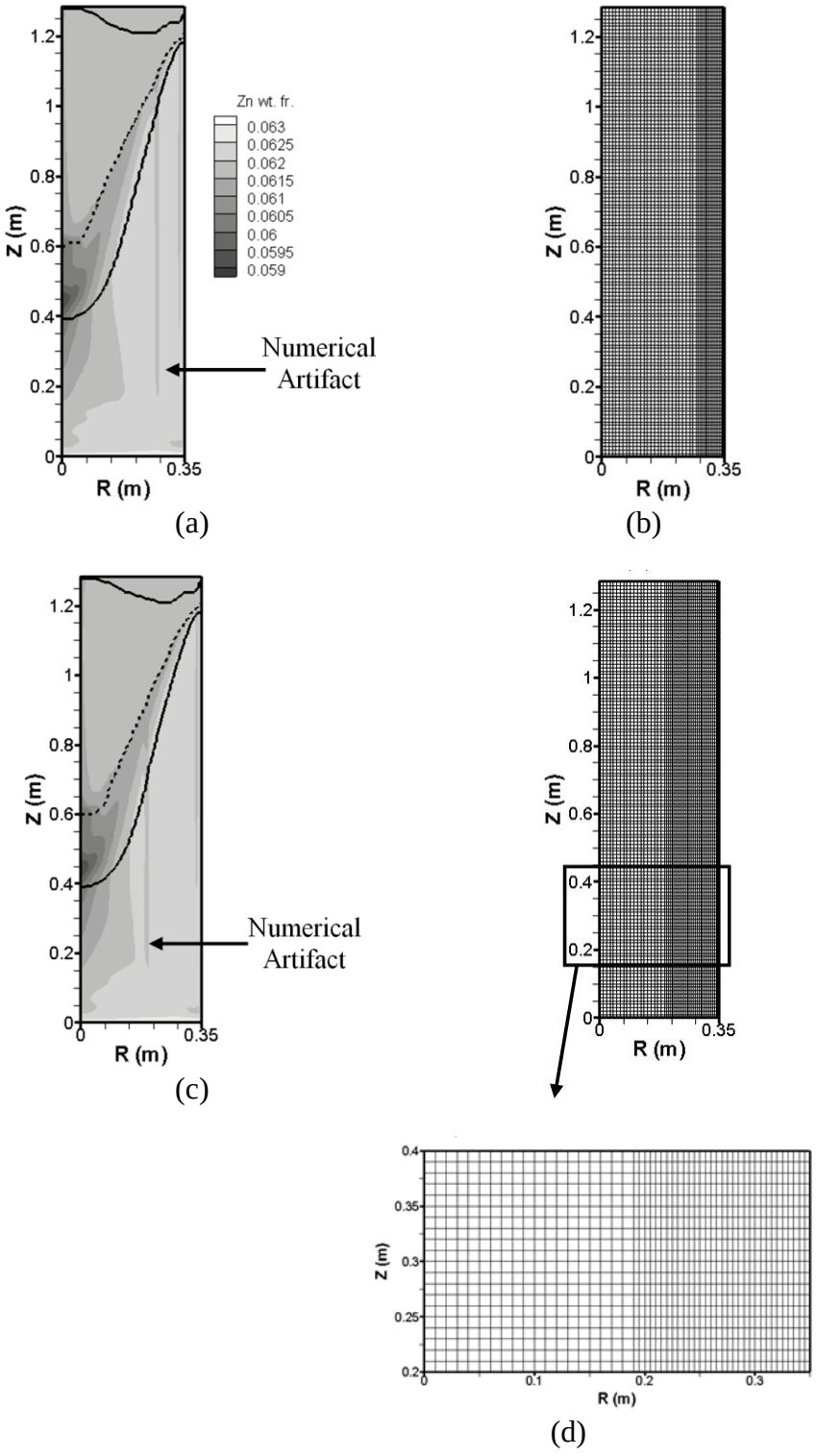

Figure 3.3: Effect of surface grid refinement showing the composition contour plots of Zn with the accompanying grid in which the abrupt transition in grid sizes produces a vertical composition streak that is depleted in solute.

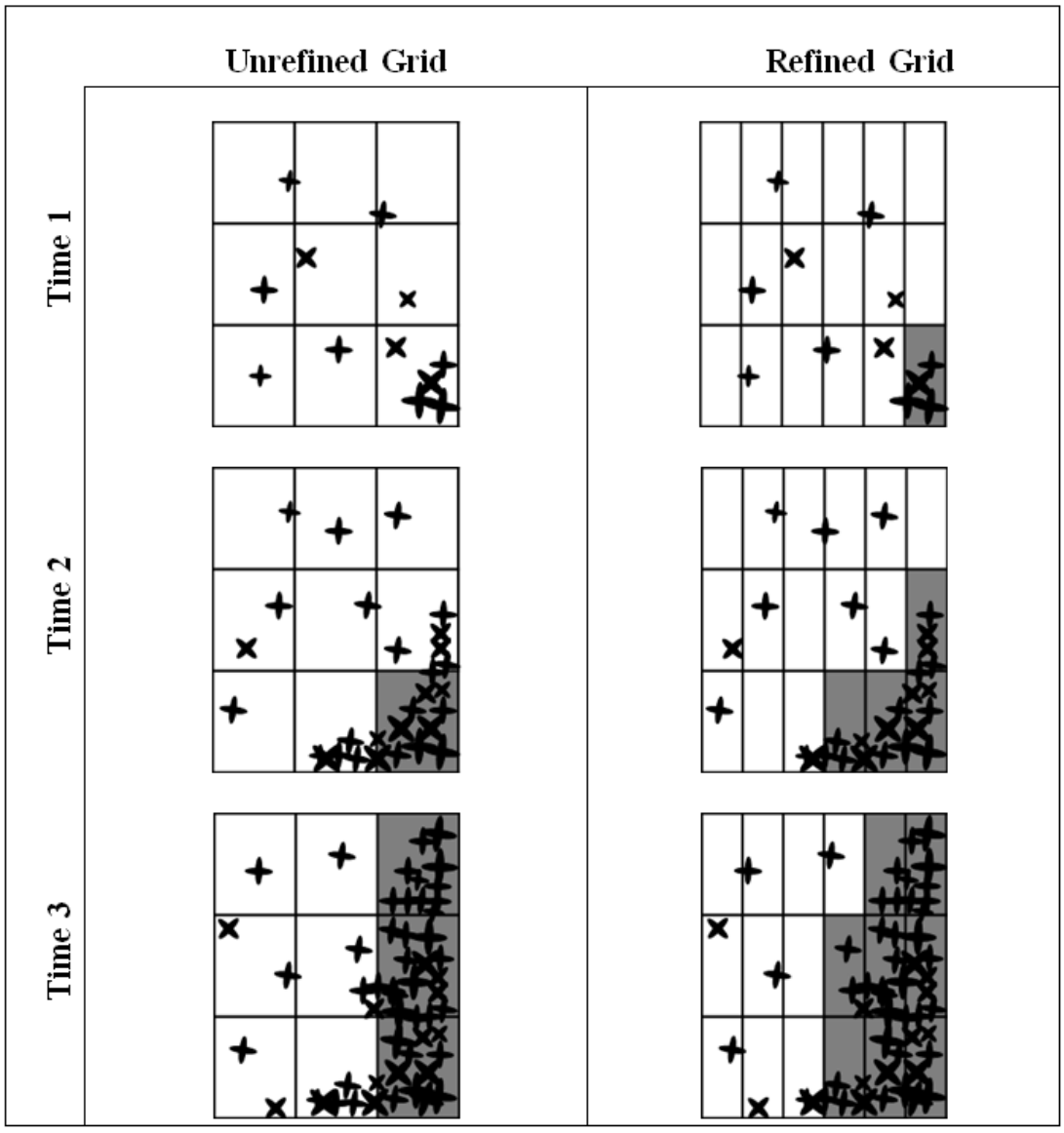

Figure 3.4: Effect of grid size on the control volume packing showing a schematic of the physical situation overlaid on 2 different numerical representations on a small portion of the domain, in which the gray control volumes are numerically considered packed and the white control volumes consist of free-floating equiaxed grains.

This difference in control volume packing then affects the flow field. The mushy zone drag terms (in equations (2.7) and (2.8)) become active once the cell becomes packed, damping much of the buoyancy driven flow, and the now dominant shrinkage driven flow is in the direction normal to the solidification front. When the grid size is locally refined, the shape of the rigid mushy zone is affected by the change in grid size due to the difference in packing (Figure 3.3). This effect becomes clearer using a larger change in grid size of 0.25 cm for the refined region and 4 cm for the unrefined region (Figure 3.5). The refined control volumes become packed easier than in the unrefined region, and at the grid transition there is a vertical region of refined, packed control volumes neighboring unpacked, unrefined control volumes. In this region, the radial component to the shrinkage flow, which dominates in the rigid mush of the refined region, pulls enriched solute from the neighboring larger control volumes, which are part of the slurry, toward the surface. Because the neighboring unrefined region is unpacked in that region at the transition, the solute is easily replaced with liquid from farther out in the slurry closer to the nominal composition. Therefore, when this unpacked, unrefined region becomes packed, and eventually fully solid, it has a composition that is depleted compared to its refined neighbor. The remaining control volumes in the unrefined region are unaffected by the grid refinement, and pack without this discontinuity. Near the bottom of the ingot, this problem does not occur because the rigid mushy zone profile is still relatively flat. It is not until the boundary of the rigid mushy zone adds a vertical component that the grid dependence becomes evident. A solution to the grid dependence of the control volume packing is to have uniform control volume sizes, or a smoother transition from the refined to unrefined region. This latter option will smear this effect

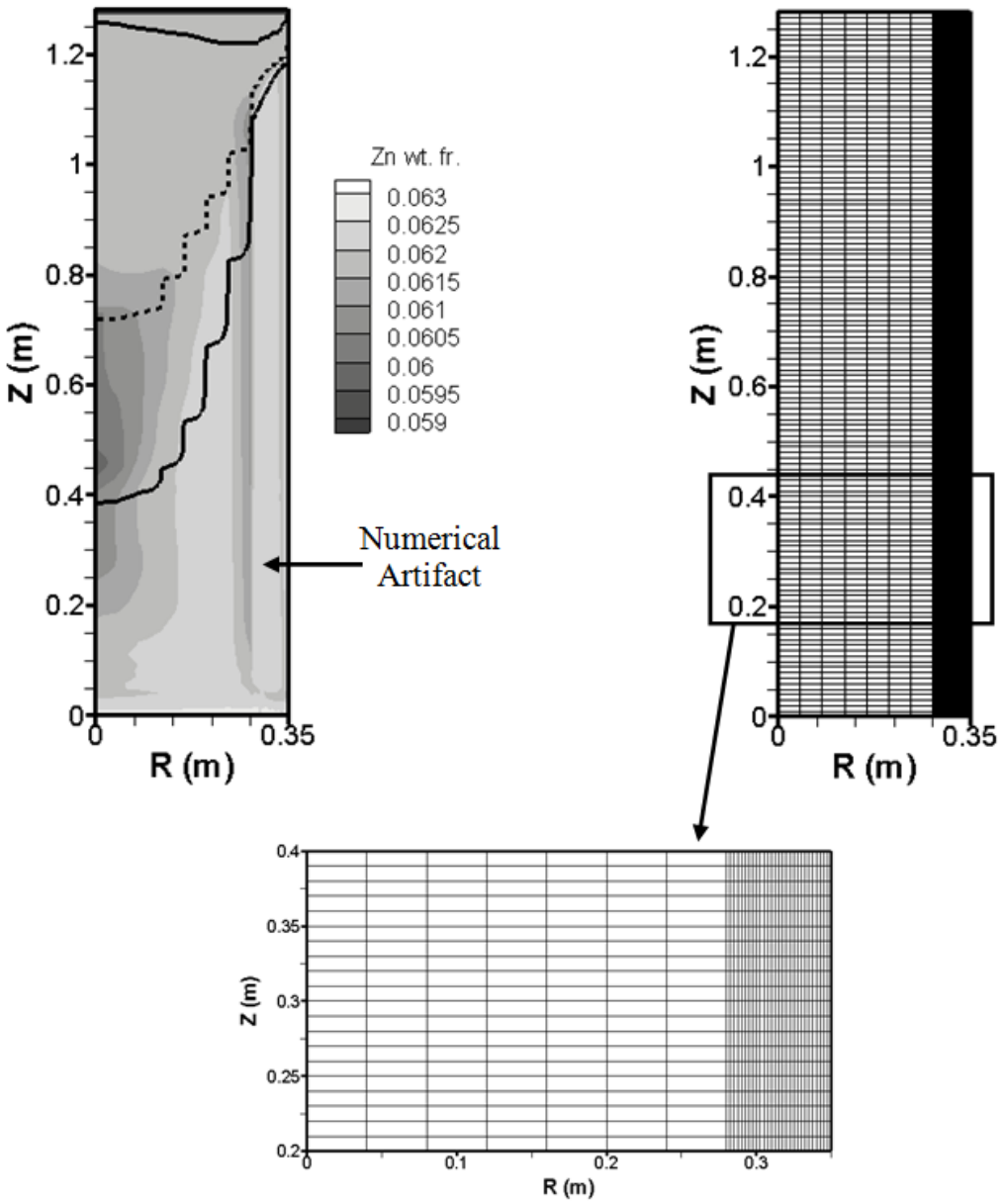

Figure 3.5: Effect of surface grid refinement showing the composition contour plots of Zn with the accompanying grid in which the abrupt transition in grid sizes produces a vertical composition streak that is depleted in solute.

out over several control volumes instead of just one. For the rest of this study, the entire domain has a uniform control volume size of 1 cm in the axial direction and 0.758 cm in the radial direction.

3.3 Effect of Ingot Diameter

The effect of ingot diameter was investigated by comparing the standard case to one with a larger diameter (φ = 70 cm). A longer time is needed for the center of the larger diameter ingot to be affected by the surface heat transfer coefficient, so the point at which the process achieves compositional steady state (Z_{ss} = 80.5 cm) is farther from the bottom block than in the smaller diameter ingot. The process reaches steady state at an axial distance that is 10.5 cm longer than the diameter of the ingot, although the Z_{ss}/φ ratio is 1.15 for both cases. The sump depth, defined as the distance from the inlet to the top of the rigid mushy zone at the centerline, is larger in the 70 cm diameter billet (SD_{ss} = 72 cm) than the 50 cm diameter billet (SD_{ss} = 43 cm). The SDss/φ ratio for the larger case (≈ 1) is larger than for the standard case (≈ 0.8), indicating a steeper rigid mushy zone interface and so stronger buoyancy driven flows. The steady state macrosegregation levels with (W^{Zn} = 0.0115, W^{Cu} = 0.0203, and W^{Mg} = 0.0142) are all slightly larger than for φ = 70 cm. However, because the majority of the relative transport of solute occurs in the rigid mushy zone by means of shrinkage driven flow, more insight is gained by examining sump shape.

The sump shape at the centerline between the two cases is also different, Figure 3.1(d) and Figure 3.6(a), as the larger diameter case has a horizontal region at the centerline creating more of a “U” shaped sump and the smaller diameter has a “V”

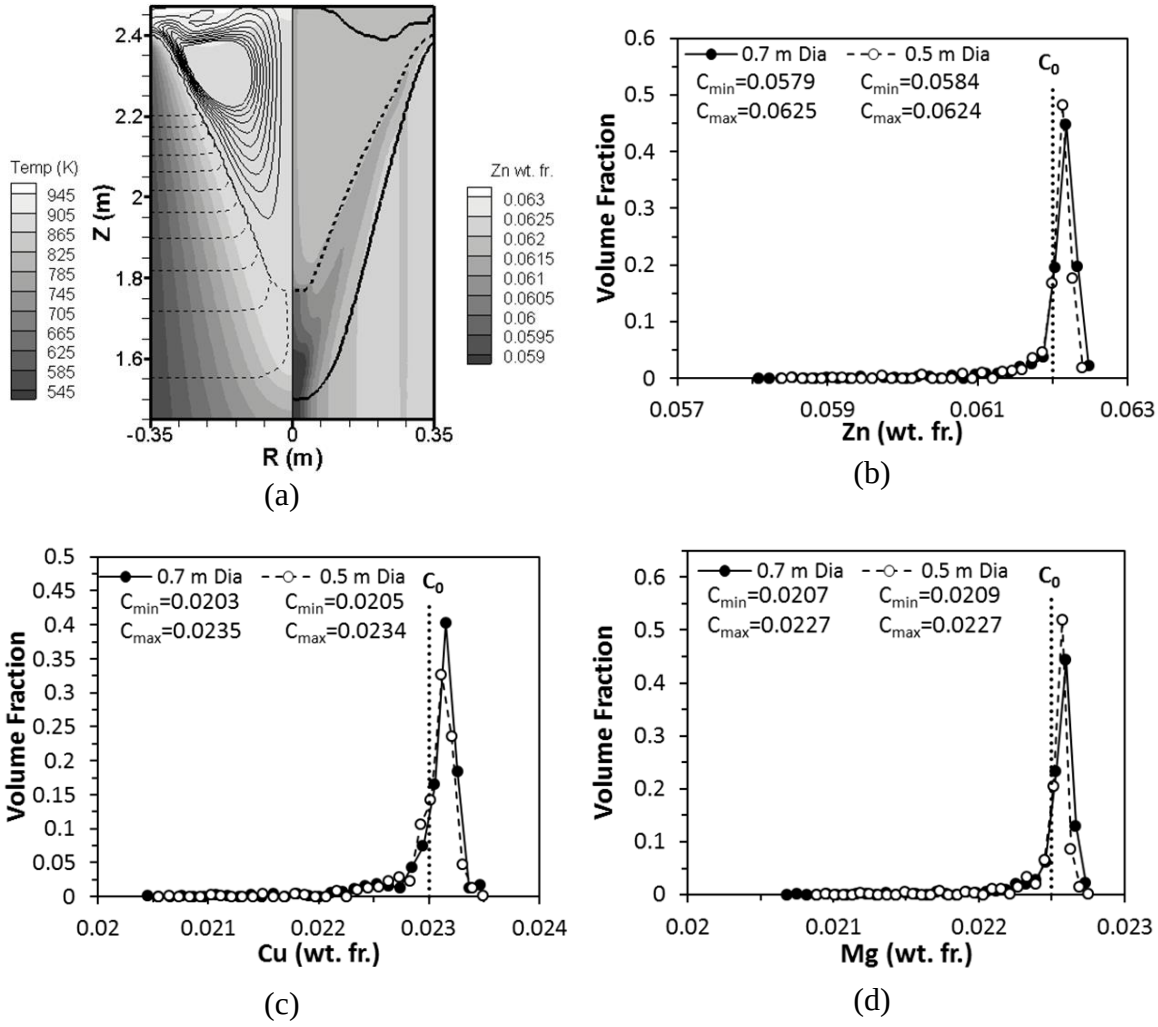

Figure 3.6: Steady state composition fields showing (a) the temperature, sump, and flow field for φ = 70 cm and the corresponding steady composition distributions for (b) Zn, (c) Cu, and (d) Mg comparing two billet diameters.

shaped sump. This distinction becomes important since the shrinkage driven flow acts vertically at the centerline in the large diameter case, and so contributes little to the macrosegregation level. This level of radial shrinkage flow at the centerline explains how the large difference in the sump depth only contributes to a small increase in the macrosegregation level. The differences in segregation distributions can also be seen in the composition distributions, Figure 3.6(b-d), which captures the volume fraction of the billet each composition occupies [30]. The larger diameter case has a longer tail, which corresponds to the centerline composition and causes a larger W^i; but this change is entirely due to increased particle settling, which offsets less shrinkage driven segregation. Although the sump depth and W^i increase in the larger diameter ingot, the ingot is still within the composition specification. Consequently, as long as the initial composition is near the middle of the specification compositionally sound castings can be produced with $\varphi = 70$ cm.

3.4 Effect of Casting Velocity

The effects of different casting velocities (30, 60, and 90 mm/min) on the transient development towards the steady state sump depth and macrosegregation level were compared. Other studies have observed that the steady state sump depth and macrosegregation level increase with the casting speed [16,78]. The radial macrosegregation level in terms of Zn, W^{Zn}, as a function of the axial height for all three cases is shown in Figure 3.7, where Z_{ss} is designated with a vertical line. Here, the 30 mm/min casting speed reaches steady state after 72.5 cm, while the two other casting speeds reach steady state after 80.5 cm. The slow casting speed allows the influence of

the thermal boundary conditions to penetrate further into the ingot at a lower axial position. The less steep steady state sump weakens the flow field, so solid particles in the slurry are more likely to settle and pack to the rigid mushy zone. The two faster casting rates have progressively larger radial temperature gradients and therefore even stronger steady state flows and deeper sumps. However, the point at which compositional steady state is achieved is similar because near the centerline the shape of the rigid mushy zone between the two faster casting speeds is similar, as shown in Figure 3.7.

The macrosegregation level increases with the casting speed due to the change in the slope of the solidification front, which also affects the direction of the shrinkage driven flow, causing more negative centerline segregation for faster casting speeds. This previously explained relationship between the sump depth, macrosegregation level, and casting speed [4,14,16] is shown in Figure 3.8. The steady state sump depth increases almost linearly from 37 cm at V_c = 30 mm/min to 96 cm for V_c = 90 mm/min. However, the macrosegregation level does not exhibit the same relationship. A 50% increase in the casting speed, from the moderate case of 60 mm/min to 90 mm/min, causes only a 6 % increase in W^{Zn} from 0.0115 to 0.0122. Decreasing the casting speed by 50% to 30 mm/min caused a decrease in W^{Zn} of 58 % from 0.0115 to 0.0048. The 30 mm/min casting speed has the smallest rigid mushy zone depth and the shallowest sump depth (Figure 3.8(c)), so less solute is transported toward the ingot surface. This casting speed has less segregation than the smaller diameter ingot (ϕ = 50 cm). The higher casting speeds have steeper isotherms, which causes more solute to be transferred by shrinkage flow toward the ingot surface and increases the level of centerline segregation. However,

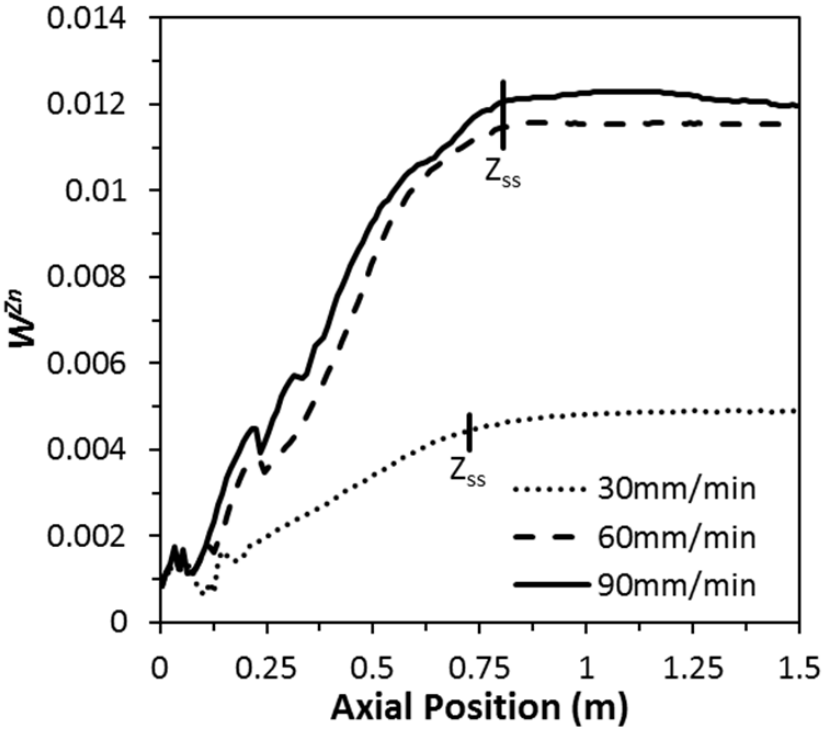

Figure 3.7: Effect of casting speed showing W^{Zn} as a function of the axial position indicating the onset of steady state (Z_{ss}) with a vertical line.

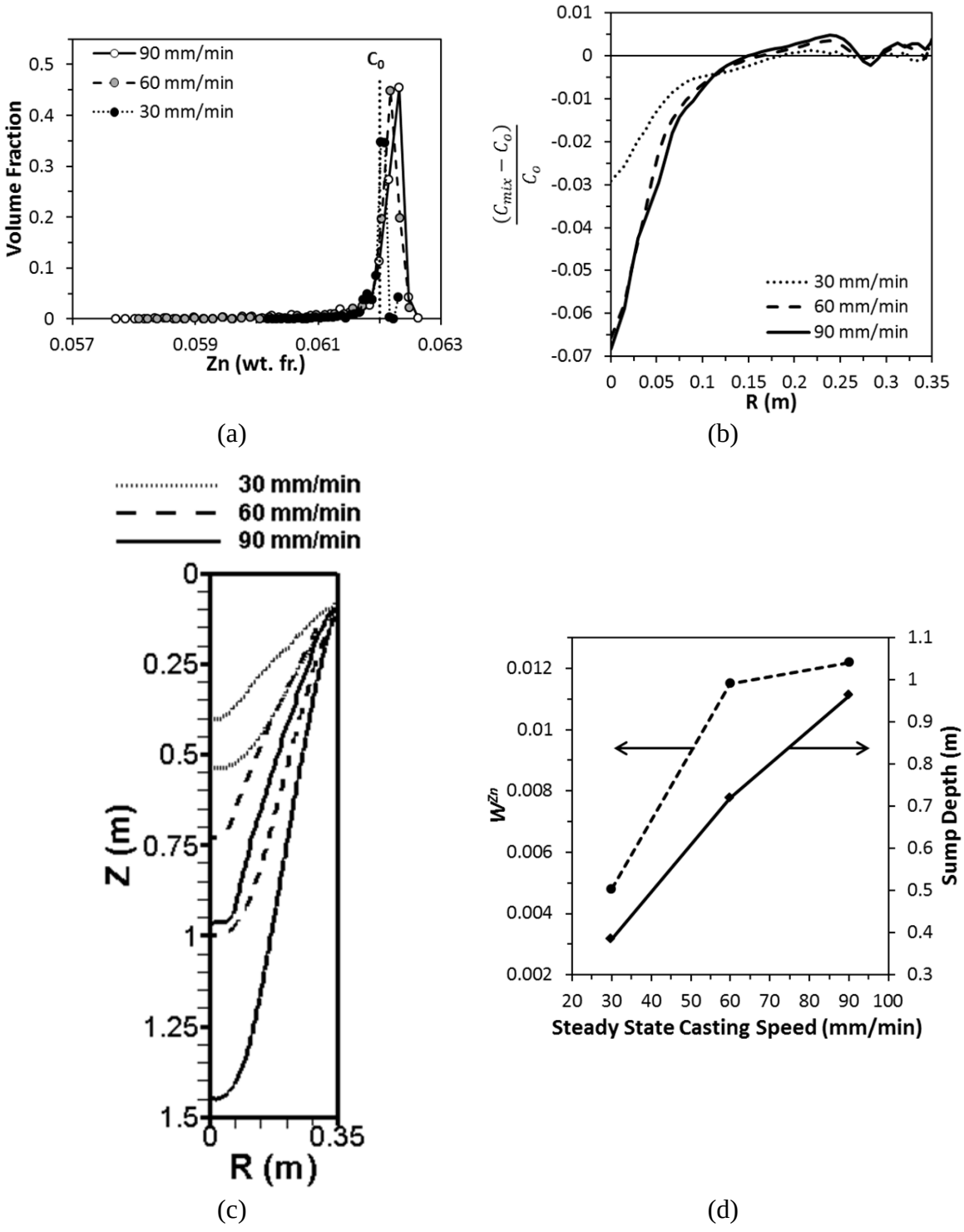

Figure 3.8: Effect of casting speed showing (a) steady state composition distributions for Zn, (b) normalized radial profile of the Zn segregation 1.5 m from the bottom block, (c) the rigid mushy zone profiles for casting velocities of 30 mm/min, 60 mm/min, and 90 mm/min, and (d) relationship between sump depth and segregation on casting speed.

the shape of the rigid mushy zone boundary for the 90 mm/min casting speed is flat at the centerline, rather than curved for 60 mm/min cases. The shrinkage driven flow for the 90 mm/min case is vertical near the rigid mushy zone boundary, which does not contribute to macrosegregation. Also, the slope of the solidus near the centerline is very similar in the 60 and 90 mm/min casting speeds, meaning the direction of the shrinkage driven flow is the same in this region. Therefore, the direction of the shrinkage driven flow is changing across the rigid mushy zone for the 90 mm/min case, adding a radial component going from the rigid boundary to the solidus. This causes the centerline segregation level to be similar for the 60 and 90 mm/min cases, shown in Figure 3.8(a-b). The centerline segregation corresponds to the tail of the distribution in Figure 3.8(a). Additionally, the mid-radius and surface segregation levels are larger for the 90 mm/min cases, and occupy more ingot volume which impacts the composition distribution more than the centerline segregation. This radial segregation pattern explains the slight increase in W^{Zn} and the same Z_{ss} for a much larger sump depth compared to the 60 mm/min case.

3.5 Effect of Superheat

The casting superheat of the base case, 44.4 K (950 K), was increased to 64.4 K (970 K) and decreased to 24.4 K (930 K) to examine the effect on the sump and macrosegregation evolution. Previous studies have shown that the superheat over a similar range had little effect on the amount of negative centerline segregation and the sump depth, however, the segregation level at the subsurface was larger for the low superheat condition [14,15]. This study shows similar trends. The low, medium, and high superheat cases have sump depths of 71.5, 71.9, and 72.3 cm respectively. The difference

between the sump depths is less than 1 cm, which is the length of the control volume in the axial direction and within the uncertainty of the calculation. Because the sump depths are very similar for each case, each of these processes achieved steady state at the same point (Z_{ss} = 80.5 cm). The heat extraction in DC casting is large enough for the superheat to be extinguished quickly and not affect the sump depth or shape greatly. Similar macrosegregation levels were calculated for these cases with W^{Zn} of 0.0116, 0.0115, and 0.0115 for superheats of 24.4 K, 44.4 K, and 64.4 K respectively. There is a slight increase in macrosegregation level when the superheat is decreased, but there are other process parameters that have a much more significant effect, like the casting speed.

3.6 Effect of Cooling Water Flow Rate

Three different jet spray water flow rates (Q = 0.002 m^3/s, 0.00416 m^3/s, and 0.00694 m^3/s) were employed to examine the effect on the heat transfer to the water spray; the range of flow rates was picked from possible industrial practice. Another study which examined the effect of the water flow rate over a similar range showed that the macrosegregation level was not strongly affected by changes in the flow rate [3]. The current study was no exception, with W^{Zn} of 0.0115, 0.0116, and 0.0116 for the low, medium, and high water flow rates. The point at which the process reaches steady state also was not affected by Q, with each process achieving steady state at 80.5 cm. If we inspect the correlations for the heat transfer coefficient, equations (2.23) and (2.25), we see that $h \sim Q^{1/3}$, which means the heat transfer rate at the ingot surface, is a weak function of flow rate. While the correlation used is not for a specific jet geometry the weak dependence of heat transfer rate on flow rate is probably similar for any jet

geometry. Changing the water flow rate is unlikely to have much effect for any given jet geometry, while the mold design will have a real effect on the heat transfer rate (and so the solidification and stress development). More complete experimental measurements under industrial conditions are needed to determine the heat transfer rates in the mold and under the jets in various DC casting configurations.

3.7 Conclusions

A fully transient numerical model for DC casting has been developed to examine the influence of several casting and model parameters on the fluid flow, sump formation, and macrosegregation of aluminum alloy 7050 during start up and at steady state. Volume weighted radial composition distributions were fit to Weibull distributions from which the normalized deviation was used to describe the level of radial macrosegregation as a function of axial position, and so also to determine where the process reached steady state. Enlarging the ingot diameter from 50 cm to 70 cm caused Z_{ss} to greatly increase, although the Z_{ss}/φ ratio is the same. The sump depth linearly increases with the casting speed, while the increase in macrosegregation level is much greater between 30 and 60 mm/min than between 60 and 90 mm/min due to the shape of the sump. Accordingly, the steady state height increased from 30 to 60 mm/min and was the same for 60 and 90 mm/min. The superheat had a small effect on the sump shape, steady state height, and the macrosegregation level and the water flow rate had an even smaller effect. The size of the grid impacts the packing model and locally refining a region of the domain causes compositional streaks to appear.

CHAPTER 4. INFLUENCE OF A WIPER AND PURE ALUMINUM ADDITIONS ON TRANSPORT PHENOMENA IN DIRECT CHILL CASTING OF ALUMINUM ALLOY 7050

In the previous chapter the DC casting model had been used to study the startup and steady state regions of all aluminum alloy 7050 ingots under a variety of process conditions similar to those found in practice. The analysis performed in this chapter will give insight into process conditions that are used to alleviate internal stress during DC casting which decrease hot tearing susceptibility. Mainly the effect of beginning the process with a layer of pure Al along the bottom block and the effect of wiper position on the macrosegregation, thermal behavior and sump shape of the developing solid ingot, for different ingot diameters and casting velocities. The purpose of diluting the initial composition of the ingot is to shrink the freezing range and limit the amount of eutectic that forms and therefore reduce the stress level brought on by shrinkage. The purpose of the wiper is to divert the falling water from the metal surface, thereby slowing the heat extraction from the ingot and hopefully reducing the transient thermal stresses in the mushy zone and the solid metal. The standard operating conditions are a casting velocity of 60 mm/min and a cooling water flow rate of 0.00416 m^3/s. The current model is not capable of predicting the stress fields; however a discussion of the temperature and composition fields will be done. Finally, observations are made regarding wiper

placement in the light of the results presented and the thermomechanical predictions in [26].

4.1 Effect of Pure Aluminum Thickness During Startup

Four cases were examined with various thicknesses of pure aluminum at the bottom of the mold. Figure 4.1 shows the results from this study in which the pure Al thickness was set to be 2.5 cm, 5 cm, and 7.5 cm, which are compared to the case with no initial Al starting layer. The steady state sump depth was hardly affected by the amount of pure Al, decreasing slightly as the Al thickness increased; with sump depths of 71.9 cm, 71.9 cm, 70.9 cm, and 69.9 cm for no Al, 2.5 cm, 5 cm, and 7.5 cm of Al, respectively. The pure Al initially dilutes the ingot and increases the liquidus temperature and decreases the freezing range, allowing the rigid mushy zone to form more quickly during the transient startup. This packing effect carries over to the steady state process and causes the sump depth to be slightly affected by the pure Al layer thickness. The axial height at which the ingot reaches compositional steady state is strongly influenced by the thickness of the Al layer, as shown in Figure 4.1(a). The process reaches steady state at 80.5 cm, 81.5 cm, 85.5 cm, and 93.5 cm for no Al, 2.5 cm, 5 cm, and 7.5 cm of Al, respectively. With more pure Al in the initial layer, the ingot butt is diluted and requires a larger volume of the nominal metal to be added before the mixture composition increases to the desired level, and so a larger region of the ingot butt must be removed from the final product as it is out of the compositional specification. The Z_{ss}/φ ratio is 1.15 for no Al and increases to 1.16, 1.22, and 1.34 for 2.5 cm, 5 cm, and 7.5 cm of Al, respectively.

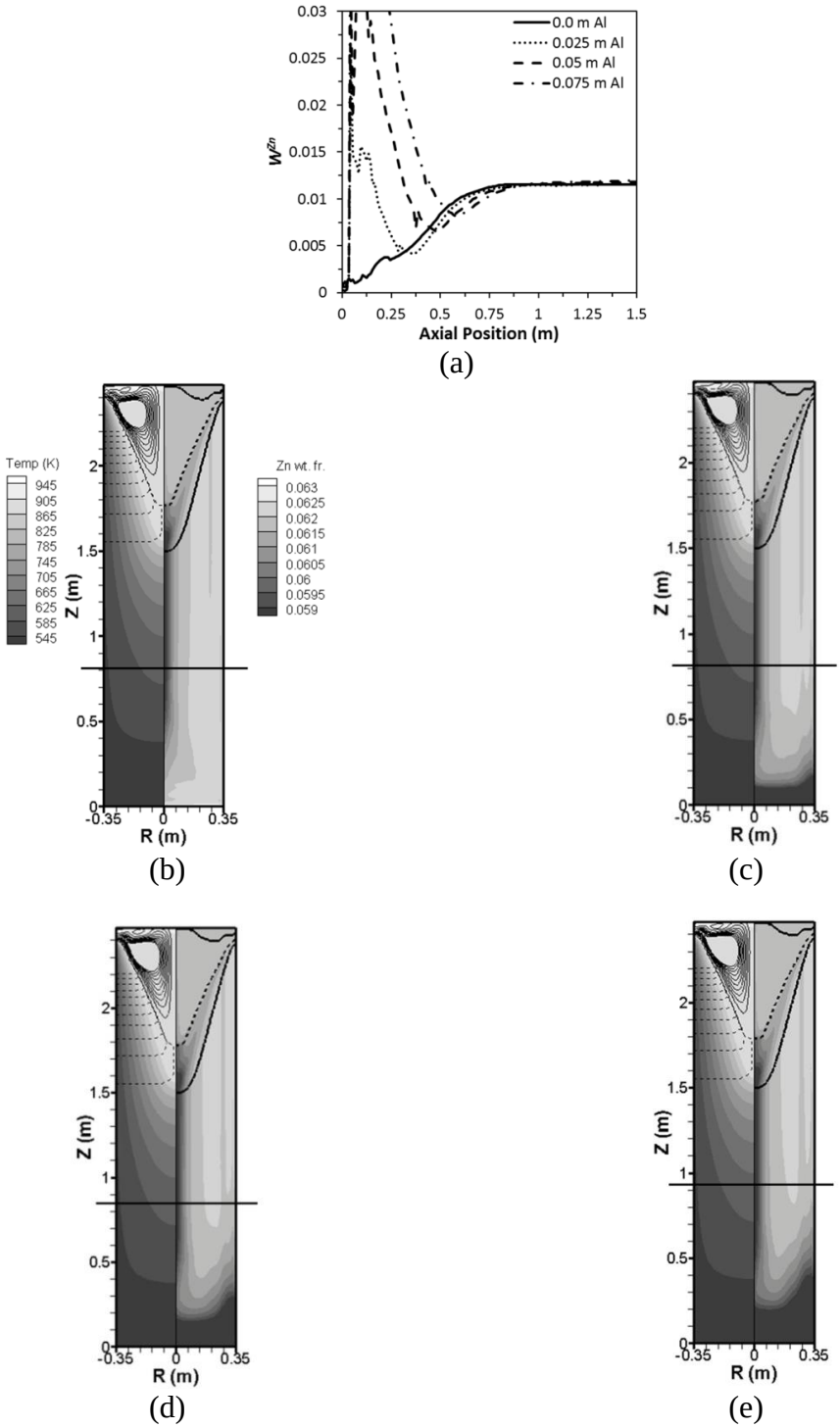

Figure 4.1: Effect of pure Al thickness layer showing (a) W^{Zn} as a function of the axial position and contour plots of the temperature and Zn fields for (b) ΔAl = 0.0 cm, (c) ΔAl = 2.5 cm, (d) ΔAl = 5 cm, and (e) ΔAl = 7.5 cm with the height at which the process reaches steady state marked with a horizontal line.

4.2 Standard Wiper Position Case

The effect of the wiper position below the mold for the standard case was studied first. The standard conditions were simulated with the wiper placed 10 cm, 20 cm, and 30 cm below the mold and compared to one without a wiper. The segregation, temperature, flow fields and the solidification fronts are seen in Figure 4.2. The case without a wiper (Figure 4.2(a)) shows a typical DC casting result, with a steady state sump depth (from inlet to packed solid mushy zone at the centerline) of 43.3 cm. The sump has a "V" shape, in which the surface is enriched followed by a slightly negative region. The centerline of the ingot is highly depleted while the mid-radius is slightly enriched. This composition field is typical to those seen in other studies [3,6,7], as shown in [79]. The flow field has two distinct regions, one including the liquid melt and the slurry and the other in the rigid mushy zone. The flow in the slurry is driven primarily by buoyancy, which keeps the slurry well mixed and is shown by the solid streamlines. In the rigid mushy zone, the buoyancy driven flow is damped due to the interconnected dendritic network and the much slower flow is dominated by shrinkage driven flow. This flow acts perpendicular to the solidification front and is shown by the dotted streamlines. The radial component of the shrinkage driven flow redistributes solute, leading to macrosegregation. Therefore, the shape of the rigid mushy zone is very important to macrosegregation development. Shrinkage driven flows were identified by Reddy and Beckermann to be an important cause of solute enrichment on the outer surface of ingots and depletion at the centerline [4].

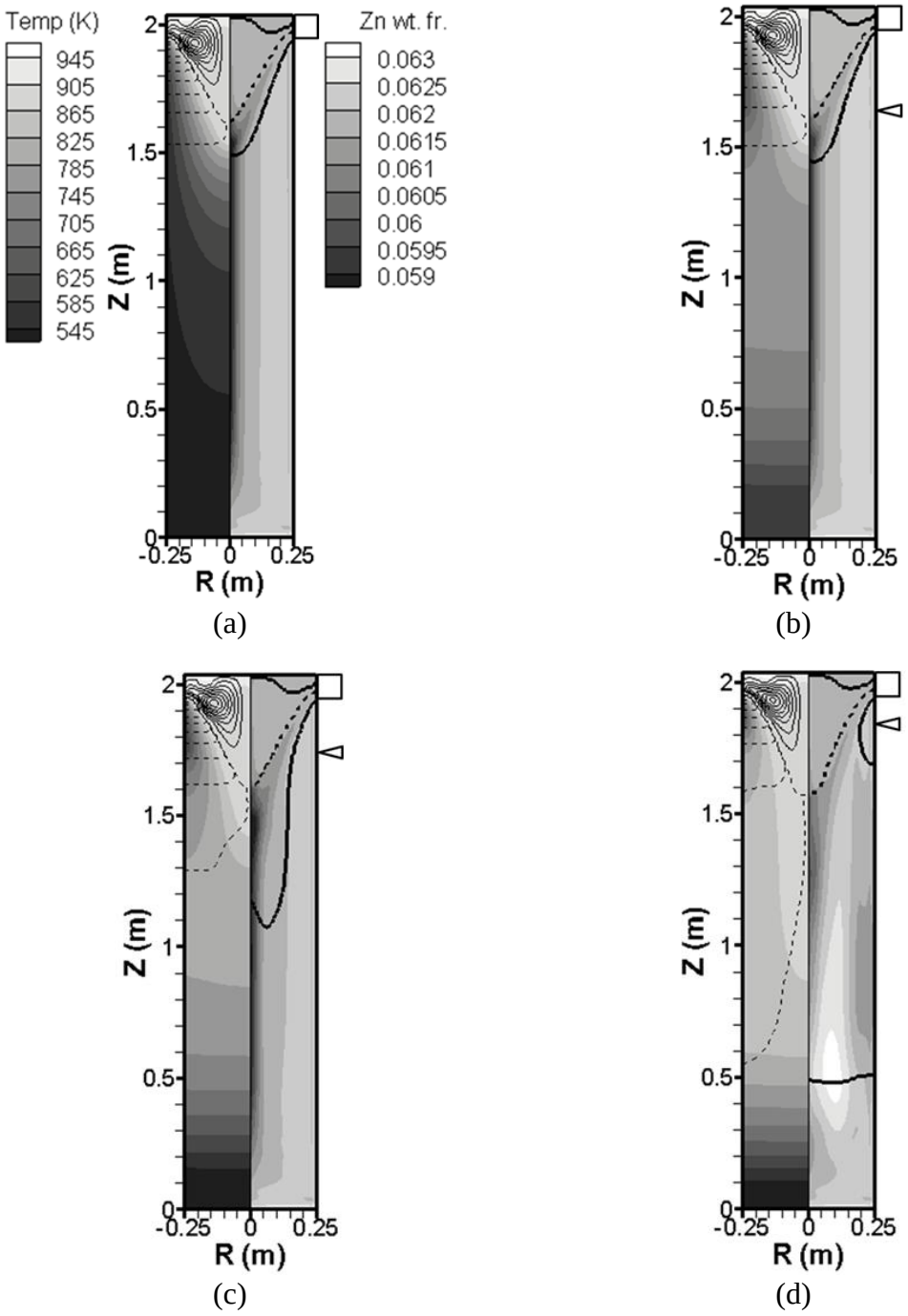

Figure 4.2: The effect of wiper position. Contour plot of the temperature and Zn fields for the base case with (a) no wiper, (b) L_w=30 cm, (c) L_w=20 cm, and (d) L_w=10 cm. The mold is represented by □ and the location of the wiper is represented by ◁. In each plot, the Zn composition and sump are on the right, with solid lines representing the liquidus and solidus and the dotted line the packing location of the free-floating solid, and the liquid flow streamlines and temperature are on the left.

Diverting the cooling water from the surface of the ingot greatly reduces the radial heat transfer rate and alters the temperature field and rigid mushy zone shape. Above the wiper, the radial Biot number ($Bi = hR/k$), is on the order of 100, so the radial heat transfer is limited by internal thermal resistance, setting up a radial temperature gradient. Below the wiper, the heat transfer coefficient is much smaller and so Bi is order 0.01, which means the radial heat transfer is limited by convection resistance at the surface. This change in dominant radial heat transfer mechanism at the wiper reduces the radial temperature gradient and increases the surface temperature.

When the wiper was placed 30 cm below the mold (Figure 4.2(b)), the rigid mushy zone is slightly affected and the sump depth is very similar to the case without a wiper, however the solidus does extend further in the axial direction for L_w = 30 cm. The slope of the sump becomes slightly steeper. There is an increase in negative centerline segregation due to the larger volume at the center in which the shrinkage driven flow transports solute towards the ingot surface.

When the wiper is placed 20 and 30 cm below the mold (Figure 4.2(b) and Figure 4.2(c)), the sump depth is 43.8 and 42.5 cm, respectively, very close to the depth without a wiper (43.2 cm). However, the rigid mushy zone occupies a much larger volume of the casting, especially near the centerline for L_w = 20 cm. The evolution of the temperature field and sump profile throughout the process for L_w = 20 cm is shown in Figure 4.3. Early in the process the shape of the sump and rigid mushy zone is very similar to the case without a wiper (Figure 4.2(a)) because the sump is initially rather flat and is entirely above the wiper. As the ingot grows in length and the sump acquires a vertical component, part of the sump that exists near the centerline is in the region affected by the

wiper. In Figure 4.3(a), the sump that exists in the ingot region with Bi << 1 is in the process of transitioning the dominant heat transfer mechanism. As the sump becomes more vertical and more volume is below the wiper, the rigid mushy zone becomes more elongated in this direction. The slope of the solidus at the centerline also transitions from a “V” shape to a “U” shape (Figure 4.3(a) and Figure 4.3(b)) before settling on a “W” shape during steady state (Figure 4.3(d)). The low heat extraction rate in the region below the wiper and a more radially uniform temperature field causes the sump shape to be more influenced by composition differences. The depleted region in the center of the casting has a higher solidus temperature than the surrounding regions, which causes the “W” shaped sump to form. The elongated shape of the shape of the sump and change in temperature field decreases the severity of the negative centerline segregation, as shown in Figure 4.4. This segregation decrease can be explained by comparing the direction of the shrinkage driven flow at the centerline in Figure 4.2(a) to Figure 4.2(b-c). In Figure 4.2(a), the flow has a very definitive radial direction which transports solute enriched liquid away from the centerline. In Figure 4.2(b-c), this flow direction has gained a vertical component, which becomes more obvious the closer the wiper is placed to the mold, lowering the amount of enriched solute that is transported to away from the ingot center. There is also a considerable dip in the radial compositional profile in Figure 4.4 for L_w = 20 cm, 15 cm from the ingot center. This location coincides with a large change, not present in the other cases, in slope of the solidus where it is nearly vertical that is not present in the other cases. Over this large axial region, shrinkage driven flow is able to transport solute radially toward the ingot surface. This causes a depleted region to form further from the ingot center.

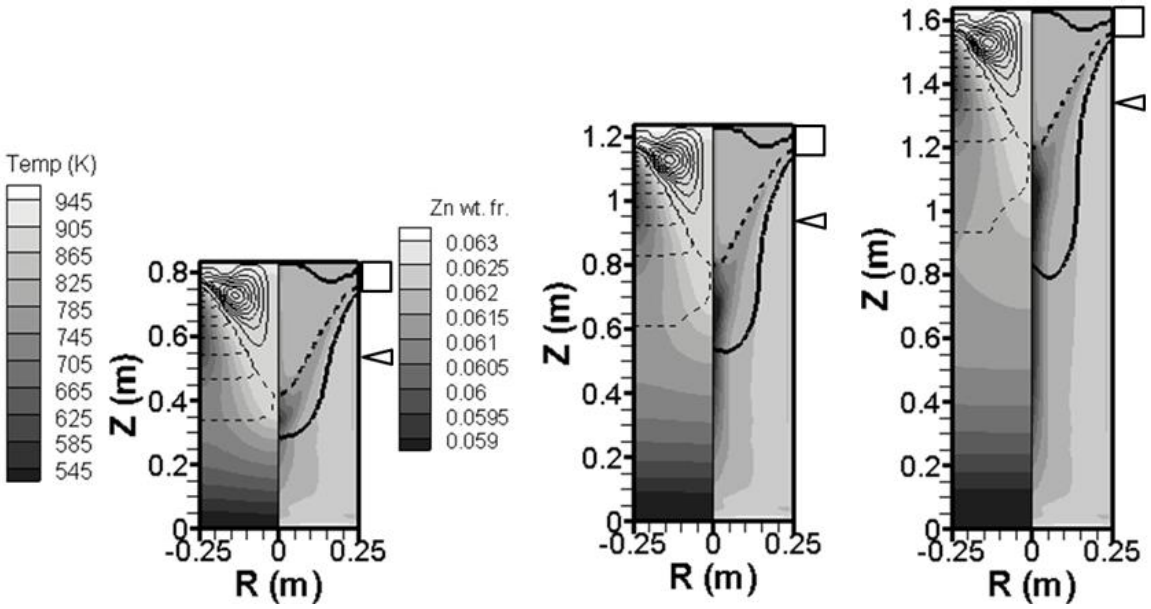

Figure 4.3: Evolution of the temperature, composition, and flow fields with L_w = 20 cm after (a) 798 s, (b) 1,198 s, (c) 1,598 s. The mold is represented by □ and the location of the wiper is represented by ◁.

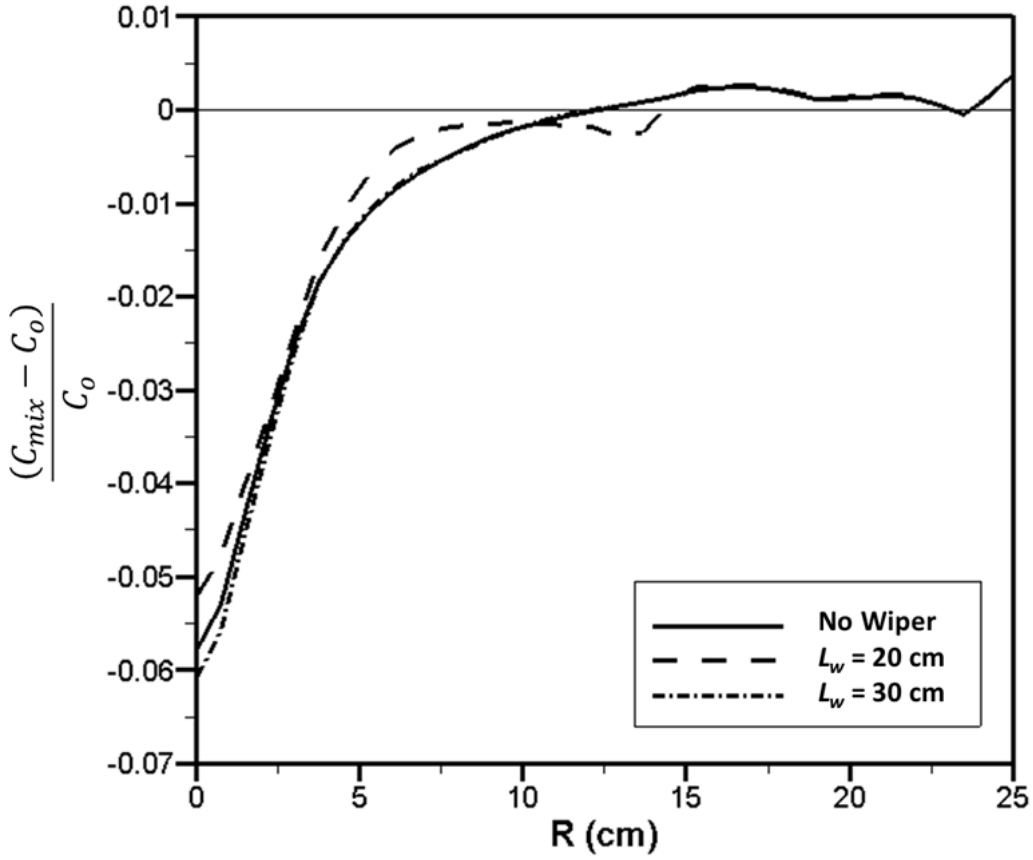

Figure 4.4: Normalized radial profile of the Zn segregation 1.05 m from the bottom block for 50 cm diameter cases comparing the effect of wiper positions.

In Figure 4.2(d), we can see the effect of the wiper at 10 cm below the mold. Placing the wiper 10 cm below the mold stops significant heat loss to the falling water before much has been removed from the interior of the ingot. Below the wiper, with such a low *Bi*, the radial temperature gradient flattens and reheats the surface, even to the point of partial remelting there for over a meter. Therefore, placing the wiper 10 cm or less below the mold introduces the strong possibility of cause bleed outs well below the mold. In Figure 4.2(c) and Figure 4.2(d), where the wiper is placed further from the mold, although the shape of the rigid mushy zone is strongly linked to the wiper placement, the internal temperature has been reduced enough to prevent the surface of the ingot from reheating to the point of remelting.

4.3 Effect of Ingot Diameter

The effect of ingot diameter was investigated by comparing the standard case, Figure 4.2(b), to one with a larger diameter (D = 70 cm), Figure 4.5(d). Because the surface heat fluxes are roughly the same, while the volume/area ratio increases with radius, there is much more heat in the larger ingot and so its sump is much deeper. To obtain comparable results to those with the smaller radius, the wiper must be placed not at the same position relative to the mold, but to the bottom of the sump (the onset of the rigid mushy zone at the centerline). Comparing the cases with different radii but L_w = 30 cm, the wiper position is further from the sump bottom in the larger diameter ingot. Therefore, to cause similar effects, the wiper placement, L_w, must be increased when increasing the ingot diameter. Figure 4.5 shows the effect of various wiper placements for

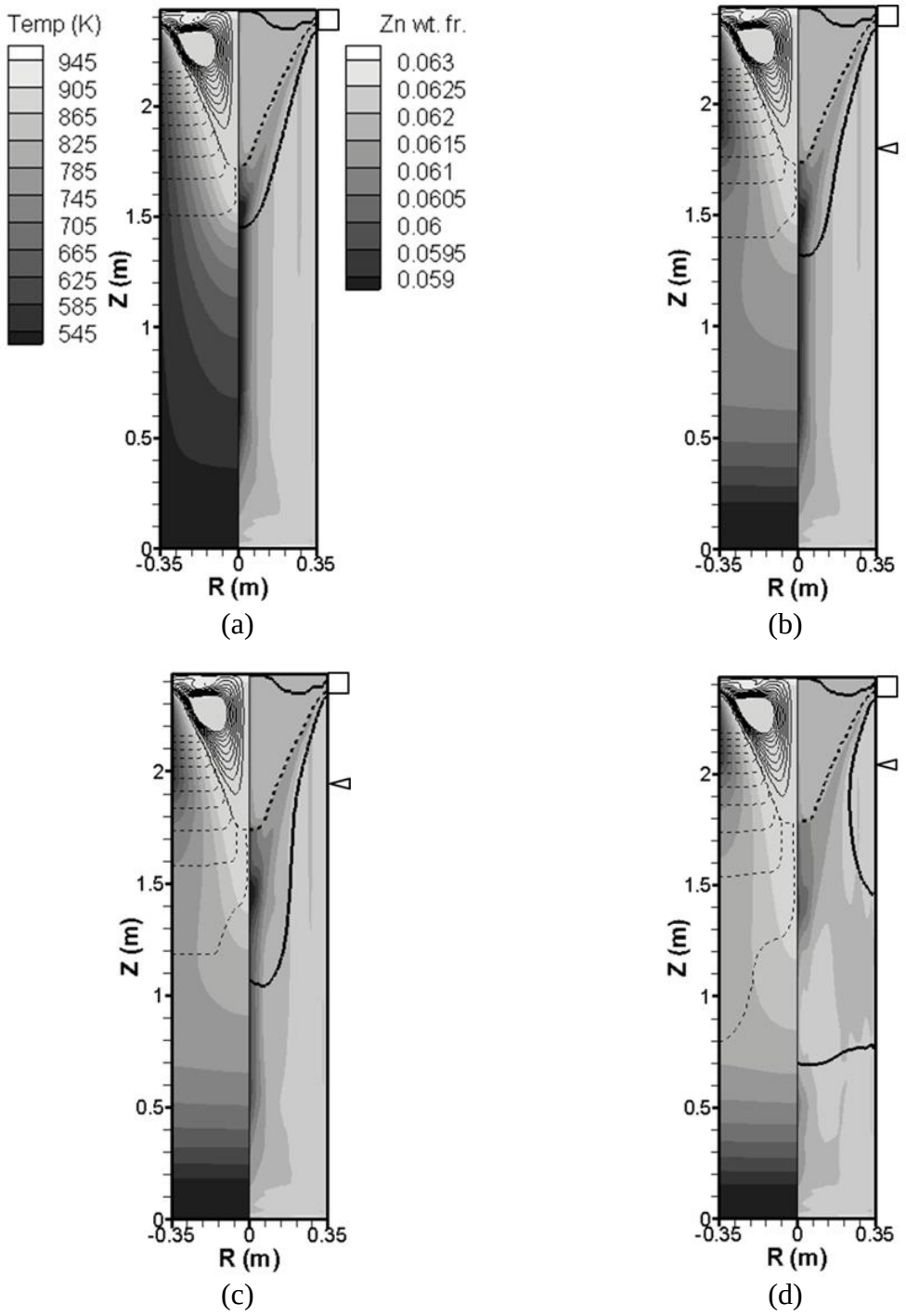

Figure 4.5: The effect of wiper position. Contour plot of the temperature and Zn fields for V_c = 60mm/min with (a) no wiper, (b) L_w=50 cm, (c) L_w=40 cm, and (d) L_w=30 cm. The mold is represented by □ and the location of the wiper is represented by ◁.

the larger diameter ingot case. Placing the wiper at the sump bottom (around 50 cm) does not affect the solidification behavior. Moving the wiper up to 40 cm below the mold still avoids any surface remelting and elongates the rigid mushy zone below the wiper. Finally, further inspection of the case with L_w = 30 cm shows that if the wiper is roughly halfway between mold and sump bottom, there is significant remelting at the surface and a very long extension of the rigid mushy zone. Figure 4.6 shows the effect of the wiper location on the radial segregation profile. At the surface, subsurface, and near mid-radius, the composition profile for the no wiper case matches the profile predicted for L_w = 40 and 50 cm. For L_w = 40 cm, the composition profile deviates from the case without a wiper r = 17 cm, corresponding to the radial location in which the lower heat transfer, below the wiper affects the sump creating a long vertical section of the solidus. This causes a small but abrupt composition decrease due to the nearly radial direction of the shrinkage driven flow. In the larger diameter ingots, with stronger flows and deeper sumps, proper wiper placement can not only reduce the internal stress and strain from solidification, but also the negative centerline segregation.

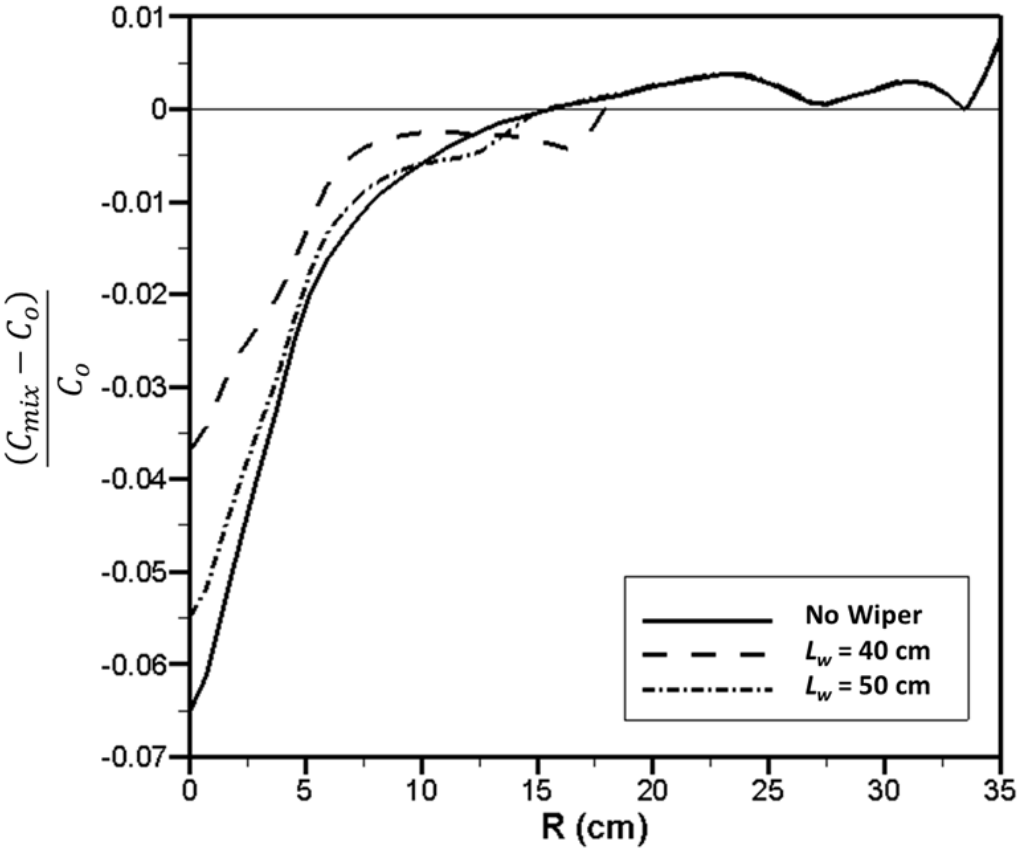

Figure 4.6: Normalized radial profile of the Zn segregation 1.02 m from the bottom block for 70 cm diameter cases comparing the effect of wiper positions.

4.4 Effect of Casting Velocity

Two additional casting velocities (30 and 90 mm/min) were examined to determine the proper wiper placement and compared to the standard casting velocity of 60 mm/min. Figure 4.7 and Figure 4.8 show the effect of various wiper placements for casting velocities of 30 and 90 mm/min, respectively. Because the wiper effect is more significant in larger diameter ingots, the D = 70 cm ingots were simulated here. The sump depth is directly dependent on the casting rate, increasing in depth from 38.4 cm for V_c = 30 mm/min to 96.2 cm for V_c = 90 mm/min. Therefore, the best location of the wiper (defined as no surface remelting) for V_c = 30 mm/min is too close to the mold for faster casting. However, the proper wiper location for a faster casting velocity will be adequate in eliminating surface remelting for a slower speed because the sump depth is shallower. This can be seen by comparing Figure 4.7(b) to Figure 4.5(b), in which L_w = 50 cm for both cases. For V_c = 30 mm/min the wiper is placed well below the bottom of the sump, in the all solid region, and does not influence the solidification process. Other factors such as internal stress reduction and segregation levels should also be considered in determining proper wiper placement. At V_c = 60 mm/min, the wiper placement roughly corresponds to the sump depth and elongates the rigid mushy zone in the axial direction near the centerline. This wiper placement is adequate for the V_c = 30 mm/min case, but can also be moved closer to the mold for maximum ingot stress relief. Placing the wiper 10 cm below the mold for V_c = 30 mm/min causes significant surface remelting, while doubling L_w eliminated surface remelting and affected the shape of the rigid mushy zone.

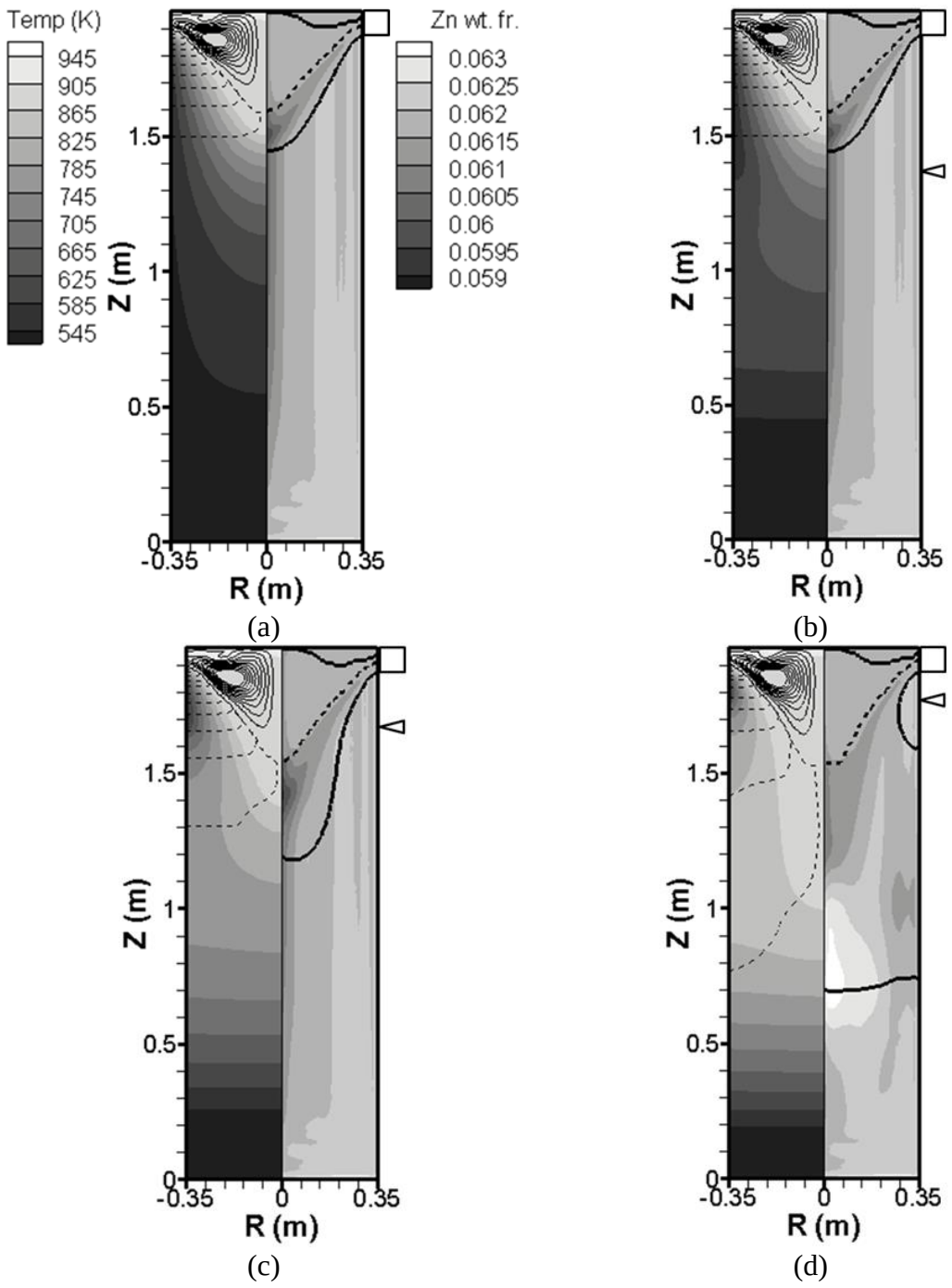

Figure 4.7: The effect of wiper position. Contour plot of the temperature and Zn fields for V_c = 30 mm/min with (a) no wiper, (b) L_w=50 cm, (c) L_w=20 cm, and (d) L_w=10 cm. The mold is represented by □ and the location of the wiper is represented by ◁.

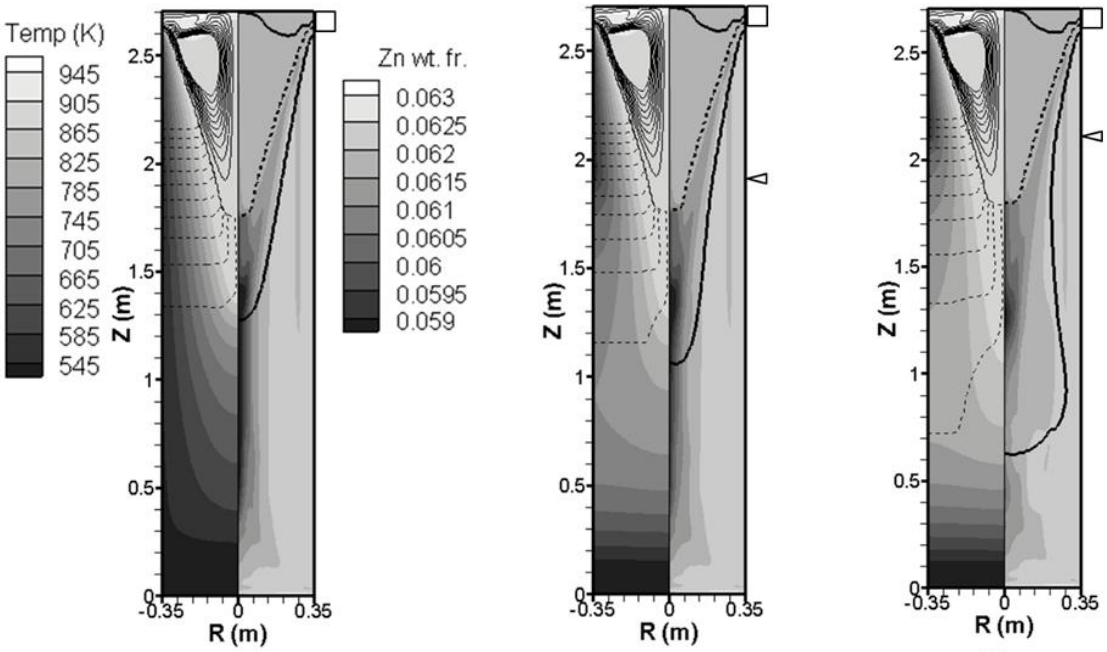

Figure 4.8: The effect of wiper position. Contour plot of the temperature and Zn fields for V_c = 90 mm/min and wiper positions of (a) no wiper (b) L_w = 70 cm, and (c) L_w = 50 cm. The mold is represented by ☐ and the location of the wiper is represented by ◁.

The sump depth for V_c = 90 mm/min is significantly deeper (96.2 cm) than either of the other two casting velocities and therefore the wiper must be placed farther from the mold. This can be seen by comparing Figure 4.5 and Figure 4.8. While placing the wiper at L_w = 50 cm for the slower speed causes significant remelting below the wiper, the remelting does not extend to the surface for the faster speed. Although the remelting is not predicted to reach the ingot surface, the possibility of such an event may still occur if the model uncertainty or process variation is large enough. Moving the wiper to L_w = 70 cm greatly reduces the amount of remelting and still lengthens the rigid mushy zone below the wiper. The level of negative centerline segregation, $(C_{\min}^{Zn} - C_o^{Zn})/C_o^{Zn}$, is also reduced from -0.068 for no wiper to -0.052 for L_w = 70 cm.

4.5 Summary of Recommendations for Wiper Placement

Based on the current set of results for various casting velocities, the proper wiper placement, in terms of surface remelting and centerline segregation, is linked to the relative position with the sump rather than an absolute distance below the mold. This wiper position corresponds to just above the sump depth. For the standard case using a wiper depth of L_w = 30 cm has the greatest effect on reducing thermal gradients (and thereby reducing thermal stresses) without remelting significant portions of the ingot. For the large ingot diameter and a casting velocity of 30 mm/min, the wiper should be between 20 and 50 cm below the mold, but still just above the sump depth. The closer the wiper is placed to the low end of that range, the greater effect the change in heat transfer mechanisms will have on the mushy zone, and composition, temperature, and flow fields. For V_c = 60 mm/min, the wiper should be placed at least 40 cm below the mold; for V_c =

90 mm/min the wiper should be placed around 70 cm below the mold. This analysis only accounts for surface remelting and segregation for round billets. The study performed by Drezet and Pirling, analyzed only the temperature and stress states of rolling slabs for the same alloy (aluminum alloy 7050) [26] and neglected convection and species transport. Their wiper position corresponded to the height of the liquidus line at the symmetry axis. Because their model does not include convection of equiaxed particles, this wiper position is similar to the placement that is deemed proper in the current work. Due to the different ingot geometry in the present study, the stress reduction that was reported by Drezet and Pirling will be different than for the ingots in the current study. For a fully comprehensive understanding of the wiper position, these two analyses should be combined.

4.6 Conclusions

A fully transient numerical model of aluminum DC casting was used to analyze the influence of techniques that reduce the cast ingot susceptibility to hot tearing on transport phenomena and segregation profiles. The two techniques were adding a layer of pure Al along the bottom block and implementing a wiper to divert cooling water from the ingot surface. Adding a layer of pure Al along the bottom block dilutes the mixture composition and delays the onset of compositional steady state. The dominant radial heat transfer resistance above the wiper was internal conduction ($Bi >> 1$) and surface convection at the ingot surface below the wiper ($Bi << 1$). This change in radial heat transfer mechanism greatly affected the temperature field below the wiper, causing the ingot surface to heat up as the convection at the surface could not readily remove the heat

being conducted there and setting up a mostly vertical temperature gradient. If the wiper was placed too close to the mold, the surface reheated enough to remelt the surface, which could cause bleed outs. The optimal wiper placement coincided positions just above the with the sump depth, wherever that may be based on other casting parameters. Additionally, if the wiper is placed near the corresponding sump depth the shape of the rigid mushy zone redirected the direction of the shrinkage driven flow decreasing the amount of negative centerline segregation, an effect more prominent in larger ingots.

CHAPTER 5. UNCERTAINTY QUANTIFICATION IN MODELING METAL ALLOY SOLIDIFICTION

As a step towards understanding the effect of uncertain inputs on solidification process modeling, uncertainty quantification (UQ) and sensitivity analysis are performed on a transient model of solidification of Al-4.5wt.%Cu in a rectangular cavity for fully columnar solidification. The numerical domain for this unidirectional chill casting process is shown in Figure 2.5. To evaluate the uncertainty of the numerical model, outputs of interest (OOI) are selected which carry with them information about multiple predicted phenomena in one value. The OOI are chosen to reflect the purpose of running the simulation in the first place. Issues of interest include how long the casting takes to freeze and possible compositional defects. Here, the solidification time is defined as the time from the application of the chill to when 95% of the domain is fully solid. In addition to the normalized Weibull deviation, W^{Cu}, the level of macrosegregation is determined based on the volume fraction of ingot outside the composition specification, V_{spec}, both above and below the acceptable range. Both of these metrics rely on interpreting the composition distribution as presented in Figure 5.1(a). Each bin in Figure 5.1(a) represents a small composition range that appears in the casting and the height of which is the volume fraction occupied by that composition range. In order to plot the histogram in Figure 5.1(a) on the same scale as the fitted Weibull function, the height of each bin was divided by the uniform bin width. Doing so, causes the total area occupied

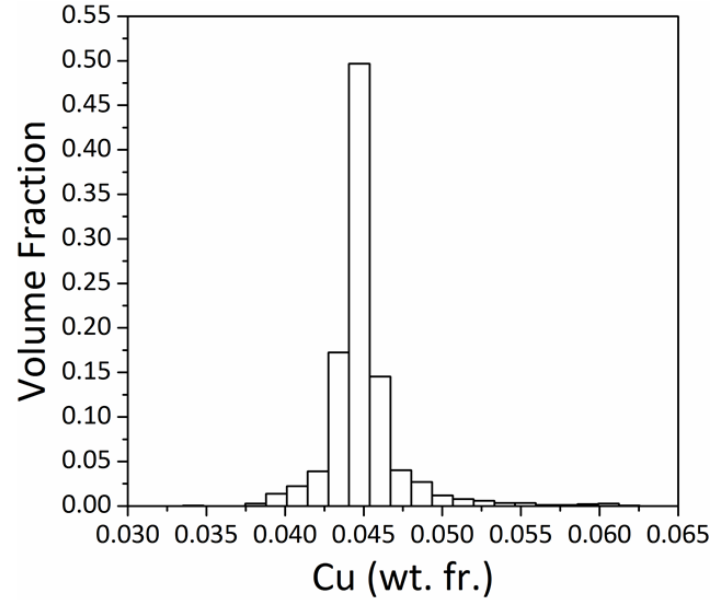

(a)

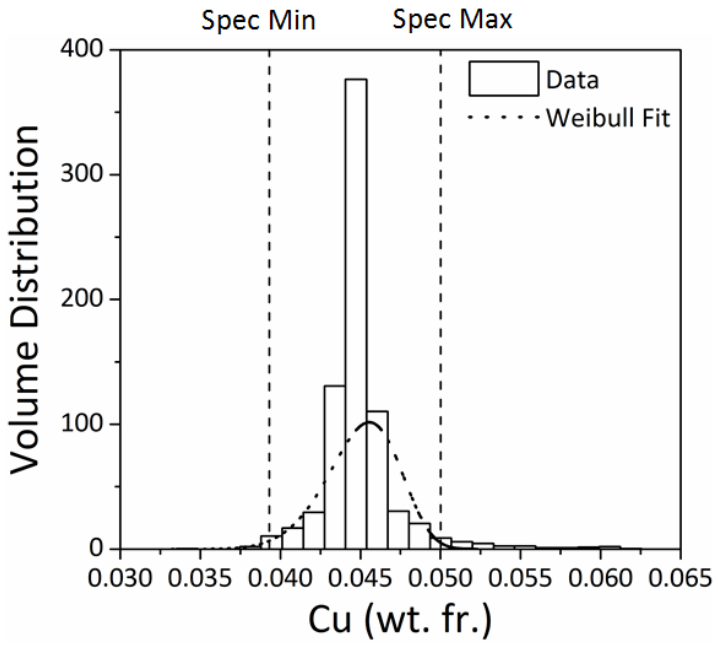

(b)

Figure 5.1: Composition distributions of a statically cast Al-4.5 wt.% alloy showing (a) the distribution as volume fraction of the ingot and (b) volume distribution function with a Weibull distribution fit and the composition specifications superimposed.

by all the bins in Figure 5.1(b) to be equal to one. For this study, the Cu compositional specification of Al alloy 2014 (ASTM B209) is used, which has a range of 3.9 – 5.0 wt.% Cu, shown as vertical dotted lines in Figure 5.1(b).

Before quantifying the uncertainty in the segregation and solidification time results, the controlling transport phenomenon are simulated to illustrate the behavior of a solidifying metal alloy. Then, the uncertainties associated with measured dendrite arm spacings are applied to three distinct permeability models, which control the critical flow in the mushy zone, and their different influences on outputs of interest are evaluated and compared. The uncertainties in material property data and thermal boundary conditions are examined next for their effect on model predictions.

5.1 Transport Phenomena Analysis

The most probable values of the input parameters (Table 2.1) are used to examine the typical behavior of the transport phenomena during solidification which contribute to macrosegregation (Table 2.1). The composition field, flow field, and mushy zone evolution are shown in Figure 5.2 for the KI permeability model. As the metal freezes from the left, a counterclockwise rotating flow cell develops in the liquid region, driven by buoyancy forces and keeping the bulk composition of the liquid metal well mixed. This flow cell penetrates the high liquid fraction region of the mushy zone, where it is aided by the compositional enrichment of the liquid there and which transports the rejected solute towards the bottom of the casting. Eventually this flow depletes the copper content at the top of the casting, while the bottom is enriched. The middle portion of the cast ingot is near the nominal composition. The buoyancy forces become damped by the

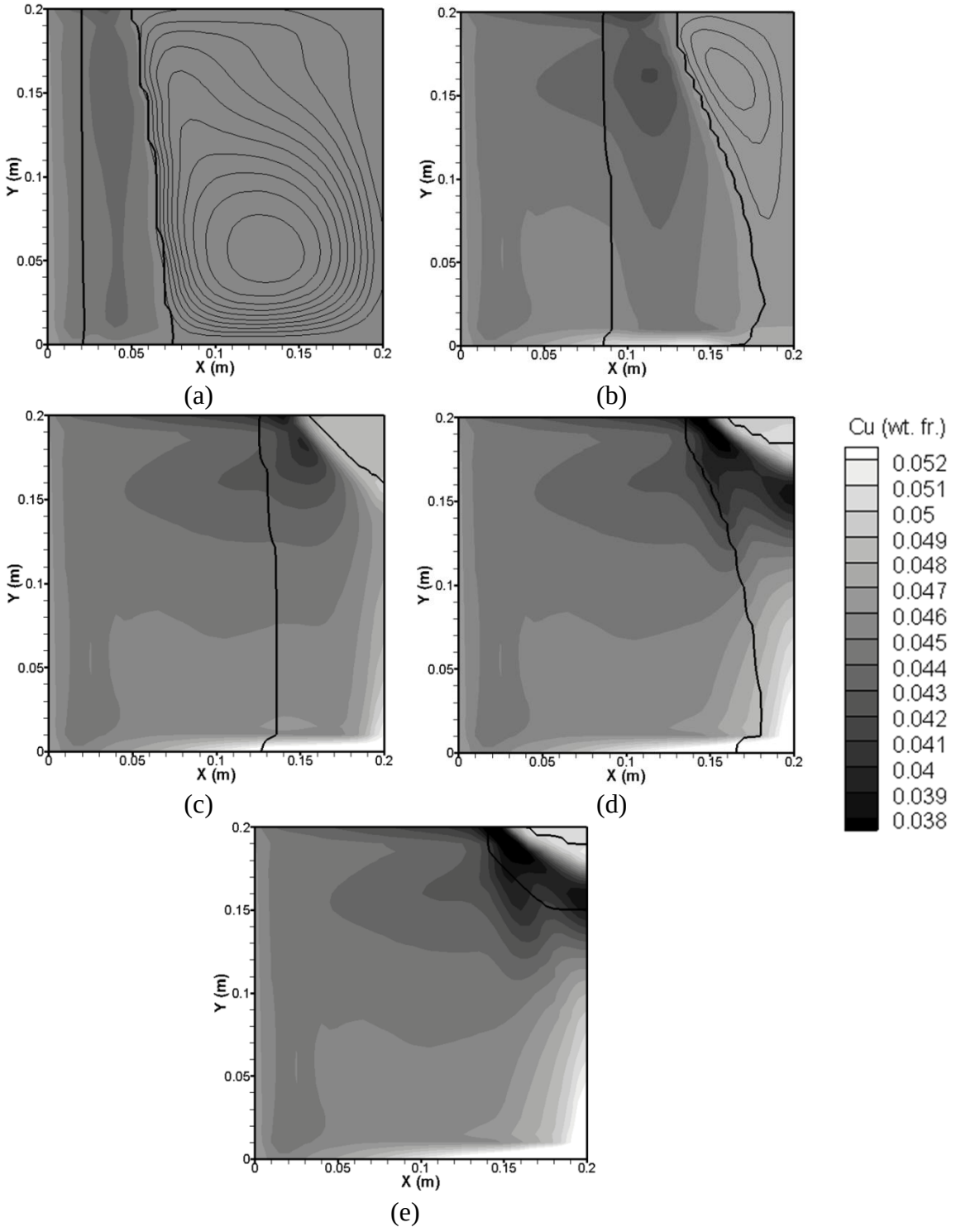

Figure 5.2: Contour plots of the Cu distribution, showing counterclockwise rotating liquid flow (streamlines are thin black lines) and the mushy zone (solidus and liquidus are bold lines) at (a) 100 s, (b) 500 s, (c) 1000 s, (d) 1300 s and (e) 1430 s.

dendritic structure deeper in the mushy zone, and the very weak flow remaining is dominated by solidification shrinkage acting perpendicular to the solidification front (almost horizontally). This flow causes an enriched layer to form near the chill wall by pulling in rejected solute. As the process progresses, the bottom portion of the mushy zone begins to advance faster than at the top of the domain. This effect is largely due to the inlet at the top being at a superheated temperature and, near the end of solidification, causes the shrinkage driven flow to develop a vertical component the bottom of the domain along the right wall. This flow causes a depleted region to form near the inlet, which forms as enriched fluid is being transported away from the inlet and replaced by nominal composition fluid. In other words, the highly enriched regions of the ingot are formed due to buoyancy induced flows and the depleted regions are caused by shrinkage driven flows.

The flow phenomena in the other two permeability models are similar to that of KI, and result in similar trends in composition field as shown in Figure 5.3 The top of the domain in all three cases is depleted in solute and the bottom right corner is enriched. The degree to which these regions are segregated depends on the permeability model. The KI permeability model has the highest maximum composition in the enriched region and the KIII model predicts the lowest composition of all three models. The KI model has the most permeable mushy zone at low and intermediate g_s, where buoyancy driven flow is the dominant transport mechanism and drives the solute towards the bottom of the domain. The KII model has the second most permeable mushy zone at low fraction solids up to g_s~0.09, above which it has the lowest overall permeability for the rest of the mushy zone. The KIII model has the second most permeable mushy zone up to ~0.45

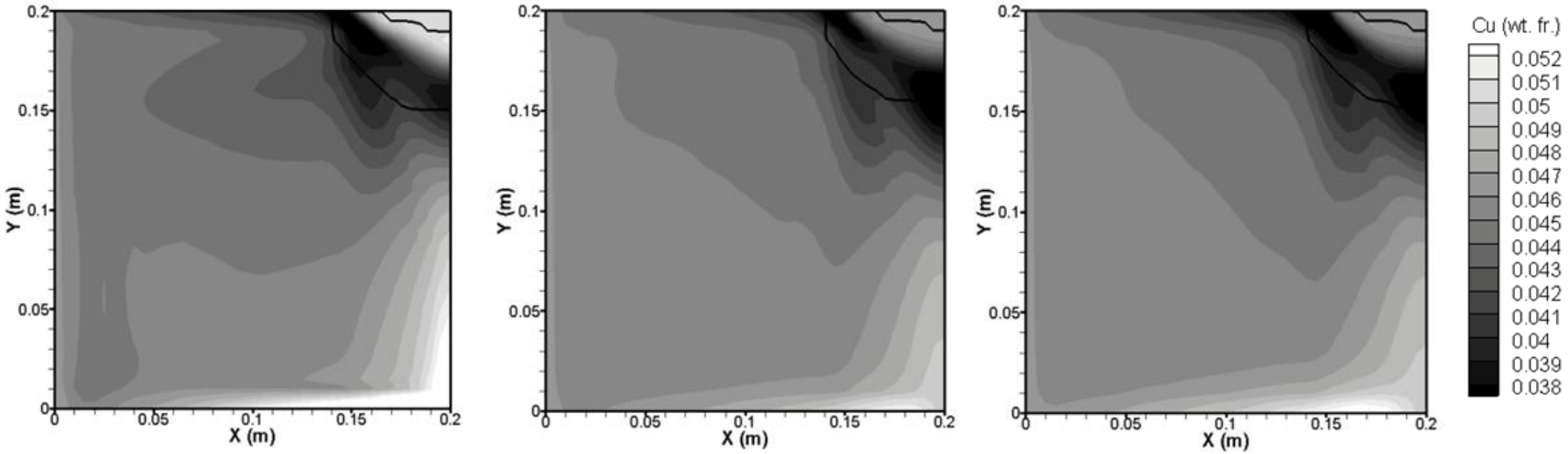

KI	KII	KIII
Cu_{min} = 0.028 wt. fr.	Cu_{min} = 0.032 wt. fr.	Cu_{min} = 0.027 wt. fr.
Cu_{max} = 0.061 wt. fr.	Cu_{max} = 0.052 wt. fr.	Cu_{max} = 0.054 wt. fr.

Figure 5.3: Final composition fields predicted with the three permeability models.

fraction solid, thereafter it is the most permeable. However, the solid fraction is so high in this region that all buoyancy driven flow is negligible for all models. Even though the KII model is the second most permeable mushy zone near the liquidus, there is still significant buoyancy driven flow after 0.09 fraction solid such that the KIII model has more positive segregation than KII. The severity of the depleted region is partially dependent on the degree of positive segregation and partially to shrinkage driven flow. Therefore, the two models with the most enrichment also have the most depleted compositions.

Similar information is also gained from the volume distributions in Figure 5.4, comparing the three permeability models. The peak of each distribution is near the nominal composition and the height of that peak increases as the distribution narrows. In other words, as the casting becomes less segregated, more ingot volume is occupied by compositions near the nominal. Therefore, the permeability model with the most segregation has the largest W^{Cu}, V_{spec}, and shortest distribution peak. Additionally, close examination of Figure 5.4 reveals that the highly enriched areas of the ingot occupy the most volume out of specification for KI. The other two permeability models have more equal contributions from the depleted and enriched areas of the ingot contributing to V_{spec}, although the KIII model has more ingot volume with negative segregation than positive.

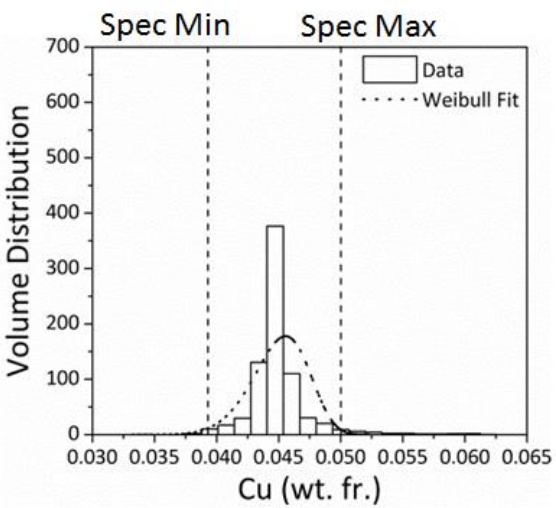

KI

WCu = 0.050 Vspec = 0.041

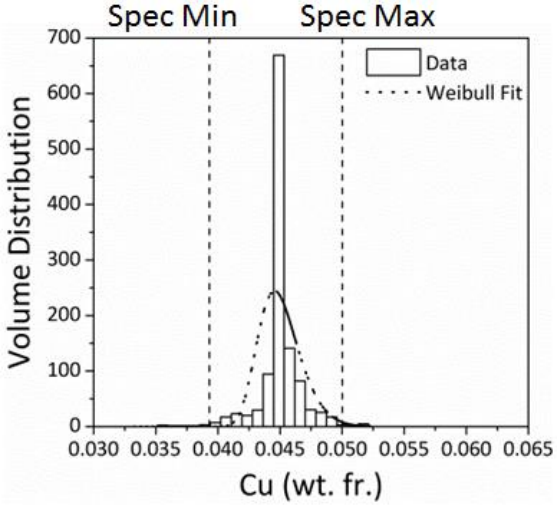

KII

WCu = 0.038 Vspec = 0.014

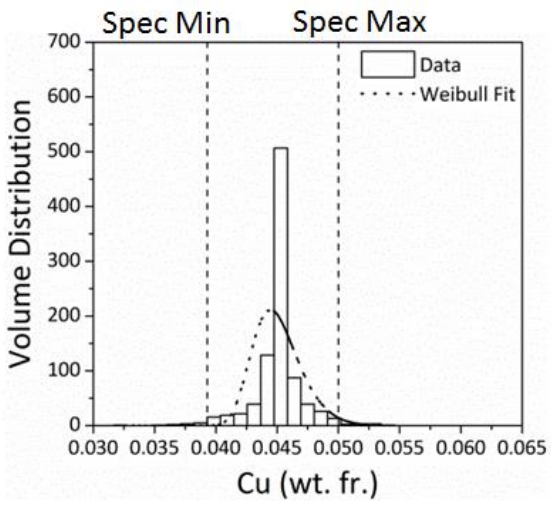

KIII

WCu = 0.044 Vspec = 0.021

Figure 5.4: Composition distributions of three permeability models plotted with the fit of the Weibull function and compositional specifications.

5.2 Uncertainty Quantification Analysis

Using the case above as a baseline, the PUQ framework was employed to evaluate first the effect of the choice of the three permeability models. It was then used to study the effect of uncertainty levels in heat transfer coefficient, the thermophysical properties, and finally a combination of the most important properties with the boundary condition and dendrite arm spacing.

In each case, the uncertainties of all the model inputs are characterized as Gaussian distributions with a mean, μ_i, and standard deviation, σ_i. Different uncertainty levels for input parameters are examined to determine the maximum values that produce a given value of output uncertainty. The surrogate models used to calculate each output PDF is given in Appendix C. When using these polynomials, it should be considered that they are only valid for this particular set of physical considerations, alloy system, and domain geometry. However, they can be used for comparison to other model predictions or experimental measurements easily.

5.2.1 Dendrite Arm Spacing and Permeability Model Uncertainty

All of the permeability models require knowledge about the alloy microstructure, specifically the secondary dendrite arm spacing (SDAS). As an example of such data, experimental measurements in a Al-4.5 wt.% Cu alloy of SDAS, were reported with uncertainties by Melo et al. (Figure 5.5(a)) [50]. The arm spacings increase with distance from the chilled surface, as do the variation in the measurements. In the current study, the dendrite arm spacing is treated as uniform and constant, using the datum at 0.175 m from

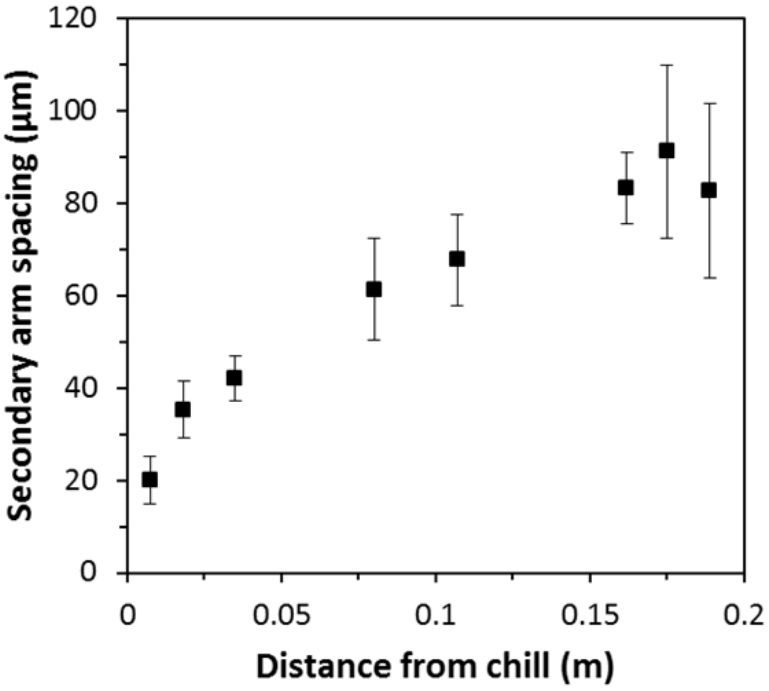

(a)

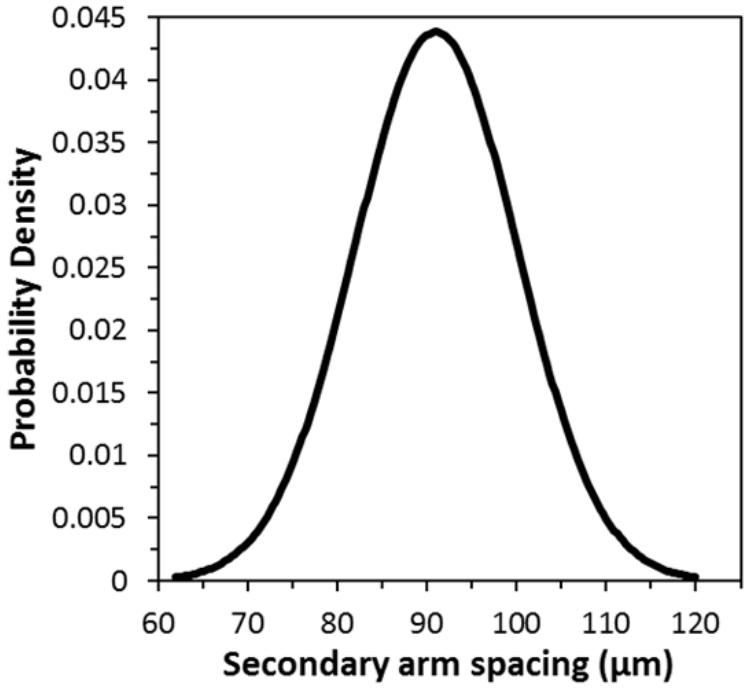

(b)

Figure 5.5: Secondary dendrite arm spacing measurements showing (a) uncertainty in experimental measurements (data taken from Figure 8 in [50]) and (b) input SDAS uncertainty.

the chill in Figure 5.5(a), with the uncertainty given as a normal distribution in Figure 5.5(b). This distribution has a mean value of 91 μm, a standard deviation of 10% of the mean (9.1 μm), and is used as the input uncertainty for all three permeability models. The aleatoric uncertainties of the outputs affected by each permeability model are the result of this uncertainty in the SDAS measurements, and are compared to understand the role of the choice of permeability model on the effect on ingot macrosegregation.

The uncertainties in predictions of V_{spec} are summarized for each permeability model in Figure 5.6(a). For each permeability model, level 2 and 3 analyses produced quadratic and cubic polynomial surrogate models, shown in Figure 5.6(b) along with the model outputs. The best polynomial fit for the KI model was a quadratic function, while the best fits for KII and KIII were cubic functions. Over all three permeability models, the predicted range of the volume out of specification (V_{spec}) varies from 0.0084 to 0.061 over the range of λ_2 values explored in this study. The KI model has the highest average V_{spec} (0.04), followed by KIII (0.022), and KII (0.014). Examining the final composition field in Figure 5.2(e), the regions of the domain that are outside of the compositional specification range are the depleted zone at the top of the domain and enriched region at the bottom right corner, the latter filling a larger volume. This metric does not capture the severity of the macrosegregation in these regions, over the ingot volume that is occupied. Therefore, the overall permeability of the mushy zone dictates the V_{spec} level, which increases as a function of λ_2 for all three models. The KI permeability model predicts the highest V_{spec} for all λ_2 examined, because it is the most permeable in the mushy zone region in which buoyancy dominates the flow. For low λ_2, both the KII and KIII models predict similar V_{spec} levels due to their similar behavior at low fraction solids, where most

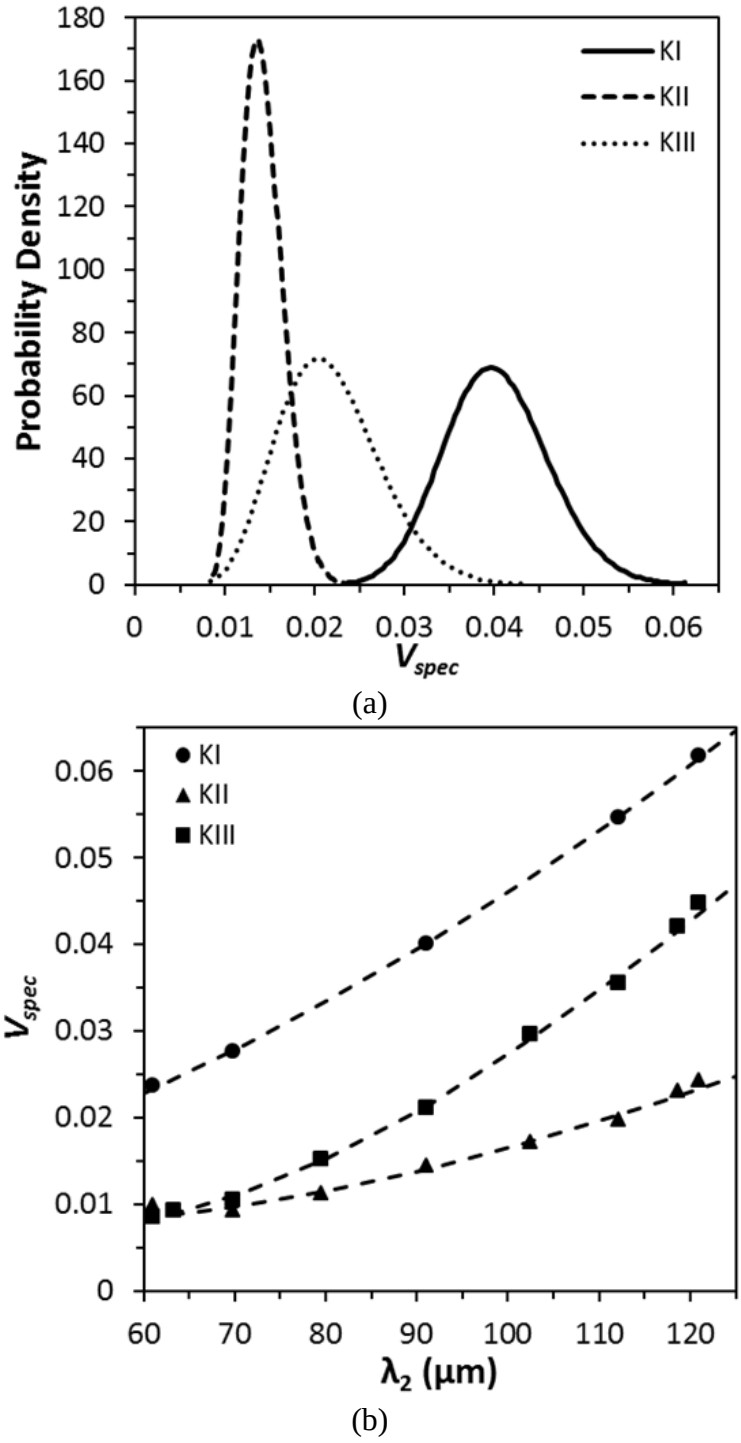

Figure 5.6: Predictions of volume fraction out of the compositional specification, from three different permeability models showing (a) the resulting uncertainty in the model predictions due to dendrite arm spacing uncertainty and (b) model predictions with the resulting surrogate model overlaid. The RMSE for each surrogate fit to the model predictions is 0.68% for KI, 4.34% for KII, and 1.66% for KIII.

of the solute is transported. The small λ_2 severely damps any buoyancy driven flow except for very close to the liquid-mush interface, where these two models have comparable mushy zone permeability. This indicates that buoyancy driven flow in the mushy zone has a larger effect on the composition field than shrinkage driven flow in the nominal case. As λ_2 increases, the difference between the models at intermediate fraction solids becomes more important and the rate of increase of V_{spec} predicted by KIII is greater than KII. The model with the narrowest PDF is KII with a deviation of 0.00231, the deviation of the V_{spec} predictions of KI and KIII are very similar with deviations of 0.0058 and 0.0056, respectively. These PDFs correspond to V_{spec} uncertainties ($2\sigma_{Vspec}/\mu_{Vspec}$) of 0.29, 0.33, and 0.51 for KI, KII, and KIII, respectively.

The model uncertainty characterized by W^{Cu} is summarized in Figure 5.7(a), showing the PDF for each permeability model. A level 3 Smolyak analysis produced cubic surrogate models for each permeability model, which are shown in Figure 5.7(b) along with the model outputs. The predicted macrosegregation levels, for all three permeability models, range from a W^{Cu} of 0.033 to 0.071. The Blake-Kozeny model, KI, has the highest mean macrosegregation level of 0.051, followed by KIII with 0.045, and KII with 0.038. The increase in the left tail of the KII and KIII PDFs is caused by the change in slope of the corresponding surrogate models at small λ_2. The slope of the $W^{Cu} = f(\lambda_2)$ function decreases and becomes nearly horizontal for λ_2 values that produce low amounts of macrosegregation. This small slope of the surrogate model produces a skewed output PDF as a given range of λ_2 predicts a narrow range of W^{Cu}. The KI model has the largest permeability at low and intermediate g_s, which allows solute transport further

before freezing causing a more average macrosegregation. For all three permeability models the macrosegregation level increases with λ_2 as expected, and the KII model, which gives the least permeable mushy zone, has the lowest macrosegregation level for all λ_2 values. For $\lambda_2 < 110$ μm, the KI model predicts the highest macrosegregation level while the KIII model predicts higher macrosegregation levels for larger λ_2. For small λ_2, where the flow in the mushy zone is very restricted throughout, the permeability at low g_s dictates the macrosegregation level since all permeability models will drastically damp the flow at high g_s. For large λ_2, the mushy zone flow at high g_s becomes stronger with the lower resistance. The KIII model has a higher permeability than the KI model at high g_s, where shrinkage driven flow is the dominant solute transport mechanism, and contributes to the enriched bottom right corner and region at the top of the domain nearest the far wall and due to the large λ_2, this model predicts more macrosegregation for this case than the other models. This also causes the uncertainty ($2\sigma_{W^{Cu}} / \mu_{W^{Cu}}$) of the KIII model to be the largest of the three at 27.1%, followed by KI at 16.5%, and KII at 15.1%. For the rest of the cases in this study the KI permeability model is used exclusively. The solidification time was not significantly affected by the uncertainty in λ_2 because permeability affects flow which only has a secondary effect on the thermal field. All three mean predicted solidification times had 95% confidence intervals less than one-half percent of 1410 s.

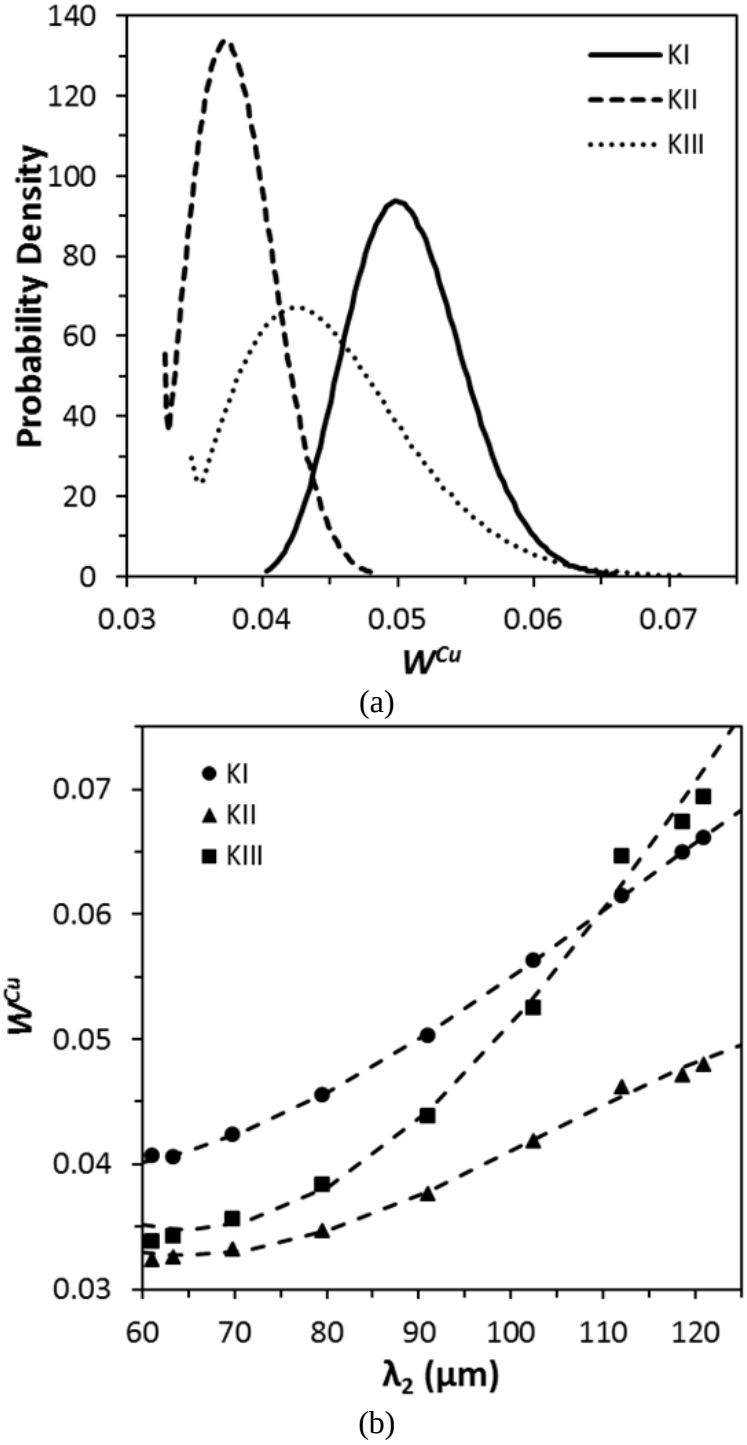

Figure 5.7: Normalized Weibull deviation predictions from three different permeability models showing (a) predicted uncertainty distributions and (b) W^{Cu} surrogate models. The RMSEs for surrogate model fits are 0.58% for KI, 2.57% for KII, and 3.71% for KIII.

5.2.2 Heat Transfer Coefficient Uncertainty Quantification

To demonstrate the effect of the boundary condition uncertainty value on the outputs of interest, the input, σ_h, was varied, as shown in Table 5.1, representing input uncertainties ($2\sigma_h / \mu_h$) of 30%, 20%, and 10% respectively. Level 3 Smolyak analyses were performed and cubic surrogate models were formed for each case (Figure 5.8), which were used to calculated the PDFs for each OOI (Figure 5.9). The macrosegregation level and solidification time decrease as the heat transfer coefficient increases over the ranges examined in this study. Low heat transfer coefficients allow more time and wider mushy zone through which solute is transported. As the heat transfer coefficient increases, the flow in the mushy zone becomes stronger, due to the larger driving force for buoyancy driven flow, but the solidification rate also increases which does not allow the solute to be transported as far before solidifying. Therefore, in this configuration higher heat transfer rates produce less macrosegregation according to both metrics.

Table 5.1: Different levels of uncertainty in the heat transfer coefficient examined with PUQ.

Case	**$2\sigma_h/\mu_h$**
A1	30%
A2	20%
A3	10%

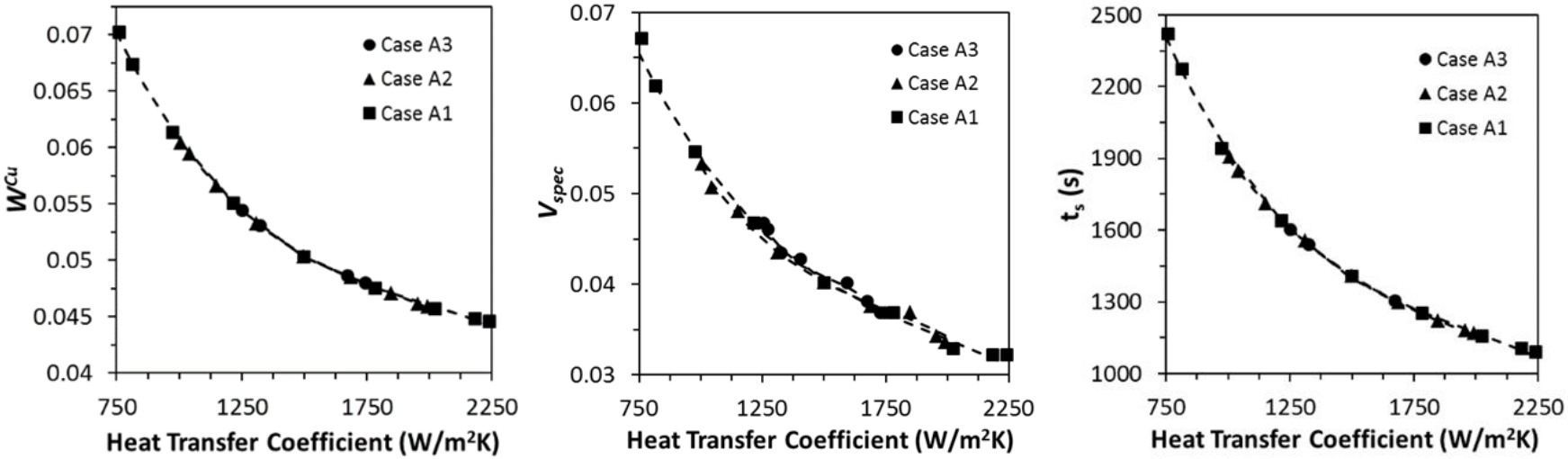

Figure 5.8: Surrogate models for each output of interest for the three different input uncertainty levels.

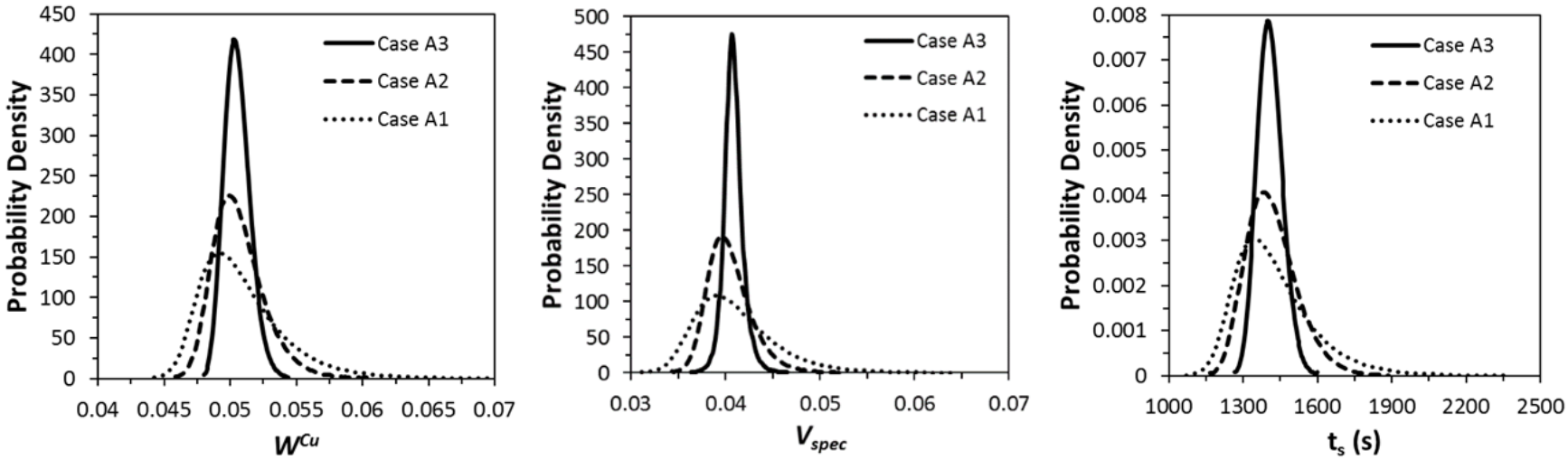

Figure 5.9: Model outputs of interest predictions from three different input levels of uncertainty showing probability density functions of (a) the normalized Weibull deviation, (b) the volume fraction outside the composition specification range, and (c) the total solidification time.

For each output of interest, the mean predicted uncertainty PDFs have similar average values. For W^{Cu} and V_{spec}, the PDF averages are 0.051 and 0.041, respectively. For t_s the PDF average decreases with input uncertainty from 1430 s (A1) to 1410 s (A3). As expected, the uncertainties of the outputs of interest decrease as the inputs become more certain (Table 5.2). In order for 95% of the W^{Cu} predictions to be within 5% of the mean, the heat transfer coefficient must be known better than ±20%, and it is recommended to be known at least ±10%. For V_{spec} and t_s to fit these same criteria, the heat transfer coefficient needs to be known better than 10%. The process can be better understood from studying the trends in model predictions, but the range of uncertainty should still be considered when reporting results and comparing to experimental measurements.

Table 5.2: Uncertainty in model predictions of the OOI for Cases A1-A3.

Output of Interest	**Case A1**	**Case A2**	**Case A3**
W^{Cu}	12.6%	7.79%	3.83%
V_{spec}	21.1%	11.6%	5.1%
t_s	22.8%	14.6%	7.05%

5.2.3 Material Property Uncertainty Quantification

Four sets of simulations were run in the PUQ framework to determine the effect of material property uncertainty levels on the OOI. Seven material properties (ρ_s, $\Delta\rho$, k, c, L_f, $\beta_{T,l}$, and $\beta_{S,l}$) were examined for the uncertainty levels shown in Table 5.3. A level 1 analysis calculated the relative OOI sensitivities and demonstrated which inputs affect the predictions the most (Figure 5.10). Higher order polynomials, with better fits to the model predictions, were calculated as surrogate models for the most influential uncertain inputs. The inputs that have the largest effect on W^{Cu} and on V_{spec} are ρ_s, $\Delta\rho$, L_f, and $\beta_{S,l}$.

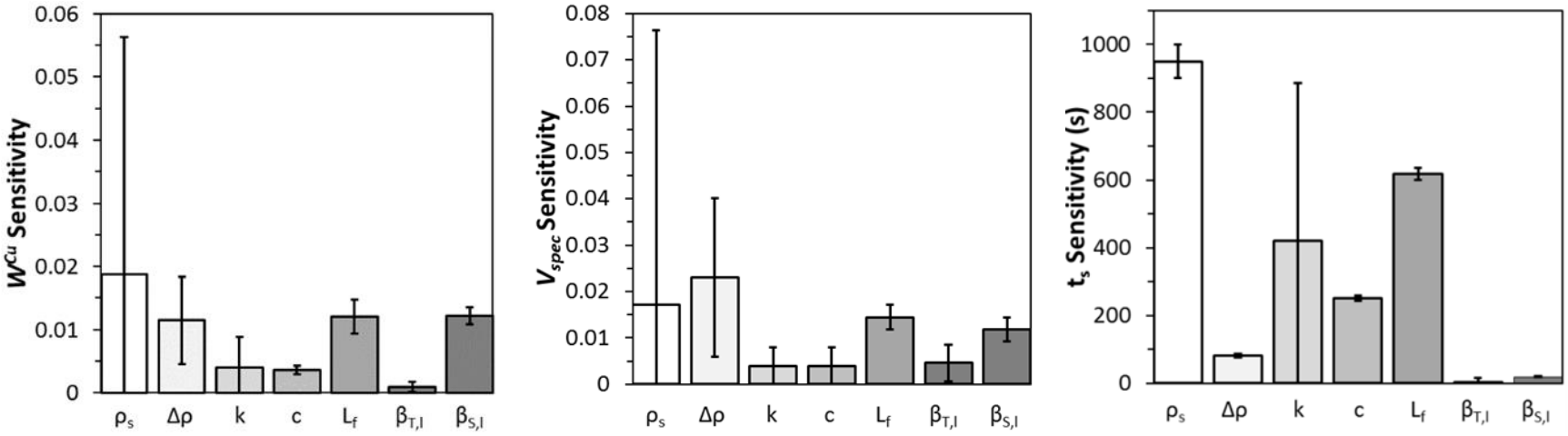

Figure 5.10: Mean OOI sensitivities (μ^*) to the uncertain inputs for Case B1. The error bars are ±2σ.

The inputs that effect t_s the most are ρ_s, k, c, and L_f. All three OOI exhibit the same relative sensitivities for cases B2, B3, and B4 as those shown in Figure 5.10.

Table 5.3: Levels of uncertainty in 7 material properties for cases B1-B4.

Case	B1	B2	B3	B4
$2\sigma/\mu$	20%	15%	10%	5%

The size of the mushy zone depends on the heat transfer rate, the amount of sensible heat, and latent heat of the mush. The heat transfer coefficient was held constant for these predictions, and the Stefan number ($St = c\Delta T_m/L_f$), the ratio of sensible to latent heat, is between 0.128 and 0.285 for the cases considered, meaning the latent heat release is more important in the mushy zone than the sensible heat in determining its size. Therefore, the latent heat is a stronger influence on the macrosegregation level than the sensible. The thermal conductivity is also important to the size of the mushy zone; however the uncertainty in this input does not strongly affect the macrosegregation level, but does strongly affect the solidification time. The solid density also controls the level of the liquid density and therefore the mixture, and is used to calculate the latent heat release, the sensible heat, and strength of the flow field. The other three input parameters, $\Delta\rho$, $\beta_{T,l}$, and $\beta_{S,l}$, contribute to determining the strength of the flow field. The density difference has an effect on the buoyancy driven flow and the shrinkage driven flow which strongly affects the segregation level of the ingot, especially at the end of the process. The solutal contribution to buoyancy driven flow has a stronger influence on the macrosegregation than the thermal buoyancy. At the very edge of the mushy zone, the thermal buoyancy contribution is stronger than the solutal component (Figure 5.11). However, the solutal contribution quickly catches up to the strength of the thermal buoyancy force as the liquid

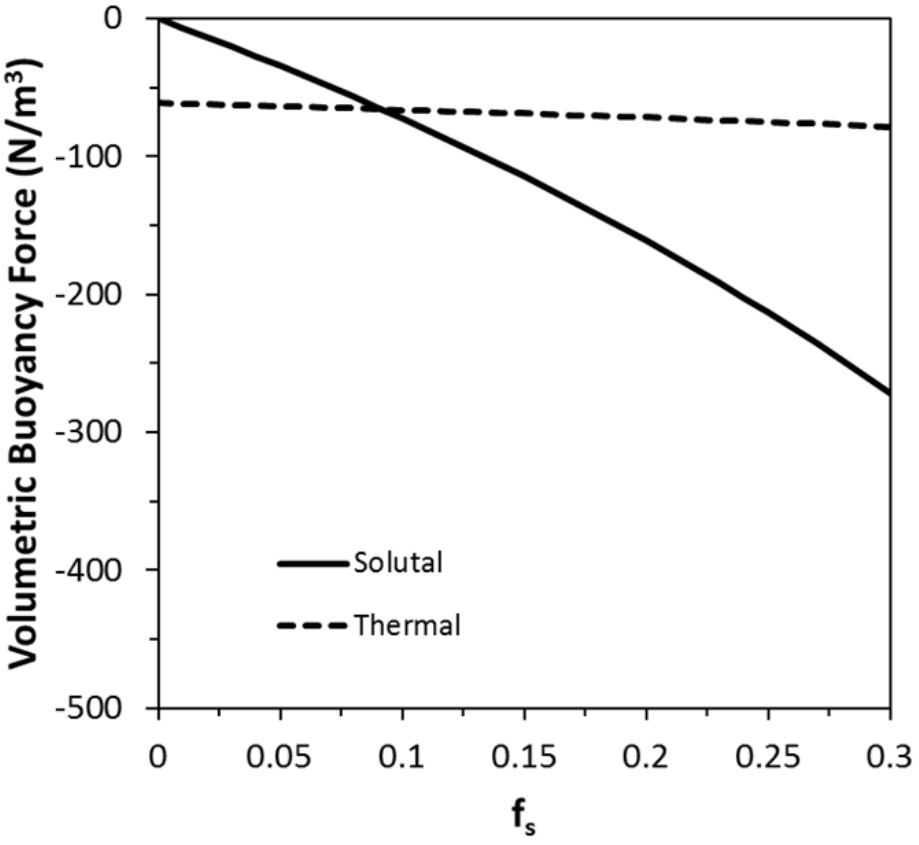

Figure 5.11: Plot of the solutal and thermal buoyancy contributions for equilibrium solidification of Al-4.5 wt.% Cu.

is enriched and overcomes it for the rest of the mushy zone. For the solidification time the most influential inputs are ρ_s, k, c, and L_f, which control the thermal diffusivity and latent heat release in the mushy zone. The parameters that control the flow do not affect the solidification time, as they do not have enough uncertainty to change how the advection affects the heat flow.

To limit the number of model evaluations in cases with higher order surrogate models, the four most important input parameters, as determined from Figure 5.10, were used to obtain a better fit to a higher order polynomial. The resulting PDFs for the outputs of interest are shown in Figure 5.12, comparing the effect of a range of input uncertainty levels. The average of the PDF for the outputs of interest changes with the uncertainty level of the inputs. The average of W^{Cu} decreases only a few percent as the inputs become more certain, with averages of ranging from 0.0516 to 0.0506 for Cases B1 and B4, respectively. Similar behavior was seen in V_{spec} and t_s, which also coincided with a decrease in the uncertainty in the OOI. The largest shift was in V_{spec}, where the mean values are 0.0454 (B1), 0.0437 (B2), 0.0407 (B3), and 0.0408 (B4). This shift of V_{spec} average values is caused by the large change in strength of buoyancy driven flows, which forms the highly enriched region in the ingot. For large input uncertainties, there are cases with large amounts of buoyancy induced flow and therefore considerable volumes of composition greater than the maximum composition specification. The volume of ingot below the minimum composition specification, caused by shrinkage driven flows, remains relatively the same across all uncertainty levels. Therefore, the shift in average V_{spec} values, seen in Figure 5.12(b), is caused by the change in dominant transport mechanism leading to the ingot having out of specification compositions.

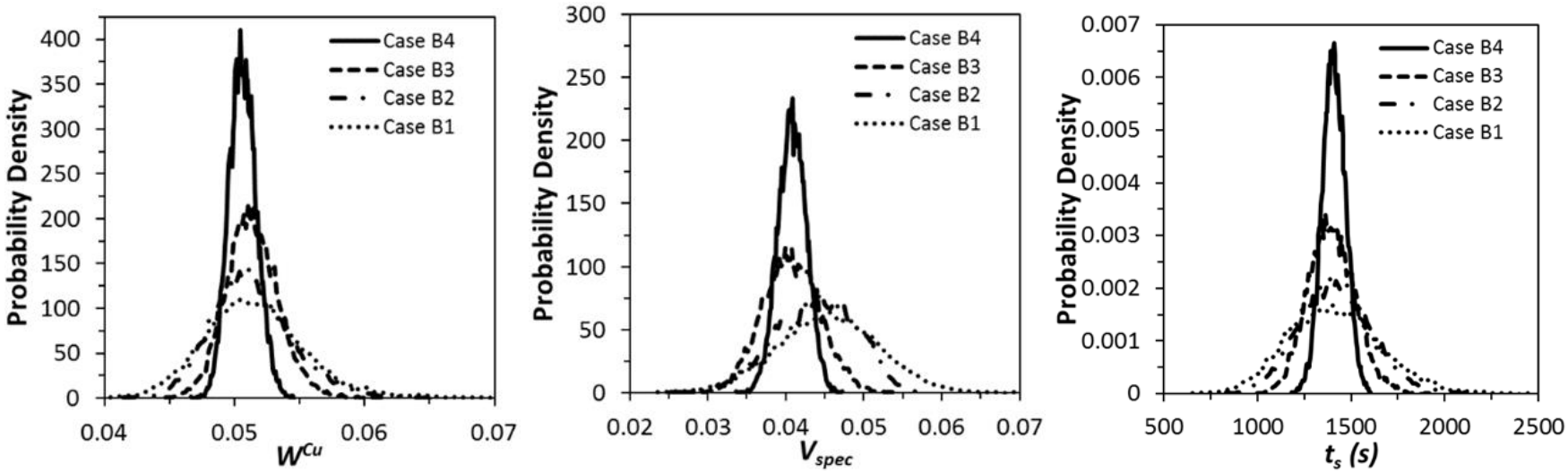

Figure 5.12: Probability density functions of the model outputs comparing the four different input uncertainty levels.

The averages of t_s were between 1420 s (B1) and 1410 s (B4), a very small change compared to the overall value and uncertainty. The corresponding uncertainties in the model predictions are shown in Figure 5.13. As anticipated, the uncertainty of the model predictions increases with the level of input uncertainty. The prediction of W^{Cu} is the most certain result for all input uncertainty levels. The uncertainty in predicting t_s and V_{spec} are nearly identical for the two low input uncertainty cases. However, for the two larger input uncertainty cases, the prediction of t_s is more uncertain than V_{spec}. To limit the uncertainty of the W^{Cu} prediction, so that 95% of the prediction is known to be less than 5% of the mean, the material property values need to be known to within 5%. For V_{spec} and t_s, the input uncertainty needs to be much stricter and well within 5%.

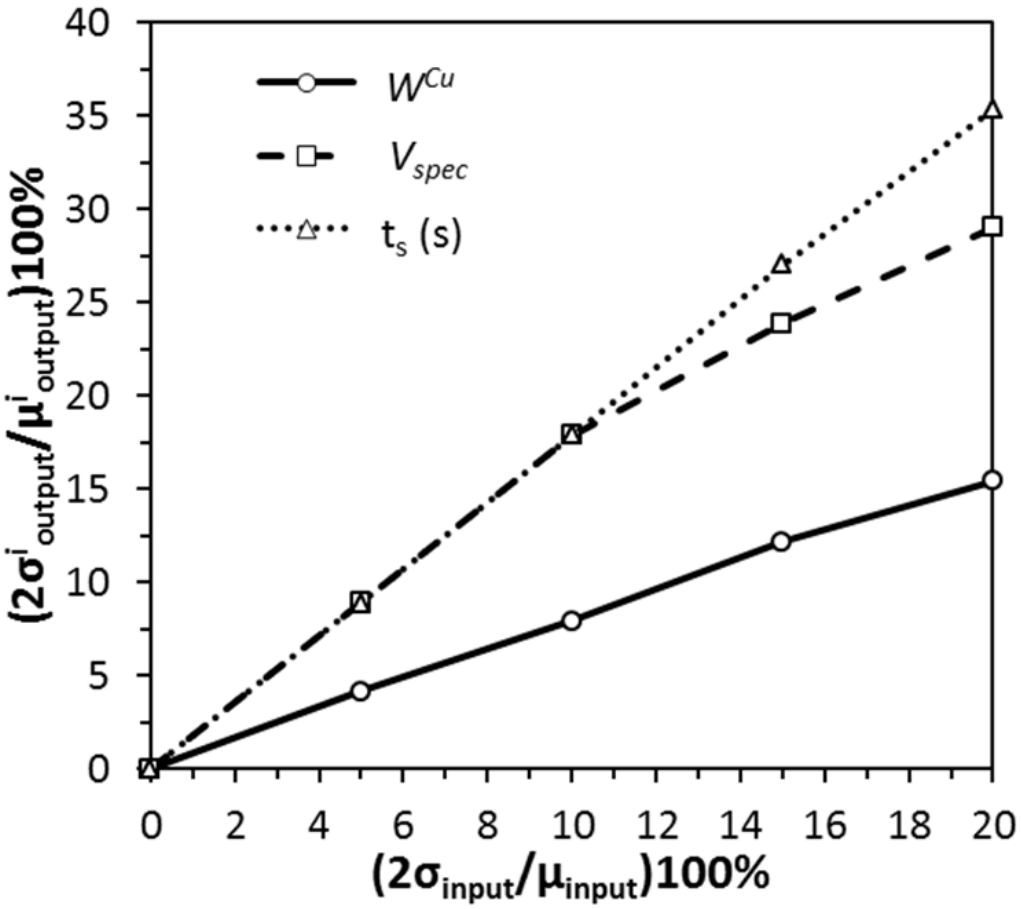

Figure 5.13: Uncertainty in model predictions of the OOI for Cases B1-B4.

5.2.4 Overall Model Input Uncertainty Quantification

The most influential material properties for each output of interest along with the dendrite arm spacing and heat transfer coefficient were examined for their effects on the outputs of interest. The uncertainties of the material properties, dendrite arm spacing, and heat transfer coefficient were set to 10%, 20%, and 20% respectively. A level 2 Smolyak analysis provided the best fitting surrogate model for all three outputs of interest with RMSE values of 3.74%, 6.20%, and 1.75% for W^{Cu}, V_{spec}, and t_s respectively. The resulting sensitivities of the OOI to the inputs are shown in Figure 5.14. The macrosegregation level in the casting is most sensitive to the dendrite arm spacing and heat transfer coefficient for both macrosegregation metrics. The dendrite arm spacing directly controls the flow in the mushy zone and therefore the amount of solute transport. The other parameters that control the flow, ρ_s, $\Delta\rho$, and $\beta_{S,l}$, have a linear relationship with the driving buoyancy force, while the dendrite arm spacing has an inverse squared relationship with the resistance to mush zone flow transports the solute. The heat transfer coefficient directly controls the size of the mushy zone and time allowed for solute transport. The latent heat also affects the size of the mushy zone, but indirectly as it is dependent on the solidification rate. For W^{Cu} the solid density is also influential, as the error bars overlap the entire range of sensitivities for the heat transfer coefficient. For V_{spec}, the density difference and solid density have a larger effect on this metric than L_f or $\beta_{S,l}$, because, more than any other parameter, V_{spec} is controlled by shrinkage driven flows. The solidification time is most affected by the heat transfer coefficient and solid density and completely unaffected by the dendrite arm spacing, as above. The PDFs of the

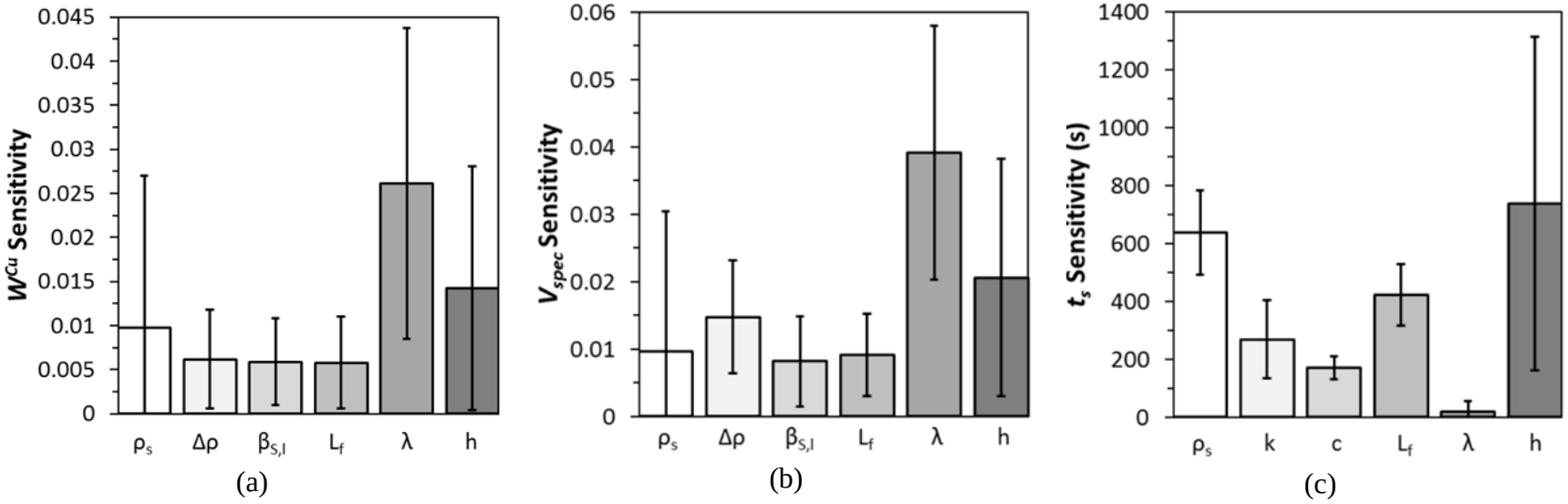

Figure 5.14: Plots of the outputs of interest sensitivities to the uncertain inputs showing μ^* as the height of each bar and $2\sigma^*$ are the error bars.

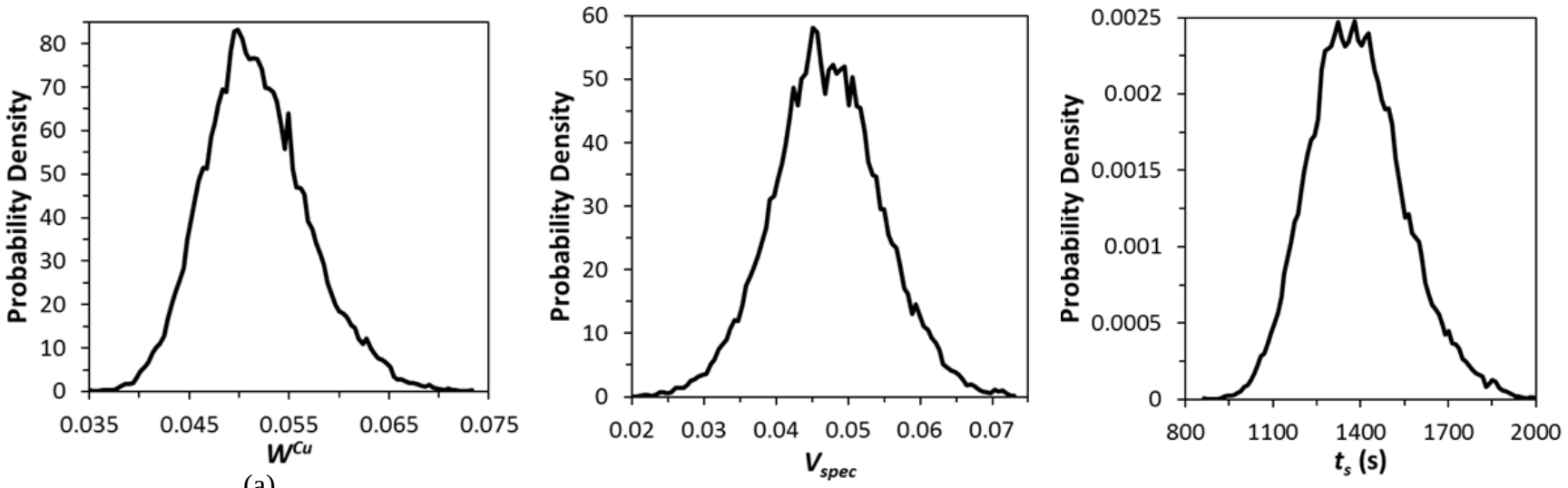

Figure 5.15: Probability density functions of the model outputs for uncertain material properties, dendrite arm spacing, and heat transfer coefficient.

outputs of interest are shown in Figure 5.15. The resulting uncertainties ($\pm 2\sigma/\mu$) of W^{Cu}, V_{spec}, and t_s are 20.3%, 32.0%, and 23.7% respectively.

5.3 Conclusions

The aleatoric uncertainty was quantified for a numerical solidification model of an Al-4.5 wt.% Cu in a rectangular domain. The outputs of interest considered for the model included the total solidification time and two metrics for the degree of macrosegregation. The input parameters in which their uncertainty was considered were the permeability model, dendrite arm spacing, heat transfer coefficient, and several thermophysical properties. The choice of permeability model strongly influenced the resulting macrosegregation as it determines the strength of the flow in the mushy zone. In order to reduce the uncertainty in macrosegregation predictions to an acceptable level, the heat transfer coefficient needs to be known within 10% of the mean. For the solidification time predictions, the heat transfer coefficient needs to be known within a narrower range. For macrosegregation model predictions, the important material properties are ρ_s, $\Delta\rho$, L_f, and $\beta_{S,l}$ while for the solidification time they were ρ_s, k, c, and L_f. The most influential input parameter on the prediction of macrosegregation was the dendrite arm spacing, which had no effect on the calculation of the solidification time; in which the most important input was the heat transfer coefficient.

CHAPTER 6. UNCERTAINTY QUANTIFICATION IN MODELING EQUIAXED ALLOY SOLIDIFICATION

The analysis of the model in the previous chapter for unidirectional chill casting has been extended to include equiaxed alloy solidification. A schematic of this process is shown in Figure 2.5. Modeling equiaxed solidification introduces new model input parameters, such as the packing fraction for the rigid mushy zone, average equiaxed particle size, and buoyancy contributions from the solid particles. These uncertain input parameters are analyzed along with the rigid mushy zone dendrite arm spacing, heat transfer coefficient, and material properties. The uncertainty in the predicted macrosegregation levels and solidification time are examined along with quantifying which input parameters have the largest effect on the outputs. The macrosegregation metrics are the same as in the previous chapter (Figure 5.1). This analysis will help determine the maximum uncertainty tolerated in model input parameters to obtain a minimum confidence in predicted output.

Before quantifying the uncertainty in the segregation and solidification time results, the controlling transport phenomenon are simulated to illustrate the behavior of a solidifying, grain-refined metal alloy. Then, the uncertainty in average free-floating particle diameter, packing fraction, dendrite arm spacing, thermal boundary conditions, and material property inputs are examined for their effect on model outputs.

6.1 Transport Phenomena Analysis

The transport phenomena and macrosegregation were predicted using the properties in Table 2.1, $g_{s,crit}$ = 0.15, and h = 1,500 W/m^{2}K. Snapshots of the composition field, mushy zone, and streamlines are shown in Figure 6.1 for this case. The slurry region (mixture of free-floating particles and liquid) very quickly encompasses the domain except near the chill and inlet, Figure 6.1(a). In the liquid and slurry regions, buoyancy forces drive a counter clockwise rotating flow. Because macrosegregation occurs when the solid and liquid separate and the free-floating particles usually move with the interdendritic liquid, this flow cell keeps the bulk composition in these regions well mixed. Near the onset of the rigid mushy zone this flow cell still has some effect, transporting interdendritic liquid. Deep in the rigid mushy zone the buoyancy driven flow is damped by the dendritic network and is primarily driven by shrinkage driven flow. This flow acts perpendicular to the solidification front. Therefore, the shrinkage driven slow primarily acts horizontally in the x-direction as the solidification front is mostly vertical, especially near the top of the domain. As the solidification front progresses through the domain the bottom of the domain approaches the far wall much faster than the top. This is due to the temperature of the fluid from the inlet being superheated, which retards the solidification front at the top of the domain. The flow cell in the liquid and slurry drives the fluid from the inlet toward the chilled wall as soon as it enters the domain. The fluid then travels down the solidification front where it is cooled and nucleates solid particles. These particles coalesce to the rigid mush zone as the temperature drops, advancing the rigid solidification front. As the rigid mushy zone

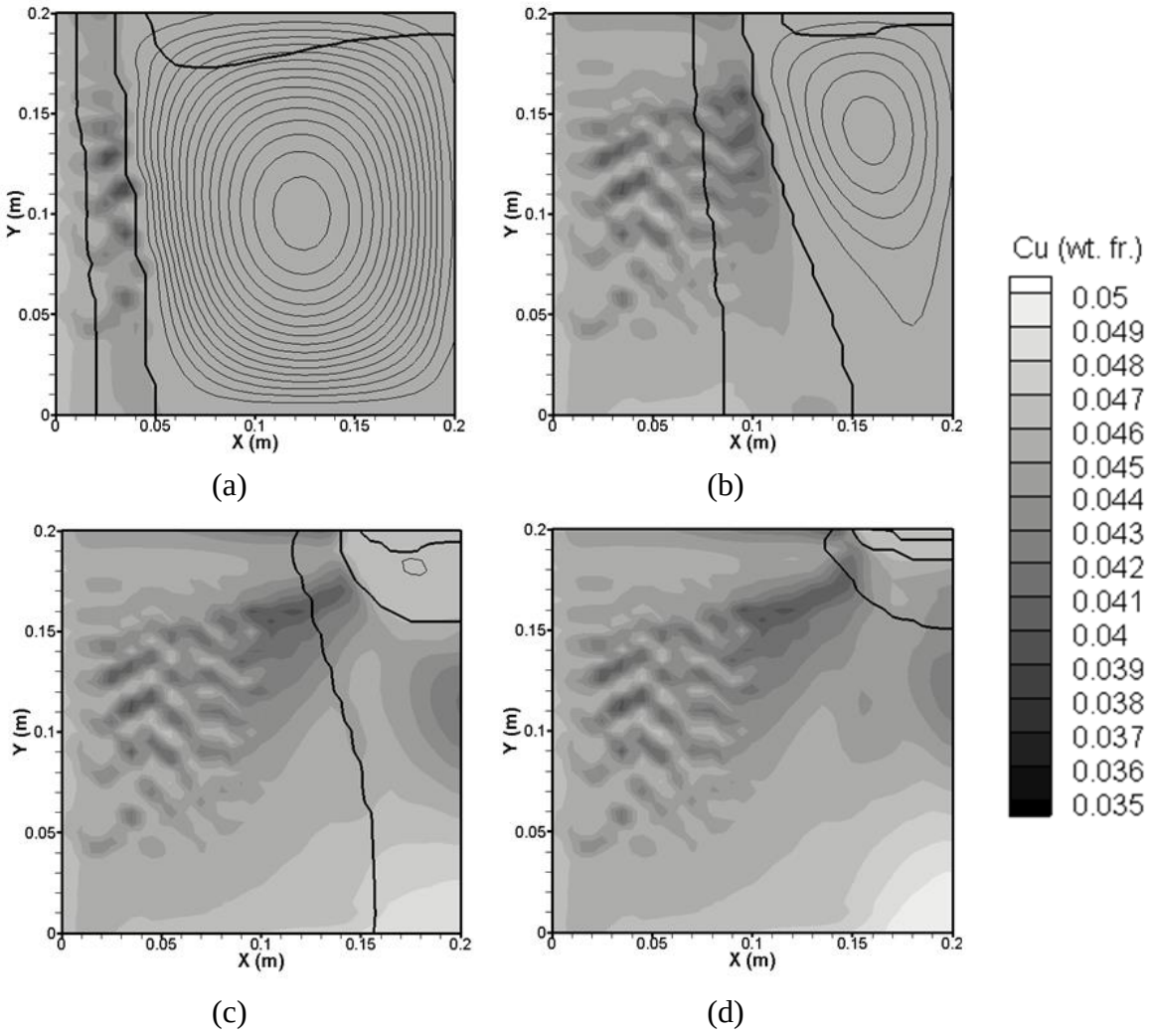

Figure 6.1: Copper composition distribution, with counter clockwise rotating flow cell ($\Delta\rho\Psi$=1 kg/s) at (a) 100 s, (b) 500 s, (c) 1200 s, and (d) 1600 s. The four zones (L to R: solid, rigid mush, slurry, and liquid) are demarcated by the bold lines.

reaches the far wall, particle settling begins to contribute to advancing the solidification front.

The mixture composition of the slurry region slowly increases due to penetration of the buoyancy driven flow cell, which transports enriched solute from the rigid mushy zone to the slurry. At the top of the domain, the shrinkage driven flow in the rigid mush is primarily in the horizontal direction, driving enriched liquid towards the chilled wall. This enriched liquid is replaced by liquid from the slurry, which is closer to the nominal composition, aiding the copper depletion of this region. Near the bottom of the domain, the shrinkage driven flow gains a vertical component which assists the negative buoyancy force driving the enriched interdendritic liquid downwards. As the rigid solidification front reaches the far wall (between (c) and (d) in Figure 6.1), the direction of the shrinkage driven flow becomes primarily vertical, which increases the enrichment at the bottom of the domain and causes a depleted region to form near the mid-height. These transport phenomena cause the composition field shown in Figure 6.1(d). The compositional freckles that appear in the ingot are not a point of emphasis in this study, but have been linked to numerical issues [80–82].

6.2 Uncertainty in Packing Fraction

One of the more uncertain parameters in this study is the critical fraction solid that chosen as the point at which a control volume packs, $g_{s,crit}$, the choice of which greatly influences the shape of the mushy zone. The value of $g_{s,crit}$ is dependent on many factors including the cooling rate, amount of grain refiner, and local composition and has been measured to be anywhere between 0.071 to 0.291 for Al-Cu alloys [83–85]. The input

uncertainty PDF of $g_{s,crit}$ used for this study is a uniform distribution from 0.05 to 0.3. A uniform distribution was chosen because $g_{s,crit}$ is an unknown function of many factors that may give it a local value anywhere in this range, but we do not have enough information to pick a most possible value. The aleatoric uncertainty of the numerical model predictions resulting from only the uncertainty in $g_{s,crit}$ is examined using the values in Table 2.1 and a constant heat transfer coefficient of 1,500 W/m^{2}K.

The numerical model uncertainty of the macrosegregation results using the normalized Weibull deviation of the copper distribution, W^{Cu}, is shown in Figure 6.2. A level 3 Smolyak analysis produced a cubic surrogate model. Figure 6.2(a) shows the model predictions of W^{Cu} and the fitted cubic polynomial function over the possible $g_{s,crit}$ range and Figure 6.2(b) shows the PDF of the uncertainty for the W^{Cu} prediction. The uniform distribution of the $g_{s,crit}$ input produced an irregular shape of the W^{Cu} PDF in Figure 6.2(b). The macrosegregation level decreases with increasing $g_{s,crit}$ as shown in Figure 6.2(a). Over most of the possible $g_{s,crit}$ range, the rigid mush has a low enough permeability that there is very little buoyancy driven flow. The size of the rigid mushy zone is large with smaller values of $g_{s,crit}$, and it has more area to redistribute copper by shrinkage induced liquid flow relative to the solid. Small values of $g_{s,crit}$, 0.1 and below, form a relatively large rigid mushy zone the edge of which is permeable enough to allow significant buoyancy driven flow. This combination of multiple transport mechanisms and large mushy zone allows more solute to be redistributed and a larger W^{Cu}. However, the rate that W^{Cu} increases levels off as $g_{s,crit}$ approaches zero. Figure 6.3 shows the composition distributions for three different $g_{s,crit}$ values and, as $g_{s,crit}$ increases, the length of the right tail increases at the expense of the left tail. This is due to the change in

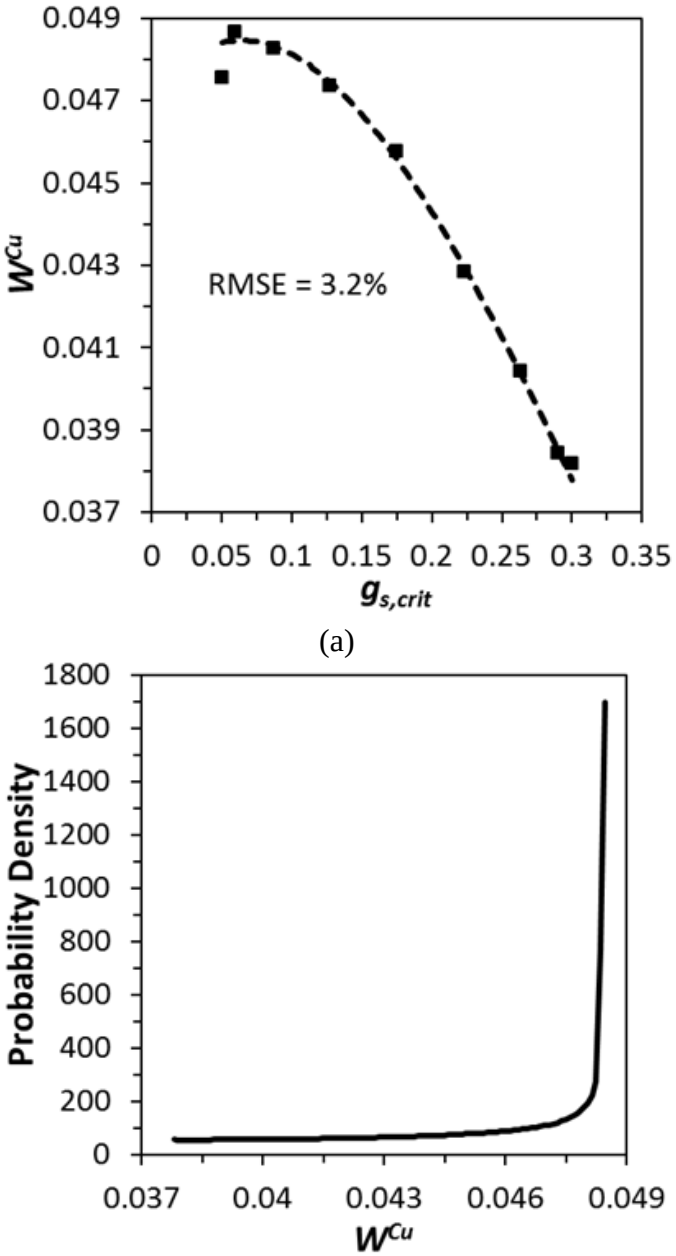

Figure 6.2: Predictions of macrosegregation level as a function of packing fraction using W^{Cu} and showing (a) model predictions with the fitted surrogate model and (b) the resulting probability density function of the model output.

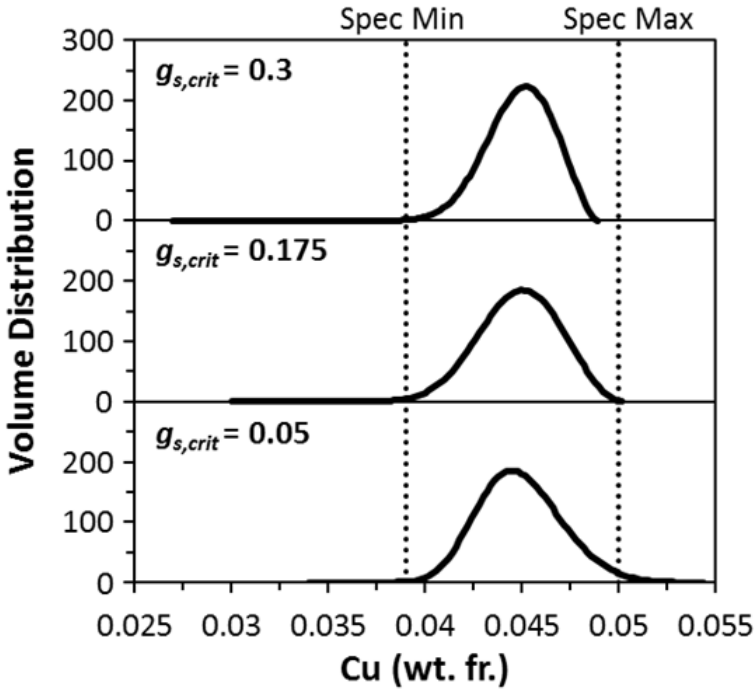

Figure 6.3: Composition distribution for 3 different packing fractions showing the composition specification with vertical dotted lines.

dominant solute transport mechanisms shifting from solely shrinkage driven flow to a combination of buoyancy and shrinkage flows. Initially this shift causes a relatively large increase in W^{Cu}, but as $g_{s,crit}$ approaches zero the contributions to the right tail increases at a similar rate as the left tail shrinks. In other words, the buoyancy driven flow causes the slurry composition to increase and therefore lessen the degree of the depleted region caused by shrinkage, because the fluid pulled in by shrinkage is taken from the slurry. The decrease in slope of the surrogate model as $g_{s,crit}$ approaches zero accounts for the large probability that the copper macrosegregation level is in a narrow range $W^{Cu} > 0.0482$.

The numerical model macrosegregation predictions using the V_{spec} metric are shown in Figure 6.4. Similar to the resulting PDF for W^{Cu}, the output PDF for V_{spec} is irregularly shaped with the highest probability output being above 0.042. The numerical predictions are shown in Figure 6.4(a) along with the surrogate model. A level 2 Smolyak analysis with a quadratic polynomial function provided the best fit to the model output. The maximum V_{spec} predicted from the range of $g_{s,crit}$ inputs occurred with a $g_{s,crit}$ value of 0.157. The volume fraction of the ingot that is outside the compositional specification decreases as $g_{s,crit}$ varies from this point. Figure 6.3 shows whether the majority of the volume out of specification is depleted or enriched depends on $g_{s,crit}$. The transition of prominent transport mechanisms causes the volume out of specification to be made up of only negative segregation regions at high $g_{s,crit}$ to both positive and negative at low $g_{s,crit}$. As $g_{s,crit}$ initially decreases, from 0.3 to 0.175, the composition distribution gains a positively segregated tail and the volume out of the specification increases. Decreasing

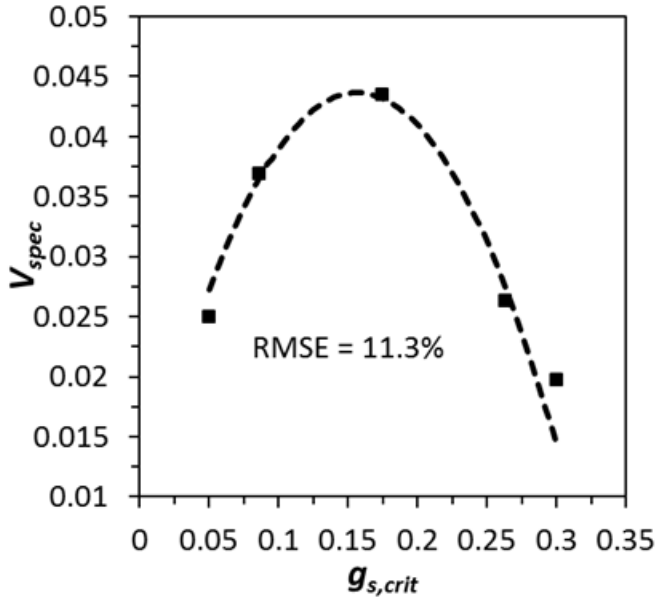

(a)

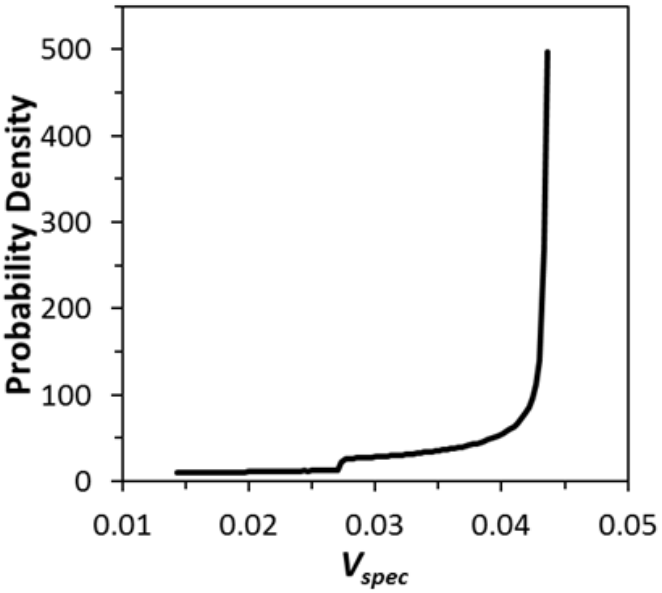

(b)

Figure 6.4: Predictions of macrosegregation level as a function of packing fraction using volume fraction out of the compositional specification (V_{spec}), showing (a) model predictions with the fitted surrogate model and (b) the resulting probability density function of the model output.

$g_{s,crit}$ further, from 0.175 to 0.05, the amount of the curve in Figure 6.3 is moving in specification faster than the amount out of specification.

The peak of the quadratic function corresponds to the maximum probability in Figure 6.4(b), because this part of the curve has the lowest slope. Due to the quadratic nature of the surrogate model, two different $g_{s,crit}$ values can achieve the same V_{spec}. However, this function is not perfectly symmetric and lower V_{spec} values are predicted at the high end of the $g_{s,crit}$ range than at the low end, explaining the jump in probability near V_{spec} = 0.27. Assuming a uniform distribution for $g_{s,crit}$ gives the low slope region in the V_{spec} surrogate model less influence on the output PDF; a Gaussian distribution centered around this input would have concentrated the probability of the V_{spec} outcome near the highest values. This affect is opposite of that in the W^{Cu} output PDF. In that case, a Gaussian input distribution of $g_{s,crit}$ would have downplayed the low sensitivity at the low end of the $g_{s,crit}$ range and made the W^{Cu} PDF more uniform.

The aleatoric uncertainty in the solidification time prediction was also analyzed based on the uniform $g_{s,crit}$ PDF and the output uncertainty is shown in Figure 6.5. A level 3 Smolyak analysis was used to generate the cubic surrogate model fit to the data in Figure 6.5(a). This function was used to generate the PDF shown in Figure 6.5(b). The solidification time increases with $g_{s,crit}$, ranging from 1440 s to 1980 s. The most probable solidification time prediction is 1477 s, which occurs for $g_{s,crit}$ values around 0.07 where the sensitivity of t_s to $g_{s,crit}$ is the lowest. The slope of the surrogate model in Figure 6.5(a) only changes by a factor of four over its range and so the output PDF in Figure 6.5(b) for t_s is much less skewed than those for W^{Cu} and V_{spec}. While the overall solidification time appears very sensitive to $g_{s,crit}$, the evolution of the total solid fraction of the domain

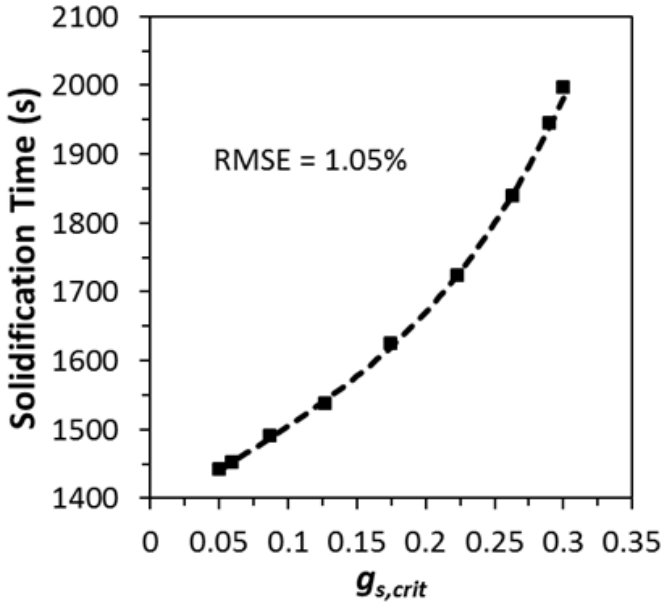

(a)

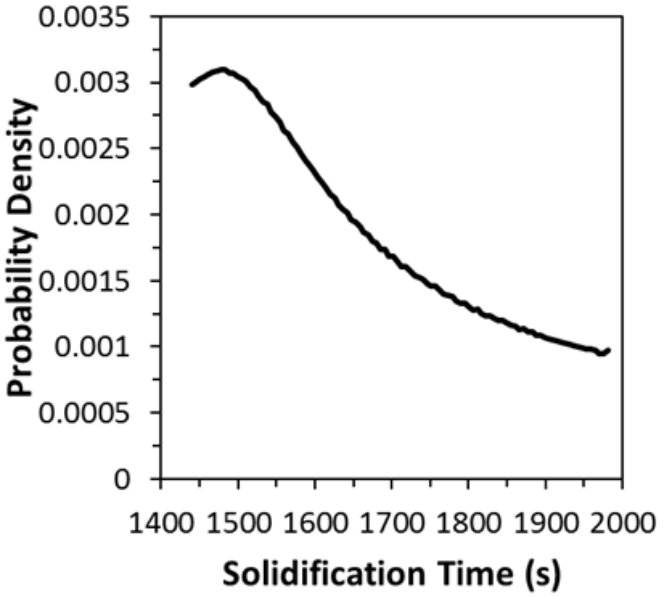

(b)

Figure 6.5: Predictions of solidification time as a function of packing fraction showing (a) model predictions with the fitted surrogate model and (b) the resulting probability density function of the model output.

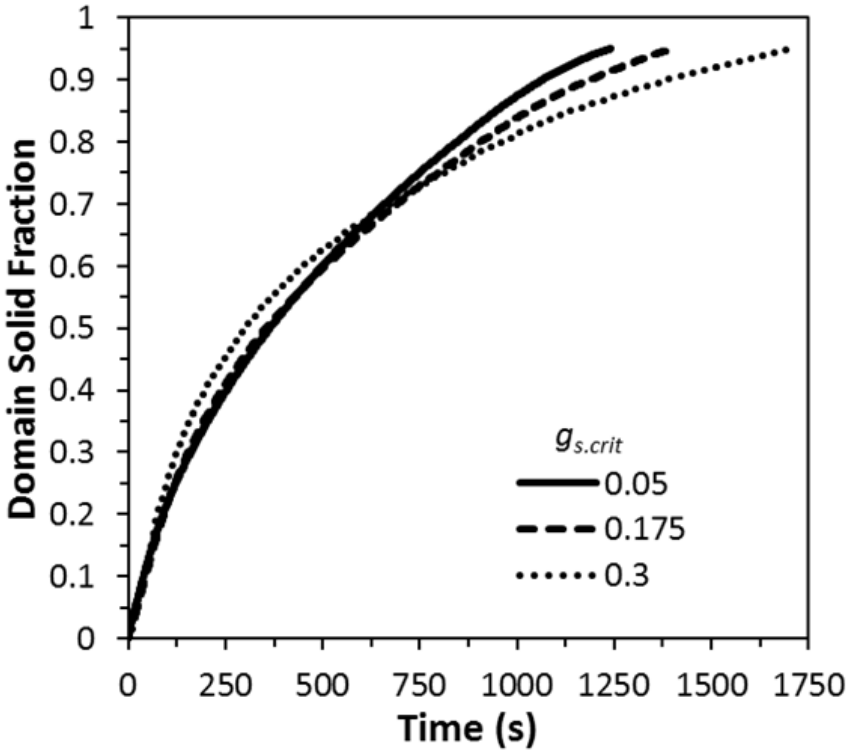

Figure 6.6: Fraction solid of the simulation domain as a function of time for three critical packing fractions, showing two solidification regimes that affect the solidification time predictions.

(Figure 6.6) indicates two different solidification regimes. Early in the process the solidification time is very similar for each packing fraction, where the higher $g_{s,crit}$ has a slightly faster solidification rate which is due to better compositional and thermal mixing allowed by a larger slurry region with stronger flows. At a certain domain fraction solid (around 0.7) the rigid mushy zone reaches the far wall and the solidification rate slows down. This is partly due to increasing thermal resistance of the thicker solid region, but also because the slurry region interacts strongly with the inlet, still bringing in fluid at the initial temperature and composition. The solid circulating in the slurry interacts with the inlet, slowing solidification even remelting some solid. Higher packing fractions have larger slurry regions and so increase the interaction with the inlet and the total solidification times, despite having less segregation. This behavior near the inlet, which is an artifact to allow shrinkage without a riser or free surface, makes determining the solidification time difficult. Therefore, the solidification time is not included in the analysis of the other input parameters.

6.3 Uncertainty in Particle Size and Packing Fraction

To calculate the velocity difference between the solid and the liquid in the slurry region, some estimate must be made regarding the solid particle size. Here a normal distribution is assumed with a mean particle size of 30 microns and a standard deviation of 7.5 microns, so the 95% confidence interval is between 15 and 45 microns. The aleatoric uncertainty of the macrosegregation model predictions are analyzed using the uncertainty of the packing fraction and particle size together. The results of the macrosegregation predictions, as characterized by W^{Cu}, are shown in Figure 6.7. A level

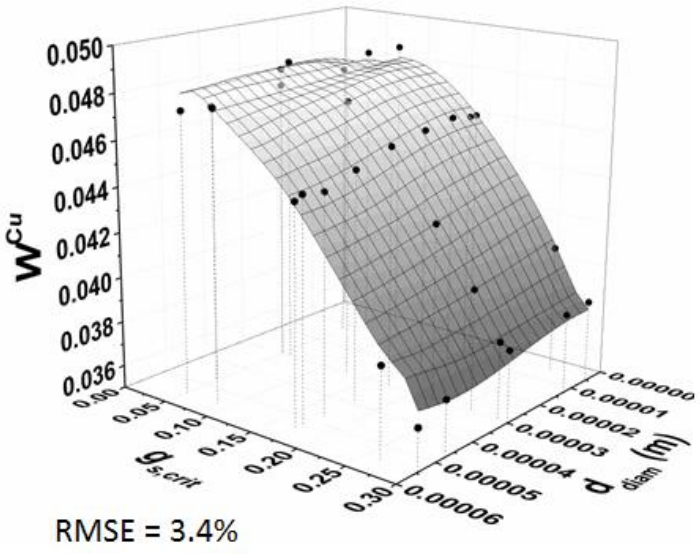

(a)

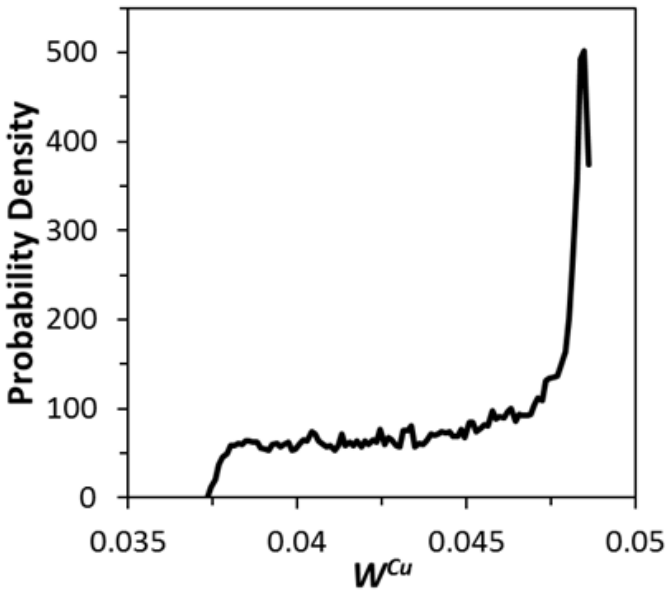

(b)

Figure 6.7: Predictions of macrosegregation level as a function of particle size and packing fraction using W^{Cu} and showing (a) macrosegregation model predictions with the fitted surrogate model and (b) the resulting probability density function of the model output.

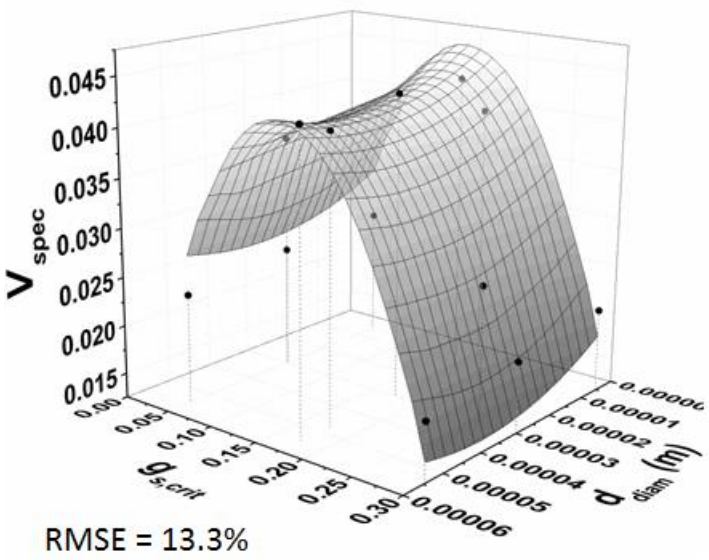

(a)

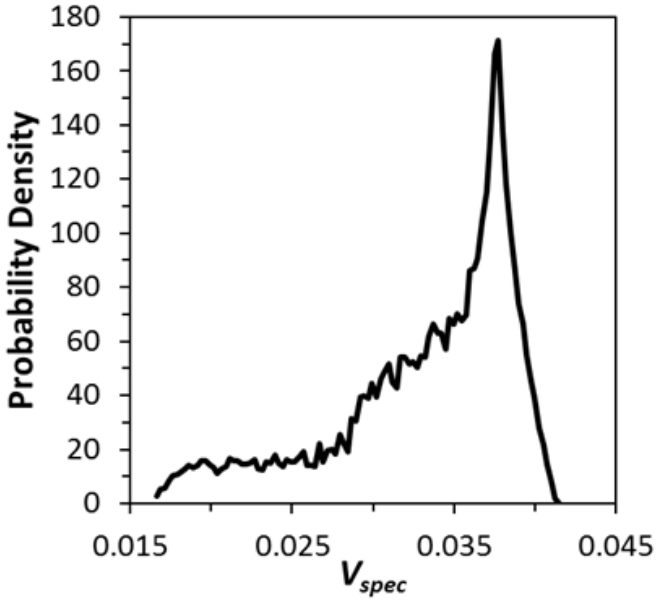

(b)

Figure 6.8: Predictions of macrosegregation level as a function of packing fraction and particle size using V_{spec}, showing (a) model predictions with the fitted surrogate model and (b) the resulting probability density function of the model output.

three analysis fit a cubic polynomial fit to the sparse model predictions, Figure 6.7(a), which produced the output PDF shown in Figure 6.7(b). The resulting W^{Cu} PDF is very similar that the one produced from the uncertainty in $g_{s,crit}$ alone, indicating that the uncertainty in $g_{s,crit}$ affects the output more than the particle size. This can also be seen in shape of the surrogate (Figure 6.7(a)), where varying $g_{s,crit}$ has a larger effect on W^{Cu} than varying the particle size over the chosen range. Increasing the particle size causes a slight increase in the ingot macrosegregation. Larger particle sizes are more likely to settle out of the slurry region than smaller particles, which leads to slightly more macrosegregation. This effect is more significant with larger packing fractions, which lead to larger slurry regions.

The uncertainty in numerical model macrosegregation predictions using the V_{spec} metric for input uncertainties in particle size and $g_{s,crit}$ are shown in Figure 6.8. The quadratic surrogate model fit to the numerical predictions is shown in Figure 6.8(a). The V_{spec} generally increases as the particle size increases and is more severe for higher packing fractions. However, this is only a slight increase compared to the changes in V_{spec} due to $g_{s,crit}$. The V_{spec} surrogate model for the model output is very similar to that shown in Figure 6.4(b) indicating that $g_{s,crit}$ is more critical in predicting V_{spec} than the particle size. For both macrosegregation metrics the input uncertainty in $g_{s,crit}$ has a much larger effect than the particle size, indicating the uncertainty in particle size, as long as there is not much particle settling, is not a critical parameter in macrosegregation predictions.

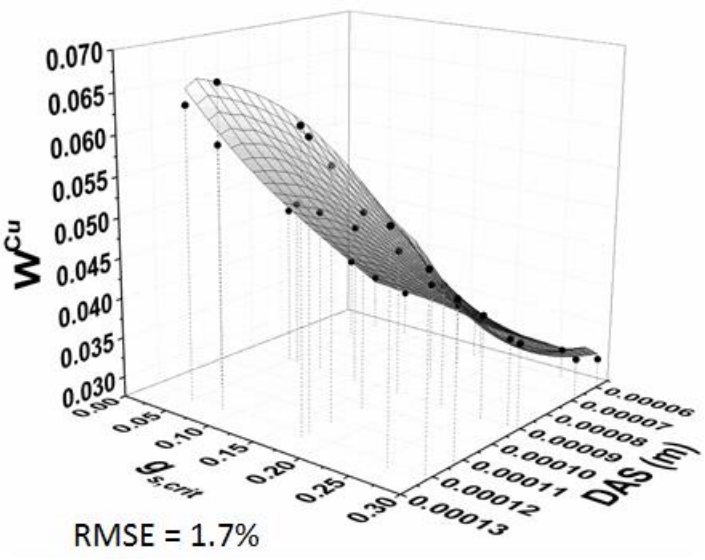

(a)

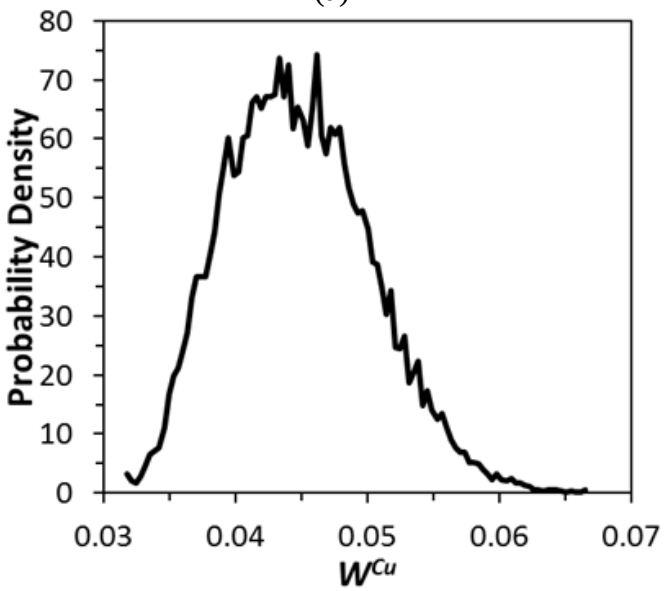

(b)

Figure 6.9: Predictions of macrosegregation level as a function of packing fraction and dendrite arm spacing using W^{Cu}, showing (a) model predictions with the fitted surrogate model and (b) the resulting probability density function of the model output.

6.4 Uncertainty in Dendrite Arm Spacing and Packing Fraction

In the rigid mushy zone the flow is damped by the Blake-Kozeny permeability model and requires knowledge about the microstructure in terms of the dendrite arm spacing. A normal distribution is chosen for the arm spacing, based on experimental measurements performed by Melto et al. [50], with a mean value of 91 microns and a standard deviation of 9.5 microns. This range of dendrite arm spacings is much larger than the equiaxed particle size used in Stokes law (equation (2.6)); however, the particle size in this expression is for the drag of a dense spherical particle. The true dendritic nature of the particles is not considered and particle sizes of realistic sized grains would produce a much larger solid velocity using this expression. The aleatoric uncertainty in the macrosegregation predictions is examined based on uncertainties in the arm spacing and packing fraction together. The resulting PDF, Figure 6.9(b), is calculated from the cubic polynomial surrogate model in Figure 6.9(a). The mean elemental sensitivity, $\mu_{W^{Cu}}$, from the PDF in Figure 6.9(b) is 0.0448 with a standard deviation, $\sigma_{W^{Cu}}$, of 0.00551, resulting in a model uncertainty ($2\ \sigma_{W^{Cu}} / \mu_{W^{Cu}}$) of 24.6 %. The predicted macrosegregation level increases with increasing dendrite arm spacing for all values of $g_{s,crit}$. The flow strength in the rigid mushy zone is strongly tied to the dendrite arm spacing (Figure 6.10), impacting the buoyancy driven flow, making it easier to transport solute and increasing the segregation level. The dendrite arm spacing also has a stronger effect on the W^{Cu} prediction than $g_{s,crit}$.

The results of the uncertainty in numerical model macrosegregation predictions using the V_{spec} metric for uncertainties in dendrite arm spacing and $g_{s,crit}$, are shown in

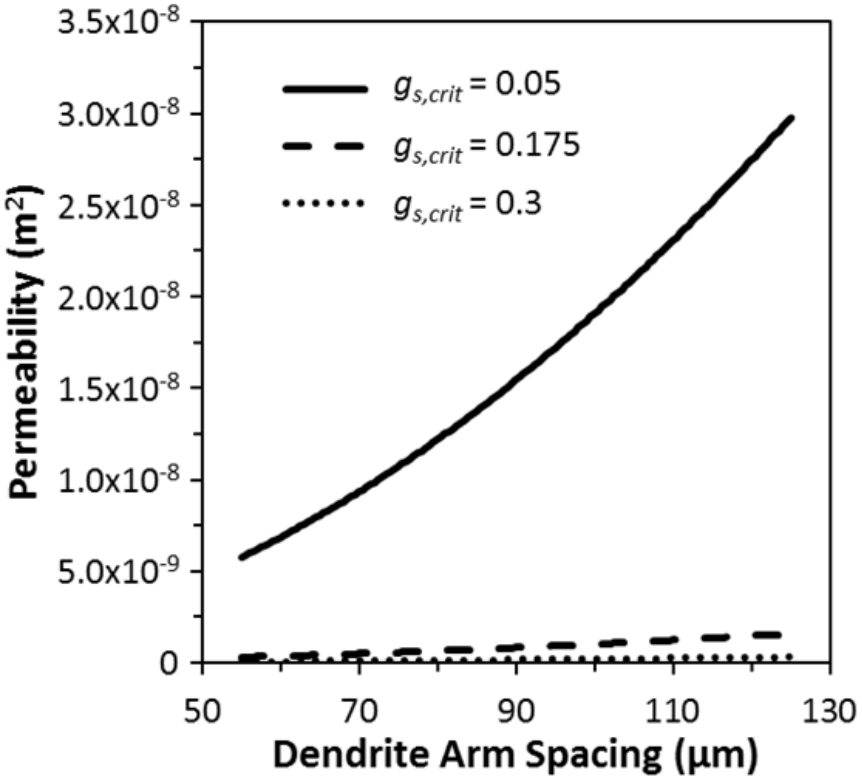

Figure 6.10: Plot of the mushy zone permeability as a function of the dendrite arm spacing for three different fraction solids.

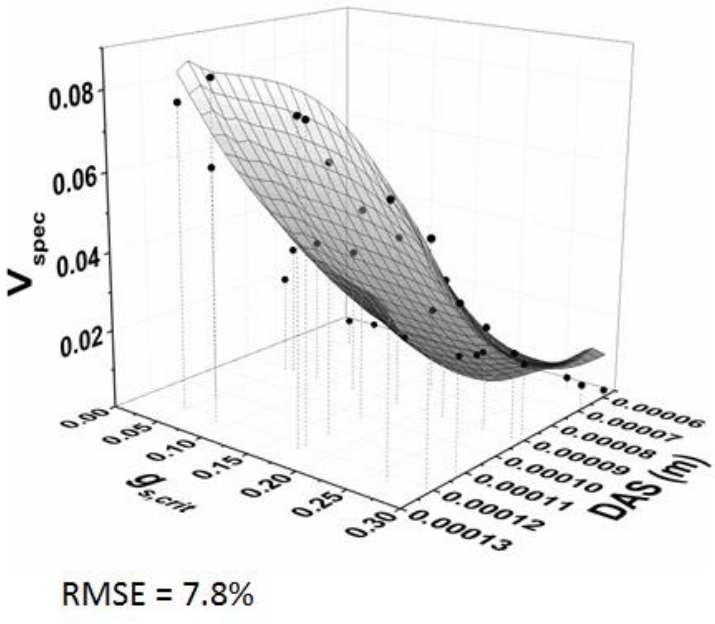

(a)

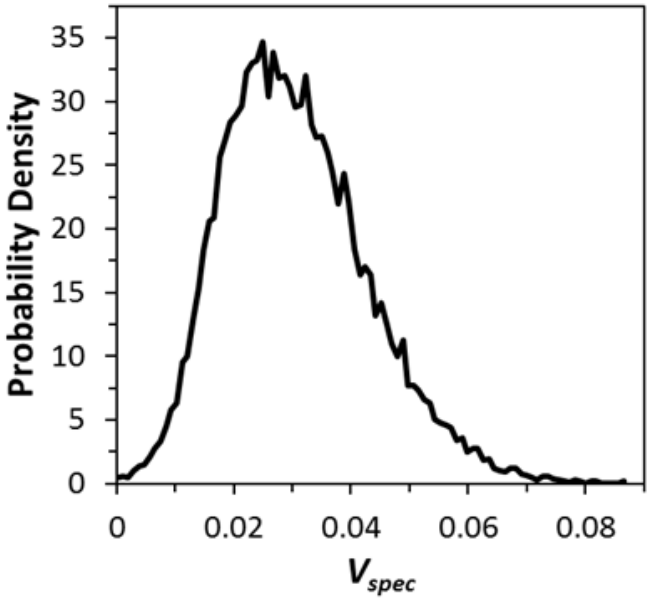

(b)

Figure 6.11: Predictions of macrosegregation level as a function of packing fraction and dendrite arm spacing using V_{spec}, showing (a) model predictions with the fitted surrogate model and (b) the resulting probability density function of the model output.

Figure 6.11. The mean of the PDF is 0.0347 with a standard deviation is 0.00728, a model uncertainty ($2\sigma_{V_{spec}} / \mu_{V_{spec}}$) of 42%. Changes in the dendrite arm spacing have a larger effect on V_{spec} than changes in $g_{s,crit}$. Increasing the arm spacing increases the volume outside the compositional specification due to the more permeable rigid mushy zone and more flow there. In the current study the arm spacing was assumed to be constant and uniform during the simulation, and the distribution chosen was based on actual experimental measurements. This uncertainty analysis does not consider spatial variations in the arm spacing, which is an additional concern when modeling flow in the mushy zone. Therefore, the uncertainty reported based on the arm spacing is truly irreducible and must be taken into consideration when analyzing the model predictions.

6.5 Uncertainty in Heat Transfer Coefficient and Packing Fraction

Three different degrees of input uncertainty in the heat transfer coefficient are analyzed, along with the uncertainty in the packing fraction. The normal distributions of input uncertainties for the heat transfer coefficient ($2\sigma_h / \mu_h$) are 30%, 20%, and 10% for Cases A, B, and C respectively. The uncertainty for $g_{s,crit}$ is the same as in the previous analyses for all three cases. The resulting PDFs for each case are shown in Figure 6.12. For Case A, a cubic surrogate was used, while the other two cases found a best fit with quadratic polynomials to the macrosegregation predictions. As expected, the uncertainty in the numerical prediction of W^{Cu} ($2\sigma_{W^{Cu}} / \mu_{W^{Cu}}$) increases with uncertainty in the heat transfer coefficient (21.7%, 18.1%, and 15.5% for Cases C1, C2, and C3, respectively). The same is true for V_{spec} which has output uncertainties of 57.6%, 48.5%, and 37.1%

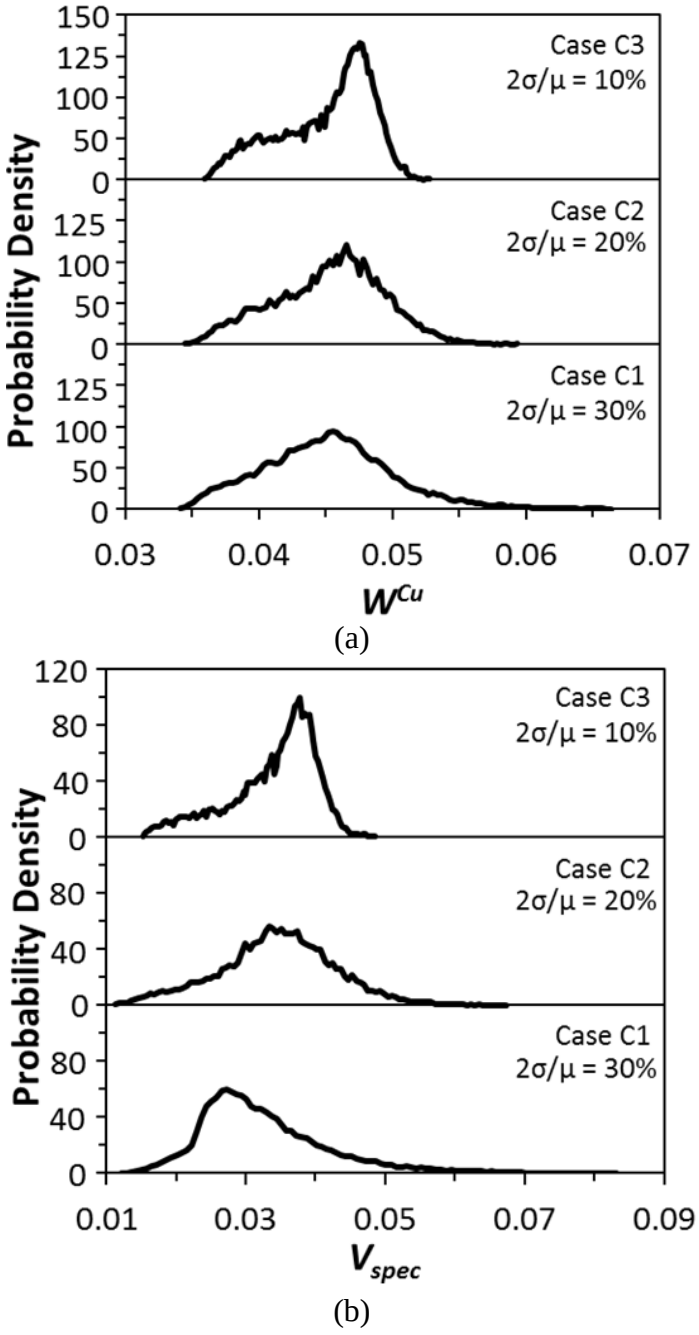

Figure 6.12: Macrosegregation prediction uncertainty for three different degrees of uncertainty in the heat transfer coefficient showing the PDF for (a) the normalized Weibull deviation and (b) volume fraction out of the compositional specification.

with decreasing input uncertainty. As the heat transfer coefficient increases, the macrosegregation level, as determined by both metrics, decreases. The largest macrosegregation levels occur for a low heat transfer coefficient and packing fraction, while the lowest macrosegregation is for high heat transfer coefficient and large packing fraction. Low heat transfer coefficients allow more time for solute to be transported in the rigid mushy zone before the drag there effectively stops the flow. Increasing the heat transfer coefficient induces larger temperature gradients leading to stronger flows, which keep the composition of the slurry well mixed. The solidification rate also increases, which limits the distance the solute can be transported before becoming entrained in the solid. The right tail of the model output PDFs becomes shorter as the heat transfer coefficient becomes more certain about its most probable values. However, the left tail remains about the same across the three cases. The heat transfer coefficient is becoming more certain from Case C1 to C3, but the uncertainty in $g_{s,crit}$ remains the same. The tails of the PDFs in Case A are due to the extreme values of the heat transfer coefficient, and the core of the PDF is due to the uncertainty in $g_{s,crit}$ and values near the mean of the heat transfer input.

This behavior of the output uncertainty for each macrosegregation metric can be seen more easily by examining their sensitivities, shown in Figure 6.13. For Case C1, both macrosegregation metrics are more sensitive to the heat transfer coefficient. Decreasing the uncertainty in Case C2, V_{spec} becomes more sensitive to $g_{s,crit}$ which means that the uncertainty in $g_{s,crit}$ needs to first be improved to reduce the model uncertainty before the uncertainty in the heat transfer coefficient; the same is true for Case C3. This causes the model uncertainty for V_{spec} to remain unchanged when the

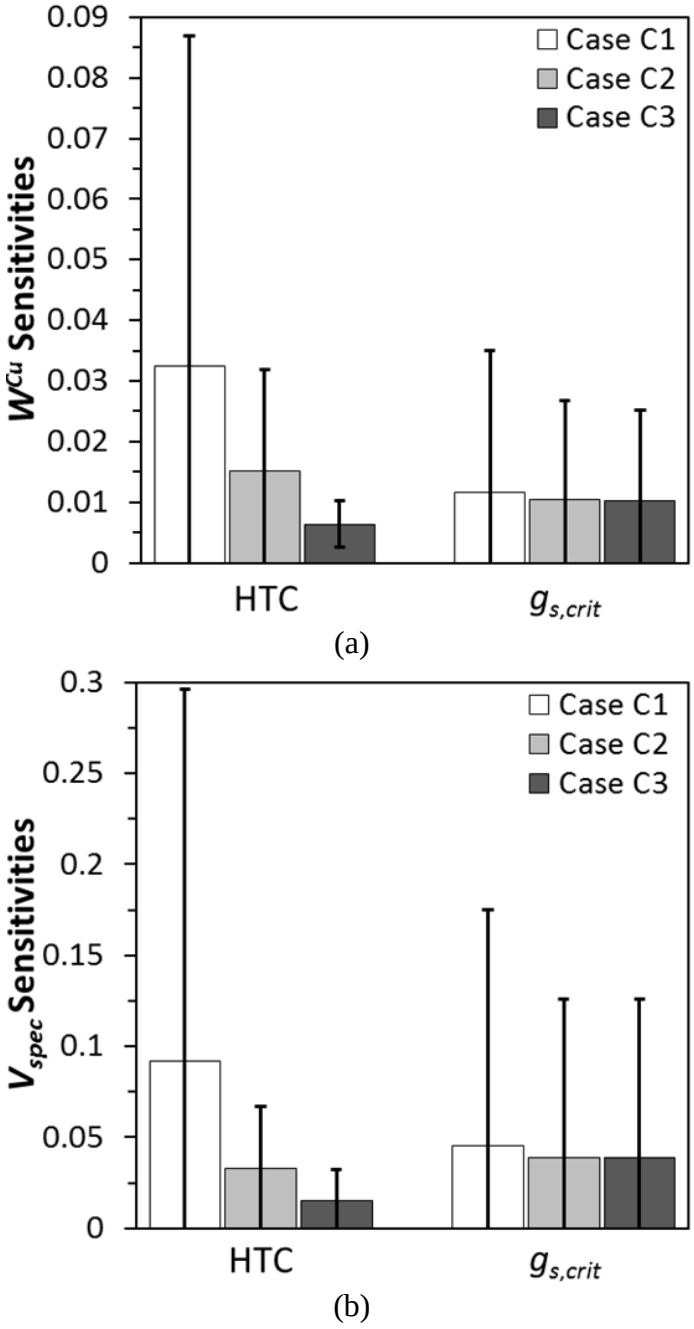

Figure 6.13: Macrosegregation output mean sensitivities for the three different levels of input heat transfer coefficient uncertainty for (a) normalized Weibull deviation and (b) volume fraction outside the compositional specification.

uncertainty in the heat transfer coefficient is reduced from Case C2 to C3. However for W^{Cu} in Cases C2, the output is still most sensitive to the heat transfer coefficient, but the level of uncertainty is closer to that of $g_{s,crit}$. For Case C3, the sensitivity of W^{Cu} on the heat transfer coefficient drops below that of $g_{s,crit}$. This means that the uncertainty in both inputs should be reduced if the uncertainty in the heat transfer coefficient is at or below 20%.

6.6 Uncertainty in Material Properties

The effect of nine material properties, ρ_s, $\Delta\rho$, k, c, L_f, $\beta_{T,l}$, $\beta_{S,l,}$ $\beta_{T,s}$, and $\beta_{S,s}$, on the macrosegregation predictions and, while some of these values may be known to have less possible variation (and some might even have more), a value of 10% input uncertainty ($2\sigma/\mu$) was used. The packing fraction for these cases was set to be 0.15. A normal distribution is assumed for each material property uncertainty where the mean property values are shown in Table 2.1. A level 1 sparse grid was constructed to determine the sensitivity of the predicted macrosegregation metrics to the uncertain material properties (Figure 6.14). The variables that have the most influence on W^{Cu} (in order) are ρ_s, L_f, $\Delta\rho$, $\beta_{S,l}$, k, and c, where the three most influential properties are ρ_s, $L_{f,}$ and $\Delta\rho$. Similarly, the most prominent material properties to V_{spec} are $\Delta\rho$, ρ_s, L_f, k, and c, where the three most important inputs are $\Delta\rho$, ρ_s, and $L_{f,}$. The Stefan number ($\frac{c\Delta T_m}{L_f}$) for this system, using the values in Table 2.1, is 0.19, so we expect the latent heat is more important than the specific heat in determining the size of the mushy zone and, as explained above, a larger mushy zone allows more macrosegregation. Suggested by equation (2.28), the density

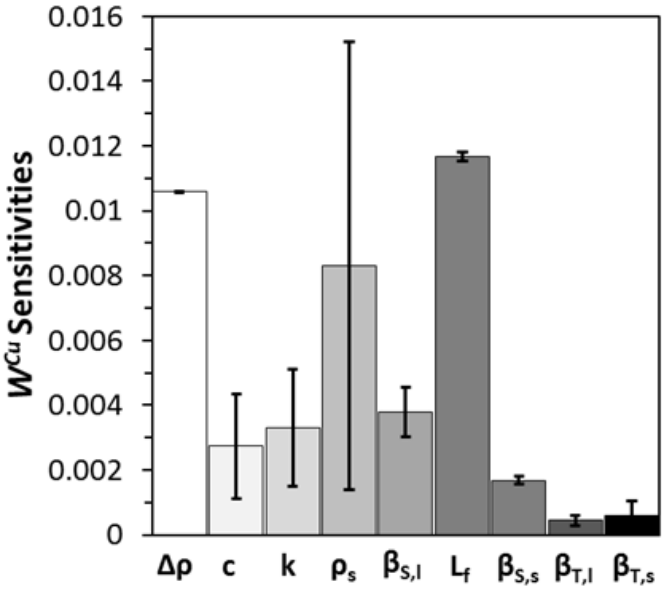

(a)

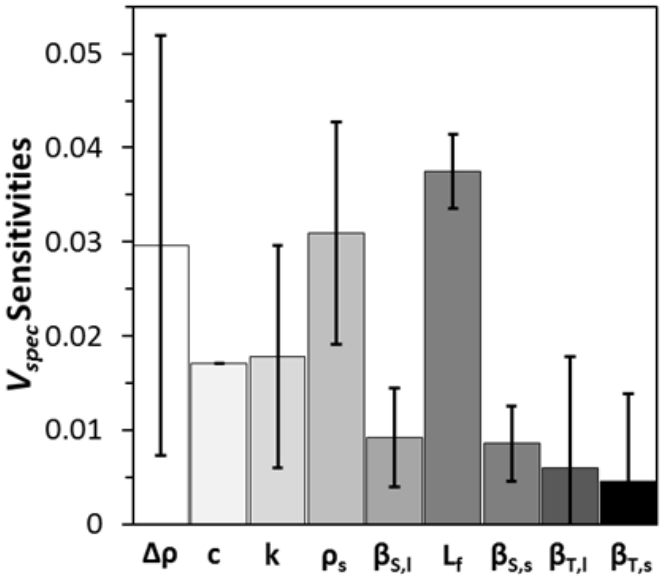

(b)

Figure 6.14: Macrosegregation output mean sensitivities for the material properties uncertainty for (a) normalized Weibull deviation and (b) volume fraction outside the compositional specification.

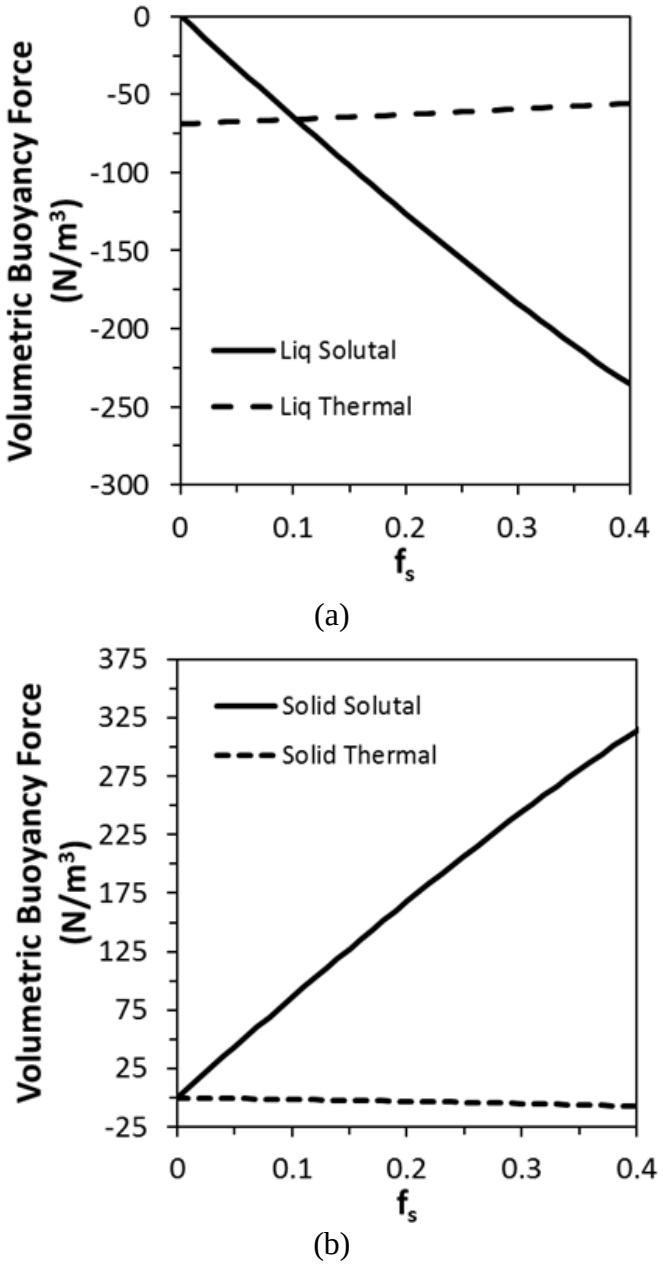

Figure 6.15: Plot of the solutal and thermal buoyancy contributions for equilibrium solidification of Al-4.5 wt.% Cu showing (a) contributions from the liquid and (b) contributions from the solid.

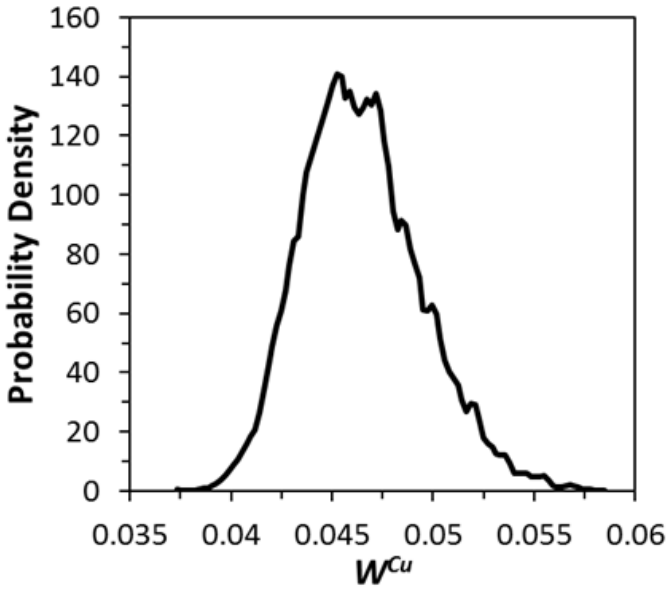

(a)

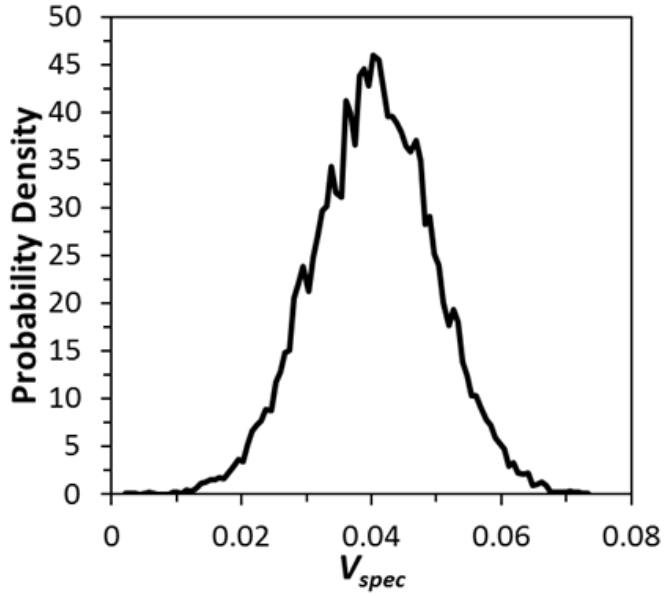

(b)

Figure 6.16: Combined aleatoric macrosegregation prediction uncertainty of the most influential uncertain material property values are (ρ_s, L_f, $\Delta\rho$, $\beta_{S,l}$, k, and c for W^{Cu} and are $\Delta\rho$, ρ_s, L_f, k, and c for V_{spec}) showing the PDF for (a) the normalized Weibull deviation and (b) volume fraction out of the compositional specification.

difference affects the shrinkage driven flow in the rigid mushy zone, where a majority of the solute transport takes place. The solid density also influences the level of the liquid and mixture density, which appear in nearly all the terms in the species and energy in equations (Equations (2.10) and (2.12)) and influences the flow field. This causes the uncertainty the density to have a profound effect on the predicted macrosegregation levels. The thermal conductivity controls the rate of conduction heat transfer, which dominates heat transfer in the solid and rigid mushy zone, and is at least as important as advection in the slurry and liquid. Although the specific heat is not as important as the latent heat in the rigid mushy zone, this property still has an effect on the macrosegregation predictions. The buoyancy driven flow is strongest in the slurry region, which keeps the composition well mixed, and in the absence of much particle settling does not contribute much to macrosegregation. The solutal buoyancy has a stronger effect on the flow than the thermal buoyancy (Figure 6.15). With an exception at the very edge of the slurry region, the thermal buoyancy contribution from the liquid is stronger than the solutal component (Figure 6.15(a)). However, the solutal contribution quickly catches up to the strength of the thermal buoyancy force as the slurry becomes enriched and remains stronger for remainder of the solidification process.

To limit the number of model evaluations for higher order analyses or to obtain better fitting surrogate models, the most influential uncertain material properties (Figure 6.14), were used to determine the aleatoric uncertainty of the model. The resulting PDFs from a level 2 analysis for W^{Cu} and level 1 for V_{spec} are shown in Figure 6.16. The aleatoric uncertainty in predicted W^{Cu} and V_{spec} ($2\sigma/\mu$) for 10% uncertainty in the material properties is 12.8% and 46.2% respectively. The uncertainty in V_{spec} is much

greater than W^{Cu}, and to improve the model predictions the uncertainty in $L_{f,}$ $\Delta\rho$, and ρ_s should first be reduced. The $g_{s,crit}$ value for these cases is 0.15, which limits the amount of buoyancy driven flow and causes the majority of the ingot to be out of specification. By changing the inputs, the degree of negative segregation (the left tail in Figure 6.3) changes the most. This change in the composition distribution affects the tails of the curve more than the area near the peak and therefore V_{spec} is affected more than W^{Cu}.

6.7 Model Uncertainty: Combined Effects

The aleatoric uncertainty from uncertainties in packing fraction, particle size, dendrite arm spacing, heat transfer coefficient, and material properties were examined. The uncertainty in the heat transfer coefficient is 15% and the uncertainties in the other input parameters are the same as in the previous sections. A level 1 sparse grid was performed to determine the effect of the uncertain inputs on both macrosegregation predictions. The most influential parameters are then used to obtain a better fit for the surrogate model to assess the numerical model uncertainty. The sensitivity results from this linear surrogate model are shown in Figure 6.17. For both macrosegregation metrics, the most influential input parameter on average is the dendrite arm spacing. The other most influential input parameters on W^{Cu} are h, L_f, $\Delta\rho$, ρ_s, and $g_{s,crit}$. The volume out of specification, is most sensitive to h, L_f, $\Delta\rho$, ρ_s, k, c, and $g_{s,crit}$, along with the dendrite arm spacing. The criterion for determining the most influential inputs was subjective, but was based on the sensitivities in Figure 6.17. The other input parameters are neglected when performing analysis with higher order surrogates in a tradeoff of ignoring their

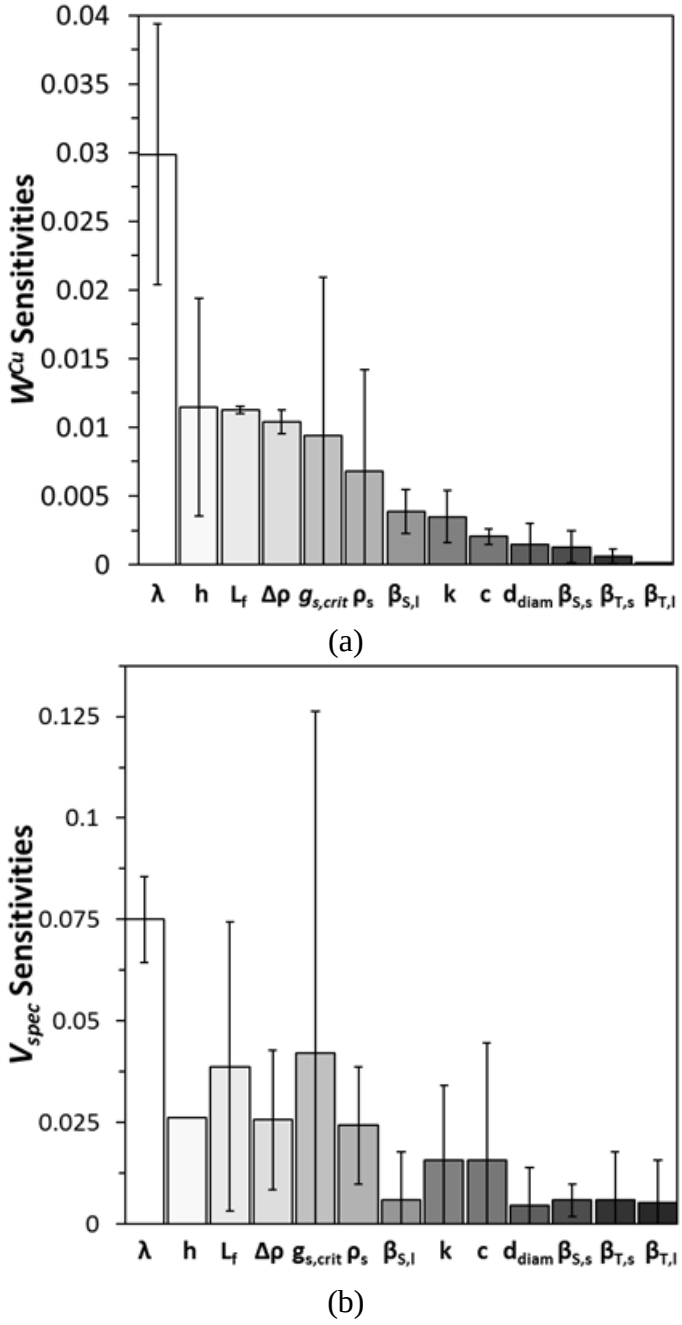

Figure 6.17: Macrosegregation output sensitivities to a combination of uncertain input parameters for (a) normalized Weibull deviation and (b) volume fraction outside the compositional specification using a linear surrogate model.

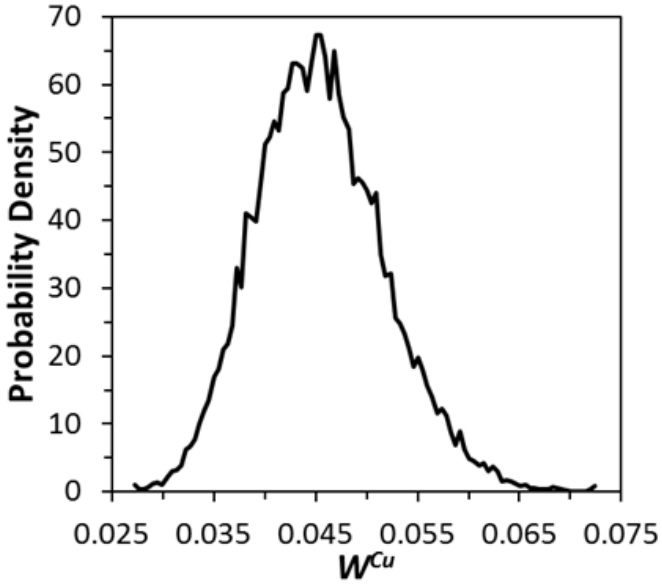

(a)

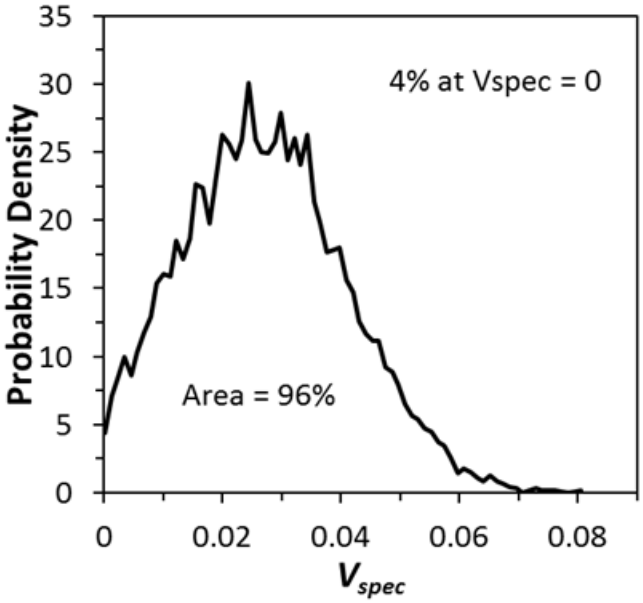

(b)

Figure 6.18: Combined aleatoric macrosegregation prediction uncertainty of the most influential uncertain inputs showing the PDF for (a) the normalized Weibull deviation and (b) volume fraction out of the compositional specification.

interactions and (albeit small) influence for many fewer model evaluations. The resulting PDFs are shown in Figure 6.18 for outputs of interest, in which the mean of W^{Cu} is 0.0454 and 0.026 for V_{spec}. The uncertainty in predicted W^{Cu} and V_{spec} macrosegregation metrics ($2\sigma/\mu$) are 27.9% and 114.6% respectively. The solidification model has a lower limit in V_{spec} of zero; however the surrogate model that is fit to the data has no such restriction. In this instance, the surrogate model predicts negative values for V_{spec} for certain sets of input parameters. The level of model uncertainty is high and in order to be reduced the most uncertainty in the most influential parameters must be reduced first, starting with λ (to which both metrics have the most sensitivity) and $g_{s,crit}$ which each metric has a large range of sensitivities to. It should be pointed out that reducing the uncertainty in these two parameters is not a trivial task, as the dendrite arm spacing and packing fraction change greatly throughout the ingot. Also, the current state of the model assumes these two parameters to be constant and uniform, and based on the current results this appears to be a poor assumption.

6.8 Conclusions

The aleatoric uncertainty was quantified for a numerical model of the equiaxed solidification of an Al-4.5 wt.% Cu alloy in a rectangular domain. The outputs of interest considered for the model included the total solidification time and two metrics for the degree of macrosegregation. Due to the superheated inlet, the solidification time was difficult to determine because of interactions with the incoming metal and the slurry, although the overall freezing rate in the domain was only significantly afftected by the uncertainty in $g_{s,crit}$ in the later stages of the process. The input parameters to which some

uncertainty was assigned included the critical packing fraction, equiaxed particle size, dendrite arm spacing, heat transfer coefficient, and several thermophysical properties. Over the range analyzed, the diameter of equiaxed particles were not large enough to cause significant settling, and so had little effect on the macrosegregation levels compared to other input parameters. The variables that have the most influence on W^{Cu} are ρ_s, $\Delta\rho$, k, c, L_f, and $\beta_{S,l}$, where the three most influential properties are L_f, $\Delta\rho$, and ρ_s. Similarly, the most prominent material properties to V_{spec} are ρ_s, $\Delta\rho$, k, c, and L_f, where the three most important inputs are L_f, $\Delta\rho$, and ρ_s. A set of simulations with the most important thermophysical properties and all the rest of the input parameters showed that the most influential input parameter on the prediction of macrosegregation uncertainty was the dendrite arm spacing.

CHAPTER 7. UNCERTAINTY QUANTIFICATION IN MODELING ALUMINUM DIRECT CHILL CASTING

Uncertainty quantification is performed on the fully transient model of the industrial DC casting process of 50 cm diameter Al-4.5 wt.% Cu ingots. The effects of uncertainties in microstructural parameters, thermal boundary conditions, and material properties are examined. Probability density functions are calculated based on these input uncertainties for metrics that characterize the ingot macrosegregation (W^{Cu}) and steady state sump depth. In this analysis, the transient startup procedure described in section 2.4.1 is used. However, once the solid ingot height reaches 1.0 m the casting speed is ramped down at the same rate it was ramped up. Once the casting speed reaches 0.3 m/min, it is then set to zero so the remaining liquid is allowed to solidify. The process to achieve a full industrial sized ingot is shown in Figure 7.1(a). To reduce the computation time, only 50 cm of the steady state region was simulated and the ingot was lengthened by duplicating this region 3 times, shown schematically in Figure 7.1(a). The top and bottom of the final ingot are “cropped” and the outer surface “machined” before analyzing the predicted results as shown in Figure 7.1(b). Approximating industrial practice, the length removed from the top and bottom is one ingot radius and 0.05 m is removed from the outer surface.

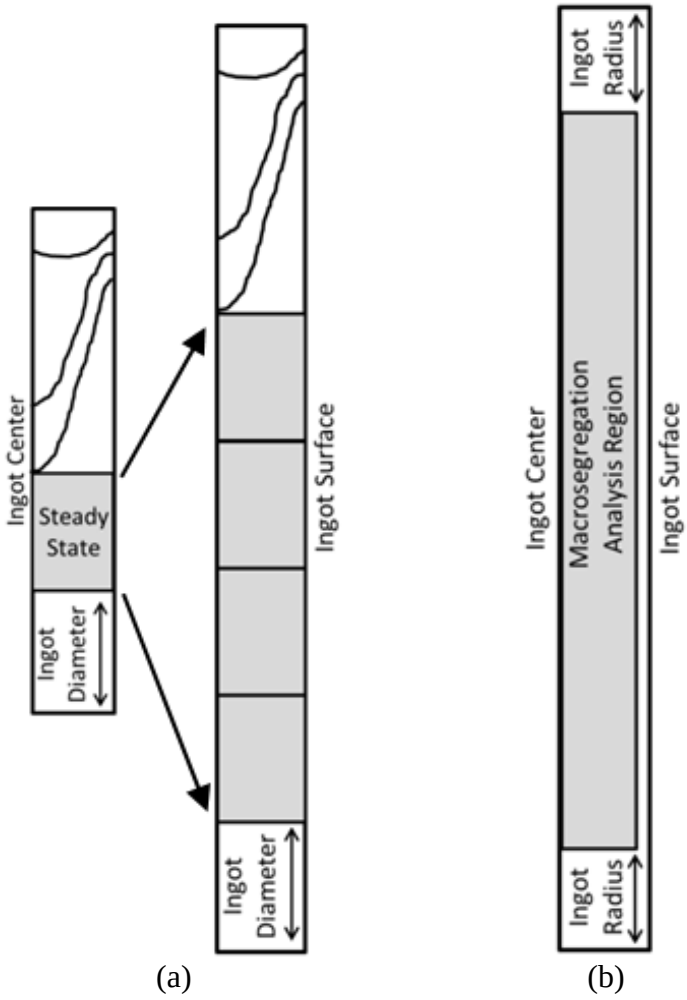

Figure 7.1: Schematic of the simulation domain showing (a) how the ingot was lengthened and (b) the area of the ingot analyzed for macrosegregation.

Before quantifying the uncertainty in the segregation and sump depth results, the controlling transport phenomenon are simulated to illustrate the behavior of a solidifying metal alloy. Then, the uncertainty in dendrite arm spacing, average free-floating particle diameter, thermal boundary conditions, packing fraction, and material property inputs are examined for their effect on model outputs.

7.1 Transport Phenomena Analysis

The composition field, sump profile, and flow field in the steady state region of the ingot for the standard case, using values in Table 2.1, are shown in Figure 7.2. The clockwise streamlines show a flow in the slurry (liquid and moving solid) region, driven by buoyancy forces and the density difference between solid and liquid. Solid nucleates in the slurry, is depleted in solute and is transported by the buoyancy driven flow cell. This motion has only a small effect on the mixture composition field because the solid and liquid move almost entirely together and so very little segregation occurs. The only relative motion of solid and liquid in the slurry occurs due to settling of the copper-poor particles, and at the centerline of the ingot the solid particles resist the upward velocity of the flow cell and collect there forming a depleted region. However, most of the redistribution of solute occurs in the rigid, and very low permeable mushy zone, where there is relative motion between the solid and liquid and shrinkage driven flow is the dominant transport mechanism. The free-floating solid particles that attach to the rigid mushy zone form an interconnected network that severely damps the buoyancy driven flow. The buoyancy driven flow in this region transports enriched liquid toward the center of the casting a small distance before becoming entrained in the mush by shrinkage

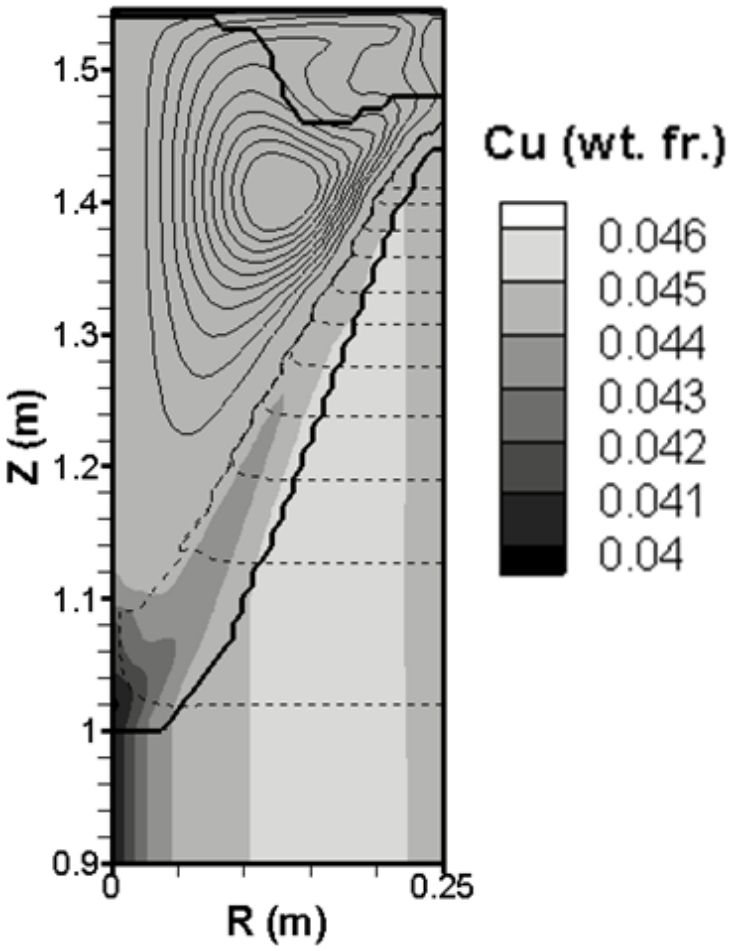

Figure 7.2: Contour plot of the Cu composition field, sump profile, and flow field during steady state. The bold solid lines indicate the extent of the mushy zone. The other lines flow streamlines. The solid lines are clockwise-rotating flow cell in the slurry with $0.1 < \rho\Psi < 1$ and $\Delta\rho\Psi=0.1$ kg/s. The dotted streamlines show the counter clockwise rotating flow in the rigid mushy zone with $-0.005 < \rho\Psi < -0.000005$ and $\Delta\rho\Psi=0.0004995$ kg/s.

driven flow. The shrinkage driven flow acts perpendicular to the advancing solidification front, transporting the enriched interdendritic liquid deep into the mushy zone from the center of the ingot outwards due to the “V” shaped steady state sump profile.

The steady-state transport phenomena described above form a solute-depleted area at the center of the ingot and a mid-radius that is slightly enriched. The depleted surface and subsurface regions are caused by another effect. The surface of the ingot is the first region to freeze and forms the rigid mushy zone. The direction of the shrinkage driven flow and subsequent surface enrichment is strongly dependent on the shape of the rigid mushy zone there. In this case the direction of the shrinkage driven flow does not have enough of a radial component to enrich the surface, by pulling in the liquid transported away by buoyancy forces. At the center of the casting, the enriched liquid is lost to the mid-radius due to shrinkage and is replaced by liquid from the slurry which is closer to the nominal composition. This exacerbates the depleted region at the center formed by settling solid particles and forms the slightly enriched region at the mid-radius.

7.2 Uncertainty in Dendrite Arm Spacing

The fluid flow in the rigid mushy zone is damped due to drag in the interconnected dendritic network and is modeled by the Blake-Kozeny permeability model. This model requires knowledge of the dendrite arm spacing, which is here assumed to be constant and uniform throughout the rigid mushy zone. The uncertainty of the dendrite arm spacing was assumed to be Gaussian, with a mean value (μ_λ) of 91 microns and a deviation (σ_λ) of 9.5 microns ($2\sigma_\lambda = 20\%\ \mu_\lambda$). The aleatoric uncertainties in the macrosegregation and sump depth predictions are examined first based solely on the

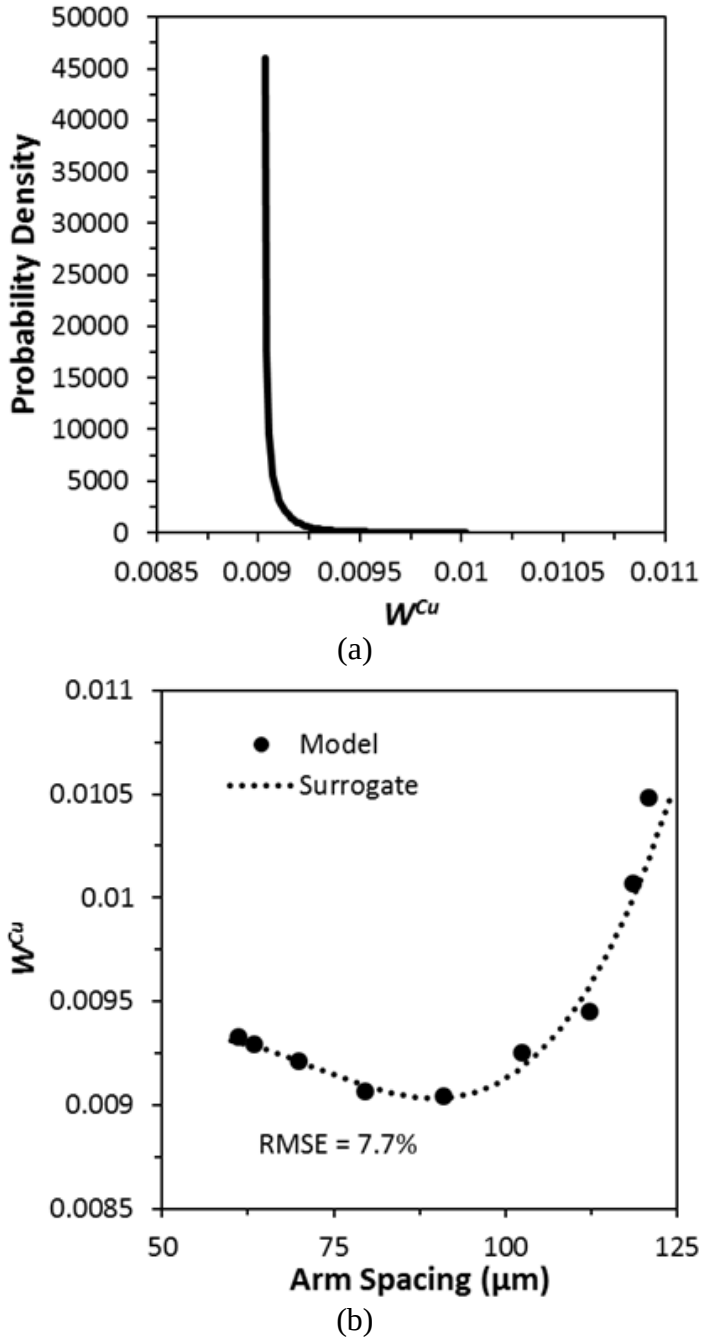

Figure 7.3: Macrosegregation level predictions showing (a) the resulting uncertainty in the model predictions based on the dendrite arm spacing uncertainty and (b) model predictions with the resulting 3rd order surrogate model overlaid.

arm spacing uncertainty. The PDF for macrosegregation is shown in Figure 7.3(a), which was calculated from the cubic polynomial surrogate model shown in Figure 7.3(b). The PDF that describes the model uncertainty is highly skewed with 95% of the possible values in the range $0.0090 < W^{Cu} < 0.0093$. This very narrow range of probable W^{Cu} values is due to the shape of the response surface shown in Figure 7.3(b). Only at high arm spacings, which have a low probability of occurring, does W^{Cu} have a higher value.

The skewed ouput PDF is due to the shape of the surrogate model of $W^{Cu} = f(\lambda)$, Figure 7.3(b), which can be explained using Figure 7.4, which shows the radial composition distribution during the steady state process for three values of arm spacing. The level of negative centerline segregation decreases with increasing length of dendrite arm spacing while, the positive mid-radius and subsurface segregation increases. The arm spacing does not affect the shrinkage driven flow, but does influence the amount of solute transported by buoyancy induced flow in the mushy zone. The buoyancy driven flow in the rigid mushy zone transports enriched solute toward the centerline and larger dendrite arm spacings allow the liquid to travel further before becoming entrained. This phenomenon increases the centerline and mid-radius segregation levels. Also, the subsurface becomes increasingly depleted as more solute is transported away from this region by buoyancy and replaced by liquid closer to the nominal from the slurry region. Although the composition at the centerline decreases with dendrite arm spacing, the overall macrosegregation level increases for large spacing because the mid-radius and subsurface regions occupy more volume than the center and so have more impact on W^{Cu}. Also, as the arm spacing initially increases from 61 to 91 microns the macrosegregation level decreases because the increase in the centerline and mid-radius is not large enough

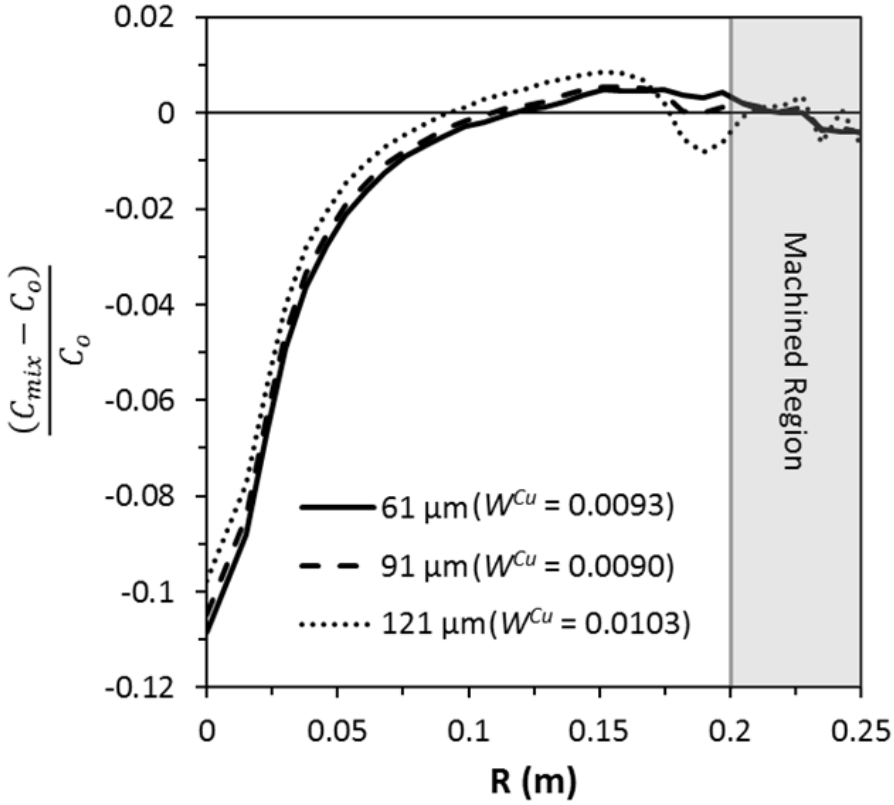

Figure 7.4: Normalized radial profile of the Cu segregation 1.0 m from the bottom block during the steady state process for 3 different dendrite arm spacing values.

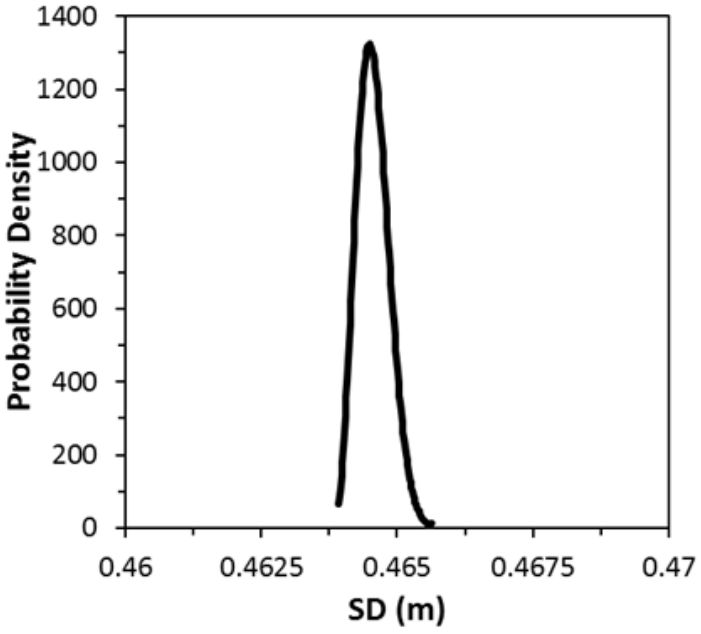

(a)

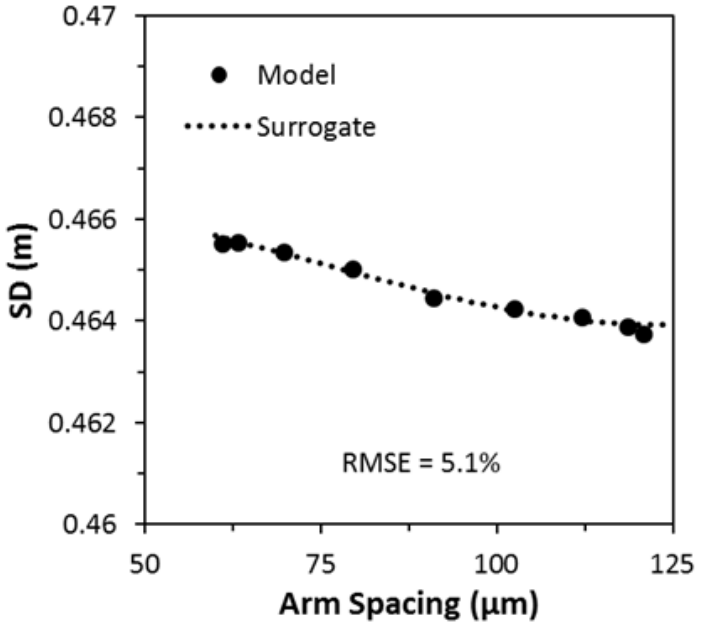

(b)

Figure 7.5: Sump depth predictions showing (a) the resulting uncertainty in the model predictions based on the dendrite arm spacing uncertainty and (b) model predictions with the resulting 3rd order surrogate model overlaid.

to offset the larger subsurface region being closer to the nominal composition. These results indicate that the arm spacing values, for the $g_{s,crit}$ value chosen, produce similar macrosegregation levels except for spacings greater than 112 microns.

The aleatoric uncertainty of the sump depth prediction is shown in Figure 7.5(a), the model predictions and 3rd order polynomial surrogate model fit is shown in Figure 7.5(b). The resulting PDF describing the model uncertainty of the sump depth predictions has a Gaussian distribution with a mean (μ_{SD}) of 0.465 m and a deviation (σ_{SD}) of 0.000293 m, which constitutes an uncertainty ($2\sigma_{SD}/\mu_{SD}$) of 0.13 %. While there is a slight decrease in the SD prediction as the arm spacing increases, the change is negligible and actually much less than the axial grid spacing (Δz = 1 cm). This result is not surprising as the sump depth is primary controlled by conduction heat transfer and the flow within the rigid mushy zone, which is controlled by the arm spacing, does not influence that depth.

7.3 Uncertainty in Equiaxed Particle Size

The relative velocity between the solid and liquid phases in the slurry region given by Stokes law (Equation (2.6)) is dependent on an average particle size. A normal distribution is assumed with a mean particle size of 30 microns and a deviation of 7.5 microns ($2\sigma_{d_{diam}}$ = 50% $\mu_{d_{diam}}$). A large uncertainty was assumed because there is really a distribution of particle sizes, depending on origins and paths of each particle. The aleatoric uncertainty of the macrosegregation predictions are shown in Figure 7.6 along with the model results and corresponding 2nd order surrogate model. The resulting PDF for W^{Cu} (Figure 7.6(a)) is slightly asymmetrical with a mean of 0.0091 and a deviation of

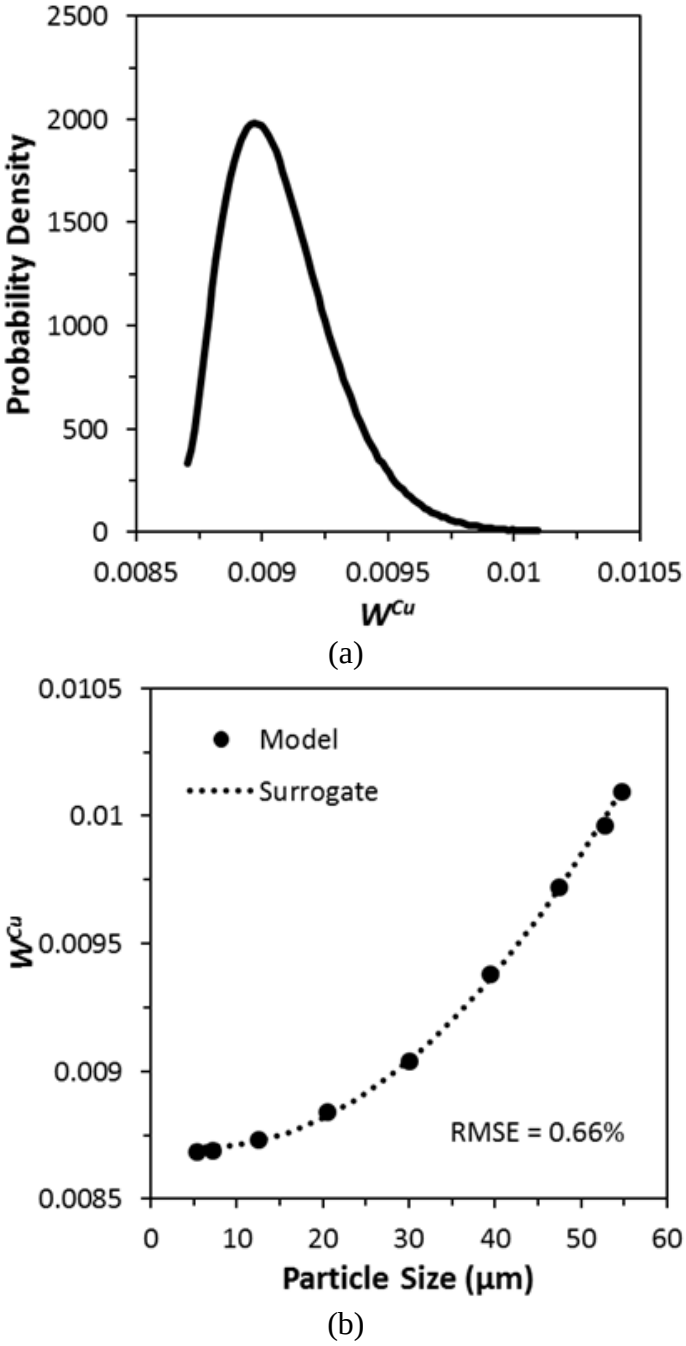

Figure 7.6: Macrosegregation level predictions showing (a) the resulting uncertainty in the model predictions based on the equiaxed particle size uncertainty and (b) model predictions with the resulting 2nd order surrogate model overlaid.

0.00022, which results in a model uncertainty ($2\sigma_{d_{diam}} / \mu_{d_{diam}}$) of 4.76%. The prediction of the macrosegregation level has a low level of uncertainty, given the uncertainty of the constant particle size, which provides confidence in the prediction capabilities of the model. The macrosegregation level increases quadratically with particle size, shown in Figure 7.6(b), so higher values of W^{Cu} are more possible than lower, explaining the asymmetric PDF. The steady state radial segregation profile for three particle sizes is shown in Figure 7.7. Increasing the particle size also increases the negative centerline segregation levels and also slightly increases the amount of positive segregation in the ingot. This is caused by the increasing likelihood of the particles to settle to the bottom of the slurry region as the particle size increases, because the settling velocity goes with the square of the particle size (Equation (2.6)). The nucleated equiaxed particles are depleted in solute and attach themselves to the rigid mushy zone near the centerline, increasing the negative centerline segregation. The increased level of solid transport toward the center also increases the local composition at the mid-radius and subsurface, so the overall macrosegregation level increases with the particle size. Similarly to the dendrite arm spacing, the uncertainty in the particle size did not affect the prediction of the sump depth with a model uncertainty ($2\sigma_{SD} / \mu_{SD}$) of 0.034%. Therefore, predictions of macrosegregation levels and sump depths are not sensitive to the choice of exact value of particle size in the range studied here.

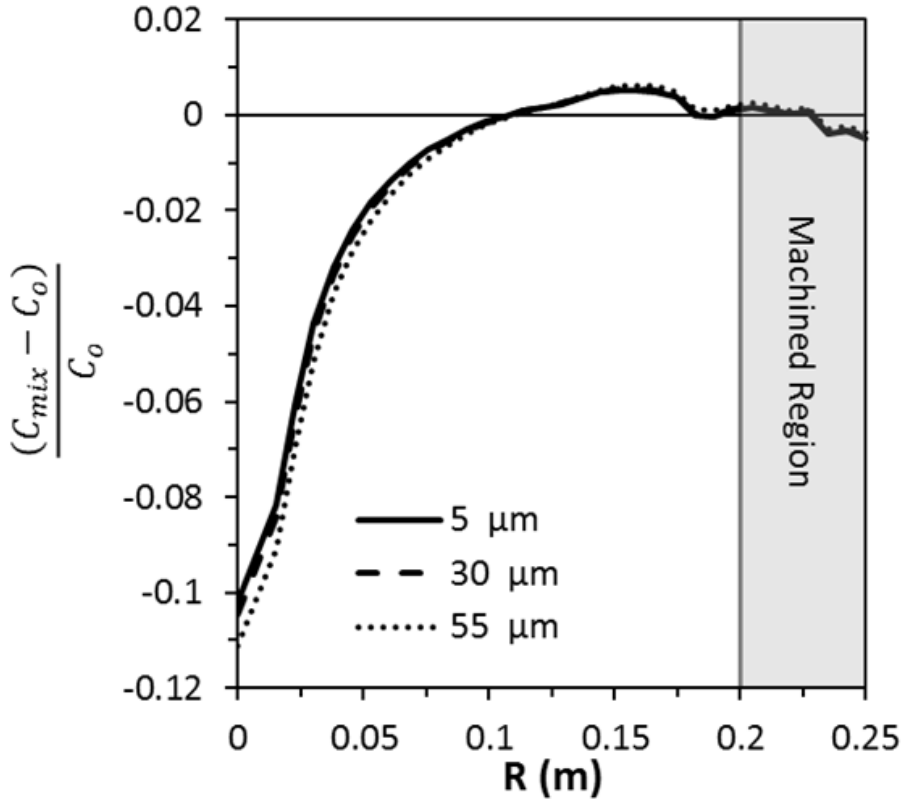

Figure 7.7: Normalized radial profile of the Cu segregation 1.0 m from the bottom block during the steady state process for 3 different particle sizes.

7.4 Uncertainty in Heat Transfer Coefficient

Actual thermal boundary conditions for DC casting are complex and depend on a number of different factors, such as the mold materials and geometry, water jet configuration of the impinging jets coming off the mold, the water flow rate, water temperature, and surface temperature of the ingot, to name a few. The thermal boundary conditions used in this analysis are an empirical fit to published experiments, with which there is inevitably some uncertainty [65]. This measurement uncertainty was not reported with the data in the original reference and so the uncertainty in the thermal boundary conditions could only be estimated. This estimation was done by applying a constant factor to the local heat transfer coefficient after the proper calculation from the correlation was performed. In other words, the heat transfer coefficients calculated in the mold region, falling water region, and bottom block were multiplied by the same constant factor to mimic uncertainty on the thermal boundary condition. A normal distribution for the heat transfer uncertainty factor was assumed, with a mean value (μ_h) of 1 and a deviation (σ_h) of 0.15. The aleatoric uncertainty in the model prediction of the macrosegregation is shown in Figure 7.8(a) and the model predictions and corresponding linear surrogate model is shown in Figure 7.8(b). The resulting PDF is a normal distribution with a mean macrosegregation level of 0.0091 and a deviation of 0.00013 ($2\sigma_{W^{Cu}}$ = 2.83% $\mu_{W^{Cu}}$). This level of model uncertainty is very low given the range of uncertainty in the thermal boundary condition. The main difference in the composition field occurs near the surface of the ingot (Figure 7.9), and the rest of the profile is the same. The region near the surface experiences the largest immediate effect from the thermal boundary conditions, which controls the strength of the shrinkage driven flow.

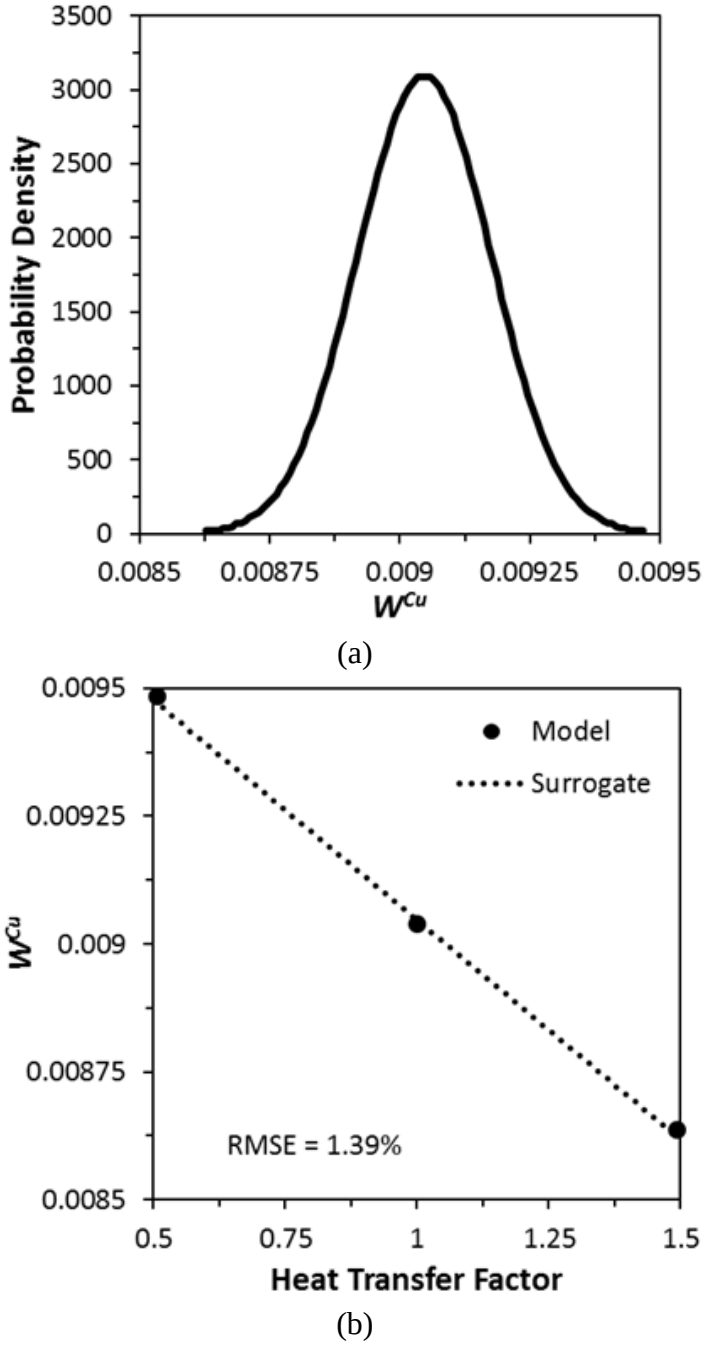

Figure 7.8: Macrosegregation level predictions showing (a) the resulting uncertainty in the model predictions based on the heat transfer coefficient uncertainty and (b) model predictions with the resulting 1st order surrogate model overlaid.

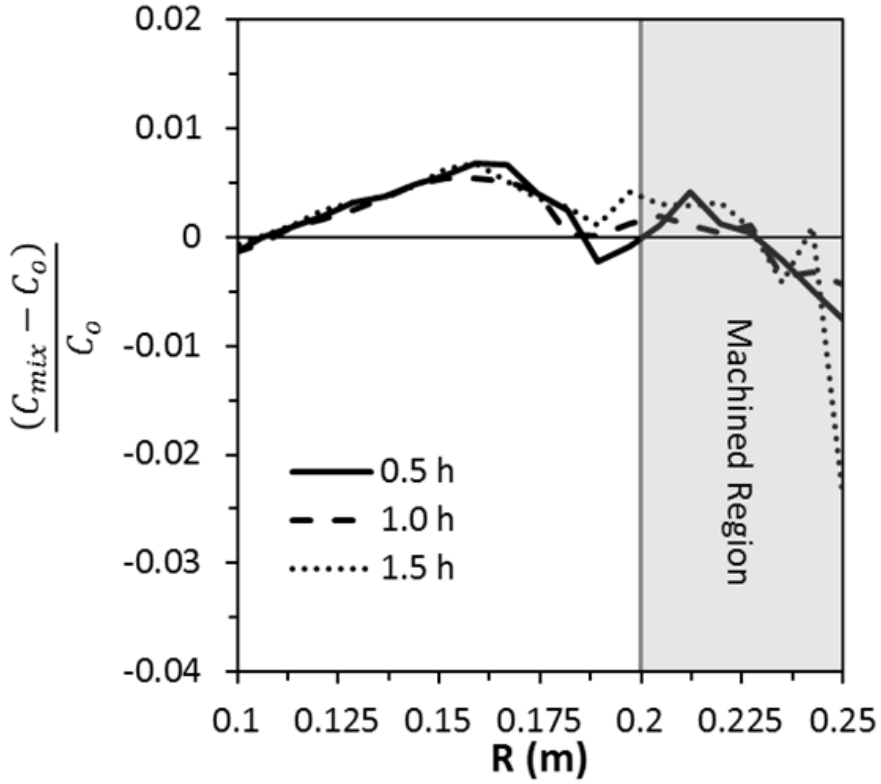

Figure 7.9: Normalized radial profile of the Cu segregation 1.0 m from the bottom block during the steady state process for 3 different heat transfer coefficient factors.

The difference in this flow strength causes the difference in the composition profile.

The aleatoric uncertainty in the sump depth prediction is shown in Figure 7.10(a) and the model predictions and the 3rd order surrogate model fit is shown in Figure 7.10(b). The resulting PDF is slightly skewed to higher depths with an average 0.465 m and a deviation of 0.00461 m ($2\sigma_{SD} < 2\%\ \mu_{SD}$). The skewed nature of the PDF is due to the slightly lower slope of the surrogate model for higher heat transfer coefficients. The uncertainty in the model prediction is still not very significant given the large uncertainty in the heat transfer factor. This result is at first surprising, as the sump depth is controlled by a balance of casting velocity and radial heat transfer. However, the thermal resistance due to the free falling water is rather small, and the Biot number (hR/k) for the ingot ranges from order 10 to 1,000 for the standard case. The radial heat transfer is always limited by conduction heat transport to the surface, so that the heat transfer coefficient has only a secondary effect. Even with a heat transfer factor of 0.5, the Biot number is still much greater than 1. Therefore, given the range of heat transfer factors used only a small change in the sump depth results. Additionally, as the heat transfer coefficient increases its effect on predicting SD decreases because the radial heat transfer is increasingly limited by conduction to the surface.

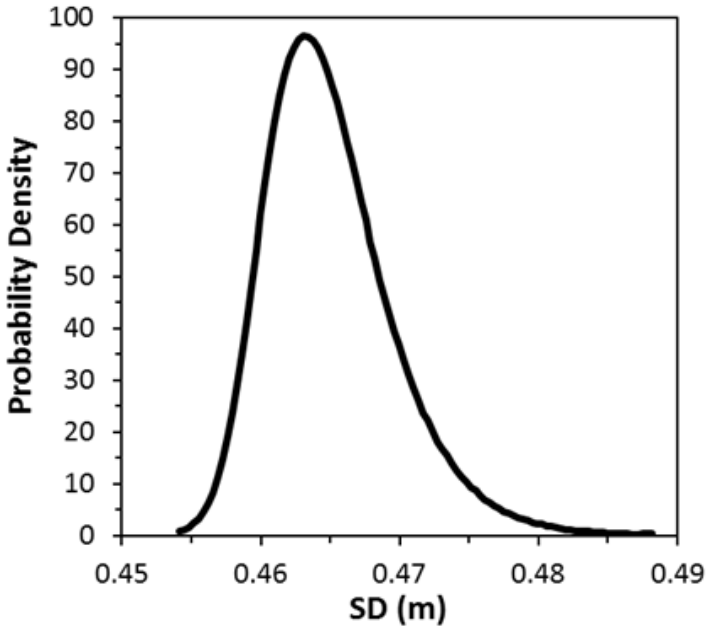

(a)

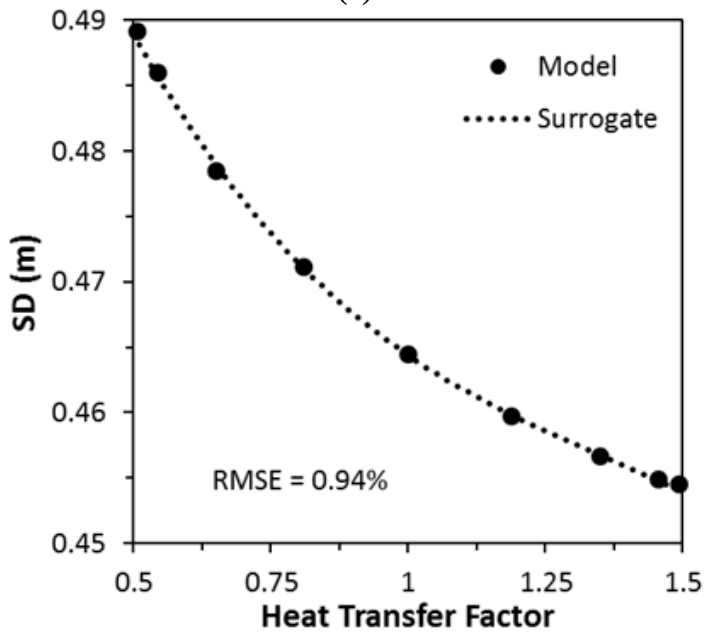

(b)

Figure 7.10: Sump depth predictions showing (a) the resulting uncertainty in the model predictions based on the heat transfer coefficient uncertainty and (b) model predictions with the resulting 3rd order surrogate model overlaid.

7.5 Uncertainty in Equiaxed Packing Fraction

The constant critical packing fraction, $g_{s,crit}$, determines the condition under which the solid in a given control volume coalesces as part of the neighboring rigid mushy zone. This input parameter is difficult to measure and is dependent on the amount of grain refiner and local alloy composition, cooling rate, and velocity field. For DC casting, this parameter is not well known and has the possibility of varying across the radius of an ingot. However, in a study performed by Vreeman et al. comparing model predictions to an industrial experiment for an Al-Cu alloy, $g_{s,crit}$ was estimated to be less than 0.3 [7]. In the present study, a uniform probability distribution for $g_{s,crit}$ is assumed, given the lack of data for this parameter, meaning no one value is more likely than any other, with a minimum of 0.05 and a maximum of 0.30. The resulting aleatoric uncertainty of the model predictions for the macrosegregation found from a linear surrogate model is shown in Figure 7.11(a). The linear form of the response surface (Figure 7.11(b)) and the uniform PDF of $g_{s,crit}$ gives a uniform PDF for W^{Cu}, with a minimum of 0.0077 and a maximum of 0.011. The entire PDF is within ±19% of the average W^{Cu} value, a much larger uncertainty than for the other parameters, indicating that more information is needed about the packing of equiaxed particles in DC casting to produce a more confident prediction of macrosegregation levels.

The chosen $g_{s,crit}$ value indirectly impacts the permeability and flow in the rigid mushy zone by determining its onset and the settling of equiaxed particles. Figure 7.12 shows the radial segregation profile for the three $g_{s,crit}$ values. Low values of $g_{s,crit}$ cause the rigid mushy zone to form when the permeability is large enough to allow significant buoyancy driven flow, flow transporting enriched liquid toward the centerline of the

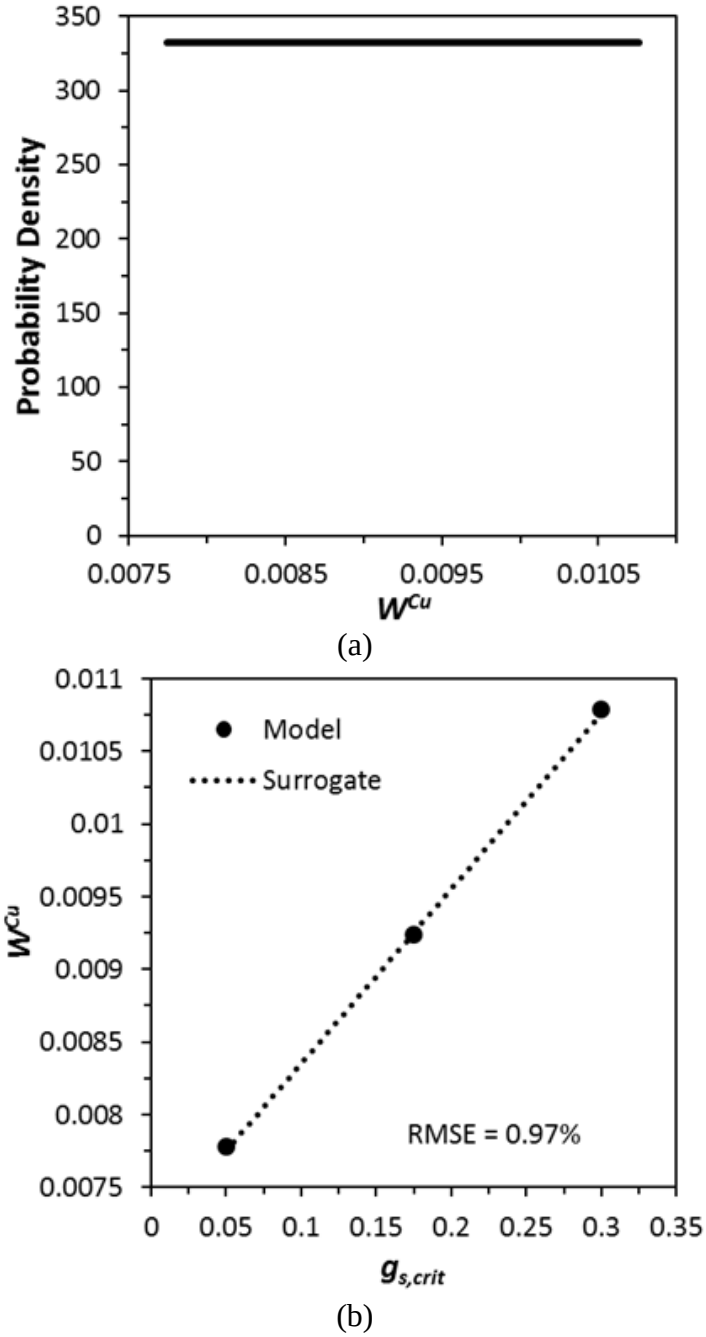

Figure 7.11: Macrosegregation level predictions showing (a) the resulting uncertainty in the model predictions based on the packing fraction uncertainty and (b) model predictions with the resulting 1st order surrogate model overlaid.

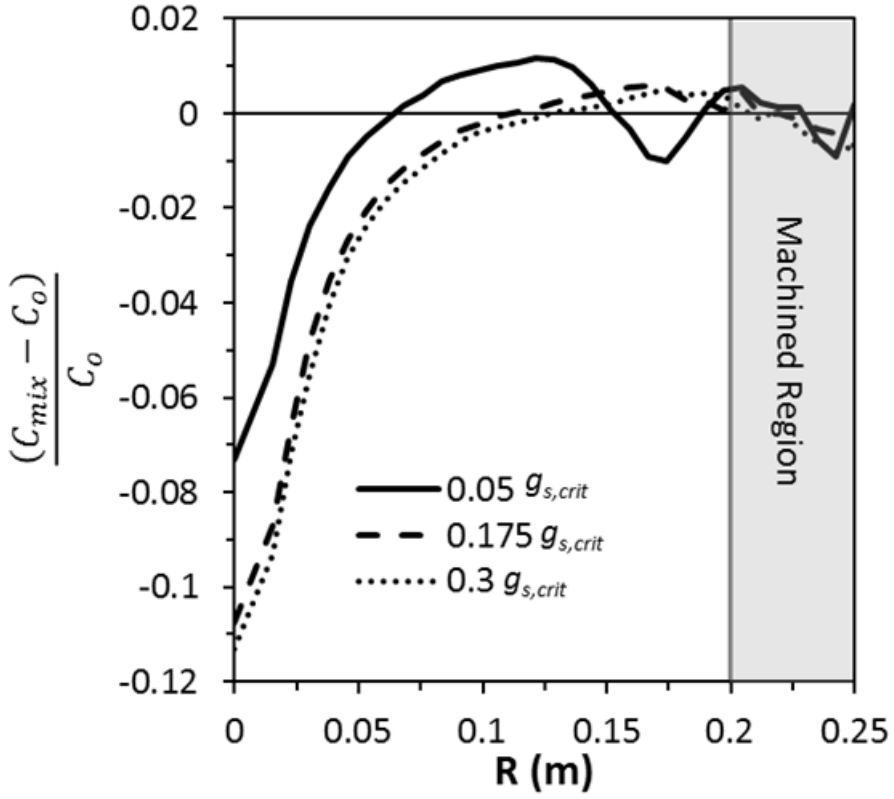

Figure 7.12: Normalized radial profile of the Cu segregation 1.0 m from the bottom block during the steady state process for 3 different packing fractions.

ingot. This phenomenon causes the 0.05 $g_{s,crit}$ case to have less negative centerline segregation and more positive segregation at the mid-radius. The early onset of the rigid mushy zone for this case also causes the surface of the ingot to be enriched due to the direction of the shrinkage driven flow in this region, which has a larger radial component than the other two cases due to the early formation of the rigid mushy zone. The surface of the ingot experiences the fastest cooling rates, which does not allow enough time for the buoyancy driven flow to transport enriched liquid away before becoming entrained by the shrinkage driven flow. This flow enriches the surface, depleting the adjacent subsurface region. These surface and subsurface regions are machined, but still influence W^{Cu}; because some of the enriched liquid, transported from the depleted subsurface, is also transported toward the center of the ingot, which further depletes the subsurface region and forms a neighboring enriched region, which is part of the unmachined portion of the ingot. Further from the ingot surface the heat extraction rate is less severe and causes a change in the slope of the sump, which subsequently alters the direction of the shrinkage driven flow. The sump becomes slightly steeper, which adds more of a radial component to the shrinkage-driven flow, contributing to the large depleted region that forms near r = 0.175 m. The radial segregation profile becomes less complicated near the surface and subsurface of the ingot for $g_{s,crit}$ values of 0.175 and 0.30 (Figure 7.12). For these cases, the rigid mushy zone forms with fraction solid values large enough to relegate the buoyancy-driven flow to a secondary effect on macrosegregation. The restriction of the buoyancy-driven flow in the rigid mushy zone is responsible for the increase in macrosegregation level with increasing $g_{s,crit}$.

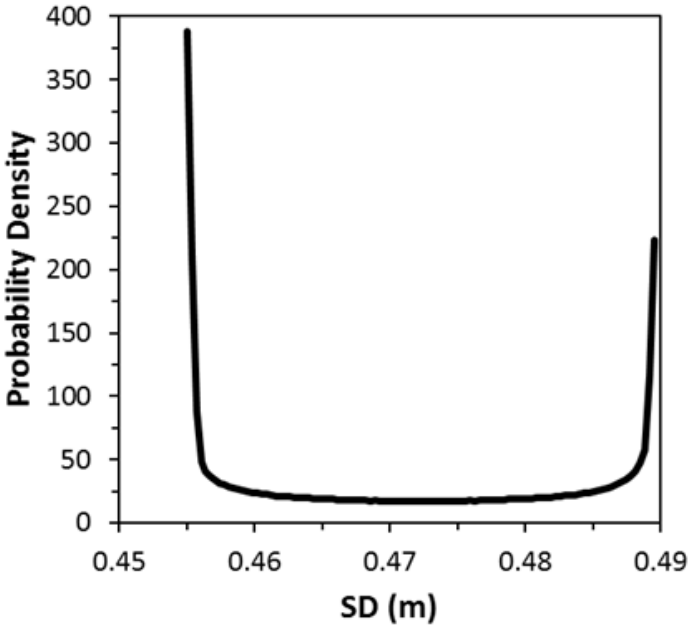

(a)

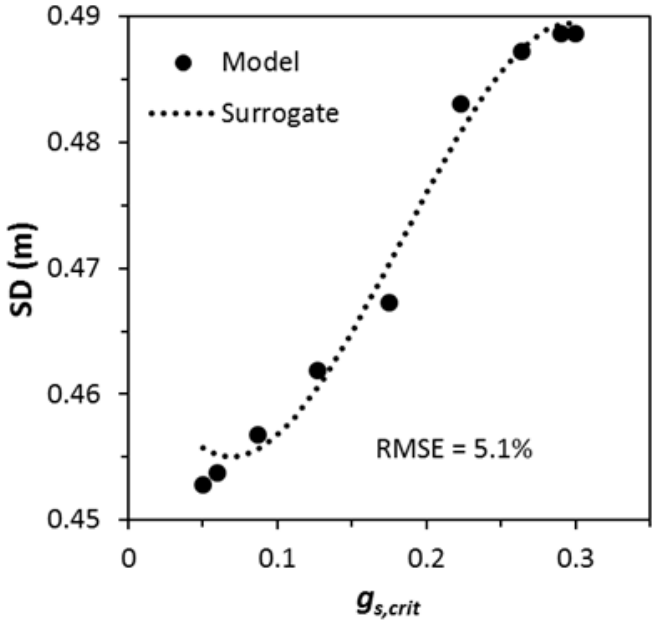

(b)

Figure 7.13: Sump depth predictions showing (a) the resulting uncertainty in the model predictions based on the packing fraction uncertainty and (b) model predictions with the resulting 3rd order surrogate model overlaid.

The aleatoric uncertainty in the sump depth prediction is shown in Figure 7.13(a) and the model predictions and the 3rd order response surface fit is shown in Figure 7.13(b). The resulting SD PDF created from sampling the surrogate is irregular with two large increases in probability for sump depths of 0.490 m and 0.455 m. These large probabilities are due to the change in slope of the surrogate model near these regions and the uniform distribution of the uncertainty in $g_{s,crit}$. The fit of the surrogate model is better for large $g_{s,crit}$ values and deeper sumps than at the low end of the curve. As $g_{s,crit}$ is decreased, the slope of the cubic polynomial goes to zero and then negative, while the data from model predictions show a continuously positive slope. A better fit in this range would entirely eliminate the spike in probabilities at low SD values. This example serves as a warning to carefully inspect the response surface to ensure such anomalies in the output PDF do not occur. Such an inspection suggests that the predicted high probability of low SD should be ignored and is not a result of the physics of the process. Nonetheless the uncertainty in the macrosegregation predictions is more significant than the uncertainty in the sump depth predictions given the level of uncertainty in $g_{s,crit}$.

7.6 Uncertainty in Material Properties

The probability distributions for the material property values were assumed to be Gaussian with the nominal reported values as the mean (Table 2.1) and a specified standard deviation. Two uncertainty levels, in which 95% (2σ) of the distributions were within 5% (Case D2) or 10% (Case D1) of the mean, were studied (Table 7.1). A level 1 Smolyak analysis was performed on both cases to examine which properties most affect the outputs of interest. Higher Smolyak level analyses, with more fidelity in the response

surface at the expense of more calculations per input parameter, were then performed using this smaller set of uncertain inputs if a better fitting surrogate was acheived. To avoid the solid and liquid densities from having overlapping uncertainty distributions, the liquid density is set based on ρ_s and $\Delta\rho$ (= $\rho_s - \rho_l$).

Table 7.1: Uncertainty of material property inputs.

Property	**Case A ($2\sigma = \pm 10\%\mu$)**	**Case B ($2\sigma = \pm 5\%\mu$)**
ρ_s [kg/m^3]	275	137.5
$\Delta\rho$ [kg/m^3]	29	14.5
k [W/m K]	13.75	6.875
C_p [J/kg K]	100.6	50.3
L_f [J/kg]	39,000	19,500
$\beta_{T,s}$ [1/K]	$2.25\text{x}10^{-6}$	$1.125\text{x}10^{-6}$
$\beta_{T,l}$ [1/K]	$1.175\text{x}10^{-5}$	$5.85\text{x}10^{-6}$
$\beta_{S,s}$	0.087	0.0435
$\beta_{S,l}$	0.073	0.0365

A level 1 Smolyak analysis was performed for Cases D1 and D2 to compare the sensitivities of the outputs of interest to changes in material property values and their uncertainty level. The sensitivity results for Case D1 are shown in Figure 7.14, in which the height of each bar is μ^* and the error bars are $\pm 2\sigma^*$. For SD and W^{Cu}, the relative sensitivities to the inputs are similar for Cases A and B, so the sensitivities for only Case D1 are shown. The sump depth was most affected by k, ρ_s, and L_f. The Stefan number (St = $c(T_{liq} - T_{sol})/L_f$) for this alloy varies between 0.23 and 0.16 based on the uncertainty of the inputs, showing that the latent heat release over the freezing range for the nominal composition is always much more than the sensible heat removal necessary to drop the temperature from T_{liq} to T_{sol}. Consequently, the overall heat removal during solidification is a stronger function of L_f than c. The rates of release and advection of latent heat are

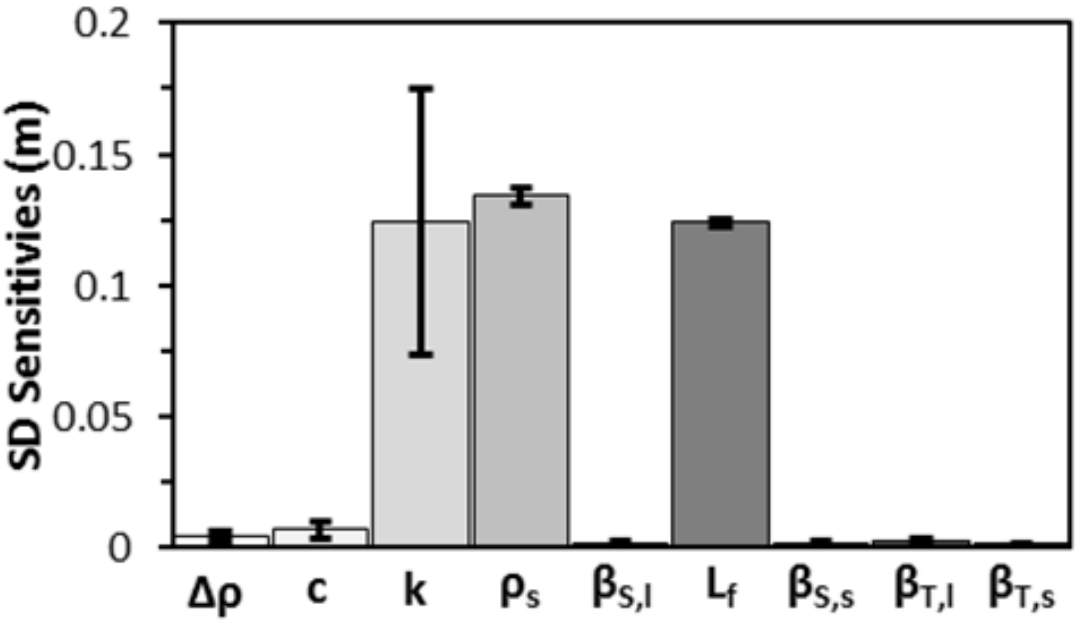

(a)

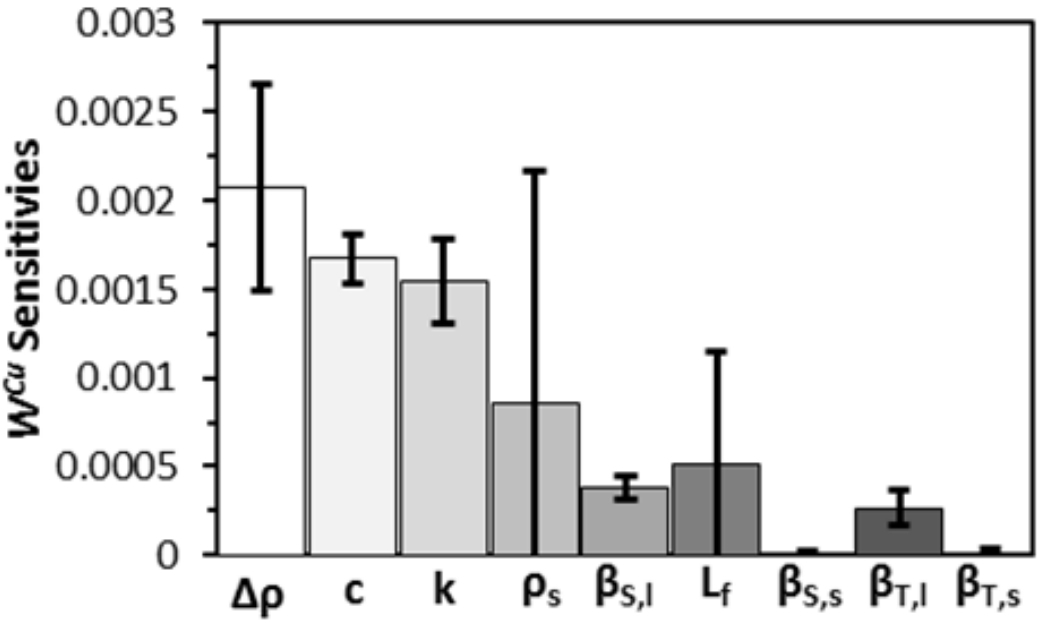

(b)

Figure 7.14: Plots of the sensitivities of the output quantities of interest to the uncertain inputs for Case D1: (a) sump depth (b) macrosegregation level.

also dictated by the density, which contributes to the importance of L_f in determining SD. The high sensitivity of SD on k is because the formation of the sump is a conduction-dominated heat transfer problem, the resistance of which is inversely proportional to thermal conductivity.

For the macrosegregation metric, W^{Cu}, the most influential material properties are $\Delta\rho$, c, k, and ρ_s for both levels of uncertainty. The solid solutal and thermal buoyancy terms had a negligible effect on W in both Case D1 and D2, while the liquid thermal and solutal expansion coefficients ($\beta_{T,l}$ and $\beta_{S,l}$) had the same mean effect as L_f, but with less variability. The solid buoyancy terms have less effect on W^{Cu} because they have no influence on the buoyancy-driven flow in the rigid mushy zone, where W^{Cu} is affected by this flow. The most influential material property on W^{Cu} is $\Delta\rho$, which is a large factor (along with the solidification rate) in determining the strength of the shrinkage-driven flow. This parameter is also a factor in Stokes Law, governing the settling of solid particles. The solidification rate depends on how quickly heat can be removed from the mushy zone and how much latent heat is released during solidification. Therefore, c, k, and ρ_s (which make up the thermal diffusivity) also have a significant impact on W^{Cu}.

The corresponding probability distributions for each output of interest are shown in Figure 7.15. The mean predicted values of SD and W^{Cu} are 0.469 m and 0.0090, respectively, for Case D1 and 0.466 m and 0.0090 for Case D2. The smaller input uncertainty in Case D2 caused more certain outputs while the mean value was not altered. In order to predict the SD within 14% of the mean ($2\sigma/\mu$), k, ρ_s, and L_f of the Al-4.5 wt.% Cu alloy must be known better than 10% of their measured values because SD is most

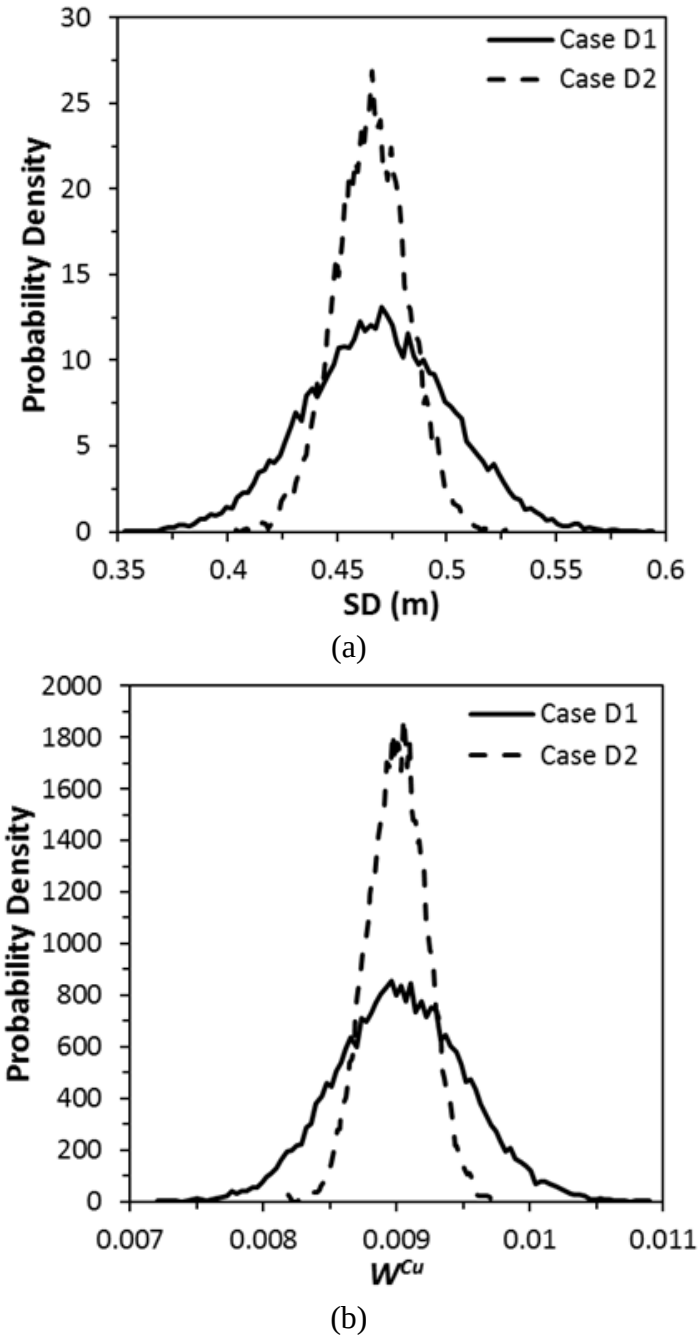

Figure 7.15: Probability distribution functions of the model outputs for Cases D1 and D2: (a) sump depth (b) macrosegregation level.

sensitive to them. For the prediction of W^{Cu} to be known within 10% of the mean value, $\Delta\rho$, c, k, and ρ_s must be known with more than 10% certainty.

7.7 Model Uncertainty: Combined Effects

The combined aleatoric uncertainty of all the model input parameters previously discussed were examined, in which the input uncertainty level in Case D1 ($2\sigma = 10\%\ \mu$) was used for the material properties. The sensitivities of the output parameters for a level 1 Smolyak analysis are shown in Figure 7.16. The sump depth prediction is most sensitive to ρ_s, k, L_f, $g_{s,crit}$, and h (heat transfer factor), while the other parameters have little to no comparative effect. The three most important material properties (ρ_s, k, and L_f) control the heat release and limited internal heat transport in the casting. The other two important parameters ($g_{s,crit}$ and h) have a secondary effect on the SD and control the formation of the rigid mush and surface heat transfer. The five most influential parameters for determining the sump depth were used to quantify the combined uncertainty of the sump depth prediction. For the macrosegregation prediction, the most important model parameters are $g_{s,crit}$, $\Delta\rho$, c, k, d_{diam}, and λ. These six parameters were used to determine the combined model uncertainty for W^{Cu} and the other input parameters were neglected. The most influential model parameter for predicting the macrosegregation level is $g_{s,crit}$, which largely determines the permeability of the rigid mush and therefore the dominant flow mechanism. The next most important parameter is $\Delta\rho$, which plays a crucial role in determining the amount of shrinkage-driven flow and settling of solid particles. This analysis shows that the flow in the rigid mushy zone is the most important factor in predicting the macrosegregation level.

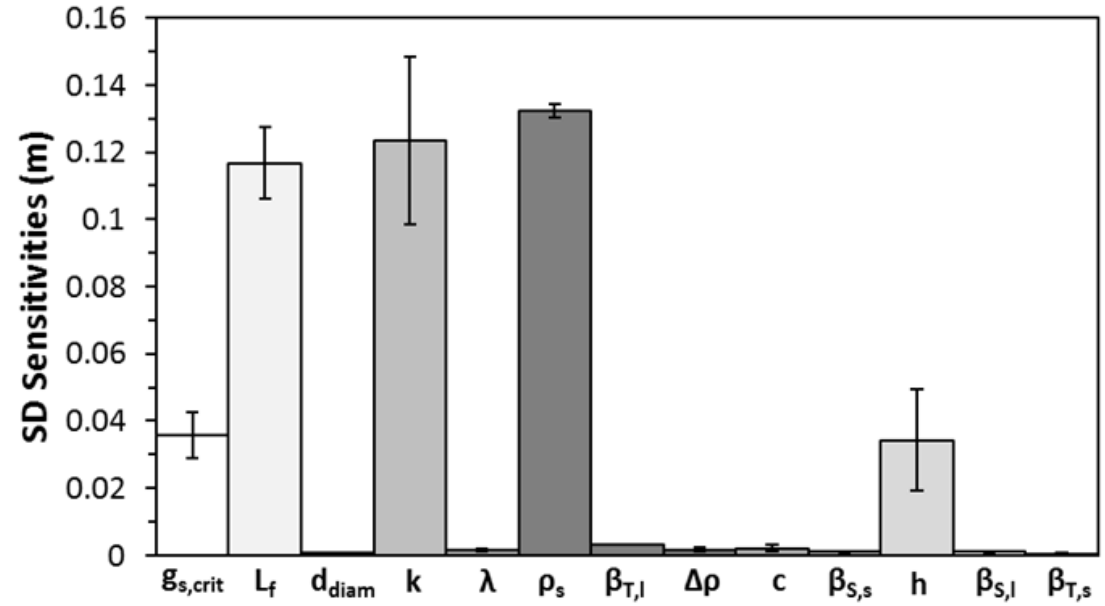

(a)

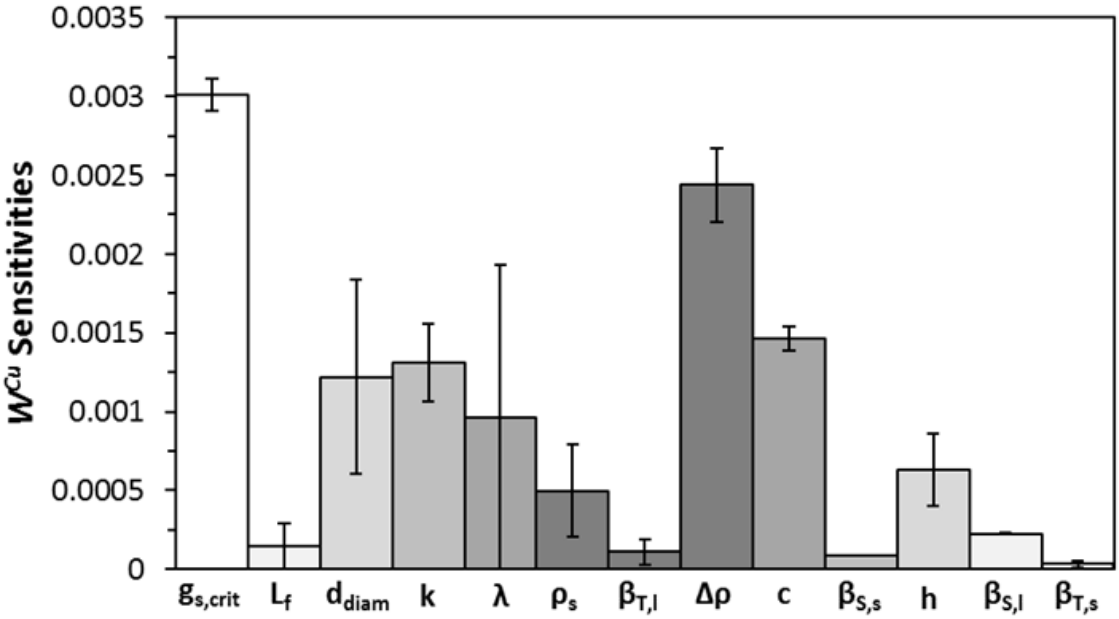

(b)

Figure 7.16: Plots of the sensitivities of the output quantities of interest, (a) sump depth and (b) macrosegregation level, for the combined uncertain inputs.

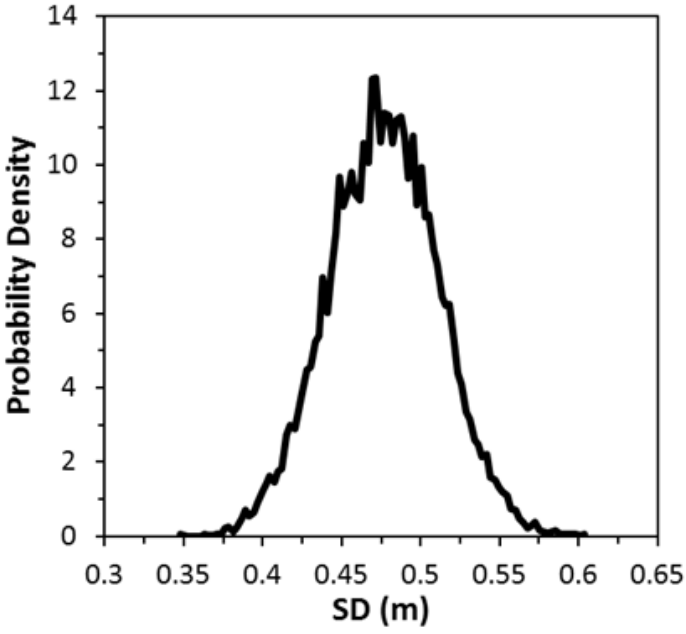

(a)

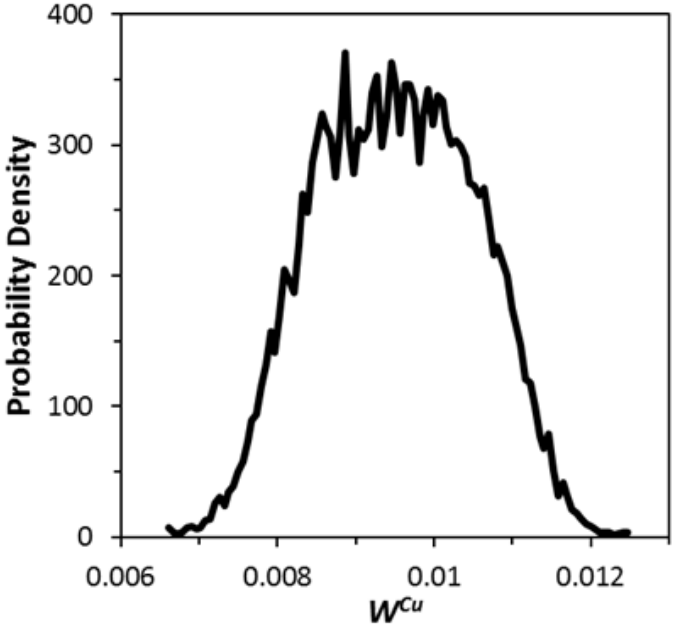

(b)

Figure 7.17: Probability distribution functions of the model outputs, (a) sump depth (b) macrosegregation level, for the combined uncertain inputs.

The aleatoric model uncertainty for the two outputs of interest, determined from the most influential inputs, is shown in Figure 7.17. For the prediction of the sump depth, the resulting PDF calculated from sampling the 1st order surrogate model has a mean of0.477 m with a deviation of 0.035 m ($2\sigma_{SD}/\mu_{SD}$ = 14.5%). The PDF for the macrosegregation level predictions was also calculated from a 1st order surrogate model and has a mean of 0.0095 and deviation of 0.0010 ($2\sigma_{W^{Cu}} / \mu_{W^{Cu}}$ = 21.2%). The most important difference between these two results is the wider PDF for W^{Cu} which has a blunter peak than SD. These differences are due to stronger influence of $g_{s,crit}$ with its uniform input PDF, on the macrosegregation prediction.

The predicted sump depth and macrosegregation have high levels of uncertainty and are influenced by different inputs whose uncertainties need to be reduced. In predicting the sump depth, the uncertainty ($2\sigma/\mu$) in L_f, k, and ρ_s should be limited to 5% if possible. Also, using an empirical relationship for the heat transfer boundary condition is sufficient for these predictions, because the radial heat transfer is more limited by transport to the ingot surface than from the surface to the ambient. The large uncertainty of the rigid mushy zone packing fraction has a secondary effect on predicting the sump depth and largest influence on W^{Cu}, which can be reduced with further experimentation. The uncertainty in material property values that have a large effect on the W^{Cu} prediction should also be limited to 5%. However, the two microstructural parameters that are important in predicting macrosegregation (d_{diam} and λ) have uncertainty levels based on distributions of sizes that exist naturally in a casting. The current model assumes these parameters to be constant and uniform, and does not consider their spatial variations. Therefore, the contribution of model uncertainty from these two parameters cannot be

reduced with further experimentation without first incorporating more physics into the model.

7.8 Conclusions

The PRISM Uncertainty Quantification (PUQ) framework has been used to quantify the aleatoric uncertainty of the sump depth and macrosegregation of an Al-4.5 wt. % alloy predicted by a fully transient numerical model for DC casting. The input parameters to which uncertainty was assigned were the dendrite arm spacing, equiaxed particle size, heat transfer coefficients, rigid mushy zone packing fraction, and several thermophysical properties. The macrosegregation prediction was strongly influenced by flow in the rigid mushy zone and settling of equiaxed particles and is therefore sensitive to uncertainties in packing fraction, particle size, dendrite arm spacing and solid-liquid density difference. The thermal conductivity and specific heat are also important in predicting W^{Cu}. The sump depth prediction is primarily dependent on heat release during solidification and internal heat transfer which are controlled by solid density, thermal conductivity and latent heat. Secondary contributions to uncertainty in SD predictions are caused by the packing fraction and heat transfer coefficient. The empirical correlation used for the thermal boundary conditions is sufficient because the radial heat transfer mechanism is always limited by heat conduction to the surface. In order to reduce the output uncertainty to reasonable levels (less than 10%), the most sensitive material properties must be known within 5% of the mean values. However, the uncertainty from the microstructural parameters cannot be reduced until they can be considered in the

numerical model as a distribution of sizes (as they exist in reality), instead of a uniform and constant parameter.

CHAPTER 8. SUMMARY AND RECOMMENDATIONS FOR FUTURE WORK

8.1 Summary

This work examined the transport phenomena leading to macrosegregation during direct chill casting and static casting of aluminum alloys using numerical models. Various DC casting parameters were varied to examine their effect on the process. Additionally, the uncertainty in the model predictions was quantified based on uncertain model inputs.

For DC casting, transport phenomena during start up through steady state were analyzed using the normalized Weibull deviation (W^i) as a macrosegregation metric. It was shown that the packing of the rigid mushy zone was dependent on the grid size and that locally refinement produced compositional streaks. Because of this numerical artifact, a coarse uniform grid size was used. At each axial position W^i was calculated to determine the point at which the process achieved compositional steady state (Z_{ss}). The effect of ingot diameter, casting velocity, superheat, and cooling water flow rate were studied. Over the ranges examined, the casting superheat and cooling water flow rate had little effect on the process. Increasing the ingot diameter, from 50 to 70 cm, caused a significant increase in Z_{ss}, however the ratio of Z_{ss} with the ingot diameter was constant. The depth of the sump increased linearly with the casting velocity; however the macrosegregation level had a larger increase when the casting velocity was raided from

30 to 60 mm/min than from 60 to 90 mm/min. This was attributed to the significant changes in the sump shape when the casting speed increased from 30 to 60 mm/min, while the sump shape was similar for casting velocities of 60 and 90 mm/min. Additionally, Z_{ss} increased when the casting speed grew from 30 to 60 mm/min and remained the same for casting speeds of 60 and 90 mm/min.

The DC casting model was then used to investigate the effect of two methods commonly used to reduce internal stresses on the sump formation and macrosegregation level. The methods were adding a layer of pure aluminum to the bottom block to dilute the initial composition and reduce the freezing range of the alloy during start-up. Additions of pure Al to the bottom block did not influence the steady state process, but did increase Z_{ss}. Placing a wiper close to the mold causes the surface of the ingot to remelt, which makes the casting susceptible to bleed outs. This is because the Biot number (hR/k) transitions from being much greater than one above the wiper to much less than one below the wiper.

As a step towards understanding the effect of uncertain inputs on solidification process modeling, uncertainty quantification (UQ) and sensitivity analysis are performed on a transient model of solidification of Al-4.5wt.%Cu in a rectangular cavity for columnar solidification. The inputs that were assigned uncertainties were microstructural parameters, heat transfer coefficient, and select material properties. Additionally, for columnar solidification three different permeability models were studied in which the choice of permeability model strongly influenced the resulting macrosegregation as it determines the strength of the flow in the mushy zone. Also when considering columnar solidification, the uncertainty in the heat transfer coefficient ($2\sigma_h/\mu_h$) should be less than

10% when prediction macrosegregation and in a narrower range for predicting the solidification time. The most important material properties for predicting macrosegregation were ρ_s, $\Delta\rho$, L_f, and $\beta_{S,l}$ while for the solidification time they were ρ_s, k, c, and L_f. The most influential input parameter on the prediction of macrosegregation was the dendrite arm spacing, which had no effect on the calculation of the solidification time; in which the most important input was the heat transfer coefficient.

When the model used to examine uncertainty in columnar solidification was extended to equiaxed solidification, additional input parameters were introduced such as the rigid mushy zone packing fraction, equiaxed particle size, and buoyancy contributions from the solid particles. The size of particles were not large enough, over the range analyzed, to cause significant settling. Therefore the diameter of equiaxed particles had little effect on the macrosegregation predictions compared to other input parameters. The material properties that were shown to have the most influence on W^{Cu} and whose uncertainties should first be reduced are ρ_s, $\Delta\rho$, k, c, L_f, and $\beta_{S,l}$. Similarly, the most prominent material properties to V_{spec} were ρ_s, $\Delta\rho$, k, c, and L_f. However, the most influential input parameter on the prediction of macrosegregation uncertainty was the dendrite arm spacing.

Lastly, the PRISM Uncertainty Quantification (PUQ) framework was used to quantify the aleatoric uncertainty of predictions by a fully transient numerical model for DC casting of an Al-4.5 wt.% alloy. The outputs of interest are the sump depth and macrosegregation level and the input parameters to which uncertainty was assigned were the dendrite arm spacing, equiaxed particle size, heat transfer coefficients, rigid mushy zone packing fraction, and several thermophysical properties. The prediction of

macrosegregation was sensitive to the packing fraction, particle size, dendrite arm spacing, and solid-liquid density difference, which indicates the prediction was strongly influenced by flow in the rigid mushy zone and settling of equiaxed particles. The sump depth prediction is primarily dependent on heat release during solidification and internal heat transfer which are controlled by solid density, thermal conductivity and latent heat. Based on the analysis of the uncertain heat transfer coefficient, it was concluded that the empirical correlation used for the thermal boundary conditions is sufficient because the radial heat transfer mechanism is always limited by heat conduction to the surface. In order to reduce the output uncertainty to reasonable levels (less than 10%), the most sensitive material properties must be known within 5% of the mean values. However, the uncertainty from the microstructural parameters cannot be reduced until they can be considered to exist as a distribution of sizes by the model.

The purpose of the uncertainty quantification work was to show how one can approach the problem of quantifying uncertainty as it propagates through a model using a common approach to simulating solidification processing. The uncertainty levels in the input parameters picked for convenience here, but the effect of those levels on output uncertainty was demonstrated. In the simulation of an industrial important problem, where the model predictions drive process design decisions, the different input uncertainties must be extracted from the literature, if possible, or from one's own experiments. This procedure is an extension of the current work and the topic of future research endeavors.

8.2 Model Improvements and Future Work

The analysis performed in this work has shown that the flow in the rigid mushy zone is very important in predicting the macrosegregation in a cast ingot. However, the permeability of the mushy zone is not well understood, especially at high fraction solids, and the current model is not capable of handling variable dendrite arm spacing. Adding this feature to the model could help reduce the uncertainty in macrosegregation predictions. Additionally, further research on the permeability of the mushy zone will be able to improve model predictions. To perform this kind of analysis, model predictions will need to be compared to experimental results, preferably with uncertainty around the results reported as well.

For equiaxed solidification, the formation of the rigid mushy zone is a really important model parameter. The current model uses a constant fraction for a constant and uniform particle size. This is unrealistic because the packing fraction is highly dependent on the grid size and particles have a distribution of sizes in actual castings. A significant model improvement would to be incorporate a distribution of particle sizes or track individual particles or various sizes. This would also introduce additional model parameters whose uncertainties in relation to model predictions would need to be understood.

Other model parameters other than the particle size, dendrite arm spacing, and packing fraction are treated as constant and uniform in this model. The material properties (besides the mixture density) are also treated as constant parameters throughout the phase change and temperature ranges analyzed. In all reality, these parameters are functions of temperature and phase, and should be treated as such by the

model. Implementing temperature-dependent property values should first be done to select material properties, like the ones singled out in sections 5.2.4, 6.7, and 0.

This work has also shown that the sump depth is highly dependent on the radial transfer of heat to the surface of the ingot. The recommendation for future work is to perform a scaling analysis on this phenomenon in order to gain a starting analytical expression or model for the calculation of the sump depth. This will be extremely useful for process design, especially in determining the proper placement of a wiper or effect of different cooling jet configurations.

LIST OF REFERENCES

LIST OF REFERENCES

[1] J.F. Grandfield, D.G. Eskin, and I.F. Bainbridge: *Direct-Chill Casting of Light Alloys*, 1st ed., John Wiley & Sons, Inc., Hoboken, New Jersey, 2013.

[2] J.A. Dantzig and M. Rappaz: *Solidification*, EPFL Press, Boca Raton, Fl., 2009.

[3] D.G. Eskin, J. Zuidema, V.I. Savran, and L. Katgerman: *Mater. Sci. Eng. A*, 2004, vol. 384, pp. 232–244.

[4] A.V. Reddy and C. Beckermann: *Metall. Mater. Trans. B*, 1997, vol. 28, pp. 479–489.

[5] C.J. Vreeman, M.J.M. Krane, and F.P. Incropera: *Int. J. Heat Mass Transf.*, 2000, vol. 43, pp. 677–686.

[6] C.J. Vreeman and F.P. Incropera: *Int. J. Heat Mass Transf.*, 2000, vol. 43, pp. 687–704.

[7] C.J. Vreeman, J.D. Schloz, and M.J.M. Krane: *J. Heat Transfer*, 2002, vol. 124, pp. 947–953.

[8] D.G. Eskin: in *TMS Annu. Meet. Exhib. Light Met.*, 2014, pp. 855–60.

[9] D.G. Eskin, Q. Du, and L. Katgerman: *Scr. Mater.*, 2006, vol. 55, pp. 715–718.

[10] Q. Du, D.G. Eskin, and L. Katgerman: *Metall. Mater. Trans. A*, 2007, vol. 38, pp. 180–189.

[11] D.G. Eskin, Q. Du, and L. Katgerman: *Metall. Mater. Trans. A*, 2008, vol. 39, pp. 1206–1212.

[12] D.G. Eskin and L. Katgerman: *Mater. Sci. Forum*, 2009, vol. 630, pp. 193–199.

[13] C.J. Vreeman and F.P. Incropera: *Numer. Heat Transf. Part B Fundam.*, 1999, vol. 36, pp. 1–14.

[14] Q. Du, D.G. Eskin, and L. Katgerman: *Mater. Sci. Eng. A*, 2005, vol. 413-414, pp. 144–150.

[15] D.G. Eskin, V.I. Savran, and L. Katgerman: *Metall. Mater. Trans. A*, 2005, vol. 36A, pp. 1965–1976.

[16] R. Nadella, D.G. Eskin, Q. Du, and L. Katgerman: *Prog. Mater. Sci.*, 2008, vol. 53, pp. 421–480.

[17] C. Flood and P.A. Davidson: *Mater. Sci. Technol.*, 1994, vol. 10, pp. 741–751.

[18] A.J. Williams, T.N. Croft, and M. Cross: *Metall. Mater. Trans. B*, 2003, vol. 34B, pp. 727–734.

[19] Dmytro V. Zagrebelnyy: PhD Dissertation, Department of Materials Engineering, Purdue University, 2007.

[20] J. Sengupta, S.L. Cockcroft, D.M. Maijer, M.A. Wells, and A. Larouche: *Metall. Mater. Trans. A*, 2003, vol. 35, pp. 523-540.

[21] W.H. Kool and L. Katgerman: *Metall. Mater. Trans. A*, 2004, vol. 35, pp. 2917–2926.

[22] H. Hao, D.M. Maijer, M.A. Wells, S.L. Cockcroft, D. Sediako, and S. Hibbins: *Metall. Mater. Trans. A*, 2004, vol. 35A, pp. 3843-3854.

[23] M. Lalpoor, D.G. Eskin, and L. Katgerman: *Metall. Mater. Trans. A*, 2010, vol. 41A, pp. 2425–2434.

[24] Suyitno, D.G. Eskin, V.I. Savran, and L. Katgerman: *Metall. Mater. Trans. A*, 2004, vol. 35A, pp. 3551–3561.

[25] M. Lalpoor, D.G. Eskin, D. Ruvalcaba, H.G. Fjær, A. Ten Cate, N. Ontijt, and L. Katgerman: *Mater. Sci. Eng. A*, 2011, vol. 528, pp. 2831–2842.

[26] J.M. Drezet and Th Pirling: *J. Mater. Process. Technol.*, 2014, vol. 214, pp. 1372–1378.

[27] A. Chernatynskiy, S.R. Phillpot, and R. LeSar: *Annu. Rev. Mater. Res.*, 2013, vol. 43, pp. 157–182.

[28] M. Hunt, B. Haley, M. McLennan, M. Koslowski, J. Murthy, and A. Strachan: *Comput. Phys. Commun.*, 2015, vol. 194, pp. 97–107.

[29] J. Yanke, K. Fezi, R.W. Trice, and M.J.M. Krane: *Numer. Heat Transf. Part A Appl.*, 2015, vol. 67, pp. 268–292.

[30] K. Fezi, J. Yanke, and M.J.M. Krane: *Metall. Mater. Trans. B*, 2015, vol. 46, pp. 766–779.

[31] R.L. Wasserstein: *Technometrics*, 1997, vol. 39, pp. 338–338.

[32] M. Koslowski and A. Strachan: *Reliab. Eng. Syst. Saf.*, 2011, vol. 96, pp. 1161–1170.

[33] H. Babaee, X. Wan, and S. Acharya: *J. Heat Transfer*, 2013, vol. 136, pp.1-11.

[34] P. Marepalli, J.Y. Murthy, B. Qiu, and X. Ruan: *J. Heat Transfer*, 2014.

[35] S. Sarangi, K.K. Bodla, S.V. Garimella, and J.Y. Murthy: *Int. J. Heat Mass Transf.*, 2014, vol. 69, pp. 92–105.

[36] M.C. Schneider and C. Beckermann: *Int. J. Heat Mass Transf.*, 1995, vol. 38, pp. 3455–3473.

[37] A. Kumar, M. Zaloznik, and H. Combeau: *Int. J. Therm. Sci.*, 2012, vol. 54, pp. 33–47.

[38] M.S. Bhat, D.R. Poirier, and J.C. Heinrich: *Metall. Mater. Trans. B*, 1995, vol. 26, pp. 1049–1056.

[39] M.S. Bhat, D.R. Poirier, and J.C. Heinrich: *Metall. Mater. Trans. B*, 1995, vol. 26, pp. 1091–1092.

[40] S.G.R. Brown, J.A. Spittle, D.J. Jarvis, and R. Walden-bevan: *Acta Mater.*, 2002, vol. 50, pp. 1559–1569.

[41] J.E. Drummond and M.I. Tahir: *Int. J. Multiph. Flow*, 1984, vol. 10, pp. 515–540.

[42] S. Ganesan, C.L. Chan, and D.R. Poirier: *Mater. Sci. Eng. A*, 1992, vol. 151, pp. 97–105.

[43] S.V. Patankar: *Numerical Heat Transfer and Fluid Flow*, Hemisphere Publishing, Washington DC, 1980.

[44] W.D. Bennon and F.P. Incropera: *Int. J. Heat Mass Transf.*, 1987, vol. 30, pp. 2161–2170.

[45] I. Vusanovic and M.J.M. Krane: *3rd Int. Conf. Adv. Solidif. Process.*, 2011, vol. 27.

[46] A.S. Iberall: *J. Res. Natl. Bur. Stand. (1934).*, 1950, vol. 45, pp. 398–406.

[47] H.J. Thevik and A. Mo: *Int. J. Heat Mass Transf.*, 1997, vol. 40, pp. 2055–65.

[48] M.J.M. Krane: in *ASM Handbook, Vol. 22B, Met. Process Simul.*, 2010, pp. 157–167.

[49] V.R. Voller and C. R. Swaminathan: *Numer. Heat Transf. Part B Fundam.*, 1991, vol. 19, pp. 175–89.

[50] M.L.N.M. Melo, E.M.S. Rizzo, and R.G. Santos: *J. Mater. Sci.*, 2005, vol. 40, pp. 1599–1609.

[51] *Specification for Aluminum and Aluminum Alloy Die Forgings, Hand Forgings, and Rolled Forgings*, ASTM International, West Conshohocken, PA, 2009.

[52] W.F. Gale: *Smithells Metals Reference Book*, 8th ed., Elsevier, 2004.

[53] C.J. Vreeman: Masters' Thesis, Mechanical Engineering, Purdue University, 1997.

[54] T Iida and R Guthrie: *The Physical Properties of Liquid Metals*, Clarendon Press, Oxford, 1988.

[55] J. Yanke, K. Fezi, R.W. Trice, and M.J.M. Krane: *Numer. Heat Transf. Part A Appl.*, 2015, pp. 268–292.

[56] M. Raessi, J. Mostaghimi, and M. Bussmann: *Comput. Fluids*, 2010, vol. 39, pp. 1401–1410.

[57] M. Rudman: *Int. J. Numer. Methods Fluids*, 1998, vol. 28, pp. 357–378.

[58] M. Malik, E. Fan, and M. Bussmann: *Int. J. Numer. Methods Fluids*, 2007, vol. 55, pp. 693–712.

[59] M.S. Kim and W.I. Lee: *Int. J. Numer. Methods Fluids*, 2003, vol. 42, pp. 765–790.

[60] S.H. Garrioch: PhD Dissertation, Department of Mechanical Engineering, Mcgill University, 2000.

[61] S. Zhang, J. Yanke, D.R. Johnson, and M.J.M. Krane: *Int. J. Numer. Methods Heat Fluid Flow*, 2014, vol. 24, pp. 468–482.

[62] J. Coleman, K. Fezi, and M.J.M. Krane: in *Light Met.*, 2016, pp. 641–646.

[63] J.F. Grandfield and P.T. McGlade: *Mater. Forum*, 1996, vol. 20, pp. 29–51.

[64] F.P. Incropera, D.P. DeWitt, L. Bergman, and A.S. Lavine: *Fundamentals of Heat and Mass Transfer*, 7th ed., Hoboken, New Jersey, 2007.

[65] D.C. Weckman and P. Niessan: *Metall. Mater. Trans. B*, 1982, vol. 13, pp. 593–602.

[66] M.J.M. Krane and F.P. Incropera: *Metall. Mater. Trans. A*, 1995, vol. 26A, pp. 2329–2339.

[67] P.J. Prescott: PhD Dissertation, Department of Mechanical Engineering, Purdue University, 1992.

[68] M.C. Schneider and C. Beckermann: *Metall. Mater. Trans. A*, 1995, vol. 26, pp. 2373–2388.

[69] K. Fezi, A. Plotkowski, and M.J.M. Krane: *Metall. Mater. Trans. A*, 2016, vol. 47A, pp. 2940–2951.

[70] V.R. Voller and I. Vušanović: *Int. J. Heat Mass Transf.*, 2014, vol. 79, pp. 468–471.

[71] K. Fezi, M. Hunt, M.J.M. Krane, B.P. Haley, and A. Strachan: https://nanohub.org/resources/21650, 2014.

[72] S. Smolyak: *Dokl. Akad. Nauk SSSR.*, 1963, vol. 4, pp. 240–243.

[73] M.S. Eldred and J. Burkardt: in *47th AIAA Aerosp. Sci. Meet. Incl. New Horizons Forum Aerosp. Expo.*, 2009, pp. 1–20.

[74] M. Eldred: in *50th AIAA/ASME/ASCE/AHS/ASC Struct. Struct. Dyn. Mater. Conf.*, American Institute of Aeronautics and Astronautics, Reston, Virigina, 2009.

[75] M.S. Eldred, C.G. Webster, and P.G. Constantine: in *49th AIAA/ASME/ASCE/AHS/ASC Struct. Struct. Dyn. Mater. Conf.*, 2008.

[76] M.D. Morris: *Technometrics*, 1991, vol. 33, pp. 161–174.

[77] F. Campolongo, J. Cariboni, and A. Saltelli: *Environ. Model. Softw.*, 2007, vol. 22, pp. 1509–1518.

[78] M. Založnik and B. Šarler: *Mater. Sci. Eng. A*, 2005, vol. 413-414, pp. 85–91.

[79] K. Fezi, A. Plotkowski, and M.J.M. Krane: *Numer. Heat Transf. Part A Appl.* (in review).

[80] I. Vusanovic and V.R. Voller: *Mater. Sci. Forum*, 2014, vol. 790-791, pp. 73–78.

[81] A. Plotkowski and M.J.M. Krane: *Int. J. Heat Mass Transf.* (in press).

[82] A. Plotkowski and M.J.M. Krane: *Appl. Math. Model.* (in review).

[83] L Arnberg, G Chai, and L Backerud: *Mater. Sci. Eng. A*, 1993, vol. 173, pp. 101–103.

[84] A. K. Dahle and L. Arnberg: *Jom*, 1996, vol. 48, pp. 34–37.

[85] M.H. Ghoncheh and S.G. Shabestari: *Met. Mater. Trans. A*, 2015, vol. 46, pp. 1287–1299.

[86] M.J.M. Krane and F.P. Incropera: *Int. J. Heat Mass Transf.*, 1997, vol. 40, pp. 3837–3847.

[87] K. Fezi and M.J.M. Krane: *IOP Conf. Ser. Mater. Sci. Eng.*, 2015, vol. 84, pp. 012001.

[88] P.J. Prescott and F.P. Incropera: *ASME J. Heat Transf.*, 1995, vol. 117, pp. 716–724.

[89] K. Fezi, J. Yanke, and M.J.M. Krane: *Metall. Mater. Trans. B*, 2014, vol. 46B, pp. 766–779.

[90] V.R. Voller and I. Vusanovic: *Int. J. Heat Mass Transf.*, 2014, vol. 79, pp. 468–471.

[91] G. Quillet, a. Ciobanas, P. Lehmann, and Y. Fautrelle: *Int. J. Heat Mass Transf.*, 2007, vol. 50, pp. 654–666.

[92] I. Vusanovic: *IOP Conf. Ser. Mater. Sci. Eng.*, 2015, vol. 84, pp. 012008.

[93] V.R. Voller: University of Minnesota, Minneapolis, private communication, 2015.

[94] M.F. Singleton, P. Nash, and K.J. Lee: in *Phase Diagrams Bin. Nickel Alloy.*, ASM International, 1991, pp. 207–212.

APPENDICES

Appendix A A Metric for the Quantification of Macrosegregation during Alloy Solidification

Abstract

A metric for quantifying the degree of solidification macrosegregation is proposed that statistically fits compositional data from experiments and simulations to a three-parameter Weibull distribution. The method for fitting such a distribution is described and examples are presented. The new metrics are compared to existing macrosegregation measures and the Weibull distribution is shown to be the best fit to data. The fitted three-parameter Weibull distribution is generally found to have better agreement with the composition data than a Gaussian distribution, upon which the macrosegregation number is based, because the Weibull better accounts for asymmetry in the data set. Trends in macrosegregation results are identified using the new metrics, specifically the normalized Weibull deviation, and compared to the trends identified by the macrosegregation number. A grid dependence study is performed using both metrics as tests for convergence. The utility of the Weibull distribution is demonstrated by comparing composition data with different degrees of asymmetry due to different solidification cooling rates. The difference between the values of the two metrics is a measure of the asymmetry in the compositional distribution.

Introduction

Macrosegregation in metallic alloys is a complex casting defect that is a function of the transport phenomena during processing, and is affected by material properties,

cooling conditions, and system geometry. One difficulty with exploring the mechanisms underlying the formation of macrosegregation patterns is the quantification of the comparison of large compositional data sets, obtained either experimentally or computationally. Commonly, either full composition fields or specific profiles are reported (e.g., [3,66,86]). These data have been used to visualize macrosegregation and explain the physical phenomena responsible for it, but these visualizations are difficult to compare quantitatively. To aid in such a comparison, a single numerical metric that represents the composition field is frequently calculated. A reliable metric is also useful for quantifying uncertainty propagation, in which the behavior of the metric can be used to understand the probable range of the macrosegregation level as a function of the variation of the process input. [87].

One metric that is commonly used for quantifying compositional variation is the macrosegregation number, [68,88], the normalized standard deviation of a Gaussian distribution fitted to the composition field:

$$M = \frac{1}{C_0}\left[\frac{1}{V_{tot}}\iiint_V (C - C_0)^2 dV\right]^{1/2} \tag{A.1}$$

where C_0 is the nominal composition, V_{tot} is the total volume of the domain, and C is the measured or predicted local composition field. The integral in Equation (A.1) is approximated as the summation

$$M = \frac{1}{C_0}\left[\frac{1}{V_{tot}}\sum_{i=1}^{N}(C_i - C_0)^2 \Delta V_i\right]^{1/2}, \tag{A.2}$$

where ΔV_i is the control volume in which C_i represents the local average composition and N is the number of samples (or control volumes in numerical results). This metric assumes that the composition field is normally distributed about the mean or nominal

composition. However, it is quite common for this volume-averaged composition distribution to be asymmetric about this mean, depending on the process parameters and material properties. It is also found that this distribution is skewed to lower compositions for elemental partition coefficients (k_p) greater than unity and to higher values for $k_p < 1$ (Figure A.1) [89]. As a consequence of the assumptions implicit in Equations (A.1) and (A.2), the commonly used macrosegregation number is only an accurate depiction of the overall compositional variation for the limiting case of a symmetric, Gaussian distribution. When fitting a Gaussian distribution to a skewed data set, the longer tail is truncated and the shorted tail is artificially extended. Overall, the fitted distribution tends to overpredict the total amount of macrosegregation and underpredict the volume of material near the nominal composition.

Fezi et al. [89] analyzed the composition fields produced by numerical simulations of the electroslag remelting process by plotting the volume averaged composition distributions for different components in a superalloy (alloy 625) for various process conditions. The composition distributions were all found to be asymmetric, and the implications of the distribution shapes were discussed. Along with the macrosegregation number, the ingot volume fraction outside of the alloy composition specification range was used to characterize the degree of macrosegregation. This latter metric is useful to consider, especially for industrial processes and alloys, but it fails to provide information about compositional variations within the specification limits.

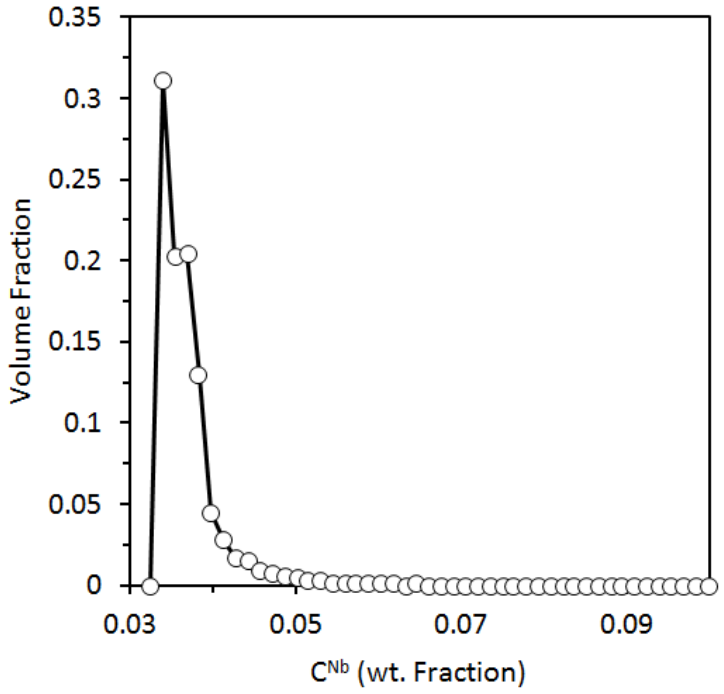

(a)

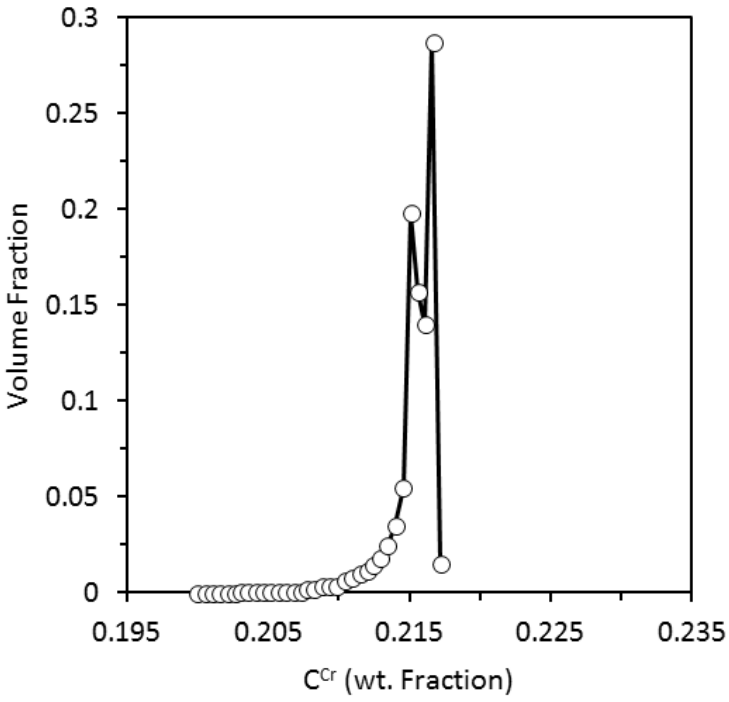

(b)

Figure A.1: Composition distributions in an ingot of Ni alloy 625 produced through electroslag remelting showing the asymmetry in (a) Nb with $k_p<1$ and (b) Cr with $k_p>1$ (data taken from [89]).

Voller and Vušanović [90] recently proposed that the normalized compositional survival function be used for verification, validation, and analysis of numerical macrosegregation predictions. They applied their method to experimental data given by Quillet et al. [91] for a cast Sn-10wt.%Bi ingot and to numerical results for this system. The composition data was sorted in descending order of the ratio C/C_0, from $j = 1$ to $j = n = 120$. Each sorted composition was given a value determined by its survival plotting position, $S = \frac{j}{n+1}$, forming the compositional survival function, $S(C/C_o)$ (although it is erroneously referred to as the cumulative distribution function in [90]). This survival function was interpreted as the ingot volume fraction corresponding to a macrosegregation level greater than or equal to the corresponding value of S. The corresponding CDF can be calculated easily from the survival function as 1 - S. They found a linear relationship between the composition and the survival function when the positive segregation was plotted on log-log axes. Also, the grid size did not affect the linear fit but did change the maximum composition in the positive segregation region. Fitting this positive portion of the survival function with a power law function yields a slope that may be used to quantify the level of macrosegregation, and the survival functions themselves may be useful for visualizing data. Such visualization was used recently to investigate the effect of permeability models [92] in segregation development. Voller and Vušanović [90] also suggested using the slope of the power law function as the shape factor for the Pareto power-law distribution, but never tested the Pareto distribution for its validity. While these approaches succeed at expressing the macrosegregation in a casting with a single metric, they ignore all negative segregation

and do not accurately reflect the shape of the full composition distribution. This shortcoming might be particularly severe in cases where the macrosegregation strongly tails towards the negative side of the distribution, or in alloys with elements with partition coefficients greater than unity, which tend to skew to lower compositions. The linearity of the positive region of the survival function does not extend throughout the positive segregation region which further limits this metric. Also, as Voller and Vušanović point out, this method is valid only when the composition data are on a uniform grid, because their survival function weights each composition measurement the same.

In an effort to address these issues and to properly capture the entire skewed composition distribution, and not just the positively segregated region, this study develops and uses a three-parameter Weibull distribution to characterize macrosegregation. In particular, the advantages over the macrosegregation number are detailed and comparisons are made to the power law function and Pareto distribution methods. (These were proposed by Voller and Vušanović, although they only demonstrate the former technique [90].) While the present analysis uses statistical functions as tools to describe composition distributions, it should not be mistaken as a rigorous statistical analysis. Statistical distributions are useful because they fit composition distributions found in solidified ingots well, but their use should not be read as a suggestion that the composition is a random variable, as the distribution of composition values is controlled by specific, non-random physical processes. The new method is first applied to experimental data given by Quillet et al. [91], and then used to describe the influence of cooling conditions, grid size, and grid uniformity in simulations of solidification of a simple binary alloy (Al-4.5wt.%Cu) and of a multicomponent

nickel-based superalloy (Inconel 625) with a columnar, rigid dendritic structure. This method can be applied without alteration to other segregation prone alloys, solidification microstructures, and industrial solidification processes, such as direct chill casting, ingot casting of steel, and electroslag remelting.

Mathematical Description

The three-parameter Weibull probability distribution function (PDF) of a random variable *x* (in this case, the composition) is defined as:

$$PDF_w(x) = \frac{\alpha}{\beta}\left(\frac{x-\gamma}{\beta}\right)^{\alpha-1} exp\left(-\left(\frac{x-\gamma}{\beta}\right)^{\alpha}\right), \tag{A.3}$$

where α is the shape parameter, also known as the Weibull slope, β the scale parameter, and γ the threshold value. The shape and scale parameters control the asymmetry and the size or range of the distribution, respectively. The lower end of the distribution is limited by the threshold value such that all random variables *x* are greater than or equal to γ. The PDF is the derivative of the corresponding cumulative distribution function:

$$CDF_W(x) = 1 - exp\left(-\left(\frac{x-\gamma}{\beta}\right)^{\alpha}\right). \tag{A.4}$$

The variance of the Weibull distribution is:

$$\sigma_W^2 = \beta^2\left[\Gamma\left(1+\frac{2}{\alpha}\right) - \Gamma^2\left(1+\frac{1}{\alpha}\right)\right], \tag{A.5}$$

where Γ is the gamma function,

$$\Gamma(z) = \int_0^{\infty} t^{z-1}e^{-t}dt, \tag{A.6}$$

and the deviation is defined as the square-root of the variance:

$$\sigma_W = \beta\left[\Gamma\left(1+\frac{2}{\alpha}\right) - \Gamma^2\left(1+\frac{1}{\alpha}\right)\right]^{1/2}. \quad \text{(A.7)}$$

The full composition field of a cast alloy is continuous, but is sampled (measured or predicted) at discrete spatial locations. Each sample is assumed to be the average of a corresponding control volume. The control volumes can be uniform in size, as in the case of Voller and Vušanović [90], or non-uniform, in which each composition measurement may characterize a different ingot volume fraction. A cumulative volume distribution function (CVDF) may be constructed which quantifies, for each unique composition in the data set, the ingot volume fraction that has a composition less than or equal to that unique composition measurement. This cumulative volume function, using discrete composition data, has a similar meaning to that of a CDF, with a random variable *x*, and for simplicity is interpreted in that way for this study. To construct this plot, a data set comprised of the composition field and corresponding control volume sizes must first be ranked by composition from lowest to greatest. This data set is taken over the full composition range (both negative and positive segregation regions) in this study. The CVDF value for each ranked composition, C_j, is calculated as shown in Equation (A.8),

$$CVDF(C_j) = \frac{\sum_{i=1}^{i=j} V_i}{\sum_{i=1}^{i=n} V_i}, \quad \text{(A.8)}$$

in which the ingot is made up of *n* control volumes, each occupying a volume V_i. The use of volume allows non-uniform grids to be used to calculate the CVDF. If all control volumes are equal in size, then Equation (A.8) reduces to a form similar to *1-S* as used by Voller and Vušanović [90]. The result of this process is a CVDF of the composition data set that can be fit to a continuous CDF.

It was found that the Weibull distribution fit the compositional data best if the data and Weibull PDF skewed towards higher compositions. For cases that skew towards lower compositions (i.e. $\left(C_0^i - C_{min}^i\right) > \left(C_{max}^i - C_0^i\right)$, where C_{min}^i and C_{max}^i are minimum and maximum compositions, respectively), the data were fit to a Weibull distribution using $\left(1 - C^i\right)$ as the random variable. The compositional CVDF data sets are linearized by using the following relationships, which can be found by rearranging Equation (A.3):

$$x_j = \ln\left(C_j - \gamma\right), \tag{A.9}$$

and

$$y_j = \ln\left\{-ln\left[1 - CVDF\left(C_j\right)\right]\right\}, \tag{A.10}$$

where C_j is the composition of data point j, and $CVDF\left(C_j\right)$ is the volume fraction of material with a composition less than or equal to C_j, as defined in Equation (A.8). A least-squares fit of a straight line is made to the linearized data set, $y_j = f(x_j)$, where the slope is the shape parameter, α, and the scale parameter, β, is related to the y-intercept by:

$$\beta = \exp\left(-\frac{y_{int}}{\alpha}\right). \tag{A.11}$$

Selection of the threshold value, γ, must be done carefully in order to obtain the best fit. In this case, a γ value of zero was used as an initial guess and then incremented up to the minimum composition found in the domain. The best possible threshold value was determined by comparing the fitted Weibull CDF and the CVDF of the compositional data and minimizing the difference calculated using the root mean square error (RMSE): $RMSE = \sqrt{\sum_{n=1}^{n} \frac{(CVDF - CDF_W)^2}{n}}$. Increments in γ of 10^{-5} were found to be

sufficiently small for the cases examined. The three-parameter Weibull distribution reduces to the two-parameter form if the best fit is found with a threshold of zero.

The shape parameter (α) controls the location of the peak value of the fitted PDF_w, while the scale parameter (β) controls the range of the distribution. Both of these parameters are important in characterizing the macrosegregation and one metric that combines the effects of these two parameters is the Weibull deviation. To compare this metric directly to the macrosegregation number, the Weibull deviation is normalized by the nominal composition of a given component, shown in equation (A.12). The raw data was converted into a volume distribution function (VDF), similar to that of a PDF, by binning the data and creating a histogram. The height of each bin corresponds to the volume fraction of ingot occupied in that composition range, divided by the bin width. This way the total area occupied by the histogram, or VDF, is equal to one.

$$W = \frac{\sigma_W}{C_0} = \frac{\beta}{C_0}\left[\Gamma\left(1+\frac{2}{\alpha}\right) - \Gamma^2\left(1+\frac{1}{\alpha}\right)\right]^{1/2} \tag{A.12}$$

It is important to understand that by ordering the data set from least to greatest in terms of the composition to construct the CVDF, the information about spatial distribution of the composition field is lost. Further manipulations of the data by fitting a particular distribution type and representing that distribution with a single parameter necessarily reduce the amount of information conveyed by the data set. Therefore, while these types of metrics are useful for comparisons of otherwise unwieldy data sets, they do not contain all the necessary information to understand the mechanisms by which macrosegregation patterns develop. Instead, trends in these metrics should be used to

point towards particular cases in which the spatial and temporal data may be examined more closely to gain a deeper understanding of the physics of the process.

Results and Discussion

Use of the three-parameter Weibull distribution and the normalized Weibull deviation is implemented in several examples presented below. First, experimental measurements of the composition profile of a Sn-10 wt.% Bi ingot [91] are used to compare the present method to the macrosegregation metrics proposed by Voller and Vušanović and the macrosegregation number. Next, numerical predictions of a static casting of Al-4.5 wt.% Cu are used to show the versatility of the Weibull distribution compared to the macrosegregation number. The normalized Weibull deviation is also used to conduct a grid dependence study for this alloy system. Finally, a multicomponent superalloy is simulated to show the relationship between the normalized Weibull deviation and the elemental partitioning.

Measured Segregation in Sn-10 wt.% Bi Ingot

The proposed characterization metric for macrosegregation was first applied to experimental data from a static casting of a Sn-10wt.%Bi alloy (Quillet et al. [91]). The ingot was 5 cm x 6 cm x 1 cm and cooled from one of the 5 cm X 1 cm vertical walls while the remaining walls were insulated. Composition measurements were reported for a uniform 10 x 12 grid from the 5 cm x 6 cm midplane of the casting. Using these data, Voller and Vušanović took the survival function in Figure A.2(a) and plotted the positive segregation region ($C/C_o \geq 1$) on a log-log plot and fitted it with a straight line (Figure A.2(b)).

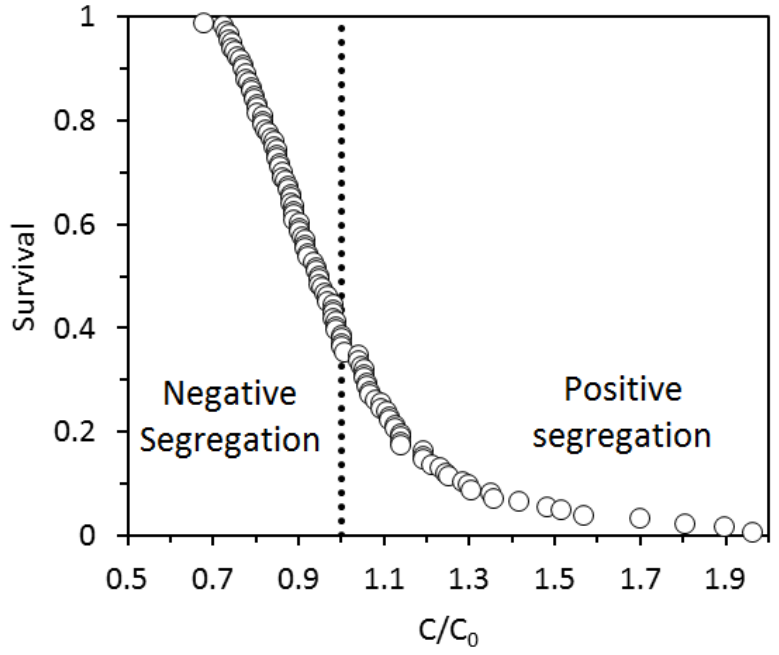

(a)

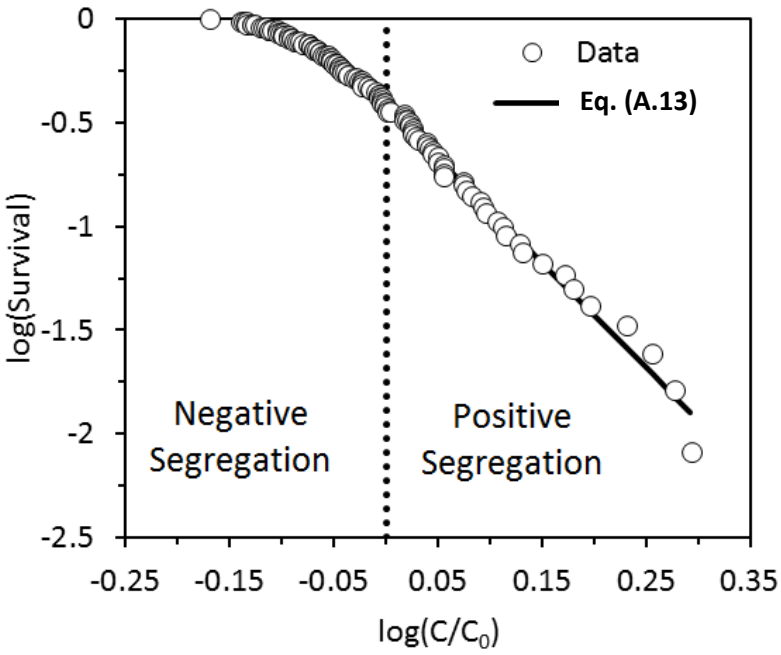

(b)

Figure A.2: Compositional survival function with (a) linear and (b) log scales. These experimental data are from the cast Sn-10wt.%Bi ingot reported by Quillet et al. [91].

A least squares fit to positive portion of Figure A.2(b) yielded the following equation:

$$y = 0.3823\frac{C}{C_0}^{-5.059} . \quad \text{(A.13)}$$

(The exponent in Equation (A.13) is not the value in [90], where m = -4.45 was picked as an estimate to indicate the power law trend in the data [93].)

Voller and Vušanović also suggested that the negative of *m* may be used as the shape factor in a Pareto distribution, although they did not compare that distribution to the measurements [90]. The Pareto survival distribution for a random variable *x* is:

$$S_P = \left(\frac{x_{min}}{x}\right)^m, \quad \text{(A.14)}$$

where x_{min} is the minimum value allowed for *x*, and $S_P = 1$ when $x < x_{min}$. Since the exponent was found from a fit the positively segregated data, x_{min} was set to the nominal composition. The Pareto PDF and CDF for $x \geq x_{min}$ are defined as:

$$CDF_P = 1 - \left(\frac{x_{\min}}{x}\right)^m \quad \text{(A.15)}$$

$$PDF_P = \frac{m x_{\min}{}^m}{x^{m+1}} \quad \text{(A.16)}$$

Equations (A.15) and (A.16) are plotted against the composition data set in Figure A.3, using the exponent in equation (A.13). The Pareto distribution follows the slope of the positively segregated region reasonably well; however it is offset from the data set. Clearly this distribution fails to adequately match the experimental results.

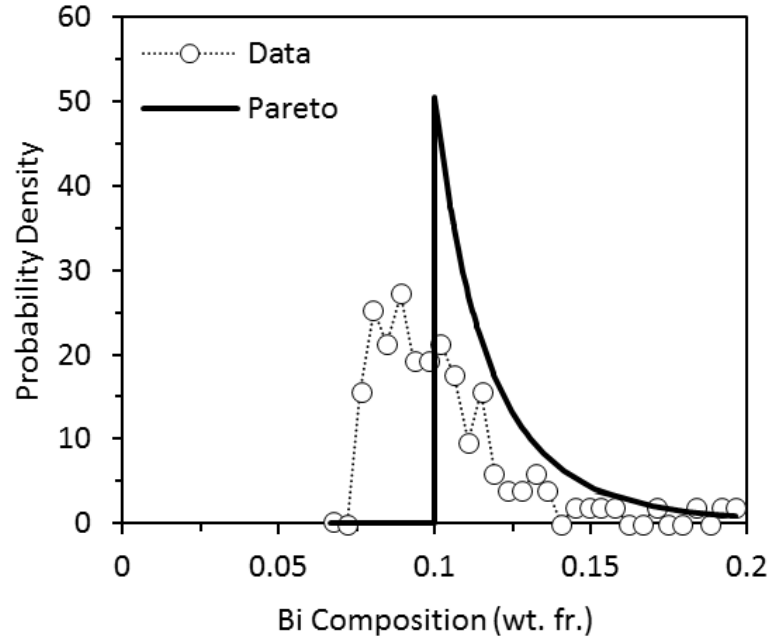

(a)

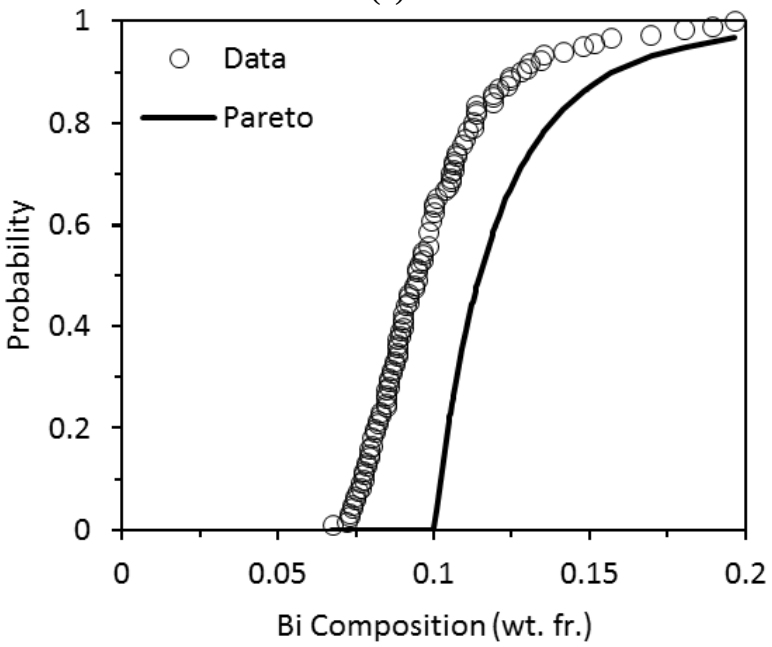

(b)

Figure A.3: (a) VDF and PDF and (b) CVDF and CDF plots of the Sn-10wt.%Bi compositional data reported by Quillet et al. [91] overlaid with corresponding Pareto distribution using the exponent in equation (A.13).

To construct the Weibull distribution, each compositional measurement was assumed to be representative of its 5 mm x 5 mm x 10 mm volume. Figure A.3(a) andFigure A.3(b) show the compositional probability and cumulative distributions functions. The compositional PDF is constructed by first grouping the data into 30 compositional bins, where the height of each bin (or probability density) is the volume fraction of the ingot that falls within each bin divided by the width of the bin.

The experimental data are plotted in both VDF and CVDF form in Figure A.4 and overlaid with the corresponding curves for the three-parameter Weibull, normal distributions, and power law using the fitting parameter given in equation (A.13). The power law function fits the measurement distribution well for the positive segregation. However, roughly half of the ingot is negatively segregated and that part of the distribution, including the compositions with the highest probability, is not described by this method. It is also clear that the experimental distribution is asymmetric, and is skewed in the direction of positive segregation. The normal distribution assumed by the usual macrosegregation number overpredicts the tail to the left, and underpredicts the likelihood of finding material near the nominal composition, while the fit to the Weibull distribution closely matches the asymmetry of the data. From these observations, it is expected that the macrosegregation number, being based on the assumption of normally distributed data, would overpredict the level of macrosegregation in the domain, as seen by comparing the macrosegregation number for this ingot (M = 0.238) to the normalized Weibull deviation (W = 0.195). To further illustrate the effectiveness of the three-parameter Weibull distribution, the RMSE of the fitted CDF_w (0.024) is compared to that

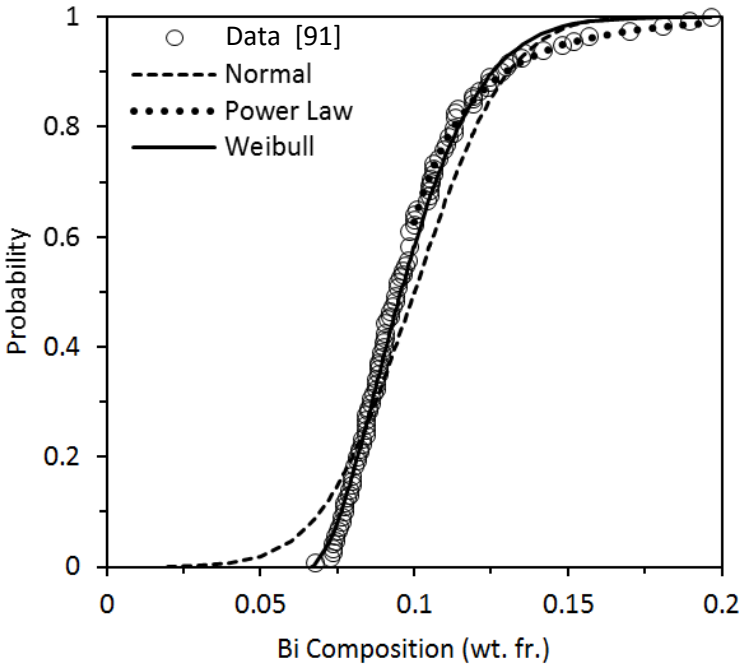

(a)

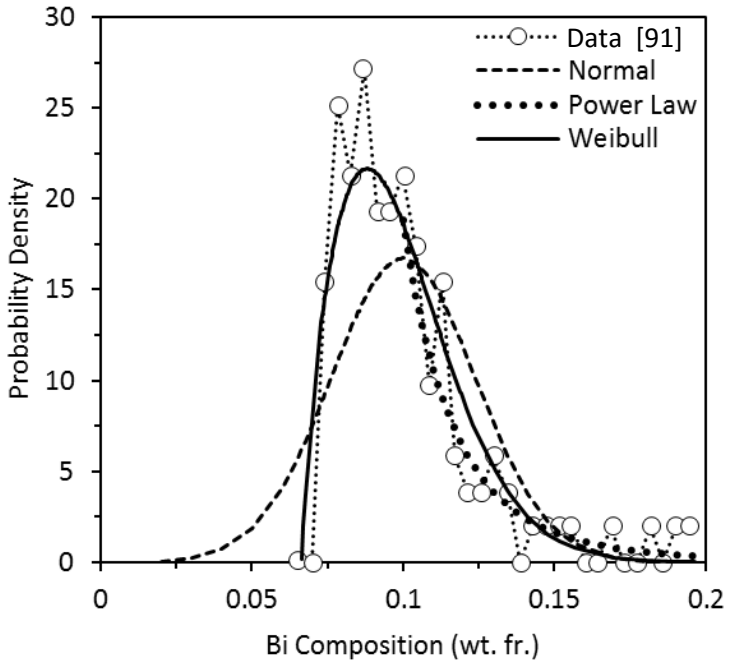

(b)

Figure A.4: (a) CVDF and CDF and (b) VDF and PDF plots of the Sn-10wt.%Bi compositional data reported by Quillet et al. [91] overlaid with corresponding three-parameter Weibull, normal, and power law distributions fit to the data. The power law CDF is covered by the experimental data, but is only plotted for the positively segregated region. It is clear that the Wiebull distribution more accurately represents the asymmetry of the experimental data.

of the normal distribution (0.076). The fit to the Weibull distribution has roughly 1/3 the error than that of the normal distribution.

Predicted Segregation in Al-4.5 wt.% Cu Ingot

One important use of the macrosegregation metrics described above is to compare the change in the composition distribution as a function of process variables or properties. Example data for this task were produced by a series of two-dimensional numerical simulations of the static casting of an Al-4.5wt.%Cu binary alloy. The model used was a standard continuum mixture-based finite volume model for columnar solidification based on the work of Bennon and Incropera [44], but including the temperature formulation of the energy equation [48], using Voller and Swaminathan's [49] linearization for the transient latent heat source term. The 10 cm x 10 cm domain was Cartesian, with an 80 x 80 uniform, structured, and staggered grid. Alloy properties were taken from Vreeman and Incropera [6]. Three of the domain walls were insulated, with a heat transfer coefficient applied to one of the side walls. This active boundary condition was varied to influence the heat transfer and fluid flow, and subsequently, the macrosegregation development within the casting.

Cases were run with heat transfer coefficients ranging from 500 to 4,000 W/m^2K. The normalized Weibull deviations and macrosegregation numbers for each of these cases are shown in Figure A.5. The macrosegregation number decreases monotonically with heat transfer coefficient. However, the normalized Weibull deviation has a minimum value near h = 1,250 W/m^2K, after which this trend reverses at intermediate values until the normalized Weibull deviation is equal to the macrosegregation number, at which point, it begins decreasing again.

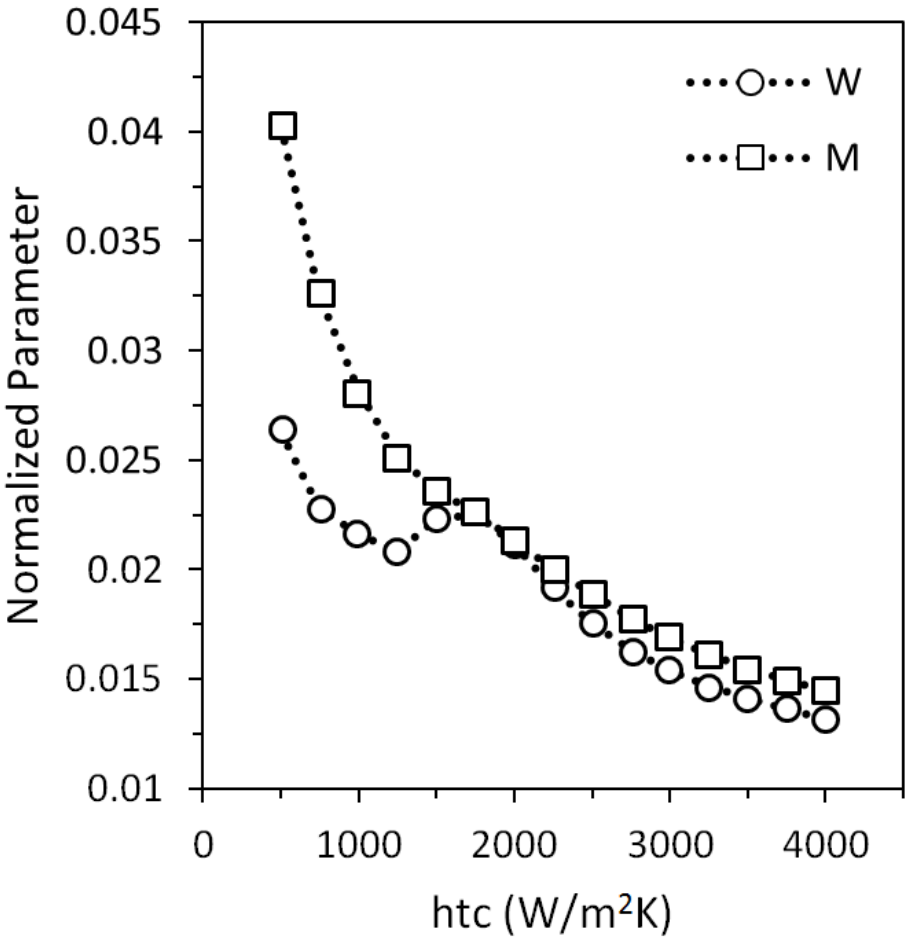

Figure A.5: Normalized Weibull deviation (W) and macrosegregation number (M) shown as functions of heat transfer coefficient for Al-4.5wt.%Cu solidification simulations.

Above h = 2000 W/m2K, *W* begins to decrease slightly faster than *M*.

The cause of the normalized Weibull deviation behavior is the changing symmetry of the composition distributions, which are shown (both PDF and CDF) for the extreme cases in Figure A.5, plotted for data divided into 50 bins. For small heat transfer coefficients, the composition distribution skews strongly to higher compositions, but has almost no tail to the left. The normal distribution in this case greatly exaggerates the overall macrosegregation since it overpredicts the negative segregation, while the Weibull distribution much more accurately represents the asymmetric shape of the data. However, as the heat transfer coefficient increases, the left tail lengthens and the right tail shrinks. Eventually, the distribution is nearly symmetric (Figure A.6 (b)). Here, both the Weibull and normal distributions represent the shape of the data reasonably well.

The results in Figure A.5 andFigure A.6 indicate several important characteristics of these two metrics. First, the three-parameter Wiebull distribution appears to be a more comprehensive method for describing the extent of macrosegregation than a normal distribution because it can fit both symmetric and asymmetric composition distributions accurately. This greater accuracy of the Weibull metric can also reveal trends that may not be apparent in the macrosegregation number, e.g., Figure A.5. Also, because the macrosegregation number is only accurate for symmetric distributions, the difference between these two values may be taken as a measure of the asymmetry of the composition distribution. This trend is shown in Figure A.7, normalized by the macrosegregation number to account for changes in the width of the distribution, along with four examples of the corresponding fitted Weibull distributions, varying from highly asymmetric (low *h*) to nearly symmetric (high *h*). As the heat transfer coefficient

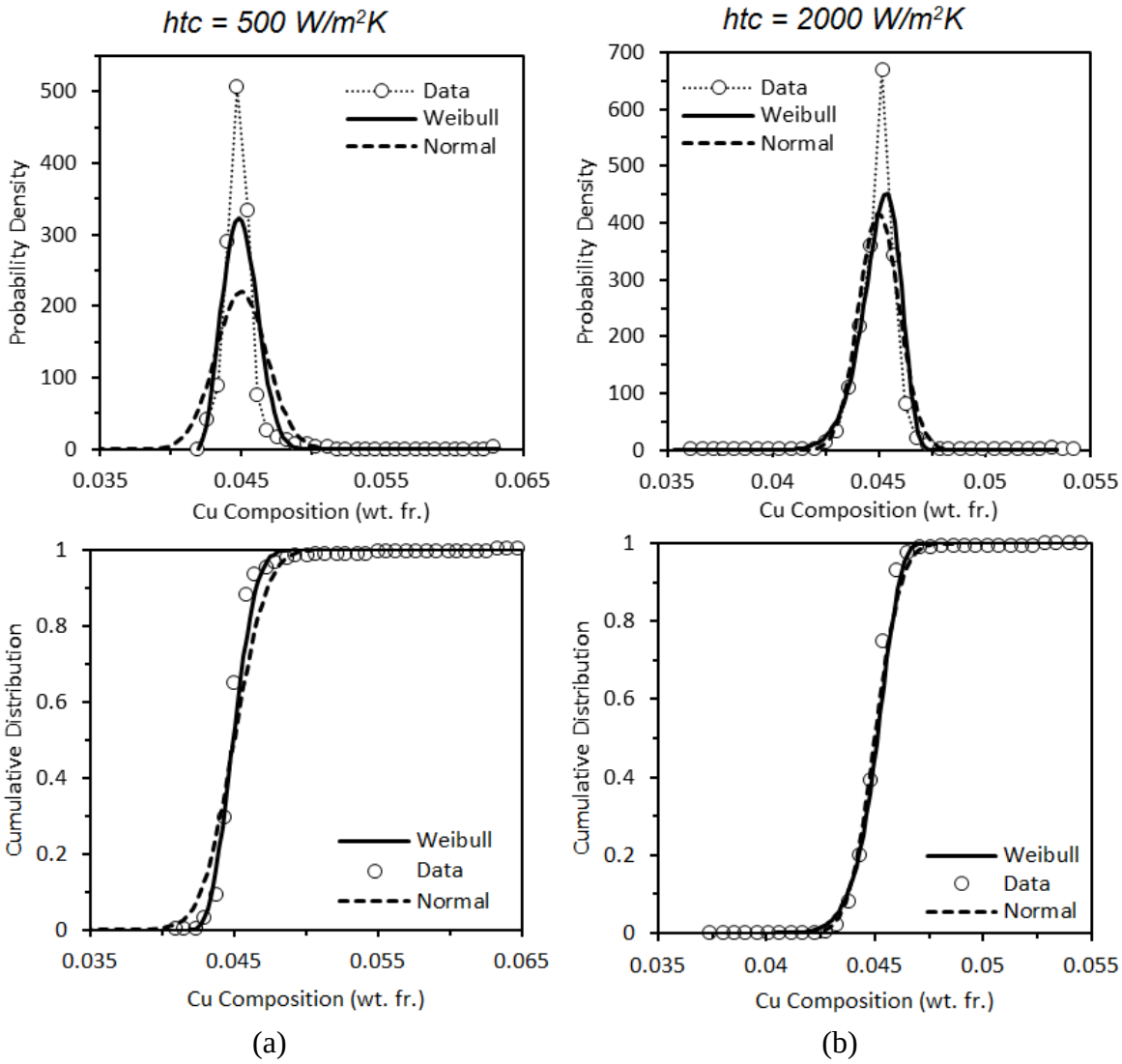

Figure A.6: Comparison of predicted composition data to fitted Weibull and normal PDFs and CDFs for Al-4.5 wt.% Cu with two different boundary conditions (a) h = 500 W/m^{2}K and (b) h = 2,000 W/m^{2}K. There is more symmetry in the distribution with higher *h*.

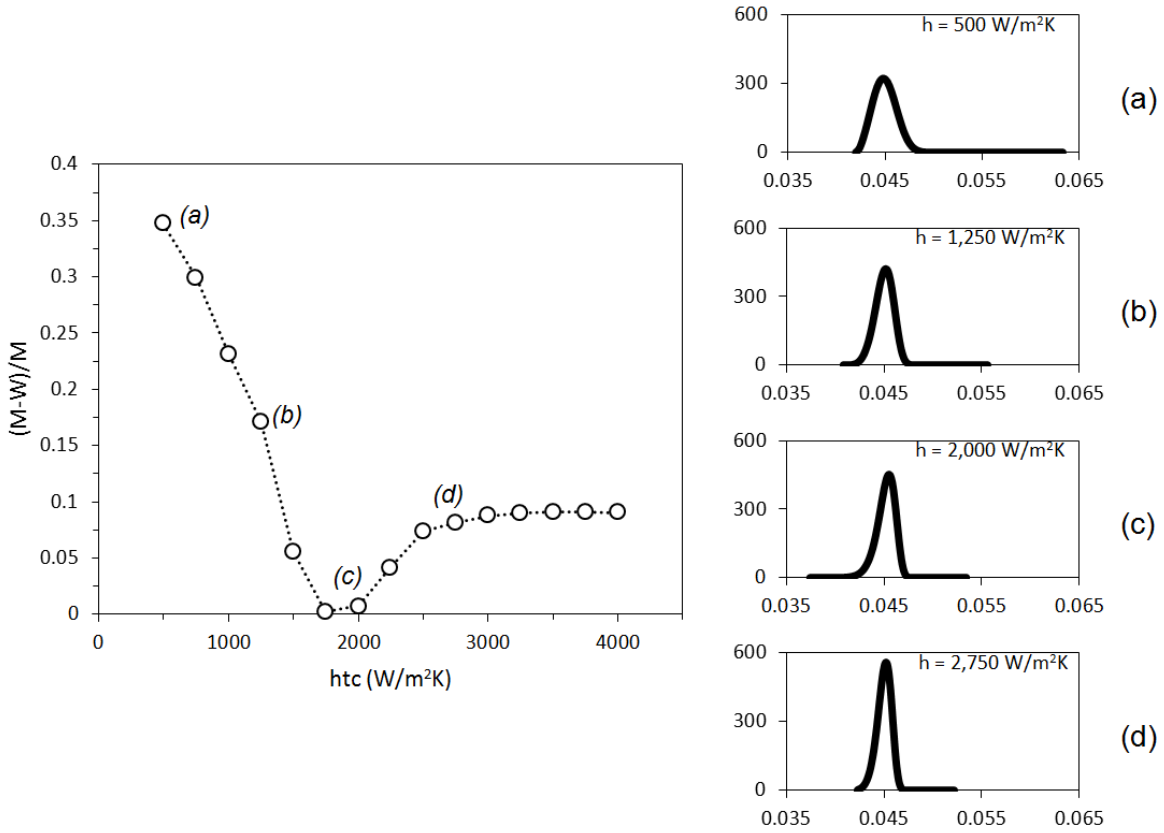

Figure A.7: The difference between the macrosegregation number (M) and the normalized Weibull deviation (W) plotted for Al-4.5wt.%Cu simulating over a range of heat transfer coefficients (M-W) indicates the asymmetry of the Weibull PDFs, shown at right for three selected cases, where the x-axes are Cu wt. fr. and the y-axes are probability density.

increases, the right tail of the distribution tends to shrink, while the left tail grows. This gradual shift in the shape of the distribution explains how the Weibull deviation first decreases with heat transfer coefficient, and then increases slightly before decreasing again, as shown in Figure A.4.

While fitting the composition field to a probability distribution and calculating these simple metrics can illuminate trends in the macrosegregation development, these advantages come at the expense of spatial information about the composition field. In order to gain a deeper understanding of the development of macrosegregation, these metrics must be related to the behavior during solidification. To this end, plots of the composition fields for the three PDFs shown in Figure A.7(a)-(c) are given in Figure A.8. The first solid solidified on the left wall, and was Cu poor ($k_p < 1$). Thermal and solutal buoyancy drive the flow in the liquid in a counterclockwise rotating cell that slightly penetrates the mushy zone (Figure A.9). This mushy zone flow moves the Cu enriched interdendritic liquid to the bottom of the domain, where it pools until fully solidified. This enriched liquid is replaced in the mushy zone by liquid closer to the nominal composition, leaving a depleted layer at the left wall. This process continues as the solidification front progresses left to right, until the average solid composition approaches the nominal composition, and the top of the domain becomes depleted. The last liquid to freeze is at the bottom right corner of the domain, where the most enriched fluid has collected. The center of the domain, where the composition is near the nominal, corresponds to the peak of the PDF. The enriched layer at the bottom and right wall corresponds to the right tail of the PDF, while the depleted regions at the left wall and top of the domain correspond to the left tail of the PDF.

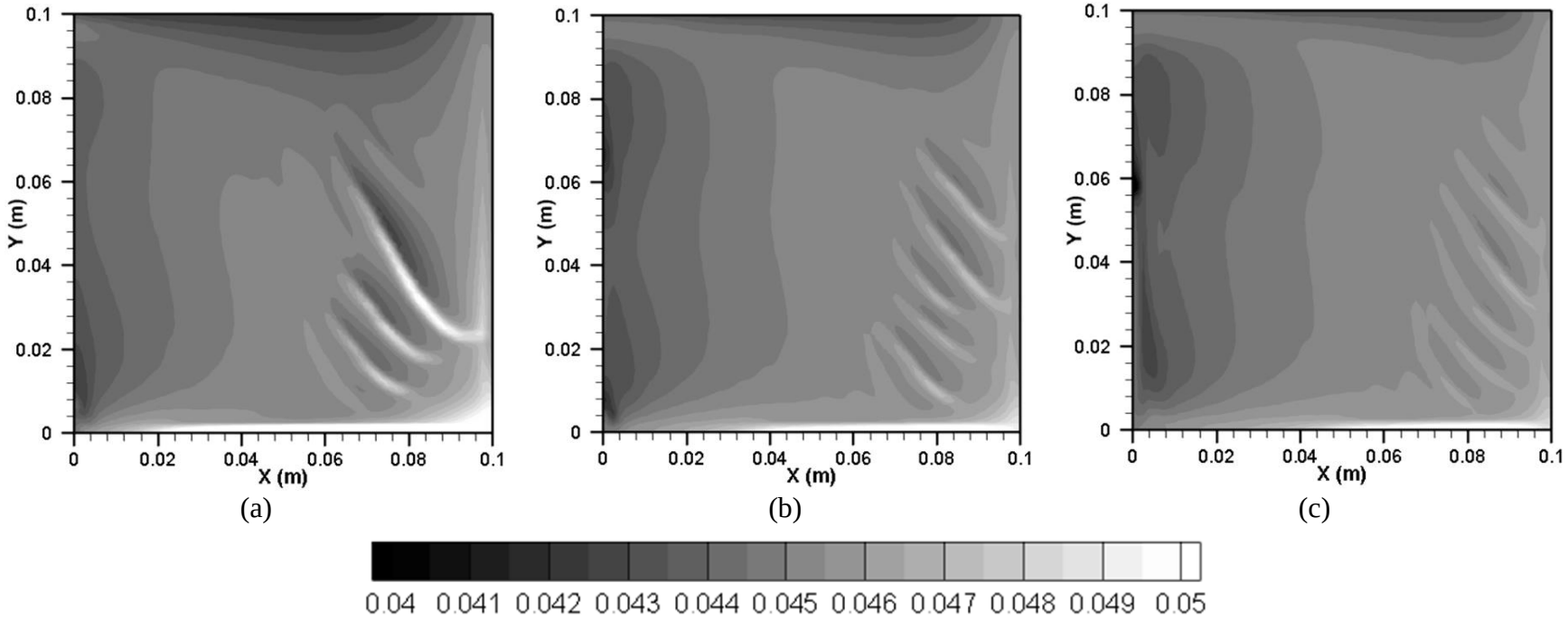

Figure A.8: Composition fields of fully solidified Al-4.5wt.%Cu for 3 different heat transfer coefficients. (a) h = 500 W/m^{2}K, (b) h = 1250 W/m^{2}K, (c) h = 2000 W/m^{2}K.

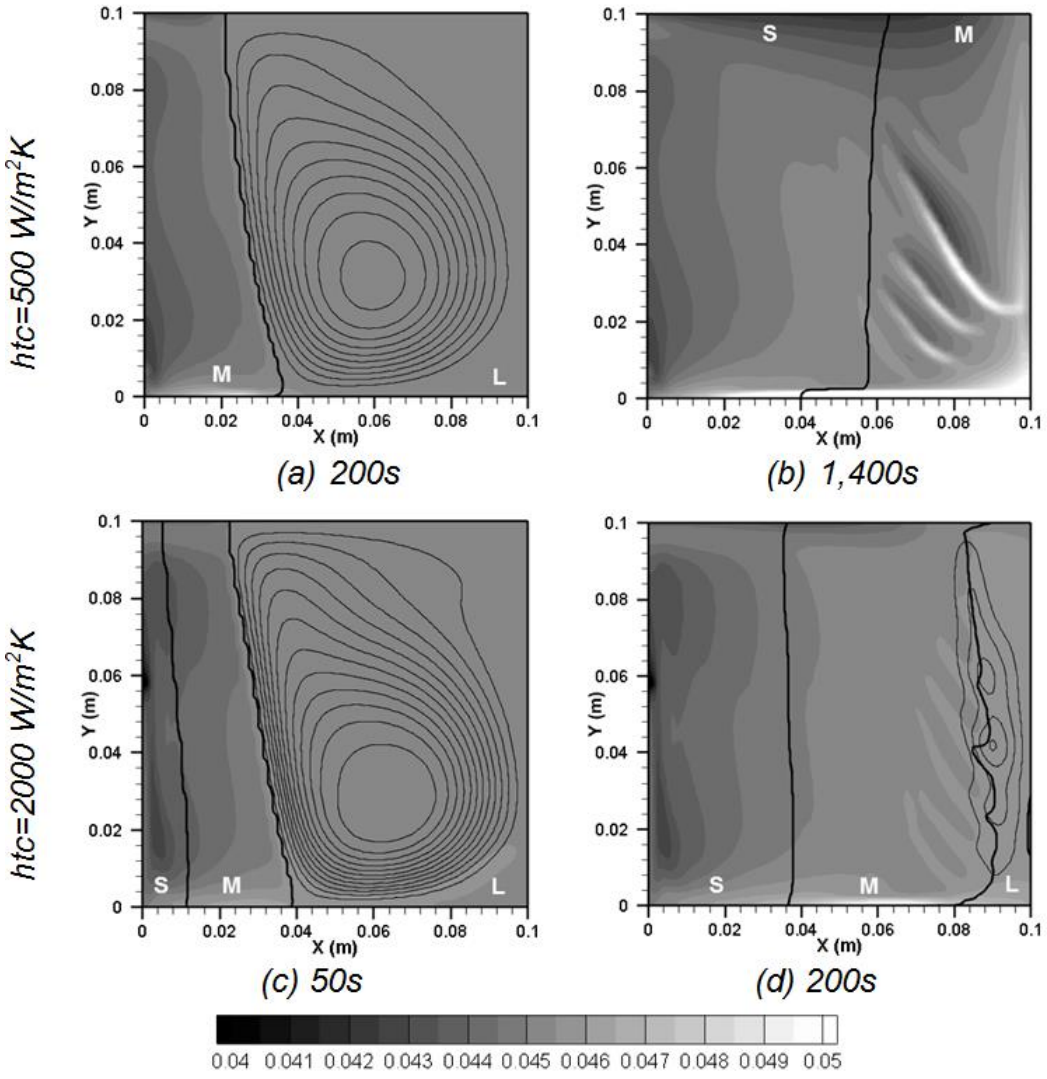

Figure A.9: Composition field plots at various times during the solidification of Al-4.5wt.%Cu with h = 500 W/m^{2}K at (a) 200 s and (b) 1400 s showing counterclockwise stream lines and the mushy zone extent. Results with h = 2,000 W/m^{2}K are shown (c) at 50 s and (d) at 200 s.

Differences in the distribution results for changes in the heat transfer coefficient are caused by coincident changes in the flow at the edge of the mush, where macrosegregation is caused by the relative motion of enriched liquid and depleted solid ($k_p<1$). Because copper is more dense than aluminum, the combined thermosolutal driving force of the enriched liquid near the liquidus temperature is downward, tending to collect in a copper rich region at the bottom of the domain. This natural convective flow is limited by the low permeability in the mush. At the beginning of the process, the thermal buoyancy is directly related to the boundary condition. For high heat transfer coefficients, a strong thermally driven convective flow carries enriched liquid away from the first solid to form towards the bottom of the domain, to be replaced by relatively lean liquid at the top. Lower heat transfer coefficients cause weaker thermally driven flow that advect less enriched liquid from the mush. The result is a region of solid at the left wall that is more depleted with stronger flows corresponding to higher cooling rates. This initially lengthens the left tail of the composition distribution with increasing heat transfer coefficient (Figure A.7). With even higher cooling rates, the amount of time available for advection of the enriched liquid become the dominant factor. Very high solidification rates freeze the liquid in place before significant macrosegregation can develop, eventually reducing the length of the left tail of the distribution as shown in Figure A.7(d). This slightly increases the asymmetry of the distribution, which explain the minimum, then increase in the difference between the macrosegregation number and the normalized Weibull deviation.

Later in the process, the level of macrosegregation is controlled by the width of the mush and the time available for the advection of solute. For low cooling rates and

therefore lower temperature gradients, the fractions solid gradient is also lower, and the mush is relatively wide, as shown in Figure A.9(a) and Figure A.9(b). The wider mush allows a larger region over which the permeability is high enough that thermosolutal buoyancy of the enriched liquid drives it out of the mush to collect at the bottom of the domain. Additionally, the slower solidification rate allows more time for advection to occur. At higher cooling rates, the mush is thinner (Figure A.8(c) and Figure A.8(d)), and other than in a very narrow region at the edge of the mush, the permeability is too low to allow significant solute transport. The distance over which solute is advected is also limited by the increased solidification rate. These factors generally result is more positive segregation at the bottom and right wall of the ingot for low cooling rates, and less for high cooling rates. Consequently, as shown in Figure A.7, the right tail of the distribution shrinks with increase heat transfer coefficient.

Next, a grid refinement study was conducted to test whether the normalized Weibull deviation was sensitive to the grid spacing, and therefore may be used to determine grid convergence. A previous study [90] showed that, in many solidification process simulations grid convergence was generally not achieved. The composition of the last liquid to freeze is averaged over its control volume, so as the grid is refined, the maximum composition tends to increase. It should be expected, therefore, that the right tail of the composition distribution will become larger, and the corresponding value of the normalized Weibull deviation will also increase similarly with the number of cells. The grid was varied from 40x40 to 180x180 and the resulting normalized Weibull deviation, macrosegregation number, and composition PDFs are shown in Figure A.10. There is a physical limitation to the grid refinement in that the permeability model for the mushy

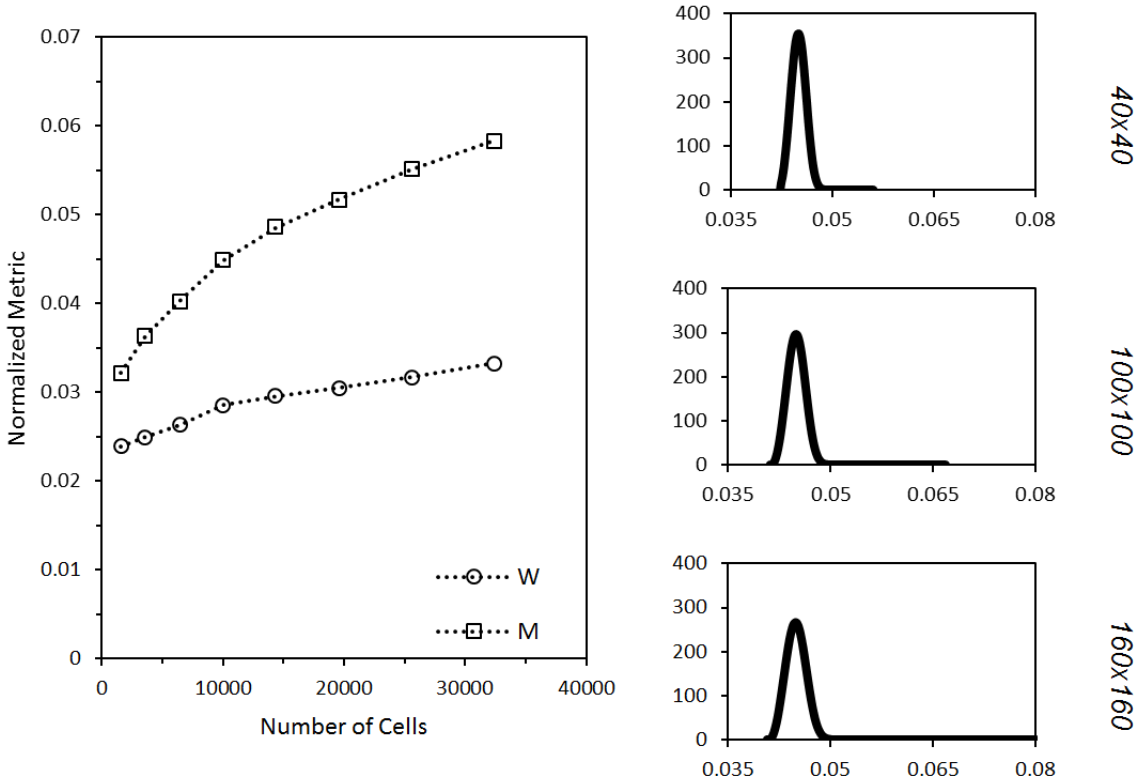

Figure A.10: The grid dependence of the normalized Weibull deviation and macrosegregation number for the case with a heat transfer coefficient of 500 W/m^{2}K. Plots at right show three examples of the fitted Weibull PDFs (x-axis is composition and y-axis is probability density), increasing in asymmetry with the number of cells.

zone assumes that the control volume is much larger than the dendrite arm spacing. Darcy's Law, used to derive the permeability terms in the momentum mixture equations, average out the details of flow through a porous medium. For fine grids, the continuum approximation breaks down and a model that predicts the alloy microstructure must be employed. As anticipated, both the macrosegregation number and normalized Weibull deviation increase with an increasing number of control volumes. This phenomenon was also reported by Voller and Vušanović, in which the composition that constituted a drop off of the survival function from the power law tail occurred at increasing values when the grid was refined [90]. Eventually the macrosegregation metrics will approach a constant value, as the composition of last liquid to freeze is limited by the eutectic point and further increasing the spatial resolution will not cause the highest solid composition to increase.

One of the disadvantages of the frequency analysis described by Voller and Vušanović [90] is that it strictly applies to a uniform grid. Here, the construction of the Weibull distribution is done by weighting each data point by its associated volume, so that results using non-uniform grids may be analyzed. To demonstrate the generality of the present method, simulations with various non-uniform grids were performed. Control volume faces were located using a power law scheme:

$$x_{face}^{i} = \left(\frac{i\, x_{tot}}{i_{max}}\right)^{n}, \tag{A.17}$$

where x_{face}^{i} is the location of control volume face *i*, x_{tot} is the size of the domain in the *x* direction, i_{max} is the total number of control volumes in the *x* direction, and *n* is the power law exponent. Equation (A.17) is only applied to the x direction (the direction of

the solidification front motion), and the y direction is left uniform. The grid was refined near the chill to have better resolution of the temperature and velocity gradients where the heat transfer and flow will be the strongest. Various values of n were used to compare the effect of successive grid refinement. Relatively small changes in the macrosegregation levels are expected, since most of the segregation occurs at the end of solidification where the grid resolution is most similar for all n values. Results are shown in Figure A.11 for both the normalized Weibull deviation and the macrosegregation number, as well as an example of the power law grid refinement in Equation (A.17) with n=1.5. Both macrosegregation metrics are unaffected by the level of grid nonuniformity as expected, which demonstrates that the Weibull deviation can be used on irregular grids.

Predicted Segregation in Multicomponent Inconel 625 Ingot

The purpose of this final example is to discuss the relationship among the macrosegregation levels of different chemical species in a complex multicomponent alloy. The model used for this study is the same as the previous Al-4.5 wt.% Cu example, with a 15 cm x 15 cm Cartesian domain. Again, the effect of the cooling condition is examined by varying the heat transfer coefficient from 1000 to 10,000 W/m^2K. The properties and solidification path of IN625 are taken from Fezi et al. [89]. The nominal compositions and partition coefficients for the primary alloying elements are given in Table A.1.

Table A.1: Nominal composition and partition coefficients for simulation of Alloy 625.

Element	**Nom. Comp. (wt.fr.)**	**k_p**
Cr	0.215	1.04
Fe	0.025	1.31
Mo	0.09	0.83
Nb	0.0365	0.54

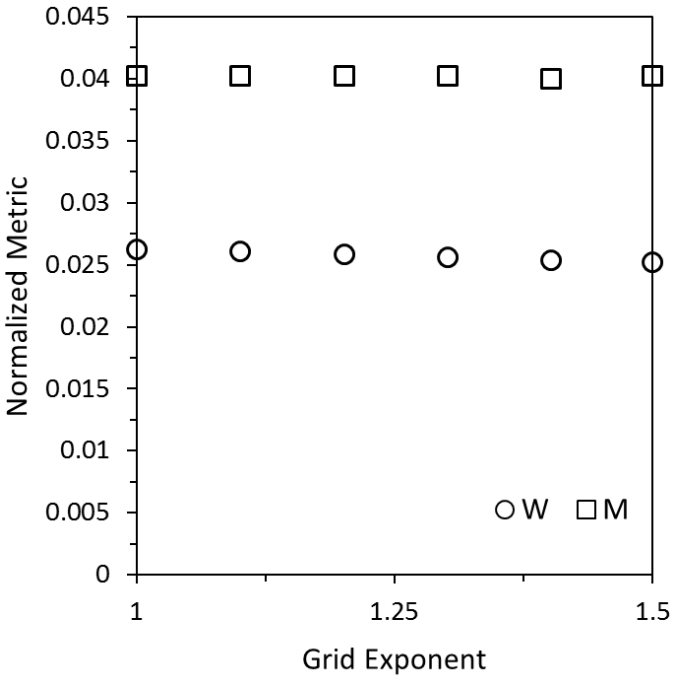

(a)

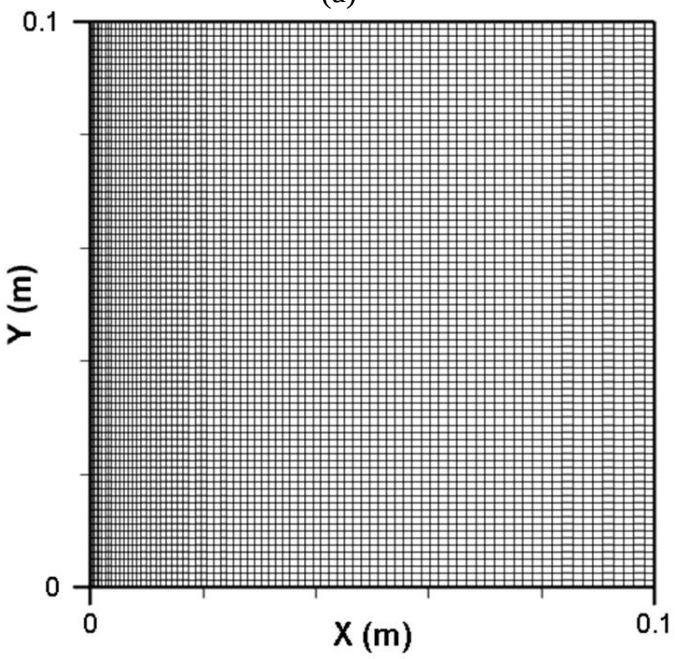

(b)

Figure A.11: The effect of a non-uniform grid on the normalized Weibull deviation and macrosegregation number plotted in (a) for power law grid spacing (in the x-direction) with various exponent values. An example of the non-uniform grids is shown in (b) for n = 1.5.

As discussed by Schneider and Beckermann [68], the macrosegregation number exhibits an interesting relationship for multicomponent alloys in which it is linear with the elemental partition coefficients on either side of k_p=1. Considering that the normalized Weibull deviation is equal to the macrosegregation for a symmetric composition distribution, it is not unexpected that a similar trend is seen with higher heat transfer coefficients (more symmetry in composition distribution), but this trend also holds for cases with less symmetric composition distributions (Figure A.12). For the case with the highest heat transfer coefficients, where the composition distributions are most symmetric, *W* is very close to *M*, and both metrics are linear with partition coefficient. At lower heat transfer coefficients, the normalized Weibull deviation is different from the macrosegregation number, indicating an asymmetric distribution, but retains linearity with partition coefficient, with a slightly different slope than the macrosegregation number. The linear relationship between *W* and k_p can be used to simplify numerical predictions of multicomponent solidification by reducing the number of composition equations, as discussed by Schneider and Beckermann [68]. They used the *M* vs. k_p relationship to reduce the number of composition equations that must be solved in solidification simulations of a 10 component steel alloy. However, when reducing the number of composition equations the solutal contribution of all pertinent alloying elements needs to be considered. Considering that the normalized Weibull deviation is a better representation of the composition field, using it to simplify the model in such a way will yield more accurate results than if the macrosegregation number was used.

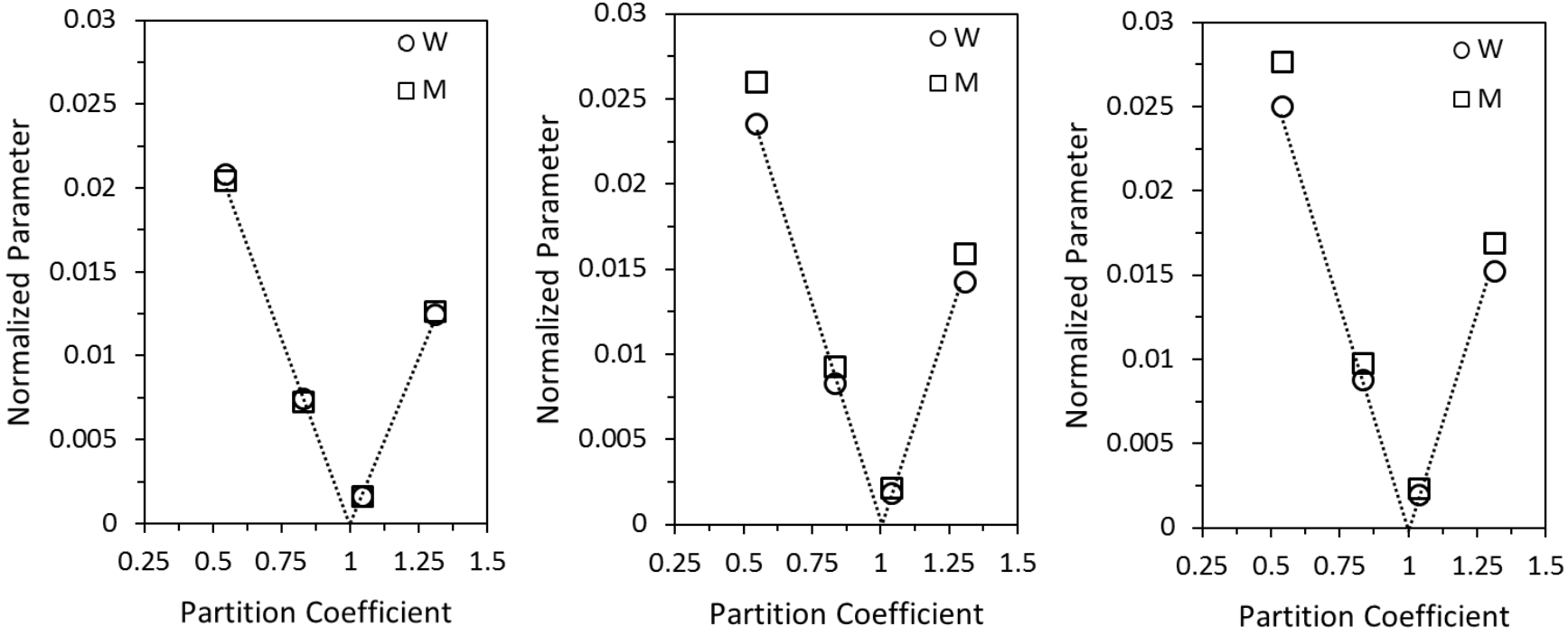

Figure A.12: Normalized Weibull deviation and macrosegregation numbers as a function of partition coefficient for the Alloy 625 cases with different cooling rates.

(a) h = 1000 W/m^{2}K, (b) h = 5000 W/m^{2}K, (c) h = 10,000 W/m^{2}K.

Conclusion

The three-parameter Weibull distribution was proposed as an improved metric for macrosegregation in alloy solidification than the macrosegregation number, Pareto distribution, or power law function. The process of fitting the distribution to a compositional data set was described and implemented for both experimental and numerical data from statically cast ingots with columnar solidification structures. Different solidification morphologies and casting processes will produce different compositional fields; however the process of fitting the distribution remains the same. (Composition distribution shapes similar to the static castings here are found in predictions of electroslag remelting [89].) The utility of the Weibull distribution was demonstrated in numerical simulations over a range of cooling rates which changed the symmetry of the composition distribution and was related to the associated transport phenomena. The normalized Weibull deviation was proposed as a new metric for quantifying macrosegregation, and was shown to illuminate trends which are not found with the macrosegregation number. The metric retains the property of being linear with partition coefficient for multicomponent alloys; which can be used to reduce the number of composition equations needed to model multicomponent solidification. The grid dependence of the Weibull deviation was analyzed and it was used to test for grid convergence. Additionally, the Weibull distribution was also able to characterize predicted segregation results using nonuniform grids.

.

Appendix B Example Uncertainty Quantification in Solidification Modeling

Abstract

Uncertainty quantification and sensitivity analysis are performed on a steady 1D model of filler rod continuous casting, including conduction, advection, and latent heat release and predicting liquidus and solidus position and solidification time. A Smolyak sparse grid algorithm constructs a model output polynomial response surface based on input uncertainty. This surface determines output PDFs and sensitivities to the inputs. A user interface for this model was developed and is publicly available online for use in teaching uncertainty quantification.

Deterministic Model Description

The solidification process modeled is the continuous casting of cylindrical welding filler rod. The cooling begins in a copper mold and secondary cooling is either water spray or natural convection in air. Figure B.1 depicts the geometry and boundary conditions. Due to the small radius, the heat transfer in the wire is treated as one dimensional:

$$k A_c \frac{\partial^2 T}{\partial x^2} - \rho c A_c V_{cast} \frac{\partial T}{\partial x} + \rho L_f A_c V_{cast} \frac{\partial f_s}{\partial x} - U P (T - T_\infty) = 0 , \quad \text{(B.1)}$$

where A_c is the cross-sectional area, L_f latent heat, U the heat transfer coefficient, c specific heat, k thermal conductivity, f_s fraction solid and P perimeter. The first term in equation 1 is the axial conduction, followed by advection of specific and latent heats and finally the heat lost radially due to cooling. The latent heat term is rewritten in terms of temperature using a relationship between T and fs, either a linear dependence or the Scheil model:

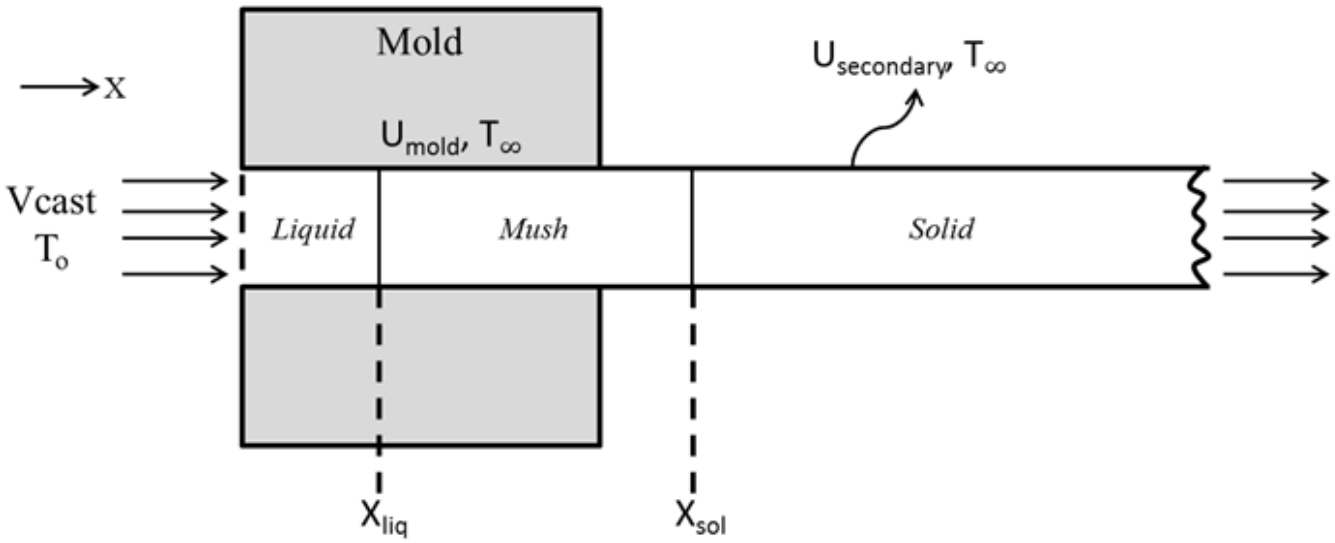

Figure B.1: Schematic diagram of the simulation domain showing the boundary conditions.

Linear: $f_s = \dfrac{T_{liq} - T}{T_{liq} - T_{sol}}$ (B.2a)

Scheil: $f_s = 1 - \left(\dfrac{T - T_m}{T_{liq} - T_m} \right)^{1/(k_p - 1)}$ (B.2b)

where T_m is the melting temperature of pure Ni and k_p the partition coefficient. After substituting the function of T in Equation (B.2a), Equation (B.1) is discretized using the finite volume method and upwind difference advection scheme over a uniform grid [43]. The alloy in this study is Ni superalloy 625, the properties of which are summarized in Table B.1.

Table B.1: Thermophysical properties of Alloy 625.

k [W/mK]	ρ [kg/m^3]	c [J/kgK]	L_f [J/kg]	T_{liq} [K]	T_{sol} [K]	T_m (Ni) [K]	k_p
25.2	8440	670	290,000	1636	1430	1728	Mo: 0.83

Discretization of the governing equation is straight forward except when in the mushy zone, where the advection of latent heat release and the f_s-T relationships become important. This term is discretized is by substituting Equation (B.2a) into the governing equation and integrating it over the "P" control volume. For the linear relationship (Equation (B.2a)) this discretization results:

$$a_E = \frac{\alpha}{\delta x_E}, \quad \text{(B.3a)}$$

$$a_W = \frac{\alpha}{\delta x_W} + V_{cast}, \quad \text{(B.3b)}$$

$$S_C = \frac{2U\Delta x}{\rho CR} T_\infty + \frac{V_{cast} T_{liq}}{St} - \frac{V_{cast} L_f}{C} \, fs_W \,, \tag{B.3c}$$

$$S_P = -\frac{2U\Delta x}{\rho CR} - \frac{V_{cast}}{St} \,, \tag{B.3d}$$

$$a_P = a_E + a_W + S_p \,, \tag{B.3e}$$

For $a_P T_P = a_E \; T_E + a_W \; T_W + S_C$, (B.3f)

where R is the radius of the wire, α (= $k/\rho c$) the thermal diffusivity, T_∞ the ambient temperature, and St (= $c(T_{liq} - T_{sol})/L_f$) is the Stefan number. The Scheil relationship (Equation (B.2b)) between the temperature and fraction is requires linearization of the form $S = S^* + \left(\frac{dS}{dT}\right)^* \left(T_P - T_P^*\right)$, where * indicates the temperature from the previous iteration, as in Patankar [43]. This linearization produces these source terms:

$$S_C = \frac{2U\Delta x}{\rho CR} T_\infty + \frac{L_f V_{cast}}{C} \left[1 - fs_W - \left(\frac{T_P^* - T_m}{T_{liq} - T_m} \right)^n + \frac{n T_P^*}{T_{liq} - T_m} \left(\frac{T_P^* - T_m}{T_{liq} - T_m} \right)^{n-1} \right], \tag{B.4a}$$

$$S_P = -\frac{2U\Delta x}{\rho CR} - \frac{L_f V_{cast} n}{C\left(T_{liq} - T_m\right)} \left(\frac{T_P^* - T_m}{T_{liq} - T_m} \right)^{n-1} \,, \tag{B.4b}$$

where n is the exponent in Equation (B.2b).

Scaling the governing equation reveals the relative importance of each term to an order of magnitude. Using the reference values X_L (distance to the liquidus temperature) for length and $\Delta T_O = T_O - T_\infty$ (T_O is the initial temperature) and $\Delta T_{OL} = T_O - T_{liq}$ for the heat loss and axial temperature differences the governing equation in the all-liquid region becomes:

$$\frac{\Delta T_{OL}}{X_L^2}, \frac{V_{cast}\Delta T_{OL}}{\alpha X_L} \sim \frac{U\Delta T_O}{kR}. \tag{B.5}$$

Assuming the conduction term is negligible, an expression for X_L is found through a balance of advection and heat loss terms:

$$X_L \approx \frac{V_{cast}kR}{\alpha U}\frac{\Delta T_{OL}}{\Delta T_O}. \tag{B.6}$$

The assumption of neglecting the conduction term is valid when advection is much larger than conduction:

$$\frac{Advection}{Conduction} \approx \frac{V_{cast}\Delta T_{OL} \big/ \alpha X_L}{\Delta T_{OL} \big/ X_L^2} \approx \frac{V_{cast}X_L}{\alpha} \approx \frac{V_{cast}^2 kR}{\alpha^2 U}\frac{\Delta T_{OL}}{\Delta T_O} >> 1. \tag{B.7}$$

As a typical example, using a rod radius of 1mm and Alloy 625 (Table B.1), Equation (B.7) is plotted in Figure B.2 for a range of heat transfer coefficients. For the lower heat transfer coefficients, the axial conduction term can be neglected for $V_{cast} > 0.1$ m/s, and for the entire range of U if $V_{cast} > 0.2$ m/s. When the conduction term is neglected, the governing equation outside of the mushy zone is:

$$\frac{\partial T}{\partial x} + \frac{2U\alpha}{kRV_{cast}}\left(T - T_\infty\right) = 0. \tag{B.8}$$

Equation (B.8) is solved analytically, and is valid between the entrance of the mold, where $T(x=0) = T_O$, and the beginning of solidification, where $T(x=X_L) = T_{liq}$. The temperature distribution and position of the liquidus interface are:

$$T(x) = T_\infty + \left(T_O - T_\infty\right)\exp\left[-\left(\frac{2U}{\rho C V_{cast} R}\right)x\right] \tag{B.9}$$

and

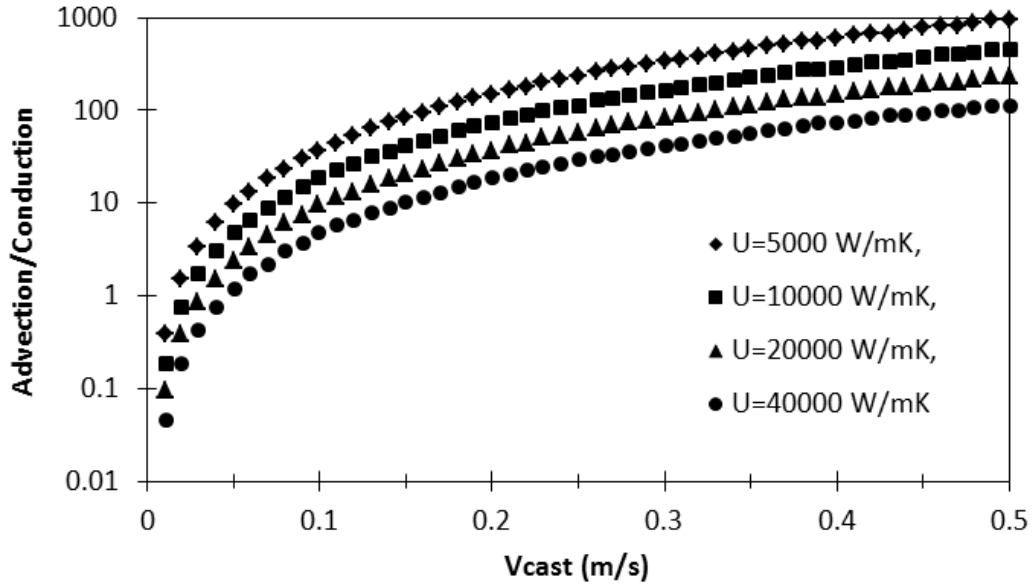

Figure B.2: Order of magnitude for the ratio of the advection and conduction of sensible heat for a 1mm wire radius for Alloy 625 showing that for casting velocities greater than 0.2 m/s that conduction can be neglected.

$$X_L = -\left(\frac{\rho C R V_{cast}}{2U}\right)\ln\left(\frac{T_{liq} - T_\infty}{T_O - T_\infty}\right). \tag{B.10}$$

In the mushy zone the latent heat is released and advected due to the phase change, and the governing equation then becomes:

$$\frac{\partial T}{\partial x} - \frac{L_f}{C}\frac{\partial fs}{\partial T}\frac{\partial T}{\partial x} + \frac{2U\alpha}{kRV_{cast}}\left(T - T_\infty\right) = 0, \tag{B.11}$$

where the spatial derivative of the fraction solid is rewritten to incorporate Equation (B.2a). Using the linear dependence (Equation (B.2a)), $\frac{\partial fs}{\partial T} = \frac{-1}{T_{liq} - T_{sol}}$ and the solution is:

$$T(x) = T_\infty + \left(T_{liq} - T_\infty\right)\exp\left[-\left(\frac{St}{St+1}\right)\left(\frac{2U}{\rho C R V_{cast}}\right)\left(x - X_L\right)\right]. \tag{B.12}$$

Equation (B.12) is valid in the mushy zone, between $x=X_L$ and $x=X_S$, where the temperature is between the liquidus and solidus. The position of the solidus temperature, where $T(x=X_S) = T_{sol}$, can be found from Equation (B.12):

$$X_S = X_L - \frac{St+1}{St}\frac{\rho C R V_{cast}}{2U}\ln\left(\frac{T_{sol} - T_\infty}{T_{liq} - T_\infty}\right). \tag{B.13}$$

In this work, both the analytical solution to the limited case (linear f_s-T, no conduction, one U value) in Equations (B.9), (B.10), (B.12), and (B.13) and the more widely applicable numerical solution of the discretized Equations (B.3a) and (B.4a) are used to illustrate the quantification of uncertainty in this simple solidification process.

Results and Discussion

Three cases were studied to quantify effects of the input uncertainties on the output of the model. The uncertainty quantification model calculates a PDF for each of the three output quantities of interest (X_L, X_S, and $t_S=[X_S-X_L]/V_{cast}$), given the known uncertainty distributions of select inputs (ρ, C_p, L_f, k, and U_m). All of the calculations used a wire radius of 0.001 m, a casting speed of 0.2 m/s, a superheat of 20 K, and an ambient temperature of 300 K. Table B.2 lists the uncertainty of the inputs used in both cases in the form of normal distributions with a mean, μ, and standard deviation, σ. The first (Case A) neglects the axial conduction term, only has one heat transfer boundary condition as a boundary condition, and assumes the $f_S(T)$ function in Equation (B.2a). Case B has the same condtions, except it includes the axial conduction term. The uncertainties in the inputs for Case A were chosen to be small, $2\sigma = 0.01\mu$, such that multivariable effects would be negligible allowing a proper comparison to analytical uncertainty quantification. A level 1 Smolyak run was used to calculate response surfaces for Cases A and B. Figure B.3 shows the PDF of each output from the model for Case A, where the mean of X_L is 0.00169 m with a deviation of $1.4\text{x}10^{-5}$ m, the mean of X_S is 0.0431 m with a deviation of $3.58\text{x}10^{-4}$ m, and the mean of t_S is 0.207 s with a deviation of $1.74\text{x}10^{-3}$ s. The behaviors of these solutions found through the model in the PUQ environment are compared to the closed form expressions from the analytical solutions (Equations (B.10) and (B.13)). These expressions are based on

$$\sigma_y = \sqrt{\sum_{i=1}^{m}\left(\sigma_i \frac{\partial y_i}{\partial x_i}\right)^2}\ , \tag{B.14}$$

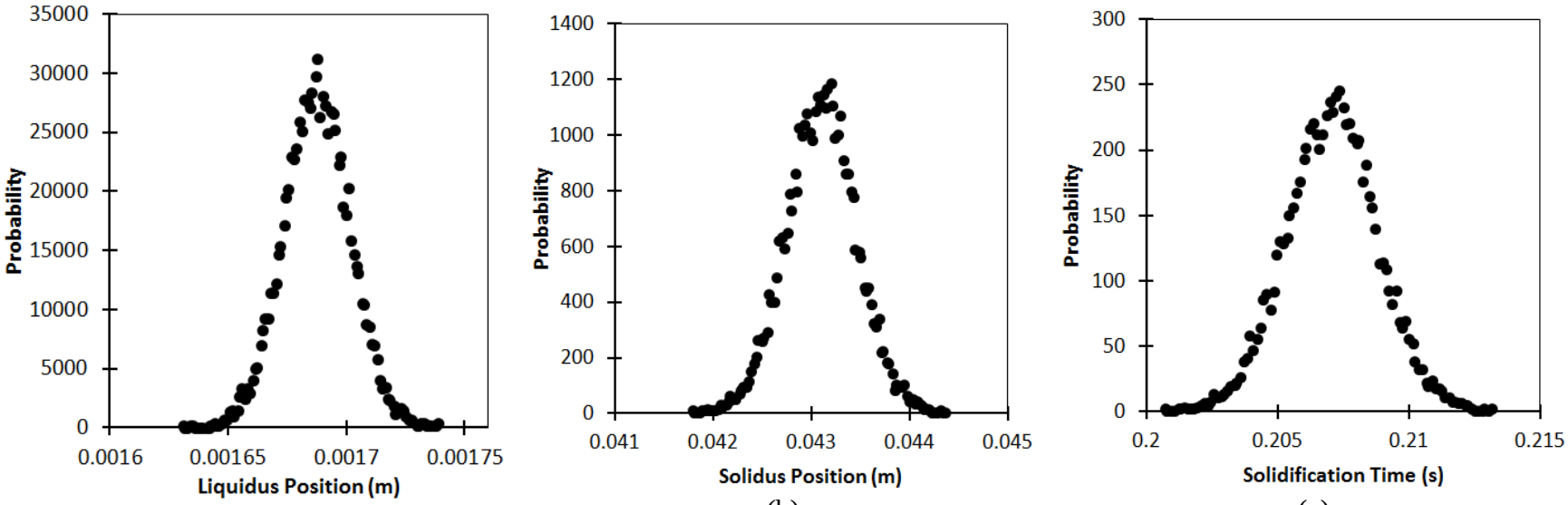

Figure B.3: Probability density functions of the model outputs for Case A as determined by PUQ.

where y is an output quantity of interest, x is an uncertain input, and m is the number of uncertain inputs. The comparison between the analytical and numerical uncertainties is shown in Table B.3, where the analytical mean was calculated using the mean values in Table B.2. The analytical and numerical uncertainties agree very well with each other, as they are both linear dependent on the inputs, with the most certain result being X_L followed by X_S and the most uncertain calculation being t_S.

Table B.2: Uncertainty of input parameters in the form of a normal distribution.

Input Parameter	**Case A**	**Case B**	**Case C**
Thermal Conductivity [W/mK]	-	μ: 25.2 σ: 0.126	μ: 25.2 σ: 0.63
Density [kg/m^3]	μ: 8440 σ: 42.2	μ: 8440 σ: 42.2	μ: 8440 σ: 211
Specific Heat [J/kgK]	μ: 670 σ: 3.35	μ: 670 σ: 3.35	μ: 670 σ: 16.75
Latent Heat [J/kg]	μ: 290000 σ: 1450	μ: 290000 σ: 1450	μ: 290000 σ: 7250
Primary Heat Transfer Coefficient [W/m^{2}K]	μ: 5000 σ: 25	μ: 5000 σ: 25	μ: 5000 σ: 750
Secondary Heat Transfer Coefficient [W/m^{2}K]	-	-	μ: 10000 σ: 1500
Partition Coefficient	-	-	μ: 0.83 σ: 0.02075

Table B.3: Comparison between the analytical and model uncertainties for Case A.

Output of Interest	**Analytical Solution**		**Case A**	
X_L [m]	μ: 0.00168	σ: 1.48x10^{-5}	μ: 0.00169	σ: 1.40x10^{-5}
X_S [m]	μ: 0.0431	σ: 3.59x10^{-4}	μ: 0.0431	σ: 3.58x10^{-4}
t_S [s]	μ: 0.207	σ: 1.74x10^{-3}	μ: 0.207	σ: 1.74x10^{-3}

The sensitivity of the output quantities of interest from the numerical model of Case A, which were calculated using the EEM, are shown in Table B.4. The table also

shows the corresponding sensitivities of the analytical solutions for X_L (Equation (B.10)), X_S (Equation (B.13)), and t_S, found from the derivatives of these equations with respect to each uncertain input parameter, which can be compared to μ^*. For the X_L sensitivity, the latent heat has no effect because no phase change occurs before the temperature reaches the liquidus. The heat transfer coefficient, density, and specific heat all had the same μ^* and varied linearly with X_L (σ = 0). The order of magnitude of the sensitivity from the analytical solution doesn't match the numerical, but the trends of the sensitivities do. The analytical sensitivity was calculated by taking the derivative of the analytical solution about a certain point, the mean, while the numerical sensitivity was calculated using the EEM which creates a distribution of sensitivities and interactions with other parameters can affect the value. This could account for the difference in the values between the two sensitivity measures. Examining the sensitivity for X_S shows that the latent heat has now become important due to the phase change that occurs in the mushy zone and varies linearly with X_S. The specific heat has the smallest effect on the position of the solidus and the heat transfer coefficient and the density have the largest effect. For t_S, the specific heat once again has the smallest effect and the heat transfer coefficient has the greatest effect. The analytical solution for X_s and t_s shows that the density and heat transfer coefficient appear in every term while the specific does not, and the density and heat transfer coefficient appear in the latent heat term in both equations. The latent heat term controls the amount of heat released and also the additional amount of heat needed to be removed during solidification to fully solidify the rod. This causes these outputs to depend more strongly on the density, heat transfer coefficient, and latent heat than the specific heat.

Table B.4: Comparison of the sensitivity of the uncertain inputs on the outputs for the analytical and numerical solutions for Case A.

Sensitivity Parameter	**Analytical Sensitivity X_L [m]**	**Case A X_L [m]**	**Analytical Sensitivity X_S [m]**	**Case A X_S [m]**	**Analytical Sensitivity t_S [s]**	**Case A t_S [s]**
Density [kg/m^3]	8.4x10^{-6}	μ^*: 5.0x10^{-5} σ: 0	2.15x10^{-4}	μ^*: 1.33x10^{-3} σ: 2.5x10^{-5}	1.04x10^{-3}	μ^*: 6.38x10^{-3} σ: 1.25x10^{-4}
Specific Heat [J/kgK]	8.9x10^{-6}	μ^*: 5.0x10^{-5} σ: 0	3.08x10^{-5}	μ^*: 1.75x10^{-4} σ: 2.5x10^{-5}	1.09x10^{-4}	μ^*: 6.25x10^{-4} σ: 1.25x10^{-4}
Latent Heat [J/kg]	0	μ^*: 0 σ: 0	1.86x10^{-4}	μ^*: 1.15x10^{-3} σ: 0	9.32x10^{-4}	μ^*: 5.75x10^{-3} σ: 2.78x10^{-17}
Heat Transfer Coefficient [W/m^{2}K]	8.4x10^{-6}	μ^*: 5.0x10^{-5} σ: 0	2.15x10^{-4}	μ^*: 1.33x10^{-3} σ: 2.5x10^{-5}	1.04x10^{-3}	μ^*: 6.38x10^{-3} σ: 1.25x10^{-4}

The 1D model was run with thermal conductivity to evaluate the scaling analysis (Case B), which showed the conduction term is deemed negligible. Table B.5 shows the identical mean outputs for X_S and t_S, and a slightly larger value for X_L in Case B. The standard deviations also differ less than 1%. The negligible effect of the axial conduction term indicates that this effect is negligible as shown by the scaling analysis.

Table B.5: Uncertainties of output quantities of interest for Case A and Case B.

Output of Interest	**Case A**	**Case B**
X_L [m]	μ: 0.00169 σ: 1.40x10^{-5}	μ: 0.00171 σ: 1.41x10^{-5}
X_S [m]	μ: 0.0431 σ: 3.58x10^{-4}	μ: 0.0431 σ: 3.6x10^{-4}
t_S [s]	μ: 0.207 σ: 1.74x10^{-3}	μ: 0.207 σ: 1.75x10^{-3}

A more complicated numerical case was run for which there is no analytical solution. Case C uses the Scheil model (Equation (B.2a)) and two different heat transfer coefficients (inside and outside the mold). The alloy was simplified to a Ni-Mo binary in

which the partition coefficient was assumed constant and calculated at several temperatures in which the uncertainty was based on the variation in those calculations. The phase diagram used to find the partition coefficient was taken from Singleton et al. [94]. A level 3 Smolyak sparse grid algorithm was run because the response surface fit was much better than levels 1 and 2 according to the root mean square error (RMSE). The sensitivities are given in Table B.6 and the output uncertainty in Table B.7. The most uncertain output is the solidification time and the most certain output is the location of the liquidus temperature. All outputs are most sensitive to the mold heat transfer coefficient, followed by material properties such as ρ, C_p, or L_f. This is because the heat transfer coefficients have a larger uncertainty than the other inputs and the mold region occupies the majority of the mushy zone. Even though the partition coefficient determines the freezing range of the alloy, other material properties determine the amount of heat needed to be removed from the system to fully solidify the rod and therefore have a larger influence on the outputs. Visually assessing the fits of the calculated response surfaces to the simulation data becomes difficult with more than two inputs, so here only the two inputs to which the three outputs are most sensitive (density and mold heat transfer coefficient) are used as uncertain inputs to assess the response surface fit for Smolyak levels 1-3 (Figure B.4-Figure B.6).

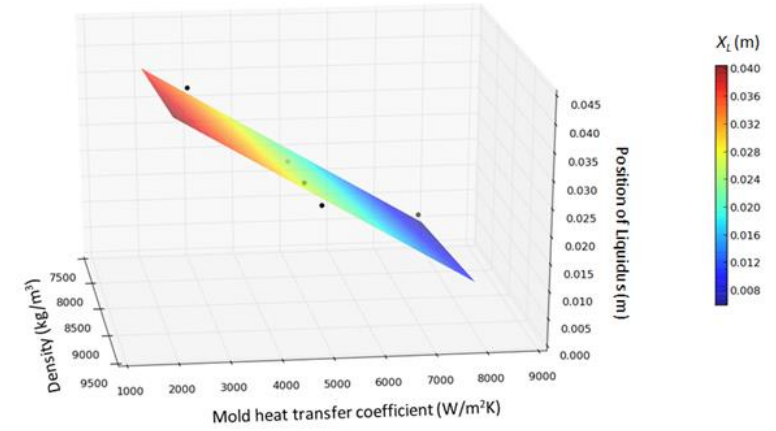

RMSE = 11.4%

(a)

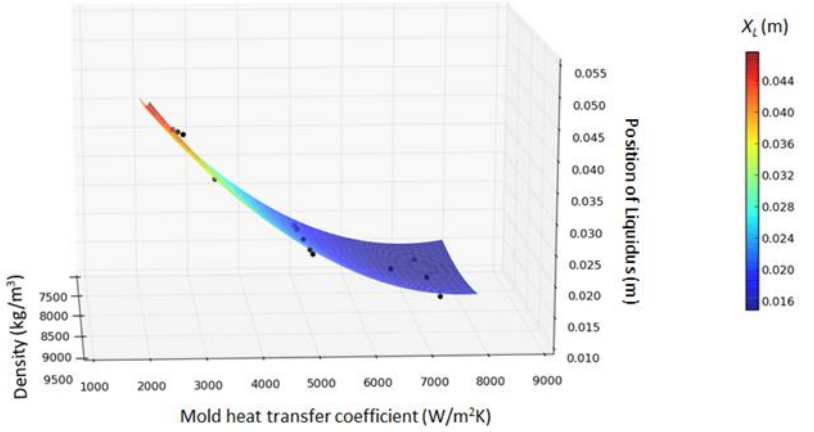

RMSE = 3.08%

(b)

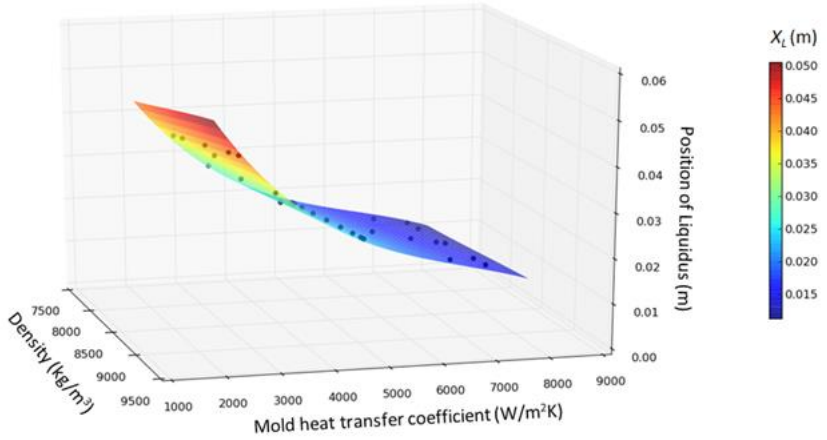

RMSE = 0.763%

(c)

Figure B.4: Response surfaces and corresponding RMSE for the position of the liquidus temperature (X_L) for Smolyak (a) level 1, (b) level 2, and (c) level 3. Black dots indicate X_L values for individual simulations chosen by the sparse grid algorithm.

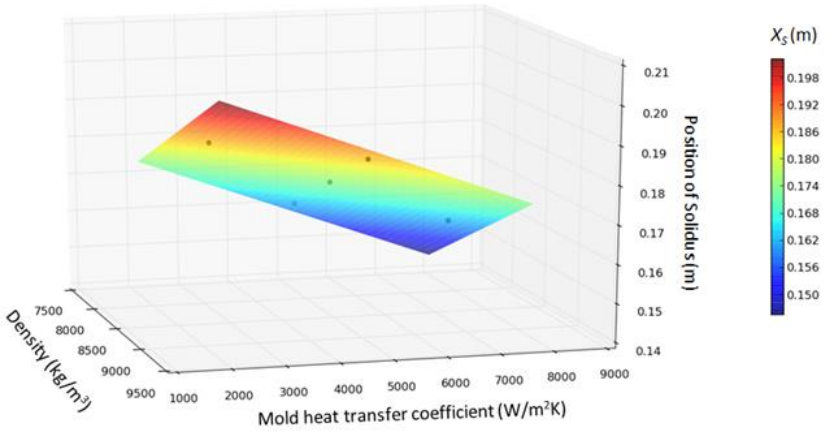

RMSE = 0.0268%

(a)

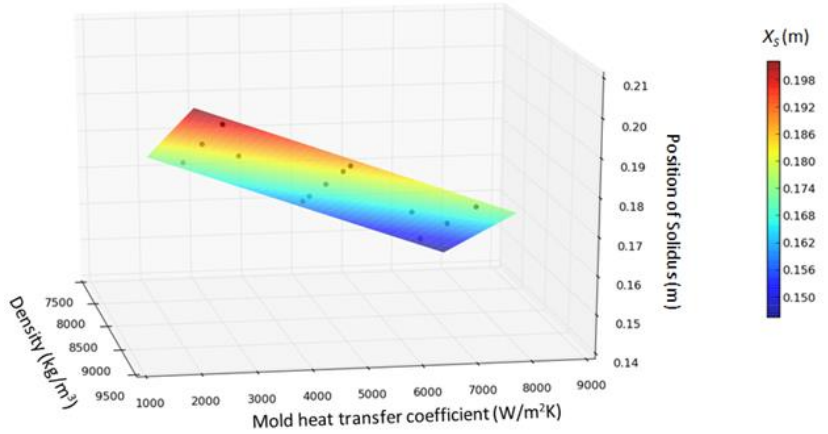

RMSE = 0.0361%

(b)

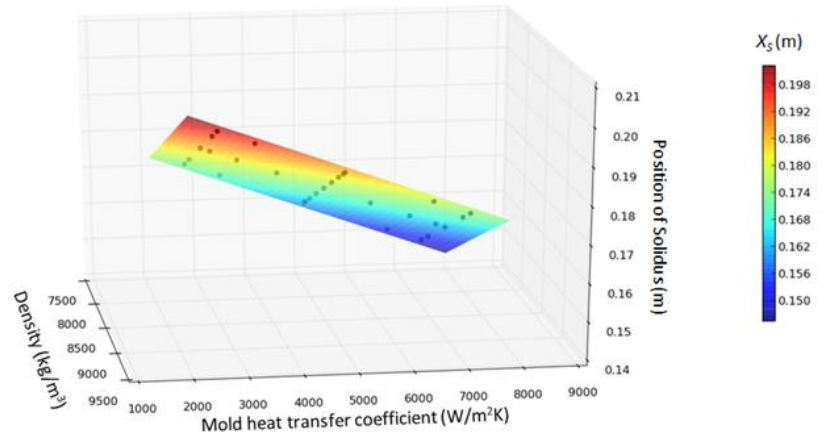

RMSE = 0.0387%

(c)

Figure B.5: Response surfaces and corresponding RMSE for the position of the solidus temperature for Smolyak (a) level 1, (b) level 2, and (c) level 3.

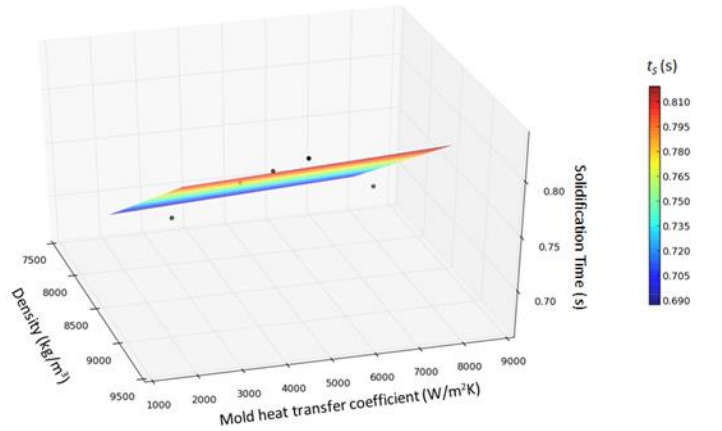

RMSE = 14.4%

(a)

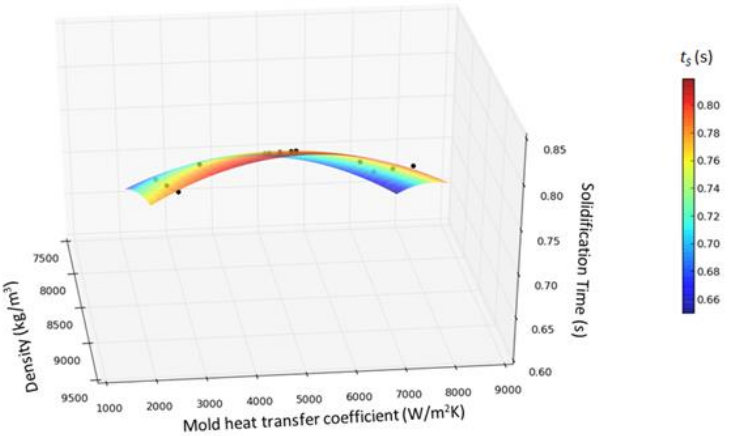

RMSE = 3.57%

(b)

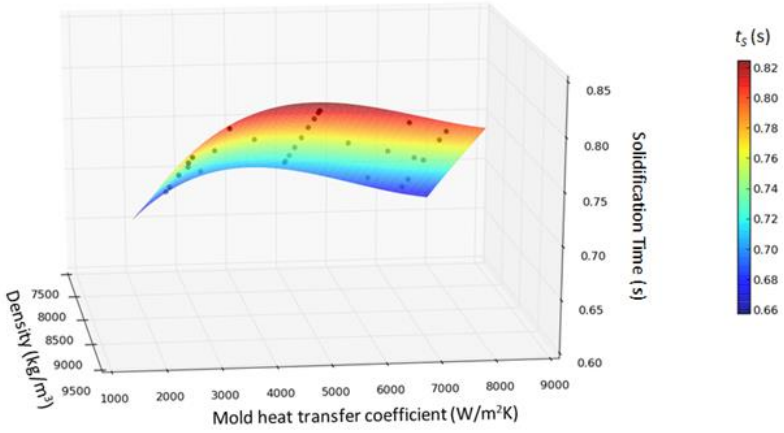

RMSE = 0.883%

(c)

Figure B.6: Response surfaces and corresponding RMSE for the solidification time for Smolyak (a) level 1, (b) level 2, and (c) level 3.

Table B.6: Sensitivity of the outputs to the uncertain inputs for Case C.

Sensitivity Parameter	X_L **[m]**	X_S **[m]**	t_S **[s]**
Density [kg/m^3]	μ^*: 2.66x10^{-4} σ: 9.38x10^{-5}	μ^*: 4.94x10^{-3} σ: 1.42x10^{-3}	μ^*: 2.33x10^{-2} σ: 7.17x10^{-3}
Specific Heat [J/kgK]	μ^*: 2.66x10^{-4} σ: 9.39x10^{-5}	μ^*: 1.78x10^{-3} σ: 5.11x10^{-4}	μ^*: 7.57x10^{-3} σ: 2.66x10^{-3}
Latent Heat [J/kg]	μ^*: 5x10^{-7} σ: 4.97x10^{-6}	μ^*: 3.16x10^{-3} σ: 9.09x10^{-4}	μ^*: 1.58x10^{-2} σ: 4.55x10^{-3}
Thermal Conductivity [W/mK]	μ^*: 3.85x10^{-6} σ: 1.68x10^{-5}	μ^*: 5x10^{-7} σ: 4.97x10^{-6}	μ^*: 2.18x10^{-5} σ: 9.04x10^{-5}
Partition Coefficient	μ^*: 1.25x10^{-6} σ:7.81x10^{-6}	μ^*: 1.35x10^{-4} σ: 4.77x10^{-5}	μ^*: 6.81x10^{-4} σ: 2.41x10^{-4}
Mold Heat Transfer Coefficient [W/m^{2}K]	μ^*: 2.02x10^{-3} σ: 1.09x10^{-3}	μ^*: 2.69x10^{-2} σ: 5.96x10^{-3}	μ^*: 1.24x10^{-1} σ: 3.21x10^{-2}
Secondary Heat Transfer Coefficient [W/m^{2}K]	μ^*: 0 σ: 0	μ^*: 5.74x10^{-3} σ: 6.54x10^{-3}	μ^*: 2.87x10^{-2} σ: 3.27x10^{-2}

Table B.7: Uncertainties of output quantities of interest for Case C.

Output of Interest	**Case C**
X_L [m]	μ: 0.00184 σ: 2.94x10^{-4}
X_S [m]	μ: 0.054 σ: 4.13x10^{-3}
t_S [s]	μ: 0.261 σ: 1.93x10^{-2}

A Level 1 analysis fits a linear or flat plane response surface to the output data and does not take into account interactions among the input variables. For Case C, the linear surface is a poor fit for X_L and t_S, but is much better for X_S, as indicated by its much lower RMSE. The Level 2 response surface takes into account the curvature of the output data and fits the data much better for X_L and t_S. Because X_S is truly linear with respect to

density and the mold heat transfer coefficient, the input interactions that the higher order schemes include give a slightly worse fit than level 1, although the RSME change is small. The level 3 surface has the best fit for X_L and t_S according to the RMSE, because this level does a better job of capturing the input interactions.

Case C was run with level 3 analyses at various casting speeds, V_c, to examine the effect of the uncertainty of the outputs. Figure B.7 shows the results from these simulations. Both the mean and deviation of X_L and X_S increase with V_c but at different rates, indicated by t_S having a maximum at a low V_c and then decreasing with increasing V_c. At low V_c X_S increases much faster than X_L, but as V_c continues to increase X_S changes slope and X_L begins to close the gap which causes the maximum in t_S. Additionally, the amount of heat required to be removed to reach the liquidus temperature remains constant over various casting speeds and is always removed by the mold region. While the heat is removed from the mushy by a combination of the mold and secondary heat transfer coefficient at large V_c and only the mold at low Vc and is dependent on the solidification rate. The uncertainty in t_S is also large at low V_c but decreases substantially for large V_c. At low V_c, X_L and X_S are similar in order of magnitude, making small differences result in large uncertainties in t_S, while, for large V_c, X_S is much larger than X_L, so small fluctuations do not impact t_S.

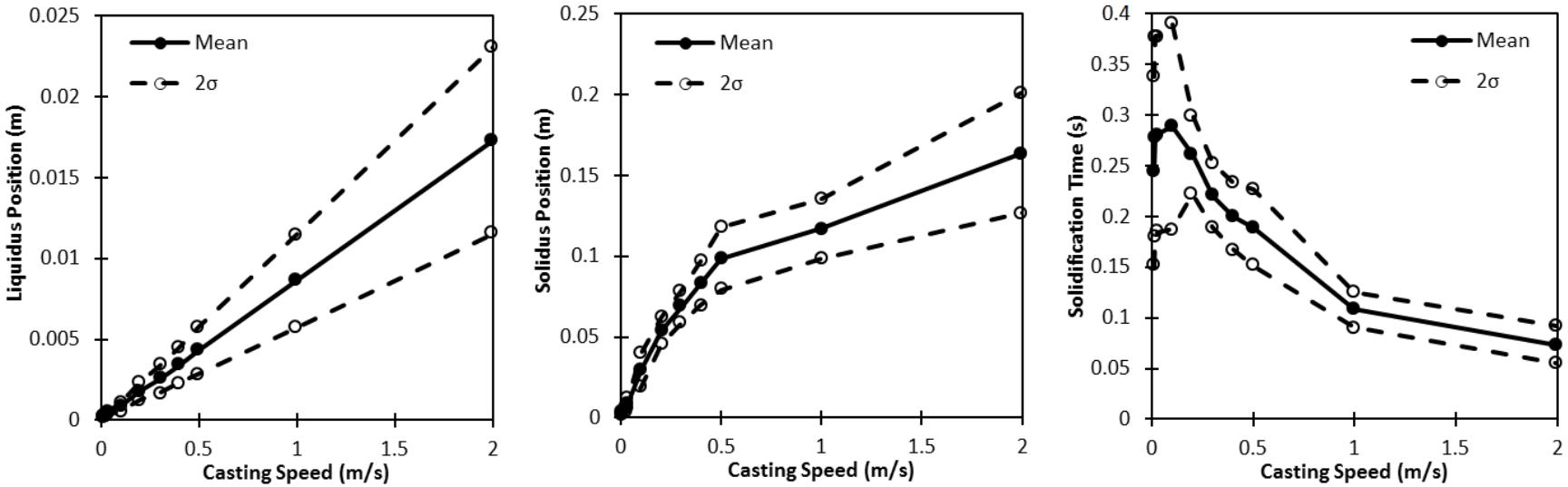

Figure B.7: X_L, X_S, and t_S for Case C as a function of Pe where the black dots are the mean values and the white dots are 2σ away from the mean.

Conclusions

PUQ was able to quantify uncertainties in a simple 1D, steady solidification model of the continuous casting of weld filler wire. The UQ software and the closed form uncertainty analysis agreed for input uncertainites that were small enough to eliminate their interactions. The sensitivity analysis showed that neglecting axial conduction was a good approximation, as suggested by scaling analysis. A more realistic and complicated model showed the inputs to which the outputs were most sensitive are the heat transfer coefficients. Material properties with the most influence on the outputs were the specific heat, density, and (for X_S) latent heat. This ranking indicates that, in this case and assuming the input uncertainties are reasonable, there should be a priority for finding better, less uncertain, estimates of the heat transfer boundary conditions over property data. The uncertainty in t_S decreased with increasing casting speed, while the uncertainty increased for X_L and X_S.

Appendix C Surrogate Model Equations Used in Uncertainty Quantification

The surrogate models that were fit to the numerical model and used to produce the output probability density functions are given in the tables below. Special care should be taken when using these functions, as they are applicable to the specific process and alloy described in this paper. These functions should also not be extrapolated for input values outside the ranges discussed previously. The authors' intent is that these functions can be used for comparison to other solidification models or experimental results that are configured for this same process. Also, predictions of this process can be done without building the numerical model. However, knowledge of the numerical considerations that went into developing the original numerical model should still be considered when analyzing the results from the functions below.

Surrogate Models Used in CHAPTER 5: Uncertainty Quantification in Metal Alloy Solidification

The equations are ordered based on their number of dependent variables (x_i) and degree of polynomial. Each constant in the equation is denoted as A_i. Equation (C.1) is a cubic polynomial with one dependent variable which is the result of a Level 3 Smolyak run. Equations (C.2)-(C.4) have four dependent variables, but are cubic, quadratic, and linear polynomials respectively. Equation (C.5) is a quadratic polynomial with six dependent variables and Equation (C.6) is a linear polynomial with seven dependent variables.

General form of the equations:

$$y = A_1 x^3 + A_2 x^2 + A_3 x + A_4 \quad \text{(C.1)}$$

$$\begin{aligned} y = {} & A_1 x_1^3 + A_2 x_1^2 x_2 + A_3 x_1^2 x_3 + A_4 x_1^2 x^4 + A_5 x_1^2 + A_6 x_1 x_2^2 + A_7 x_1 x_2 x_3 \\ & + A_8 x_1 x_2 x_4 + A_9 x_1 x_2 + A_{10} x_1 x_3^2 + A_{11} x_1 x_3 x_4 + A_{12} x_1 x_3 + A_{13} x_1 x_4^2 \\ & + A_{14} x_1 x_4 + A_{15} x_1 + A_{16} x_2^3 + A_{17} x_2^2 x_3 + A_{18} x_2^2 x_4 + A_{19} x_2^2 + A_{20} x_2 x_3^2 \\ & + A_{21} x_2 x_3 x_4 + A_{22} x_2 x_3 + A_{23} x_2 x_4^2 + A_{24} x_2 x_4 + A_{25} x_2 + A_{26} x_3^3 + A_{27} x_3^3 x_4 \\ & + A_{28} x_3^2 + A_{29} x_3 x_4^2 + A_{30} x_3 x_4 + A_{31} x_3 + A_{32} x_4^3 + A_{33} x_4^2 + A_{34} x_4 + A_{35} \end{aligned} \quad \text{(C.2)}$$

$$\begin{aligned} y = {} & A_1 x_1^2 + A_2 x_1 x_2 + A_3 x_1 x_3 + A_4 x_1 x_4 + A_5 x_1 + A_6 x_2^2 + A_7 x_2 x_3 + A_8 x_2 x_4 \\ & + A_9 x_3 + A_{10} x_3^2 + A_{11} x_3 x_4 + A_{12} x_3 + A_{13} x_4^2 + A_{14} x_4 + A_{15} \end{aligned} \quad \text{(C.3)}$$

$$y = A_1 x_1 + A_2 x_2 + A_3 x_3 + A_4 x_4 + A_5 \quad \text{(C.4)}$$

$$\begin{aligned} y = {} & A_1 x_1^2 + A_2 x_1 x_2 + A_3 x_1 x_3 + A_4 x_1 x_4 + A_5 x_1 x_5 + A_6 x_1 x_6 + A_7 x_1 + A_8 x_2^2 \\ & + A_9 x_2 x_3 + A_{10} x_2 x_4 + A_{11} x_2 x_5 + A_{12} x_2 x_6 + A_{13} x_2 + A_{14} x_3^2 + A_{15} x_3 x_4 \\ & + A_{16} x_3 x_5 + A_{17} x_3 x_6 + A_{18} x_3 + A_{19} x_4^2 + A_{20} x_4 x_5 + A_{21} x_4 x_6 + A_{22} x_4 + A_{23} x_5^2 \\ & + A_{24} x_5 x_6 + A_{25} x_5 + A_{26} x_6^2 + A_{27} x_6 + A_{28} \end{aligned} \quad \text{(C.5)}$$

$$y = A_1 x_1 + A_2 x_2 + A_3 x_3 + A_4 x_4 + A_5 x_5 + A_6 x_6 + A_7 x_7 + A_8 \quad \text{(C.6)}$$

Surrogate Models with One Uncertain Input

Table C.1: Polynomial surrogate model constants for equation (C.1) using a level 3 sparse grid fit to three permeability models in which x = λ_2.

	y	A_1	A_2	A_3	A_4
KI	W^{Cu}	-4.38×10^{-8}	1.51×10^{-5}	-1.18×10^{-3}	0.066
	V_{spec}	0	2.57×10^{-6}	-1.70×10^{-4}	0.0034
	t_s [s]	0	0	-0.27	1430.8
KII	W^{Cu}	-8.36×10^{-8}	2.60×10^{-5}	-2.32×10^{-3}	0.097
	V_{spec}	-1.18×10^{-8}	5.44×10^{-6}	-4.38×10^{-4}	0.018
	t_s [s]	0	-0.011	2.19	1306.1
KIII	W^{Cu}	-7.98×10^{-8}	3.18×10^{-5}	-3.13×10^{-3}	0.13
	V_{spec}	-3.76×10^{-8}	1.54×10^{-5}	-1.26×10^{-3}	0.036
	t_s [s]	8.19×10^{-5}	-0.043	5.55	1203.6

Table C.2: Polynomial surrogate model constants for equation (C.1) using a level 3 sparse grid fit to different levels of uncertainty in the heat transfer coefficient, in which x = h.

	y	A_1	A_2	A_3	A_4
Case A1	W^{Cu}	-8.48×10^{-12}	5.04×10^{-8}	-1.07×10^{-4}	0.125
	V_{spec}	-1.01×10^{-11}	5.94×10^{-8}	-1.27×10^{-4}	0.132
	t_s [s]	-4.56×10^{-7}	2.65×10^{-3}	-5.51	5235.4
Case A2	W^{Cu}	-1.13×10^{-11}	6.24×10^{-8}	-1.23×10^{-4}	0.133
	V_{spec}	-1.75×10^{-11}	9.22×10^{-8}	-1.73×10^{-4}	0.151
	t_s [s]	-2.80×10^{-7}	1.76×10^{-3}	-4.07	4487
Case A3	W^{Cu}	-4.30×10^{-12}	3.17×10^{-8}	-7.89×10^{-5}	0.112
	V_{spec}	-1.59×10^{-10}	7.24×10^{-7}	-1.11×10^{-3}	0.617
	t_s [s]	0	4.74×10^{-4}	-2.10	3491.6

Table C.3: Polynomial surrogate model constants for equation (C.2) using a level 3 sparse grid fit to different levels of uncertainty in the reduced set of material properties, in which $x_1 = \beta_{S,l}$, $x_2 = \Delta\rho$, $x_3 = L_f$, $x_4 = \rho_s$.

	Case B1		**Case B2**		**Case B3**	**Case B4**
y	W^{Cu}	V_{spec}	W^{Cu}	V_{spec}	V_{spec}	W^{Cu}
A_1	-0.14	0.054	0.36	0.19	-0.62	-0.95
A_2	$1.37\text{x}10^{-4}$	$1.47\text{x}10^{-3}$	$2.19\text{x}10^{-4}$	$-5.21\text{x}10^{-4}$	$-7.92\text{x}10^{-3}$	$8.48\text{x}10^{-5}$
A_3	$2.03\text{x}10^{-7}$	$-2.77\text{x}10^{-7}$	$4.75\text{x}10^{-7}$	$1.60\text{x}10^{-6}$	$-9.34\text{x}10^{-7}$	$1.19\text{x}10^{-6}$
A_4	$-2.53\text{x}10^{-5}$	$9.93\text{x}10^{-5}$	$6.69\text{x}10^{-6}$	$-1.01\text{x}10^{-4}$	$3.03\text{x}10^{-4}$	$3.63\text{x}10^{-5}$
A_5	-0.27	0.27	0.65	-0.16	-2.50	-2.62
A_6	$8.03\text{x}10^{-7}$	$1.19\text{x}10^{-6}$	$-9.58\text{x}10^{-7}$	$1.12\text{x}10^{-6}$	$1.28\text{x}10^{-5}$	$-1.20\text{x}10^{-5}$
A_7	$1.84\text{x}10^{-11}$	$-2.80\text{x}10^{-11}$	$1.74\text{x}10^{-10}$	$-2.65\text{x}10^{-10}$	$-2.24\text{x}10^{-9}$	$5.51\text{x}10^{-10}$
A_8	$-1.22\text{x}10^{-8}$	$-7.93\text{x}10^{-9}$	$-5.93\text{x}10^{-8}$	$-4.70\text{x}10^{-8}$	$-1.27\text{x}10^{-7}$	$4.87\text{x}10^{-8}$
A_9	$6.42\text{x}10^{-4}$	$2.78\text{x}10^{-3}$	$-1.98\text{x}10^{-4}$	$9.14\text{x}10^{-5}$	$3.02\text{x}10^{-3}$	$-7.31\text{x}10^{-3}$
A_{10}	$-4.81\text{x}10^{-13}$	$-1.12\text{x}10^{-13}$	$-8.92\text{x}10^{-13}$	$-9.45\text{x}10^{-13}$	$-6.59\text{x}10^{-12}$	$-5.04\text{x}10^{-12}$
A_{11}	$-1.10\text{x}10^{-10}$	$-4.72\text{x}10^{-11}$	$-4.74\text{x}10^{-11}$	$-5.59\text{x}10^{-11}$	$-7.08\text{x}10^{-11}$	$4.06\text{x}10^{-11}$
A_{12}	$8.96\text{x}10^{-7}$	$-2.40\text{x}10^{-7}$	$1.51\text{x}10^{-6}$	$3.18\text{x}10^{-6}$	$3.36\text{x}10^{-6}$	$5.61\text{x}10^{-6}$
A_{13}	$-1.25\text{x}10^{-8}$	$-1.27\text{x}10^{-8}$	$8.88\text{x}10^{-9}$	$2.74\text{x}10^{-8}$	$7.97\text{x}10^{-8}$	$-3.39\text{x}10^{-8}$
A_{14}	$4.53\text{x}10^{-5}$	$2.02\text{x}10^{-4}$	$-6.60\text{x}10^{-5}$	$-3.10\text{x}10^{-4}$	$9.15\text{x}10^{-4}$	$2.10\text{x}10^{-4}$
A_{15}	-0.31	0.30	0.25	-0.38	-1.71	-4.33
A_{16}	3.48x10-10^{-7}	$2.86\text{x}10^{-9}$	$-2.64\text{x}10^{-9}$	$3.05\text{x}10^{-8}$	$3.25\text{x}10^{-9}$	$3.02\text{x}10^{-8}$
A_{17}	$1.73\text{x}10^{-12}$	$5.21\text{x}10^{-12}$	$2.16\text{x}10^{-12}$	$6.13\text{x}10^{-12}$	$-2.03\text{x}10^{-11}$	$-6.79\text{x}10^{-12}$
A_{18}	$3.23\text{x}10^{-11}$	$4.45\text{x}10^{-10}$	$-1.47\text{x}10^{-11}$	-1.37x10-9	$-1.00\text{x}10^{-9}$	$-1.52\text{x}10^{-9}$
A_{19}	$1.23\text{x}10^{-7}$	$-1.80\text{x}10^{-7}$	$-3.62\text{x}10^{-6}$	$2.85\text{x}10^{-5}$	$2.36\text{x}10^{-5}$	$2.42\text{x}10^{-5}$
A_{20}	$1.70\text{x}10^{-15}$	$-6.54\text{x}10^{-16}$	$1.39\text{x}10^{-15}$	$-3.70\text{x}10^{-16}$	$-9.67\text{x}10^{-15}$	$1.01\text{x}10^{-14}$
A_{21}	$1.84\text{x}10^{-13}$	$-4.45\text{x}10^{-14}$	$8.88\text{x}10^{-14}$	$7.04\text{x}10^{-14}$	$2.97\text{x}10^{-13}$	$-8.02\text{x}10^{-14}$
A_{22}	$-6.70\text{x}10^{-10}$	$3.72\text{x}10^{-9}$	$1.69\text{x}10^{-10}$	$3.55\text{x}10^{-9}$	$-6.20\text{x}10^{-9}$	$-1.10\text{x}10^{-8}$
A_{23}	$-6.89\text{x}10^{-12}$	$-1.65\text{x}10^{-11}$	$-2.29\text{x}10^{-11}$	$-8.88\text{x}10^{-11}$	$-1.60\text{x}10^{-10}$	$-2.79\text{x}10^{-10}$
A_{24}	$6.52\text{x}10^{-8}$	$5.14\text{x}10^{-7}$	$1.34\text{x}10^{-7}$	$-1.87\text{x}10^{-7}$	$3.10\text{x}10^{-7}$	$8.35\text{x}10^{-7}$
A_{25}	$6.06\text{x}1^{-5}$	$-1.02\text{x}10^{-3}$	$-1.53\text{x}10^{-3}$	$7.27\text{x}10^{-3}$	$6.22\text{x}10^{-3}$	$5.00\text{x}10^{-3}$
A_{26}	$8.92\text{x}10^{-19}$	$-8.58\text{x}10^{-19}$	$-1.91\text{x}10^{-18}$	$-1.26\text{x}10^{-18}$	$-8.95\text{x}10^{-18}$	$-1.57\text{x}10^{-17}$
A_{27}	$9.30\text{x}10^{-17}$	$-1.60\text{x}10^{-16}$	$-9.00\text{x}10^{-17}$	$2.17\text{x}10^{-16}$	$-1.93\text{x}10^{-15}$	$9.12\text{x}10^{-17}$
A_{28}	$-1.07\text{x}10^{-12}$	$9.91\text{x}10^{-13}$	$2.23\text{x}10^{-12}$	$-2.67\text{x}10^{-13}$	$7.82\text{x}10^{-12}$	$1.72\text{x}10^{-11}$
A_{29}	$2.92\text{x}10^{-14}$	$-5.22\text{x}10^{-14}$	$-1.98\text{x}10^{-14}$	$-3.11\text{x}10^{-14}$	$-3.05\text{x}10^{-13}$	$-1.12\text{x}10^{-14}$
A_{30}	$-2.02\text{x}10^{-10}$	$4.41\text{x}10^{-10}$	$2.21\text{x}10^{-10}$	$3.77\text{x}10^{-11}$	$3.31\text{x}10^{-9}$	$5.59\text{x}10^{-11}$
A_{31}	$8.22\text{x}10^{-7}$	$-5.04\text{x}10^{-7}$	$-6.24\text{x}10^{-7}$	$1.85\text{x}10^{-6}$	$-7.05\text{x}10^{-6}$	$-6.30\text{x}10^{-6}$
A_{32}	$1.90\text{x}10^{-13}$	$-6.26\text{x}10^{-12}$	$-8.26\text{x}10^{-12}$	$-9.22\text{x}10^{-13}$	$-1.15\text{x}10^{-11}$	$-3.13\text{x}10^{-11}$
A_{33}	$-1.22\text{x}10^{-8}$	$7.36\text{x}10^{-8}$	$8.84\text{x}10^{-8}$	$2.78\text{x}10^{-8}$	$2.49\text{x}10^{-7}$	$1.73\text{x}10^{-7}$
A_{34}	$6.57\text{x}10^{-5}$	$-1.82\text{x}10^{-4}$	$-3.23\text{x}10^{-4}$	$-2.44\text{x}10^{-4}$	$-1.67\text{x}10^{-3}$	$-3.3.\text{x}10^{-4}$
A_{35}	-0.18	0.17	0.33	0.52	2.58	0.58

Table C.4: Polynomial surrogate model constants for equation (C.2) using a level 3 sparse grid fit to different levels of uncertainty in the reduced set of material properties, in which x_1= c, x_2 = k, $x_3 = L_f$, $x_4 = \rho_s$.

	Case B1	**Case B2**
y	t_s **[s]**	t_s **[s]**
A_1	-6.78×10^{-8}	-1.86×10^{-7}
A_2	-5.89×10^{-7}	-3.05×10^{-6}
A_3	-4.24×10^{-10}	-8.65×10^{-10}
A_4	1.28×10^{-7}	-1.35×10^{-7}
A_5	2.17×10^{-4}	1.80×10^{-3}
A_6	1.24×10^{-5}	-4.03×10^{-6}
A_7	1.61×10^{-10}	5.28×10^{-10}
A_8	-7.05×10^{-7}	-5.68×10^{-7}
A_9	-2.71×10^{-3}	6.45×10^{-3}
A_{10}	-2.54×10^{-12}	6.20×10^{-12}
A_{11}	-1.47×10^{-10}	-2.85×10^{-10}
A_{12}	3.25×10^{-6}	7.23×10^{-6}
A_{13}	-2.46×10^{-8}	3.30×10^{-8}
A_{14}	2.43×10^{-4}	4.86×10^{-4}
A_{15}	-0.71	4.03
A_{16}	-3.94×10^{-4}	-1.98×10^{-4}
A_{17}	5.95×10^{-8}	-1.80×10^{-7}
A_{18}	4.11×10^{-5}	4.53×10^{-6}
A_{19}	0.062	0.17
A_{20}	-2.76×10^{-12}	3.53×10^{-11}
A_{21}	-3.75×10^{-9}	3.33×10^{-9}
A_{22}	-1.73×10^{-5}	1.75×10^{-5}
A_{23}	2.28×10^{-8}	-6.38×10^{-7}
A_{24}	-0.012	1.53×10^{-3}
A_{25}	7.61	-35.34
A_{26}	1.75×10^{-15}	-2.86×10^{-14}
A_{27}	4.37×10^{-13}	-3.02×10^{-12}
A_{28}	1.03×10^{-9}	4.35×10^{-8}
A_{29}	-2.00×10^{-10}	-8.55×10^{-11}
A_{30}	2.89×10^{-6}	5.09×10^{-6}
A_{31}	-3.18×10^{-3}	-0.026
A_{32}	-5.05×10^{-8}	1.70×10^{-8}
A_{33}	5.05×10^{-4}	-3.06×10^{-5}
A_{34}	-0.75	-0.83
A_{35}	869.6	6888.0

Table C.5: Polynomial surrogate model constants for equation (C.3) using a level 2 sparse grid fit to different levels of uncertainty in the reduced set of material properties, in which $x_1 = \beta_{S,l}$, $x_2 = \Delta\rho$, $x_3 = L_f$, $x_4 = \rho_s$.

	Case B3	**Case B4**
y	W^{Cu}	V_{spec}
A_1	-0.016	0.046
A_2	$-7.64\text{x}10^{-5}$	$-1.15\text{x}10^{-4}$
A_3	$-7.80\text{x}10^{-8}$	$-8.54\text{x}10^{-8}$
A_4	$-3.14\text{x}10^{-5}$	$-1.44\text{x}10^{-19}$
A_5	0.046	0.020
A_6	$-5.35\text{x}10^{-8}$	$1.01\text{x}10^{-6}$
A_7	$1.37\text{x}10^{-10}$	$4.30\text{x}10^{-10}$
A_8	$1.086\text{x}10^{-7}$	$2.13\text{x}10^{-7}$
A_9	$5.10\text{x}10^{-4}$	$-4.17\text{x}10^{-4}$
A_{10}	$-4.25\text{x}10^{-14}$	$-7.99\text{x}10^{-13}$
A_{11}	$5.87\text{x}10^{-11}$	$2.27\text{x}10^{-11}$
A_{12}	$-9.97\text{x}10^{-8}$	$7.09\text{x}10^{-7}$
A_{13}	$1.05\text{x}10^{-8}$	$1.77\text{x}10^{-8}$
A_{14}	$-6.36\text{x}10^{-5}$	$-3.45\text{x}10^{-5}$
A_{15}	0.062	0.17

Table C.6: Polynomial surrogate model constants for equation (C.3) using a level 2 sparse grid fit to different levels of uncertainty in the reduced set of material properties, in which x_1= c, x_2 = k, $x_3 = L_f$, $x_4 = \rho_s$.

	Case B3
y	t_s **[s]**
A_1	$2.86\text{x}10^{-4}$
A_2	$-2.10\text{x}10^{-3}$
A_3	$6.34\text{x}10^{-8}$
A_4	$1.71\text{x}10^{-4}$
A_5	-0.27
A_6	0.067
A_7	$-1.55\text{x}10^{-5}$
A_8	$-2.91\text{x}10^{-3}$
A_9	-8.22
A_{10}	$5.13\text{x}10^{-9}$
A_{11}	$1.58\text{x}10^{-6}$
A_{12}	$3.02\text{x}10^{-3}$
A_{13}	$2.24\text{x}10^{-5}$
A_{14}	0.18
A_{15}	996.9

Table C.7: Polynomial surrogate model constants for equation (C.4) using a level 1 sparse grid fit to different levels of uncertainty in the reduced set of material properties, in which x_1= c, x_2 = k, $x_3 = L_f$, $x_4 = \rho_s$.

	Case B3
y	t_s **[s]**
A_1	0.53
A_2	-5.94
A_3	3.20×10^{-3}
A_4	0.69
A_5	-1463.4

Surrogate Models with Six Uncertain Inputs

Table C.8: Polynomial surrogate model constants for equation (C.5) using a level 2 sparse grid fit to the all of the important inputs studied, in which $x_1 = \lambda$, $x_2 = \beta_{s,l}$, $x_3 = \Delta\rho$, $x_4 = h$, $x_5 = L_f$, $x_6 = \rho_s$.

y	W^{Cu}	V_{spec}
A_1	386119.9	-3332407
A_2	-568.3	-548.8
A_3	1.35	0.81
A_4	-0.28	-0.37
A_5	$1.19\text{x}10^{-3}$	$1.20\text{x}10^{-3}$
A_6	0.45	0.50
A_7	-899.2	-177.6
A_8	0.073	-0.22
A_9	$-7.64\text{x}10^{-5}$	$-5.74\text{x}10^{-5}$
A_{10}	$1.67\text{x}10^{-5}$	$8.32\text{x}10^{-6}$
A_{11}	$-7.80\text{x}10^{-8}$	$-8.54\text{x}10^{-8}$
A_{12}	$-3.14\text{x}10^{-5}$	$-3.03\text{x}10^{-5}$
A_{13}	0.20	-0.23
A_{14}	$4.68\text{x}10^{-7}$	$-1.11\text{x}10^{-6}$
A_{15}	$-2.95\text{x}10^{-8}$	$-2.10\text{x}10^{-8}$
A_{16}	$1.37\text{x}10^{-10}$	$2.15\text{x}10^{-10}$
A_{17}	$1.09\text{x}10^{-7}$	$1.68\text{x}10^{-8}$
A_{18}	$-2.85\text{x}10^{-4}$	$-1.44\text{x}10^{-3}$
A_{19}	$9.86\text{x}10^{-9}$	$1.95\text{x}10^{-8}$
A_{20}	$-2.94\text{x}10^{-11}$	$-1.04\text{x}10^{-11}$
A_{21}	$-1.15\text{x}10^{-8}$	$-1.18\text{x}10^{-8}$
A_{22}	$2.95\text{x}10^{-5}$	$-6.12\text{x}10^{-6}$
A_{23}	$1.87\text{x}10^{-13}$	$-1.81\text{x}10^{-12}$
A_{24}	$5.87\text{x}10^{-11}$	$4.53\text{x}10^{-11}$
A_{25}	$-3.45\text{x}10^{-7}$	$1.26\text{x}10^{-6}$
A_{26}	$2.32\text{x}10^{-9}$	$5.49\text{x}10^{-9}$
A_{27}	$-4.06\text{x}10^{-5}$	$-4.02\text{x}10^{-5}$
A_{28}	0.17	-0.50

Table C.9: Polynomial surrogate model constants for equation (C.5) using a level 2 sparse grid fit to the all of the important inputs studied, in which $x_1 = \lambda$, $x_2 = c$, $x_3 = h$, $x_4 = k$, $x_5 = L_f$, $x_6 = \rho_s$.

y	t_s **[s]**
A_1	31752201064
A_2	8.07
A_3	415.0
A_4	2932.2
A_5	-0.057
A_6	-610.4
A_7	-5517495.6
A_8	7.92×10^{-4}
A_9	-1.85×10^{-4}
A_{10}	-2.10×10^{-3}
A_{11}	6.34×10^{-8}
A_{12}	1.71×10^{-4}
A_{13}	-1.00
A_{14}	5.62×10^{-4}
A_{15}	-1.44×10^{-3}
A_{16}	-1.18×10^{-6}
A_{17}	-2.86×10^{-4}
A_{18}	-0.79
A_{19}	0.055
A_{20}	-1.55×10^{-5}
A_{21}	-2.29×10^{-3}
A_{22}	-2.69
A_{23}	9.58×10^{-9}
A_{24}	1.58×10^{-6}
A_{25}	4.62×10^{-3}
A_{26}	1.73×10^{-5}
A_{27}	0.71
A_{28}	1884.9

Surrogate Models with Seven Uncertain Inputs

Table C.10: Polynomial surrogate model constants for equation (C.6) using a level 1 sparse grid fit to input uncertainty in the full set of material properties, in which $x_1 = \beta_{S,l}$, $x_2 = \beta_{T,l}$, $x_3 = c$, $x_4 = \Delta\rho$, $x_5 = k$, $x_6 = L_f$, $x_7 = \rho_s$.

	y	A_1	A_2	A_3	A_4	A_5	A_6	A_7	A_8
Case B1	W^{Cu}	-0.025	11.59	5.39×10^{-3}	-5.99×10^{-5}	-4.36×10^{-5}	4.67×10^{-8}	5.98×10^{-6}	-0.017
	V_{spec}	-0.036	59.81	6.96×10^{-6}	-1.41×10^{-4}	-6.54×10^{-5}	7.18×10^{-8}	1.09×10^{-6}	-0.055
	t_s [s]	55.38	14351	0.51	0.55	-6.57	3.17×10^{-3}	0.69	-1099
Case B2	W^{Cu}	-0.025	11.83	5.76×10^{-6}	-6.00×10^{-5}	-3.92×10^{-5}	4.66×10^{-8}	6.42×10^{-6}	-0.020
	V_{spec}	-0.033	79.7	7.95×10^{-6}	-1.61×10^{-4}	-5.82×10^{-5}	7.52×10^{-8}	2.91×10^{-6}	-0.072
	t_s [s]	51.16	41733	0.51	0.57	-6.20	3.21×10^{-3}	0.70	-1207
Case B3	W^{Cu}	-0.026	11.48	5.88×10^{-6}	-5.93×10^{-5}	-4.19×10^{-5}	4.91×10^{-8}	7.58×10^{-6}	-0.025
	V_{spec}	-0.036	102.5	9.94×10^{-6}	-1.72×10^{-4}	-5.82×10^{-5}	7.69×10^{-8}	5.82×10^{-6}	-0.093
	t_s [s]	44.07	45845	0.51	0.57	-6.00	3.21×10^{-3}	0.70	-1254
Case B4	W^{Cu}	-0.027	14.72	5.34×10^{-6}	-5.86×10^{-5}	-3.60×10^{-5}	4.85×10^{-8}	9.60×10^{-6}	-0.033
	V_{spec}	-0.049	102.5	7.95×10^{-6}	-1.93×10^{-4}	-1.45×10^{-4}	9.23×10^{-8}	7.27×10^{-6}	-0.106
	t_s [s]	75.77	-63897	0.53	0.63	-5.94	3.20×10^{-3}	0.69	-1220

Surrogate Models Used in CHAPTER 6: Uncertainty Quantification in Modeling Equiaxed Alloy Solidification

The equations are ordered based on their number of dependent variables (x_i) and degree of polynomial. Each constant in the equation is denoted as A_i. Equations (C.7) and (C.8) have one dependent variable and are cubic and quadratic polynomials respectively. Equations (C.9) and (C.10) have two dependent variables and are cubic and quadratic polynomials respectively. Equation (C.11) is a linear polynomial with five dependent variables. Equation (C.12) is a quadratic polynomial with six dependent variables. Equation (C.13) has eight dependent variables for the linear polynomial. Equations (C.14) and (C.15) are both linear polynomials with eight and thirteen dependent variables respectively.

General form of the equations:

$$y = A_1 x^3 + A_2 x^2 + A_3 x + A_4 \tag{C.7}$$

$$y = A_1 x^2 + A_2 x + A_3 \tag{C.8}$$

$$y = A_1 x_1^3 + A_2 x_1^2 x_2 + A_3 x_1^2 + A_4 x_1 x_2^2 + A_5 x_1 x_2 + A_6 x_1 + A_7 x_2^3 + A_8 x_2^2 + A_9 x_2 + A_{10} \tag{C.9}$$

$$y = A_1 x_1^2 + A_2 x_1 x_2 + A_3 x_1 + A_4 x_2^2 + A_5 x_2 + A_6 \tag{C.10}$$

$$y = A_1 x_1 + A_2 x_2 + A_3 x_3 + A_4 x_4 + A_5 x_5 + A_6 \tag{C.11}$$

$$y = A_1 x_1^2 + A_2 x_1 x_2 + A_3 x_1 x_3 + A_4 x_1 x_4 + A_5 x_1 x_5 + A_6 x_1 x_6 + A_7 x_1 + A_8 x_2^2 + A_9 x_2 x_3 + A_{10} x_2 x_4 + A_{11} x_2 x_5 + A_{12} x_2 x_6 + A_{13} x_2 + A_{14} x_3^2 + A_{15} x_3 x_4 + A_{16} x_3 x_5 + A_{17} x_3 x_6 + A_{18} x_3 + A_{19} x_4^2 + A_{20} x_4 x_5 + A_{21} x_4 x_6 + A_{22} x_4 + A_{23} x_5^2 + A_{24} x_5 x_6 + A_{25} x_5 + A_{26} x_6^2 + A_{27} x_6 + A_{28} \tag{C.12}$$

$$y = A_1 x_1 + A_2 x_2 + A_3 x_3 + A_4 x_4 + A_5 x_5 + A_6 x_6 + A_7 x_7 + A_8 x_8 + A_9 \tag{C.13}$$

$$y = A_1 x_1 + A_2 x_2 + A_3 x_3 + A_4 x_4 + A_5 x_5 + A_6 x_6 + A_7 x_7 + A_8 x_8 + A_9 x_9 + A_{10} \tag{C.14}$$

$$y = A_1 x_1 + A_2 x_2 + A_3 x_3 + A_4 x_4 + A_5 x_5 + A_6 x_6 + A_7 x_7 + A_8 x_8 + A_9 x_9 + A_{10} x_{10} + A_{11} x_{11} + A_{12} x_{12} + A_{13} x_{13} + A_{14} \quad \text{(C.15)}$$

Surrogate Models with One Uncertain Input

Table C.11: Polynomial surrogate model constants for equation (C.7) using a level 3 sparse grid fit uncertainty in the packing fraction where x = $g_{s,crit}$.

y	A_1	A_2	A_3	A_4
W^{Cu}	0.33	-0.33	0.038	0.047
t_s **[s]**	20245.4	-4824.3	1678.0	1365.3

Table C.12: Polynomial surrogate model constants for equation (C.8) using a level 2 sparse grid fit uncertainty in the packing fraction where x = $g_{s,crit}$.

y	A_1	A_2	A_3
V_{spec}	-1.43	0.45	0.0084

Surrogate Models with Two Uncertain Inputs

Table C.13: Polynomial surrogate model constants for equation (C.9) using a level 3 sparse grid fit to different levels of uncertainty in the packing fraction, particle size, dendrite arm spacing, and heat transfer coefficient.

	$x_1 = g_{s,crit}$; $x_2 = d_{diam}$	$x_1 = \lambda_2$; $x_2 = g_{s,crit}$		$x_1 = g_{s,crit}$; $x_2 = h$ **Case C1**	
y	W^{Cu}	W^{Cu}	V_{spec}	W^{Cu}	V_{spec}
A_1	0.51	25814314764.6	55851751942.7	-0.50	-3.36
A_2	1936.3	8690015.4	10046216.8	$1.98\text{x}10^{-4}$	$3.43\text{x}10^{-4}$
A_3	-0.48	-5667343.8	-6160488.9	-0.24	0.87
A_4	4973058.2	-7254.2	-34165.0	$-9.41\text{x}10^{-9}$	$-1.15\text{x}10^{-7}$
A_5	-1079.4	140.3	7979.2	$-1.97\text{x}10^{-5}$	$2.93\text{x}10^{-4}$
A_6	0.078	808.1	451.9	0.035	-0.37
A_7	33701388946.9	0.58	-3.62	$-8.71\text{x}10^{-12}$	$-1.59\text{x}10^{-11}$
A_8	-4096997.2	0.19	4.97	$5.58\text{x}10^{-8}$	$1.32\text{x}10^{-7}$
A_9	178.3	-0.024	-1.15	$-1.21\text{x}10^{-4}$	$-3.26\text{x}10^{-4}$
A_{10}	0.044	$-8.10\text{x}10^{-6}$	0.019	0.13	0.29

Table C.14: Polynomial surrogate model constants for equation (C.10) using a level 2 sparse grid fit to different levels of uncertainty in the packing fraction, particle size, dendrite arm spacing, and heat transfer coefficient.

	$x_1 = g_{s,crit}$; $x_2 = d_{diam}$	$x_1 = g_{s,crit}$; $x_2 = h$ **Case C2**		$x_1 = g_{s,crit}$; $x_2 = h$ **Case C3**	
y	V_{spec}	W^{Cu}	V_{spec}	W^{Cu}	V_{spec}
A_1	-1.34	-0.23	-0.95	-0.23	-1.00
A_2	-53.3	$2.50\text{x}10^{-5}$	$5.33\text{x}10^{-5}$	$2.94\text{x}10^{-5}$	$4.80\text{x}10^{-5}$
A_3	0.42	-0.0019	0.20	-0.0060	0.23
A_4	3735681.7	$1.24\text{x}10^{-8}$	$3.96\text{x}10^{-8}$	$1.39\text{x}10^{-8}$	$5.36\text{x}10^{-8}$
A_5	-284.5	$-5.66\text{x}10^{-5}$	$-1.65\text{x}10^{-4}$	$-6.01\text{x}10^{-5}$	$-1.96\text{x}10^{-4}$
A_6	0.015	0.10	0.18	0.11	0.19

Surrogate Model with Five Uncertain Inputs

Table C.15: Polynomial surrogate model constants for equation (C.11) using a level 1 sparse grid fit to uncertainty in the materials properties where $x_1 = c$, $x_2 = \Delta\rho$, $x_3 = k$, $x_4 = L_f$, and $x_5 = \rho_s$.

y	A_1	A_2	A_3	A_4	A_5	A_6
V_{spec}	$-5.18\text{x}10^{-5}$	$-3.10\text{x}10^{-4}$	$-3.93\text{x}10^{-4}$	$2.92\text{x}10^{-7}$	$3.42\text{x}10^{-5}$	-0.15

Surrogate Model with Six Uncertain Inputs

Table C.16: Polynomial surrogate model constants for equation (C.12) using a level 2 sparse grid fit to uncertainty in the materials properties where $x_1 = \beta_{S,l}$, $x_2 = c$, $x_3 = \Delta\rho$, $x_4 = k$, $x_5 = L_{f,}$ and $x_6 = \rho_s$.

y	W^{Cu}
A_1	-0.029
A_2	$-7.77\text{x}10^{-6}$
A_3	$-3.44\text{x}10^{-5}$
A_4	$9.58\text{x}10^{-5}$
A_5	$-3.82\text{x}10^{-8}$
A_6	$-2.21\text{x}10^{-5}$
A_7	-0.0020
A_8	$4.20\text{x}10^{-8}$
A_9	$6.99\text{x}10^{-9}$
A_{10}	$-5.20\text{x}10^{-8}$
A_{11}	$1.91\text{x}10^{-11}$
A_{12}	$-1.65\text{x}10^{-9}$
A_{13}	$-8.80\text{x}10^{-5}$
A_{14}	$1.47\text{x}10^{-7}$
A_{15}	$6.62\text{x}10^{-8}$
A_{16}	$-1.21\text{x}10^{-10}$
A_{17}	$2.48\text{x}10^{-8}$
A_{18}	$-8.23\text{x}10^{-5}$
A_{19}	$-4.66\text{x}10^{-7}$
A_{20}	$-4.66\text{x}10^{-10}$
A_{21}	$-1.22\text{x}10^{-7}$
A_{22}	$6.95\text{x}10^{-4}$
A_{23}	$5.75\text{x}10^{-13}$
A_{24}	$7.96\text{x}10^{-11}$
A_{25}	$-5.88\text{x}10^{-7}$
A_{26}	$9.37\text{x}10^{-9}$
A_{27}	$-6.32\text{x}10^{-5}$
A_{28}	0.18

Surrogate Model with Eight Uncertain Inputs

Table C.17: Polynomial surrogate model constants for equation (C.13) using a level 1 sparse grid fit to uncertainty in the materials properties where $x_1 = \lambda_2$, $x_2 = c$, $x_3 = \Delta\rho$, $x_4 = g_{s,crit}$, $x_5 = h$, $x_6 = k$, $x_7 = L_f$, and $x_8 = \rho_s$.

y	V_{spec}
A_1	1252.3
A_2	$-4.77\text{x}10^{-5}$
A_3	$-2.69\text{x}10^{-4}$
A_4	-0.021
A_5	$-3.55\text{x}10^{-5}$
A_6	$-3.49\text{x}10^{-4}$
A_7	$3.02\text{x}10^{-7}$
A_8	$2.69\text{x}10^{-5}$
A_9	-0.20

Surrogate Models with Nine Uncertain Inputs

Table C.18: Polynomial surrogate model constants for equation (C.14) using a level 1 sparse grid fit to uncertainty in the materials properties where $x_1 = \beta_{S,l}$, $x_2 = \beta_{S,s}$, $x_3 = \beta_{T,l}$, $x_4 = \beta_{T,s}$ $x_5 = c$, $x_6 = \Delta\rho$, $x_7 = k$, $x_8 = L_f$, and $x_9 = \rho_s$.

y	W^{Cu}	V_{spec}
A_1	-0.016	-0.038
A_2	0.0058	0.030
A_3	11.69	85.44
A_4	80.49	88.86
A_5	$-8.28\text{x}10^{-6}$	$-5.17\text{x}10^{-5}$
A_6	$-1.11\text{x}10^{-4}$	$-3.10\text{x}10^{-4}$
A_7	$-7.30\text{x}10^{-5}$	$-3.93\text{x}10^{-4}$
A_8	$9.09\text{x}10^{-8}$	$-2.92\text{x}10^{-7}$
A_9	$9.18\text{x}10^{-6}$	$3.42\text{x}10^{-5}$
A_{10}	-0.036	-0.16

Surrogate Models with Thirteen Uncertain Inputs

Table C.19: Polynomial surrogate model constants for equation (C.15) using a level 2 sparse grid fit to uncertainty in the materials properties where $x_1 = \lambda_2$, $x_2 = \beta_{S,l}$, $x_3 = \beta_{S,s}$, $x_4 = \beta_{T,l}$, $x_5 = \beta_{T,s}$ $x_6 = c$, $x_7 = \Delta\rho$, $x_8 = g_{s,crit}$, $x_9 = h$, $x_{10} = k$, $x_{11} = L_f$, $x_{12} = d_{diam}$ and $x_{13} = \rho_s$.

y	W^{Cu}	V_{spec}
A_1	498.8	1252.3
A_2	-0.016	-0.020
A_3	0.0045	0.021
A_4	-2.95	-34.2
A_5	80.91	88.9
A_6	$-6.18\text{x}10^{-6}$	$-4.77\text{x}10^{-5}$
A_7	$-1.09\text{x}10^{-4}$	$-2.69\text{x}10^{-4}$
A_8	-0.037	-0.021
A_9	$-1.55\text{x}10^{-5}$	$-3.55\text{x}10^{-5}$
A_{10}	$-7.73\text{x}10^{-5}$	$-3.49\text{x}10^{-4}$
A_{11}	$8.77\text{x}10^{-8}$	$3.02\text{x}10^{-7}$
A_{12}	-29.4	66.6
A_{13}	$7.55\text{x}10^{-6}$	$2.69\text{x}10^{-5}$
A_{14}	-0.046	-0.20

Surrogate Models Used in CHAPTER 7: Uncertainty Quantification in Modeling Aluminum Direct Chill Casting

The equations are ordered based on their number of dependent variables (x_i) and degree of polynomial. Each constant in the equation is denoted as A_i. Equations (C.16), (C.17), and (C.18) have one dependent variable and are cubic, quadratic, and linear polynomials respectively. Equations (C.19)-(C.24) are linear polynomials with three, four, five, six, nine and thirteen dependent variables respectively.

General form of the equations:

$$y = A_1 x^3 + A_2 x^2 + A_3 x + A_4 \quad \text{(C.16)}$$

$$y = A_1 x^2 + A_2 x + A_3 \quad \text{(C.17)}$$

$$y = A_1 x + A_3 \quad \text{(C.18)}$$

$$y = A_1 x_1 + A_2 x_2 + A_3 x_3 + A_4 \quad \text{(C.19)}$$

$$y = A_1 x_1 + A_2 x_2 + A_3 x_3 + A_4 x_4 + A_5 \quad \text{(C.20)}$$

$$y = A_1 x_1 + A_2 x_2 + A_3 x_3 + A_4 x_4 + A_5 x_5 + A_6 \quad \text{(C.21)}$$

$$y = A_1 x_1 + A_2 x_2 + A_3 x_3 + A_4 x_4 + A_5 x_5 + A_6 x_6 + A_7 \quad \text{(C.22)}$$

$$y = A_1 x_1 + A_2 x_2 + A_3 x_3 + A_4 x_4 + A_5 x_5 + A_6 x_6 + A_7 x_7 + A_8 x_8 + A_9 x_9 + A_{10} \quad \text{(C.23)}$$

$$y = A_1 x_1 + A_2 x_2 + A_3 x_3 + A_4 x_4 + A_5 x_5 + A_6 x_6 + A_7 x_7 + A_8 x_8 + A_9 x_9 + A_{10} x_{10} + A_{11} x_{11} + A_{12} x_{12} + A_{13} x_{13} + A_{14} \quad \text{(C.24)}$$

Surrogate Models with One Uncertain Input

Table C.20: Polynomial surrogate model constants for equation (C.16) using a level 3 sparse grid fit to uncertainty in the dendrite arm spacing, heat transfer coefficient, and packing fraction.

	y	A_1	A_2	A_3	A_4
x = λ_2	W^{Cu}	14224737565.3	-3086701.7	210.5	0.0047
x = λ_2	**SD [m]**	5624347562.6	-1270956.9	58.0	0.47
x = h	**SD [m]**	-0.025	0.10	-0.16	0.55
x = $g_{s,crit}$	**SD [m]**	-5.68	3.13	-0.35	0.47

Table C.21: Polynomial surrogate model constants for equation (C.17) using a level 2 sparse grid fit to uncertainty in the packing fraction where x = d_{diam}.

y	A_1	A_2	A_3
W^{Cu}	593217.2	-7.25	0.0087

Table C.22: Polynomial surrogate model constants for equation (C.18) using a level 1 sparse grid fit to uncertainty in the particle size, heat transfer coefficient, and packing fraction.

	y	A_1	A_2
x = d_{diam}	**SD [m]**	-10.57	0.46
x = h	W^{Cu}	$-8.59\text{x}10^{-4}$	0.0099
x = $g_{s,crit}$	W^{Cu}	0.012	0.0071

Surrogate Models with Three Uncertain Inputs

Table C.23: Polynomial surrogate model constants for equation (C.19) using a level 1 sparse grid fit to different levels of uncertainty material properties, where x_1 = k, x_2 = L_f, and x_3 = ρ_s.

	y	A_1	A_2	A_3	A_4
Case D1	**SD [m]**	-0.0027	$9.64\text{x}10^{-7}$	$1.48\text{x}10^{-4}$	0.055
Case D2	**SD [m]**	-0.0027	$9.55\text{x}10^{-7}$	$1.49\text{x}10^{-4}$	0.051

Surrogate Models with Four Uncertain Inputs

Table C.24: Polynomial surrogate model constants for equation (C.20) using a level 1 sparse grid fit to uncertainty in the materials properties where x_1 = c, x_2 = $\Delta\rho$, x_3 = k, and x_4 = ρ_s.

	y	A_1	A_2	A_3	A_4	A_5
Case D1	W^{Cu}	$5.15\text{x}10^{-6}$	$-2.17\text{x}10^{-5}$	$-3.42\text{x}10^{-5}$	$-9.44\text{x}10^{-7}$	0.0050
Case D2	W^{Cu}	$5.42\text{x}10^{-6}$	$-1.96\text{x}10^{-5}$	$-1.80\text{x}10^{-5}$	$-9.89\text{x}10^{-7}$	0.0031

Surrogate Model with Five Uncertain Inputs

Table C.25: Polynomial surrogate model constants for equation (C.21) using a level 1 sparse grid fit to uncertainty in the materials properties where x_1 = $g_{s,crit}$, x_2 = h, x_3 = k, x_4 = L_f, and x_5 = ρ_s.

y	**SD [m]**
A_1	0.14
A_2	-0.035
A_3	-0.0027
A_4	$9.10\text{x}10^{-7}$
A_5	$1.46\text{x}10^{-4}$
A_6	0.10

Surrogate Model with Six Uncertain Inputs

Table C.26: Polynomial surrogate model constants for equation (C.22) using a level 1 sparse grid fit to uncertainty in the materials properties where x_1 = λ_2, x_2 = c, x_3 = d_{diam}, x_4 = $\Delta\rho$, x_5 = $g_{s,crit}$, and x_6 = k.

y	W^{Cu}
A_1	8.92
A_2	$4.42\text{x}10^{-6}$
A_3	24.74
A_4	$-2.55\text{x}10^{-5}$
A_5	0.012
A_6	$-2.90\text{x}10^{-5}$
A_7	-0.0020

Surrogate Models with Nine Uncertain Inputs

Table C.27: Polynomial surrogate model constants for equation (C.23) using a level 1 sparse grid fit to uncertainty in the materials properties where $x_1 = \beta_{S,l}$, $x_2 = \beta_{S,s}$, $x_3 = \beta_{T,l}$, $x_4 = \beta_{T,s}$ $x_5 = c$, $x_6 = \Delta\rho$, $x_7 = k$, $x_8 = L_f$, and $x_9 = \rho_s$.

	Case D1		**Case D2**	
y	W^{Cu}	**SD [m]**	W^{Cu}	**SD [m]**
A_1	0.0016	-0.0040	0.0019	-0.0048
A_2	$1.96\text{x}10^{-5}$	0.0030	$-2.38\text{x}10^{-4}$	0.0041
A_3	6.92	-68.11	11.54	-68.96
A_4	-2.11	46.29	-0.72	52.06
A_5	$5.05\text{x}10^{-6}$	$1.92\text{x}10^{-5}$	$5.42\text{x}10^{-6}$	$1.94\text{x}10^{-4}$
A_6	$-2.17\text{x}10^{-5}$	$4.23\text{x}10^{-5}$	$-1.96\text{x}10^{-5}$	$4.03\text{x}10^{-5}$
A_7	$-3.42\text{x}10^{-5}$	-0.0027	$-1.80\text{x}10^{-5}$	-0.0027
A_8	$3.98\text{x}10^{-9}$	$9.64\text{x}10^{-7}$	$-2.85\text{x}10^{-9}$	$9.55\text{x}10^{-7}$
A_9	$-9.44\text{x}10^{-7}$	$1.48\text{x}10^{-4}$	$-9.89\text{x}10^{-7}$	$1.49\text{x}10^{-4}$
A_{10}	0.0038	0.062	0.0040	0.050

Surrogate Models with Thirteen Uncertain Inputs

Table C.28: Polynomial surrogate model constants for equation (C.24) using a level 2 sparse grid fit to uncertainty in the materials properties where $x_1 = \lambda_2$, $x_2 = \beta_{S,l}$, $x_3 = \beta_{S,s}$, $x_4 = \beta_{T,l}$, $x_5 = \beta_{T,s}$, $x_6 = c$, $x_7 = d_{diam,}$ $x_8 = \Delta\rho$, $x_9 = g_{s,crit}$, $x_{10} = h$, $x_{11} = k$, $x_{12} = L_f$, and $x_{13} = \rho_s$.

y	W^{Cu}	**SD [m]**
A_1	8.92	-25.31
A_2	$9.46\text{x}10^{-4}$	-0.0043
A_3	$3.17\text{x}10^{-4}$	0.0033
A_4	2.90	-82.36
A_5	4.56	62.20
A_6	$4.20\text{x}10^{-6}$	$5.95\text{x}10^{-6}$
A_7	24.74	-12.51
A_8	$-2.55\text{x}10^{-5}$	$1.79\text{x}10^{-5}$
A_9	0.012	0.14
A_{10}	$-6.37\text{x}10^{-4}$	-0.035
A_{11}	$-2.90\text{x}10^{-5}$	-0.0027
A_{12}	$5.46\text{x}10^{-10}$	$9.10\text{x}10^{-7}$
A_{13}	$-5.51\text{x}10^{-7}$	$1.46\text{x}10^{-4}$
A_{14}	$4.99\text{x}10^{-4}$	0.11

VITA

VITA

Kyle Fezi
Graduate School, Purdue University

Kyle Fezi was born in Kendallville Indiana and grew up in Fort Wayne Indiana with his mother, father, and older sister until graduating from Homestead High School in 2006. He enrolled in engineering at Purdue University in August 2006 and completed his BS in Materials Engineering in May 2010. While in the last semester of his undergraduate education, he started graduate school as a quarter time graduate Masters' student in Materials Engineering at Purdue University. Upon graduating with his BS, he began his full time graduate research project on modeling transport phenomena in electroslag remelting in May 2010. He graduated with his Masters' degree in May 2013 after which he began pursuing his PhD in Materials Engineering at Purdue University.